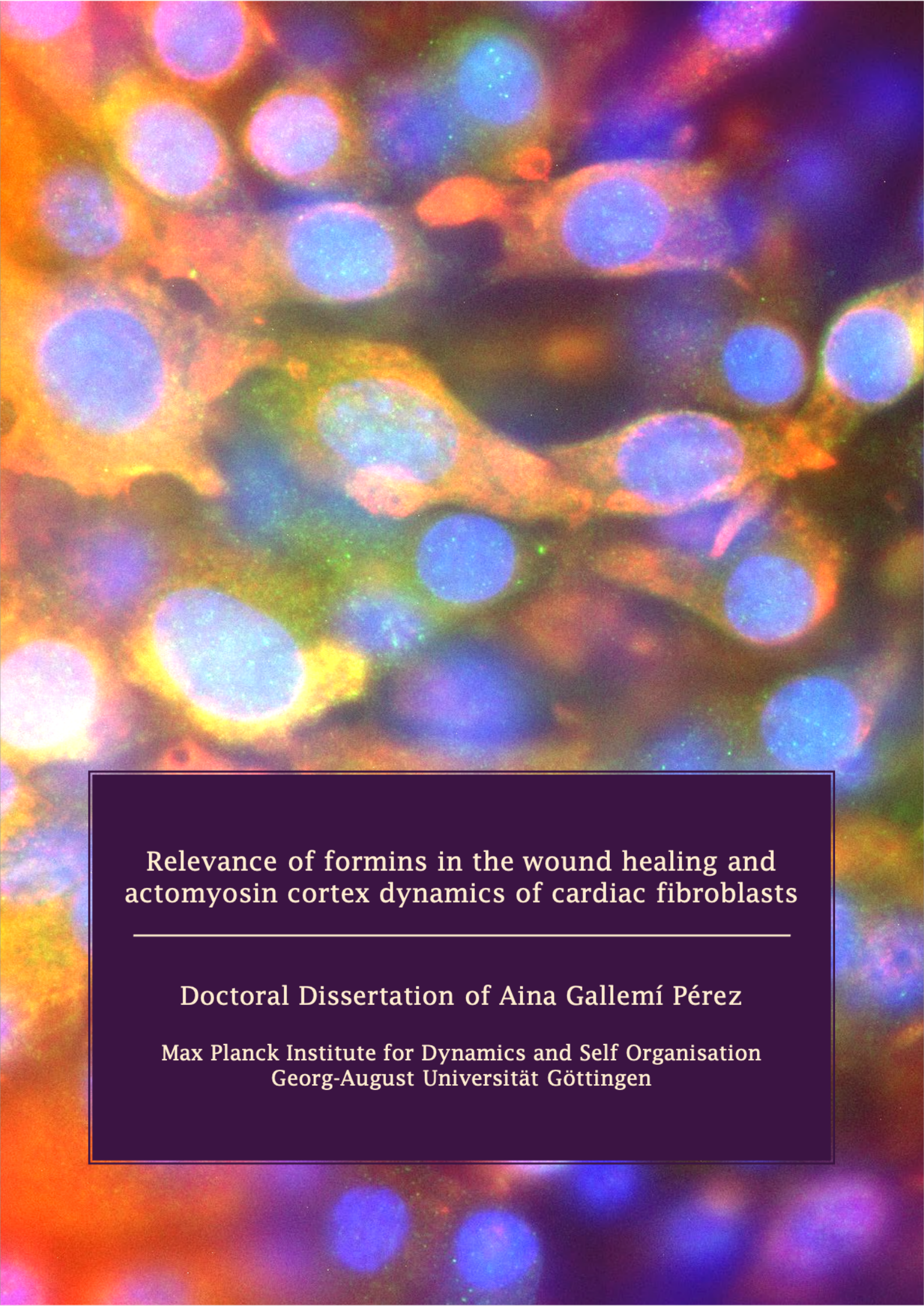

Relevance of formins in the wound healing and actomyosin cortex dynamics of cardiac fibroblasts

Doctoral Dissertation of Aina Gallemí Pérez

Max Planck Institute for Dynamics and Self Organisation
Georg-August Universität Göttingen

Relevance of formins in the wound healing and actomyosin cortex dynamics of cardiac fibroblasts

Doctoral Dissertation

for the award of the degree
„Doctor rerum naturalium“
of the Georg-August-Universität Göttingen

within the doctoral program

Physics of Biological and Complex Systems (PBCS)
of the Göttingen Graduate School of Neurosciences, Biophysics, and Molecular Biosciences (GGNB)
of the Georg-August University School of Sciences (GAUSS)

Submitted by
Aina Gallemí Pérez from Argentona, Spain

Göttingen 2023

Thesis Committee

Dr. Marco Tarantola (Referee)
Department of Fluid Dynamics, Pattern Formation and Biocomplexity
Max Planck Institute for Dynamics and Self-Organization

Prof. Dr. Claudia Steinem (Co-Referee)
Institute for Organic and Biomolecular Chemistry
Georg-August-University Göttingen

Prof. Dr. Sarah Köster
Institute for X-Rays Physics
Georg-August-University Göttingen

Further members of the Examination Board

Prof. Dr. Stefan Klumpp
Theoretical Biophysics Group
Georg-August-University Göttingen

Dr. David Zwicker
Theory of Biological Fluids
Max Planck Institute for Dynamics and Self-Organization

Prof. Dr. Burkhard Geil
Institute of Physical Chemistry
Georg-August-University Göttingen

Date of oral examination: 25$^{\text{th}}$ of April, 2023
DOI:10.53846/goediss-9927

"Wisdom comes from experience. Experience is often a result of lack of wisdom."
-Terry Pratchett

Abstract

Upon myocardial infarction, the natural healing response triggers the fibroblast-to-myofibroblast transition (FMT). Through this process, fibroblasts acquire a myofibroblast phenotype by which they present increased mobility, contractility, and capacity to produce components of the extracellular matrix. These factors contribute to their migration towards the injured site and their effective participation in scar formation. However, the FMT involves a stringent regulation of the mechanics of the cellular cytoskeleton and, therefore, of the dynamics of the actomyosin cortex upon directed cell migration.

As actin nucleators, formins are therefore of central relevance in the study of the interplay between collective wound healing dynamics and cortical adaptations. In this thesis, the role of formins is quantified by comparing the behavior and properties of wild type NIH 3T3 fibroblasts against those of mutant lines with deletions of the formin isoforms mDia1, mDia3, and of their combination. Atomic force microscopy (AFM) is employed to retrieve, in accordance to the Evans model, the prestress, area compressibility modulus and fluidity of single cells presenting different degrees of cell adhesion, hence mimicking different stages of the initial chemotactic migrating process. In parallel, the Electric Cell-Substrate Impedance Sensing (ECIS) device, in combination with fluorescence microscopy, is used to determine the wound closure dynamics of the different cell lines. Recovery kinetics are analysed in terms of the parameters derived from the passive electrical properties of the cell layer, namely: surface coverage, cell membrane integrity, cell-cell and cell-substrate morphology. Changes in the biological activity linked to formin modulations are further quantified via variance-, micromotion- and detrended fluctuation analysis of height oscillations in the cellular ventral membranes. Finally, recent studies have suggested that fibroblasts could close voids via purse-string contraction, mechanism traditionally ascribed to epithelial cultures. To test their capability to do so, fibroblast recovery on planar wounds of different sizes is analysed.

Thereby, in this thesis it is shown that the roles of the formins mDia1 and mDia3

are essential to maintain the structural integrity of the cortex. Upon initial adhesion, fibroblasts fluidise to allow cellular spreading; once stabilised, prestress increases to maintain structural integrity. Formin deletions lead to structural defects in the cortex that are reflected in significantly delayed recovery dynamics upon wound formation. While mDia1 is central in migration and thus recovery kinetics, mDia3 is necessary for re-establishing mechanical integrity of the cortex. However, wound closure can still be initiated in their absence. Finally, based on wound size, two regimes are identified in the closure kinetics; according to fluorescence imaging, the fastest may be provided by purse-string contraction.

Contents

Nomenclature

AFM	Atomic Force Microscopy
Arp2/3	Actin related proteins 2 and 3
BE	Bare electrode
Cad	Cadherin
CM	Cardiomyocyte
CVD	Cardiovascular disease
Cx43	Connexin 43
Cx45	Connexin 45
DAD	Diaphanous auto-regulatory domain
DFA	Detrended fluctuation analysis
DID	Diaphanous inhibitory domain
dKo	Double knock-out fibroblasts
DMEM	Dulbecco's modified Eagle's medium
DRF	Diaphanous-related Formins
ECIS	Electric Cell-Substrate Impedance Sensing
ECM	Extracellular matrix
ELC	Essential light chain
F-actin	Filamentous actin
Fb	Fibroblast
FBS	Fetal bovine serum
FFT	Fast Fourier transformation
FH	Formin-homology domain
FMT	Fibroblast-to-myofibroblast transition
G-actin	Globular actin
GDA	Glutardialdehyde
IF	Individual fitting routine for the Evans model
mDia1	mDia1 single knock-out fibroblasts
mDia3	mDia3 single knock-out fibroblasts
NA	Numerical aperture
NAd	Nascent adhesion
NIH	National Institutes of Health in Bethesda, Maryland (USA)
PE	Pre-exposure
PEG	Polyethylenglycol
PSD	Power spectral density
RGD	Arginyl-glycyl-aspartic acid moiety
PW	Pre-wounding
SCFS	Single-cell force spectroscopy
SF	Serial fitting routine for the Evans model
SI	Supplementary information

SMIFH2	Small molecular inhibitor of formin FH2 domains
SNR	Signal-to-noise ratio
TGF-β	Tumour growth factor β
TNF-α	Tumour necrosis factor α
WT	Wild type fibroblasts
WASP	Wiskott-Aldrich Syndrome protein
α-SMA	α-smooth muscle actin

Experimental parameters

AFM-related

$\boldsymbol{E}$	Young's modulus
$\boldsymbol{K_A}$	Area compressibility modulus
$\boldsymbol{T_0}$	Cortical prestress
β	Fluidity coefficient

ECIS-related

$\boldsymbol{C_m}$	Membrane capacitance
$\boldsymbol{f_{SNR}}$	Frequency of optimal SNR or optimal frequency
$\boldsymbol{R}$	Recovery rate
$\boldsymbol{R_b}$	Cell-cell resistance
$\boldsymbol{S_{PSD}}$	PSD slope
$\boldsymbol{t_{1/2}}$	Recovery half time
$\boldsymbol{Var}$	Variance
$\boldsymbol{Z_{im}}$	Imaginary part of the impedance
$\boldsymbol{Z_{real}}$	Real part of the impedance
α	Cell-substrate distance sensitive parameter
α_{DFA}	DFA slope

Part I

Preface

Chapter 1

Introduction

Cardiovascular diseases (CVDs) represent, today, the leading cause of death worldwide. From these, 85 % are consequence of strokes and heart attacks [1], thus carrying a large social and economic cost. The impact of CVDs is further magnified by the consequences associated to a natural healing response that, upon myocardial infarction, results insufficient: following recovery, the properties of the scar tissue differ from those of the healthy organ, hence increasing its vulnerability. Fibrous areas can act as insulators [2] or perturb wave propagation [3], thus disrupting the transmission of the electrical impulses that cause heart contraction. Simultaneously, tissue contractility can result negatively affected due to increased stiffness in scar regions [4]. Furthermore, a deregulated healing response can lead to fibrosis or even cancer development [5].

These starkly negative consequences underline the need of building up basic knowledge and developing better biomedical strategies to improve the natural wound healing response in cardiac tissue. To this purpose, large benefits could derive from better understanding the progression of the natural process. Upon tissue necrosis, several mechanisms concatenate in order to re-establish tissue homeostasis. During its course, cardiac fibroblasts undergo a phenotypic adaptation referred to as the fibroblast-to-myofibroblast transition (FMT) [6], through which they can express large amounts of extracellular matrix (ECM) components [7] and effectively contribute to scar formation. The adaptation involves transient increased mobility, cytoskeletal re-organization and expression of α-smooth muscle actin (α-SMA), increased formation of cell-cell contacts, and contractile behavior [8]. Accordingly, it is strongly linked to both cortical mechanics as well as environmental geometrical cues.

Due to the increased migration capabilities and cytoskeletal re-organization, myofibroblasts require a stringent regulation of the elements constituting the cellular architec-

ture. In this regard, the actomyosin cortex becomes especially relevant. The cortex is a densely cross-linked actin mesh that, by action of myosin II motors, presents a compliant but contractile structure [9]. It is located underneath the cell membrane, to which it is connected via several anchoring proteins [10], and provides the cell with resistance to external deformation. The regulation of the cortex is essential for fundamental cellular processes such as cell division, migration, adhesion and differentiation [11]. Cortical dynamics are determined by myosin-mediated contraction but also by the structure of the actin mesh. Accordingly, the role of actin polymerising factors, such as formins or the Arp2/3 complex, is of central relevance both to cortical mechanics as well as to the study of the healing dynamics of cardiac fibroblasts.

Formins modulate the cytoskeleton by nucleating and elongating actin filaments [12], but can also regulate microtubule dynamics [13]. Within the formin family, composed by 15 members in mammals [13], Diaphanous-related formins (DRFs) are a major subgroup. DRFs are characterised by the ability to establish auto-inhibition through the interaction between their Diaphanous inhibitory (DID) and Diaphanous auto-regulatory (DAD) domains. This interaction can be disrupted by the action of Rho-like GTPases, molecular switches that participate in the regulation and coordination of several signal transduction pathways related to cytoskeletal organisation [14, 15]. Research on mutants devoid of Diaphanous-related formin-1 (mDia1) and mDia3 in model amoeba and melanoma cells has shown that their absence negatively impacts cellular motility in a cooperative way. In addition, the deletion of one of the formin forms induces compensatory over-activation of other family members, hence underlining their fundamental role, reflected as well in the trans-species evolutionary conservation of formin structure and functionality [16].

In vitro research on fibroblast cultures has identified active cell crawling as their mechanism of wound re-colonisation [17], characterized by the appearance of leader cells that migrate towards the injured site via lamellipodia formation [18]. However, the use of purse-string contraction, believed to be exclusive of epithelial wounds, has also been recently observed in fibroblasts when forming free-standing bridges in order to overcome up to 300 µm wide voids [19]. The purse-string mechanism depends on the formation of supracellular actomyosin cables at the wound periphery to promote closure by collective cellular contraction [20]. These actin cables have also been detected in the advancing front of fibroblast tissue growing in 3D clefts [21]. In contrast, using a 3D bioengineered culture system, M. S. Sakar *et al.* observed that fibroblasts are able to restore open gaps in the absence of actin cables via the combination of force-dependent tissue contraction, cell migration around the wound edge, and *de novo* synthesized fibronectin scaffolding [22]. Together, these diverse findings illustrate the need of better understanding the

capabilities of cardiac fibroblasts upon injury and, as studied in the present thesis, of the interplay between formin-dependent wound closure and the spreading state-dependent cortical mechanics.

Thesis objectives

To address this need, this thesis investigates the wound healing dynamics of migratory NIH 3T3 fibroblasts, the cortical adaptations involved in the corresponding adhesion-deadhesion cycle, and the role that formins fulfill in this interplay. Within this frame, four research questions are tackled:

I. How do the rheological properties of the actomyosin cortex adapt during cell adhesion?

During cell migration, the cellular body polarises and protrusions such as lamellipodia and filopodia are formed at the advancing front. Subsequently, new adhesions are established while those at the rear are disassembled to allow the retraction of the trailing edge [23]. To study the cortical adaptations stemming from the continuous adhesion and deadhesion cycles within the migration process, three experimental setups are prepared in order to mimic discrete phases of the cellular displacement based on the type of cell-substrate interaction. Accordingly, single cells are cultured on substrates promoting different degrees of cell adhesion. In these scenarios, the properties of the cell cortex are obtained by analysing the cellular response to compression-relaxation experiments, performed via atomic force microscopy (AFM), according to the Evans model [9]. Before proceeding with its application, however, the experimental and analytical limitations of the Evans model are explored.

II. What is the role that mDia1 and mDia3 play in the regulation of the cortical adaptations upon (de)adhesion?

Following the methodology described above, the behavior of wild type NIH 3T3 fibroblasts is compared to that of modified cells lacking the formins mDia1, mDia3, or their combination; the corresponding cell lines are referred to as mDia1, mDia3 or dKo (double knock-out) cells. In addition, comparison is established between the behavior of these clones and the impact of the general formin inhibitor SMIFH2 [24] on wild type fibroblasts.

III. How is the activity of formins impacting the motile capabilities of fibroblasts during cell migration?

In the ambit of *in vitro* wound healing studies, the Electrical Cell-substrate Impedance Spectroscopy (ECIS) device, based on the detection of the passive electrical properties of adherent cells, has been extensively adopted in literature [25, 26, 27, 28]. The ECIS can cause reproducible wounds that result circumscribed by the surface of the electrodes embedded in the culture material. In parallel, it can measure the complex impedance Z generated by the insulating properties of cells when exposed to an AC electric field as a function of time. Analysis of the resulting frequency spectra can provide information on the surface coverage, cell membrane integrity, cell-cell and cell-substrate morphology, and cellular motility of the cultures [25, 26]. Information on cellular viability, and thus metabolic activity, can also be obtained through the analysis of minuscule fluctuations in the height of cellular ventral membranes [29]. Due to these features, the ECIS is here employed to analyse collective cellular dynamics upon wound formation on monolayers of wild type fibroblast, but also of mDia1, mDia3 and dKo cells.

IV. Are fibroblasts able to close wounds via the purse-string mechanism, and is gap size a relevant geometrical trigger?

The cellular mechanism employed in epithelial wound closure is regulated by a number of factors. Throughout different tissues, wound size has been regarded as an important determinant: while epithelial leader cells initiate re-colonisation of large wounds (over several cell sizes), smaller gaps in the range of tens of microns are predominantly closed via purse-string contraction [30]. Accordingly, ECIS-based wound healing assays and fluorescence imaging of the cellular architecture are combined, upon the formation of wounds of varying diameter, in order to determine the closure mechanism used in the process.

Chapter 2

Background fundamentals

2.1 Cardiovascular diseases

Cardiovascular diseases (CVDs) are, to date, the leading cause of death worldwide and irrespective of sex. As illustrated in figure 2.1, they encompass a large number of affections and in 2019 alone, they caused 32 % of all global deaths; from those, around 85 % were consequence of strokes and heart attacks [1, 31]. Early misdiagnosis of the latter, which affects nearly 1 out of every 3 patients of acute myocardial infarction[1], inevitably leads to a higher mortality rate; herein, women are 50 % more likely to be misdiagnosed than men [33]. Consequently, CVDs have a large impact in the worldwide economy with an estimated total cost of €210 billion per year in the European Union alone [34].

2.1.1 Targeting CVDs

Given the impactful cost that CVDs represent both economically and personally, it is not surprising that a wide range of strategies have been developed, and are being developed today, in order to target the affections of the blood vessels and the heart.

Although they may be combined, regenerative strategies can be broadly categorised into those based on the use of biomaterials, and into those involving paracrine [36] or cellular therapy. The former, which comprise organ and tissue decellularisation [37], 2D or 3D scaffolds, hydrogels, and bioprinted tissue constructs [38], are mostly applied in

[1]The longer a heart attack is left undiagnosed and untreated, the more the heart muscle can be irreversibly damaged. Ultimately aiming to contribute to the eradication of CVDs, it is within the scope of this thesis to disseminate the symptoms of myocardial infarction, which include: pain or discomfort -over days or weeks- in the chest and upper abdomen, in one or two arms or shoulders, in the space between shoulder blades, jaw, neck and back; shortness of breath, dizziness and sweating; persistent tiredness, nausea, vomiting and fear [32].

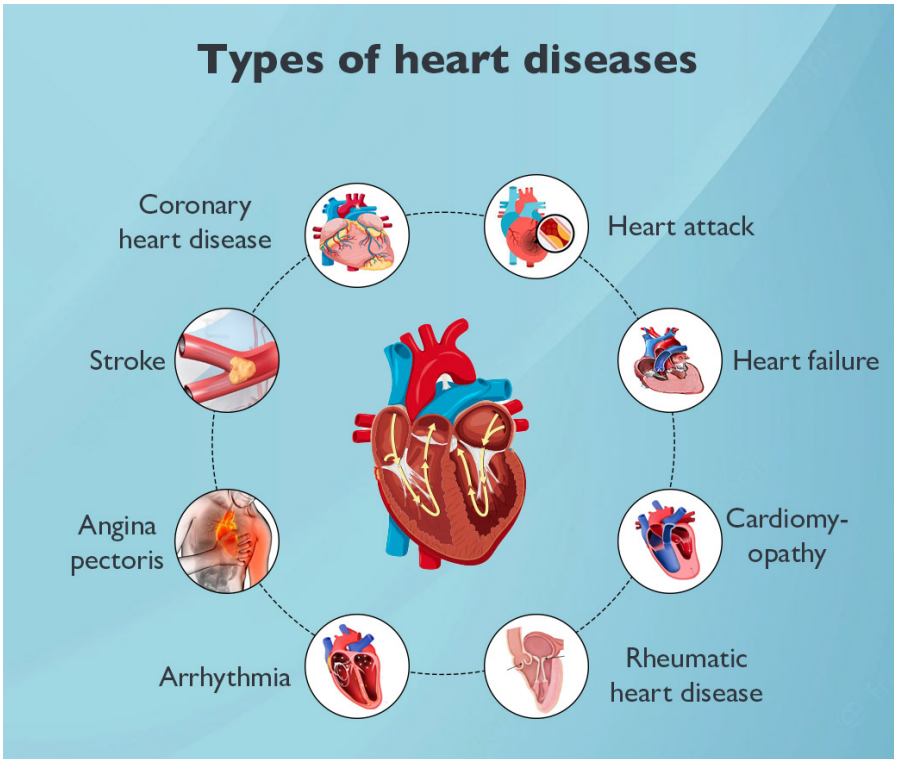

Figure 2.1: **Types of heart diseases.** Based on the affected location, CVDs can be broadly classified amongst those involving the blood vessels, such as coronary artery disease or stroke, and those directly impacting the heart. Diseases of the vasculature can ultimately transfer to the heart through infarction. Source: Sprint Medical [35].

order to prevent organ failure progression, addressable only via heart transplantation. In contrast, approaches based on paracrine therapy, thus involving the introduction of stem cells or trophic factors -such as cytokines, growth factors or chemokines- that may elicit a response or the reprogramming of native cells, have a larger potential in preventing the appearance of CVDs in the first place [39]. However, these approaches require the development, in parallel, of fitting delivery techniques: while the use of extracellular vesicles is suitable for proteins, mRNA or lipids [40], the introduction of stem cell populations demands delivery systems based on pre-formed patches or injectable hydrogels, which result more invasive and have, to date, difficulties in reaching clinical trials [41].

Beyond the biomaterial/paracrine categorisation, recent years have seen the development of a novel third strategy: synthetic cells. This specific branch of synthetic biology aims to reverse-engineer and recreate a particular biological function using minimal biomimetic components: a compartmentalising body such as a giant unilamellar vesicle (GUV), and a specific proteinic cocktail to carry out the desired function [42]. Resolving an automated and high yield production of synthetic cells, microfluidic devices are

primarily employed, which additionally allow a fine control of size distribution and the formation of internal compartments within synthetic cells [43, 44]. Furthermore, they are compatible with a number of chemical compositions, relevant for the functionality of the synthetic constructs: while lipid-based vesicles closely resemble biological cells, they are relatively sensitive to the presence of multivalent cations and to pH changes; in contrast, polymersomes, formed by amphiphilic block copolymers, are more stable but simultaneously restrictive in the encapsulation of biomolecules. Accordingly, a compromise between their properties is often desirable, and microfluidic technology can allow this via the synthesis of GUVs that are temporarily stabilised with polymersomes, thus providing them with mechanical integrity for the duration of their functionalisation [45], the decoration of the synthetic membranes with re-constituted proteins [46], or the formation of organelles [43]. Advancements in this direction can provide synthetic cells with adhesive molecules to promote mechanical coupling, connectivity to enable communication, and energy sources to drive the system out of equilibrium. Accordingly, they are key in achieving a higher organisational level via the self-association of individual synthetic cells: synthetic tissues or living foams (Fig. 2.2). Such hybrid tissues, deliverable as injectable composites or extrudable scaffolds, have the potential to provide support to a wounded tissue while the synthetic cells promote the healing response [47], and therefore hold great promise in the targeting of CVDs.

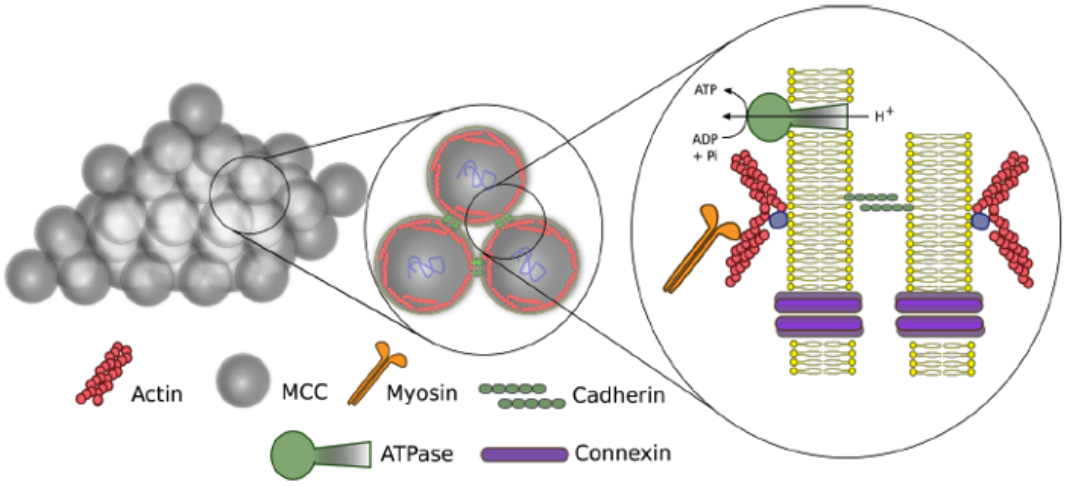

Figure 2.2: **Synthetic cells and living foams.** Synthetic cells are composed of a compartmentalising body (minimal cell compartment; MCC) that presents re-constituted proteins to provide them with structure (actin, myosin), connectivity (cadherin), communication (connexin) and an energy source to drive the system out of equilibrium (ATPase). By interacting with each other, synthetic cells form living foams that could be used for different therapeutic purposes.

2.2 Cell populations of the heart

In a lifetime the heart beats, on average, more than two billion times. An intricate interplay between the mechanical forces and electrical signals is therefore necessary to ensure the controlled contraction of the organ. Inevitably, this is reflected in the cellular composition of the heart (Fig. 2.3), formed by cardiac fibroblasts (Fbs), cardiomyocytes (CMs), smooth muscle cells (SMCs) and endothelial cells (ECs). Fibroblasts are the most common cells and major producers of extracellular matrix (ECM) in the organ, thus providing it with scaffolding. Cardiomyocytes, on the other hand, are contractile and, despite representing only the 30 % of the heart population, constitute 70 % of its weight due to their large size. Less abundant are SMCs, which support the vascular system, and ECs, which form the interior lining of tissues such as the cardiac valves or blood vessels [48]. Despite recent studies contesting the percentiles in the precise distribution of cell populations [49], the relevance of fibroblasts and cardiomyocytes is undeniable for the specific function of the heart.

2.2.1 Cardiac fibroblasts

Despite being one of the most prevalent cell types, fibroblasts remain, to date, poorly defined. Such contradiction arises from the fact that there is an absence of distinguishable markers to track them. Incidentally, any stromal cell that lacks the biological markers for a more specific mesenchymal lineage falls within the 'fibroblast' category [51]. Morphologically, fibroblasts are generally described like elongated spindles with numerous cytoplasmic projections. As stromal cells and major producers of extracellular matrix, they are present in connective tissues and provide structure to their surroundings. However, they also express collagenases that allow degradation and thus remodelling of the surrounding ECM [52].

One of the most interesting features of fibroblasts is their inherent plasticity: they are able to alter their function or physiology based on the environmental cues and, as a matter of fact, they are largely heterogeneous depending on the tissue of origin [51]. It is in the specific ambit of cardiac wound healing, however, that fibroblasts show one of their most dramatic adaptations: the fibroblast-to-myofibroblast transition (FMT). Besides the mesenchymal–epithelial transition (MET) [53] and the reverse process (EMT) [54], the FMT, described below, is probably the most studied fibroblast adaptation.

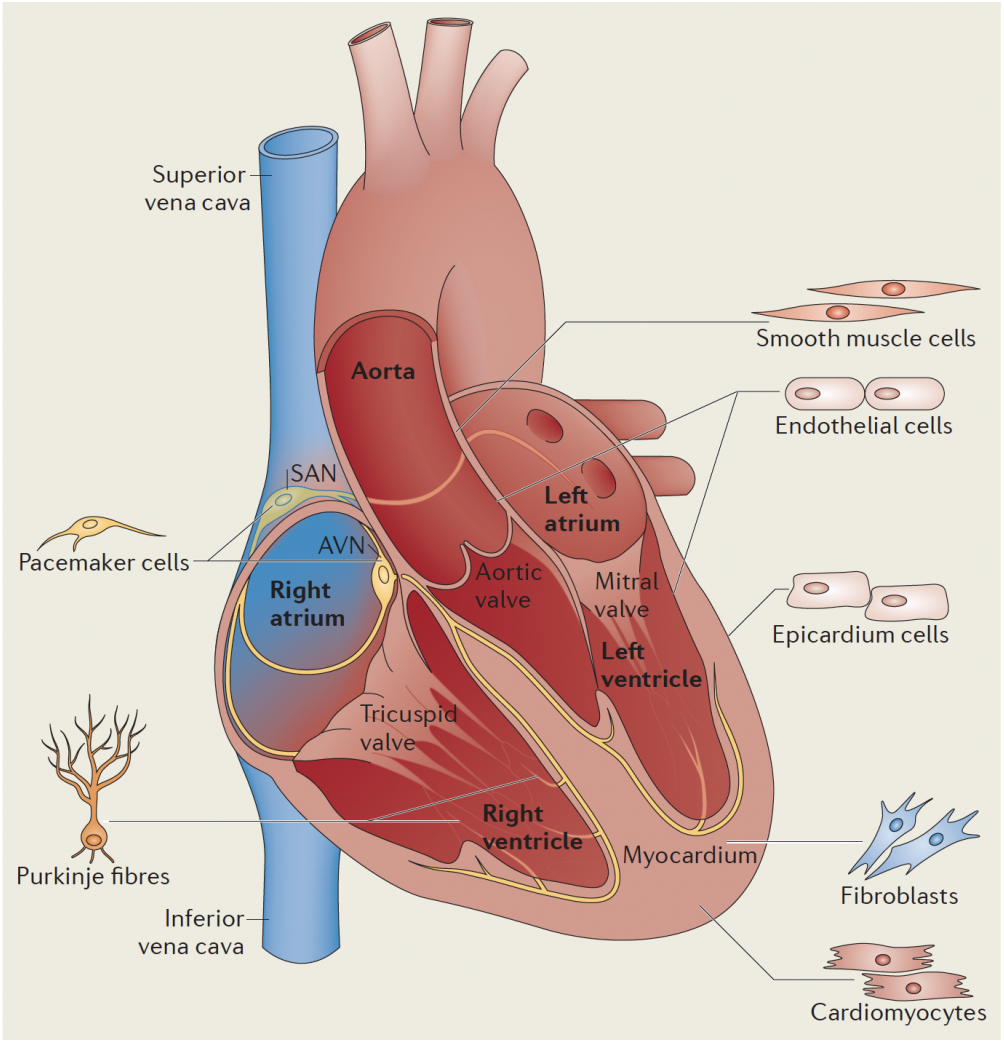

Figure 2.3: **Cell populations of the heart.** Through the four chambers that form the heart, several cell types co-exist. Cardiomyocytes and fibroblasts constitute the larger populations, respectively providing the organ with contractility and structure. While the vascular system is mostly constituted by smooth muscle and endothelial cells, the epicardium hosts the precursors of the vascular and cardiac fibroblasts. Pacemaker cells are specialised cardiomyocytes that generate the electrical impulses at the sinoatrial node (SAN). Purkinje cells then conduct these signals through the atrioventricular node (AVN), located between the atria and the ventricles of the heart. Reprinted from [50] with permission from Springer Nature.

2.2.2 Myofibroblasts

Upon myocardial infarction, tissue necrosis triggers the wound healing process, in which several recovery mechanisms concatenate in order to reestablish the tissue homeostasis by scar formation. In its course, fibroblasts undergo several phenotypical changes in a process defined as the **fibroblast-to-myofibroblast transition** [6]. The FMT encom-

passes the acquisition of a phenotypic profile in which myofibroblasts can migrate to the wound and close it while maturating it into a scar. To this purpose, they become transiently more mobile, re-organize their cytoskeletal architecture upon α-smooth muscle actin (α-SMA) expression, become more static again while establishing cell-cell contacts, and become contractile [8].

Several chemical and mechanical cues are released upon wound formation that promote the FMT. Amongst them is the the Tumor Growth Factor β (TGF-β), which is able to induce the expression of α-SMA in fibroblasts, and consecutively elicit their transition to myofibroblasts [55, 56]. In parallel, the high tension in the wound induces stress fiber formation within the cells which, albeit unable to initiate the FMT by itself, has a synergistic effect [52]. In fact, ECM remodeling and mechanotransduction may present several positive reinforcing mechanisms to support the phenotypical adaptation. For example, fibronectin is able to promote, through the expression of the alternatively spliced domain A (EDA), the immobilisation of the latent TGF-β-binding protein-1 (LTBP-1), which binds to TGF-β in the form of the large latent complex (LLC), hence storing the cytokine in the matrix [57]. As mentioned, myofibroblasts produce large amounts of ECM components, such as collagen I and fibronectin-EDA, but simultaneously release matrix metalloproteinases (MMPs) that degrade the ECM. Accordingly, a positive loop exists by which the mechanical and chemical signals from the ECM induce the FMT and, thereafter, myofibroblasts produce fibronectin-EDA and MMPs to remodel the ECM and reinforce the phenotypic adaptation via the release of stored TGF-β [58]. Moreover, the release of TGF-β can be further reinforced by the activity of other agents such as integrins, a big family of transmembrane proteins that mediate cell adhesion by binding to arginyl-glycyl-aspartic acid (RGD) moieties in the ECM. By binding to the LLC and its proteinases, thus improving enzymatic activity by bringing them to close vicinity, or by directly generating a conformational change in LLC, integrins can facilitate the release of TGF-β, which can then reenter the positive feedback loop [59]. This process is illustrated in figure 2.4.

TGF-β mediated FMT activation

TGF-β is a multifunctional growth factor that can act as a chemotactic agent, enzyme activator and regulator of collagen deposition [52] and contraction. It elicits, in addition, concentration-dependent biphasic responses: in human Tenon's capsule fibroblasts, peak proliferation and migration are achieved with 10^{-12} and 10^{-9} M TGF-β concentrations, respectively [60].

The cytokine is produced by a number of cell types including platelets, white blood

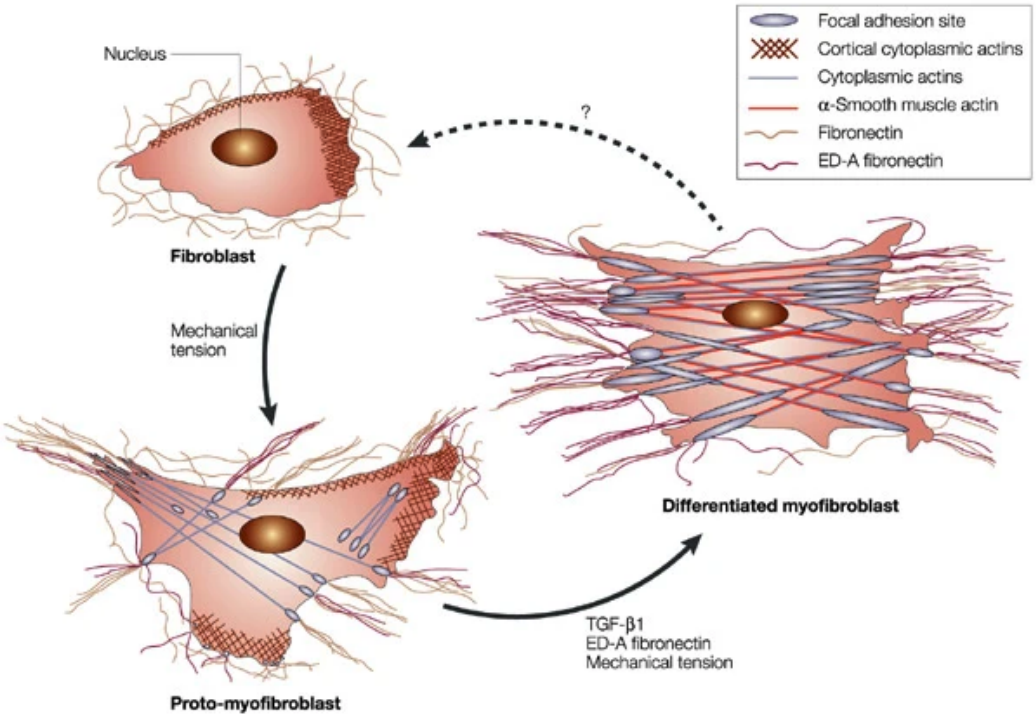

Figure 2.4: **Fibroblast-to-myofibroblast transition.** In normal conditions, fibroblasts do not present stress fibers and look spindle-like. Upon wounding, mechanical stress promotes the formation of stress-fibers that terminate in adhesion complexes. As *proto-myofibroblasts*, they re-organise the ECM by fibronectin-EDA expression which, together with the cleavage and release of TGF-β, reinforces the acquisition of myofibroblast phenotype. Upon complete transition, myofibroblasts express α-SMA and generate contractile forces through large focal adhesion sites. Reprinted from [55] with permission from Springer Nature.

cells, epithelial cells, and fibroblasts themselves [52]. Incidentally, autocrine production of TGF-β is relevant in preserving fibrogenic activity when the inflammatory process ceases [55]. Once TGF-β is released from the LLC, it is then free to interact with fibroblast receptors and induce the Smad signaling pathway, which can also be activated via shear stress mechanotransduction [61]. Upon translocation to the nucleus, phosphorylated Smad leads to the transcription of target genes [62] like FN1 and LAMA1, respectively encoding fibronectin 1 and laminin. As major components of the ECM, both are implicated in cell adhesion, differentiation, migration and signalling [63].

Myofibroblast contractility via α-SMA and myosin activity

As shown in figure 2.4, myofibroblasts differ considerably in morphology with respect to fibroblasts. Structurally, this is largely associated with the presence of α-SMA. Actins

are a highly conserved family of globular proteins that form filaments in the cellular cytoplasm. Several isoforms exist, and α-SMA, also known as actin alpha 2 (ACTA2), is one of them. In order to present contractility, actin fibers associate with myosin molecular motors. Like actins, myosins represent a superfamily of proteins with conserved functionality. In this case, however, several classes with specific roles exist. For example, myosin I is ubiquitous and acts in vesicle transport; in contrast, myosin V transports vesicles and organelles to the cell periphery while keeping them tethered for a prolonged time [64]. Despite the structural differences associated to the specific functions, myosins present three elements: 1) a motor domain that interacts with actin in response to ATPase cycling, 2) a neck region with a light-chain-binding domain (LCBD) that functions as a lever arm, and 3) a tail domain to bind to their specific cargo [65].

This is the case of myosin II as well, which is specifically conformed as an hexamer of two coiled heavy chains, each associated at the neck domain with a pair of regulatory (RLC) and essential (ELC) light chains (Fig. 2.5). In the non-phosphorylated form, the RLCs promote the interaction between the tail and the motor domain, thus rendering the motor inactive. Conversely, RLC phosphorylation by the myosin light chain kinase (MLCK) leads to motor activation, eliciting the assembly of hemotypic bipolar filaments via the anti-parallel interaction and self-assembly of myosin long tails. Single filaments containing up to around 30 individual myosin II molecules can be found cross-linking actin filaments or in bundles such as stress fibers (Fig. 2.5) [66].

Cell-cell connectivity in myofibroblasts

During scar-formation and fibrosis, cell-cell contacts undergo remodelling. Gap junctions connect the cytoplasm of adjacent cells and, in cardiac muscle, ensure heart contraction via the propagation of the electrical impulse [67]. Like fibroblasts, myofibroblasts are not excitable cells. However, they are capable of electrically coupling to cardiomyocytes through the establishment of gap junctions via connexin 43 (Cx43) [68] and 45 (Cx45) [6]. This coupling allows the passive conduction of the electric signal through the body of the myofibroblasts, thus supporting trans-scar conduction events by which the electric signal is transmitted across regions lacking continuity in the cardiomyocyte population [69]. However, a large volume of the bibliography available ascribes negative effects to this coupling, including signal dampening, arrhythmia generation and alteration of the membrane potential of cardiomyocytes [70, 71, 72].

In contrast to fibroblasts, myofibroblasts can also connect stress fibers at cadherin (Cad) mediated adherent junctions. In fact, both dermal [73] and lung myofibroblasts [74] show a transition from N-cadherin to cadherin-11, which promotes force and ten-

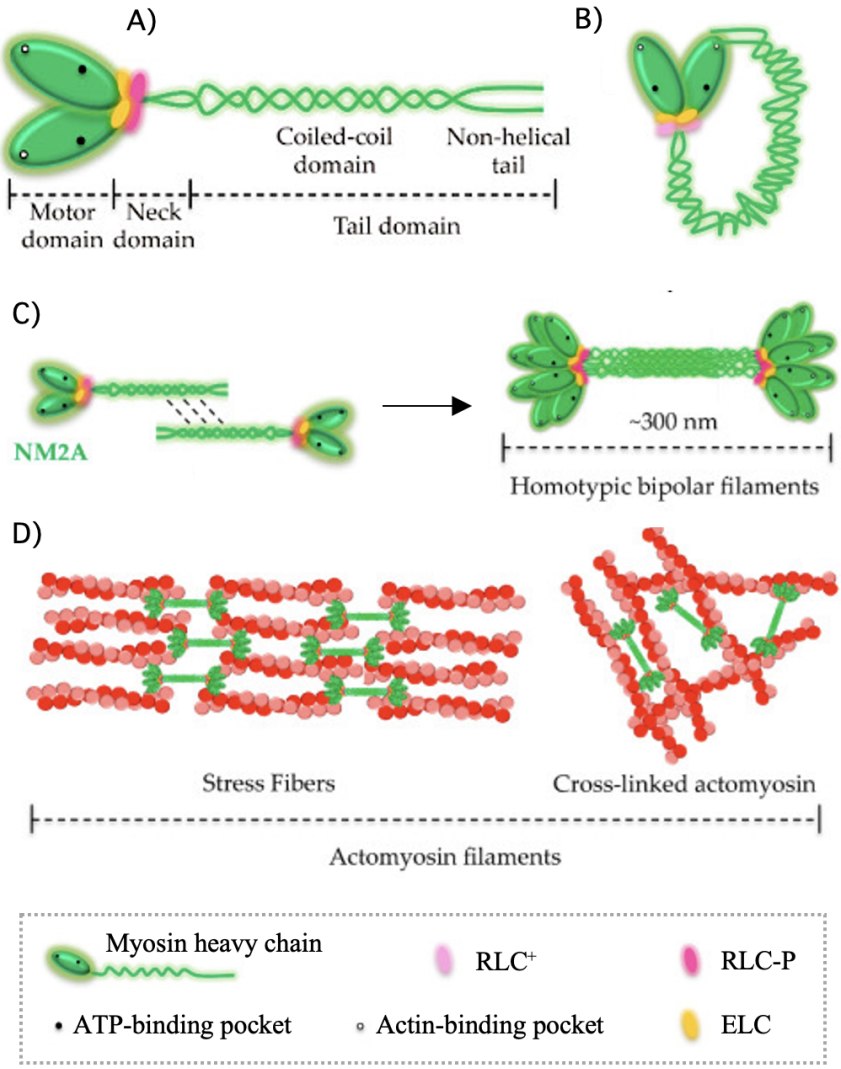

Figure 2.5: **Myosin II motors. A)** Myosin II motor with three domains: motor, neck and tail. Motor regions contain ATP and actin binding centers. In the neck region, the RLC and ELC interact with the myosin heavy chain. **B)** In the non-phosphorylated form, RLC interaction induces the inactivation of the motor. **C)** In the phosphorylated form, the tails of several motors can interact and self-assemble into coils, thus forming homotypic bipolar filaments. **D)** Upon interaction with actin filaments, different mesh structures such as stress fibers or cross-linked actomyosin can be found. Modified with permission from [66].

sion development through stronger intercellular connections. Even though myofibrast contractility may hinder electric conduction through the mechanical coupling provided by the adherent contacts [75], it also up-regulates the progression of the healing process via wound contraction [8].

2.2.3 Cardiomyocytes

Cardiomyocytes are the cells that generate the contractile forces that lead to the beating of the heart. To this purpose, they need to contract and relax in a well orchestrated cycle via the propagation of the action potential. When resting, cells present a negative membrane potential: they are more negative on the cytoplasmic side. Working to maintain this potential, transmembrane ion pumps regulate ion gradients of Ca^{2+} and Na^{+}, predominant at the extracellular space, and of K^{+}, more concentrated in the cytoplasm.

An action potential is a brief reversal of the membrane potential. When Na^{+} and Ca^{2+} travel between cells through gap junctions, they induce a small depolarisation of the membrane (it becomes less negative). This induces the action of voltage-gated channels that create a fast influx of sodium into the cell, thus accelerating the membrane depolarisation. Slow calcium channels open at this higher voltage, causing a slow influx of calcium that is equilibrated by an output of sodium, thus creating a voltage plateau. The influx of calcium generates the so-called calcium-induced calcium release at the sarcoplasmic reticulum (SR), which acts as a calcium reservoir (Fig. 2.6). The free calcium then elicits cell contraction via its interaction with troponin C, which promotes the interaction between myosin and actin filaments. When the voltage-gated calcium channel closes, the potassium pump remains open, leading the membrane potential to its resting value. Meanwhile, Ca^{2+} is actively captured in the SR or sequestered from the cell, and the cell enters in its refractory period before being re-stimulable [76].

Despite their essential function, cardiomyocytes lose their ability to divide around the time of birth. Very limited restoration preserves the integrity of the adult heart, but upon ischemia or after important changes in the pressure or volume loads, or in the aged organ, the restoration capabilities fail [77]. This can be overcome *in vitro* by studying immortalised cardiac cell lines like the HL-1 cardiac muscle cell line [78].

2.3 Natural healing response upon myocardial infarction

Upon myocardial infarction, several recovery mechanisms conforming the wound healing response concatenate in order to reconstitute the damaged tissue by scar formation. This process consists of four stages, and starts with the formation of a fibrin-fibronectin clot at the injury site via coagulation and platelet activation. Cytokines and growth factors released by platelets and damaged cells initiate the second stage, inflammation. This phase can last for days and induces recruitment and proliferation of neutrophils and macrophages. Neutrophils are a first defense against bacteria; macrophages sustain bacteria depletion while removing necrotic tissue and releasing, amongst others, TGF-

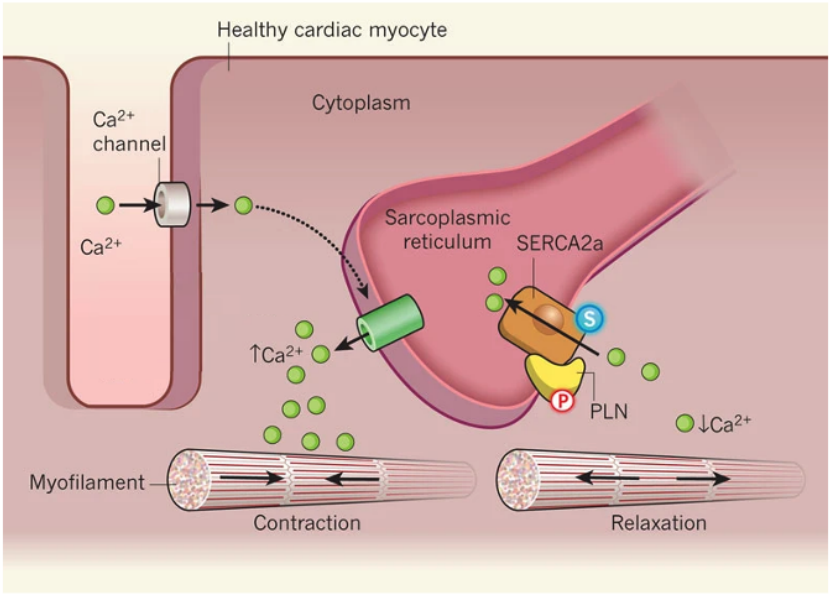

Figure 2.6: **Calcium-induced calcium release at the sarcoplasmic reticulum.** During the propagation of the action potential, the alteration of the membrane polarisation caused by Na^+ and Ca^{2+} influx causes the opening of calcium channels in CMs. The further increased membrane potential leads to the calcium-induced calcium release at the SR. Consequently, the free Ca^{2+} ions generate contraction of actomyosin filaments until they are sequestered back into the SR via the action of specialised ATPase pumps like SERCA2a. Modified with permission from [79].

β and platelet-derived growth factor (PDGF). Initiation of the proliferative phase is defined by fibroblast invasion of the injured region upon cytokine recruitment, followed by simultaneous propagation and FMT progression. By synthesising large amounts of ECM [7], myofibroblasts initiate the final phase of remodeling and scar formation [80].

Even after scar formation is completed, however, a mismatch between the physical properties of the normal and scar tissues is retained: fibrous areas disrupt electrical excitability by acting as insulating patches [2] or by obstructing wave propagation [3]; simultaneously, tissue contractility is reduced and can negatively affect overall heart stiffness [4]. Such a precarious balance can result in further complications, which is highlighted by the fact that myofibroblast over-activation can lead to fibrosis or even cancer development [5].

2.3.1 Wound closure mechanisms

In vitro two-dimensional wound healing of epithelial cultures has led to the identification of two distinct closure mechanisms: active crawling and purse-string contraction (Fig. 2.7). **Active crawling** involves leader cells initiating the re-colonisation of wounds

through multiple fronts based on lamellipodia formation [18]. In this process, leader cells become more fibroblast-like through an extensive cytoskeletal re-organisation that involves the assembly of actin filament bundles tangential to the wound perimeter, and active lamellae. In addition, cell-cell contacts are re-distributed to allow increased contractility [81]. **Purse-string contraction**, on the other hand, requires the formation of a supracellular actin cable at the rim of the wound that is collectively contracted via the action of myosin II motors [20].

Throughout different tissues, wound size has been regarded as an important factor in determining the closure mechanism followed by cells. Accordingly, wounds expanding over several cell sizes are closed via active crawling [18] whereas smaller gaps in the range of tens of microns to single-cell defects are closed through purse-string contraction. However, other factors like wound curvature or the physicochemical properties of the wound microenvironment can influence the behavioral outcome [30].

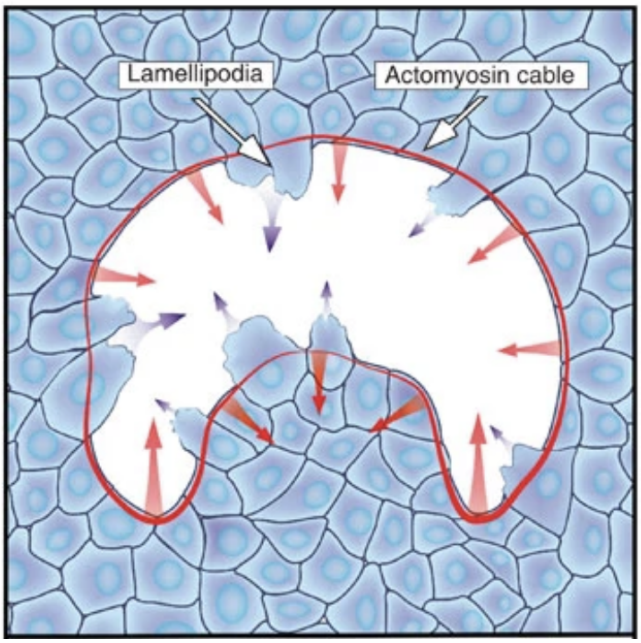

Figure 2.7: **Wound healing mechanisms.** Schematics showing active crawling (blue) and purse-string contraction (red). Arrows indicate magnitude and direction of the cell-generated stress. Reprinted with permission from [82].

Historically, fibroblasts have been believed to target gap closure exclusively via active crawling [17]. In fact, the use of the purse-string contraction was considered characteristic of epithelial wounds. Recently, however, such mechanism has also been observed

in NIH 3T3 fibroblasts (Fig. 2.8): in order to overcome deep voids up to 300 µm wide, fibroblasts aligned at the gap periphery and, forming ECM-rich free-standing bridges, closed the void via contraction of supracellular actomyosin cables aligned at its edge [19]. Supracellular actin cables have also been observed at the advancing front of fibroblasts closing 3D clefts. In this case, the tensile forces at the edge stabilised the myofibroblast phenotype even in the absence of supplementary TGF-β. Accordingly, tissue maturation presented a transitioning gradient from the myo- to the fibroblast phenotype towards the inner regions of the cleft [21]. In both scenarios, contraction of the cell front was dependent on myosin II activity and supported by the *de novo* synthesised ECM scaffolding.

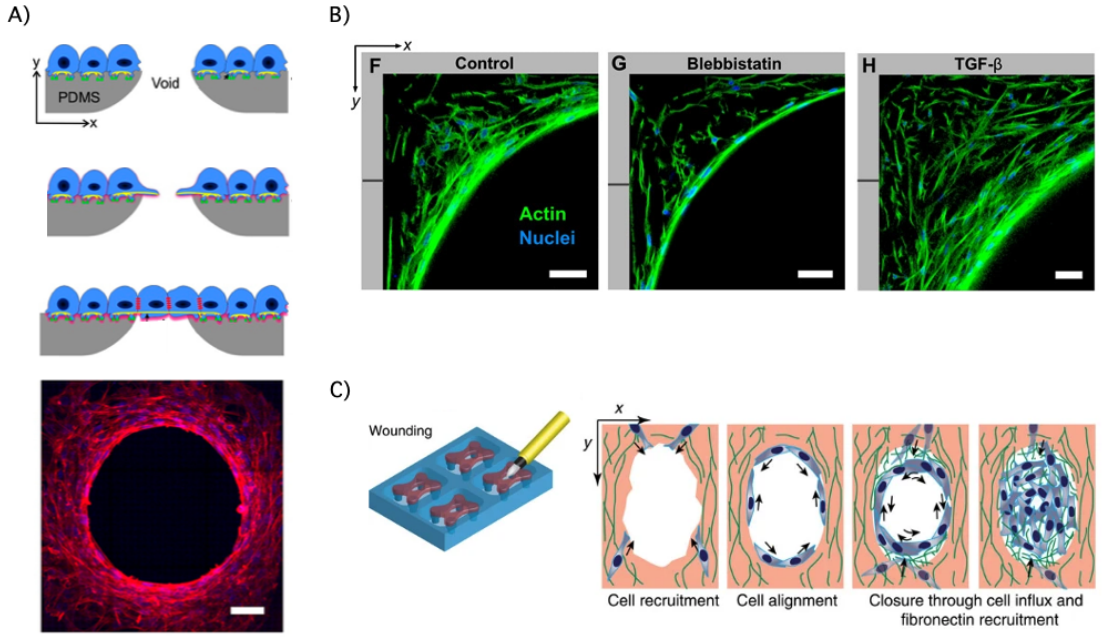

Figure 2.8: **Wound healing mechanisms of fibroblasts. A)** Fibroblasts generate void closure by the formation of free-standing bridges and collective contraction of supracellular actin cables. Fluorescence imaging (bottom panel) shows the cellular alignment around the void (nuclei in blue) and the formation of a continuous actin cable at the gap edge (actin in red). Scale bar: 20 µm [19]. **B)** Fibroblast tissue (actin in green; nuclei in blue) advancing in a cleft via actomyosin cable contractin in normal conditions (left), with myosin II down-regulation upon 10 µM blebbistatin addition (middle) and upon 1 ng/mL TGF-β addition. Drug addition respectively down- and up-regulates cable formation. Scale bar: 50 µm [21]. **C)** Wounds in suspended microtissues cause fibroblast recruitment and tangential alignment at the wound edge; synthesis of fibronectin further promotes cell influx, reinforcing actomyosin cable-independent wound closure [22]. Panels modified with permission from [19] (© 2022 American Chemical Society), [21, 22] (CC BY 4.0).

Wound closure of similarly engineered 3D culture systems, however, has also been accomplished by fibroblasts in the absence of actomyosin cables: microtissues in suspen-

sion closed wounds by combining coordinated tissue contraction, cell migration around the wound edge, and the formation of a fibronectin scaffold that allowed both restoration of the tissue integrity and reparation (Fig. 2.8) [22]. These collectively contrasting observations highlight the fact that a lot remains unknown on the wound closure capabilities of fibroblasts and the factors influencing the mechanisms employed in the process.

2.4 Cellular migration and adhesion

2.4.1 Components of the cellular cytoskeleton

The cytoskeleton is a structure that provides the cell with mechanical support and internal organisation. Accordingly, it is involved in any process requiring shape adaptation or cellular movement. The cytoskeleton is constituted by filamentous proteins that, based on size and composition, are divided into three families: microtubules, intermediate filaments, and actin filaments (Fig. 2.9).

Microtubules are typically formed by thirteen protofilaments of dimeric tubulin that associate to create a 25 nm wide hollow structure, rendering microtubules the widest type of filaments. They are anchored to the microtubule organising centers (MTOCs) at one end while growth continues on the other (+) direction. The primary MTOC is the centrosome, adjacent to the nucleus. From there, microtubules provide structure and an intracellular transport infrastructure for secretory vesicles and organelles. During cell division, they form the mitotic spindles to carry chromosome separation. **Intermediate filaments** are formed by a variety of subunit proteins. They are strong and rope-like, with an average diameter of 10 nm. They are less dynamic than the relatively fragile microtubules, with which are commonly associated. Intermediate filaments also provide cohesion to the whole cell sheet, thus preventing rupture under tension. Based on their composition, the filaments can result cell-specific: neurofilaments are present in neuronal axons, desmin is characteristic of muscle cells and keratins of epithelial cells. In contrast, vimentin intermediate filaments tend to co-localise with microtubules in a range of cell types, and lamins, found in meshworks reinforcing the interior of the nuclear membrane, are ubiquitous [83].

Actin filaments

Actin filaments (F-actin) are the helical polymerised form of globular actin (G-actin). They are 6 nm wide and constitute the smaller of the filament types conforming the cytoskeleton. Actin polymerisation can occur naturally via the spontaneous association

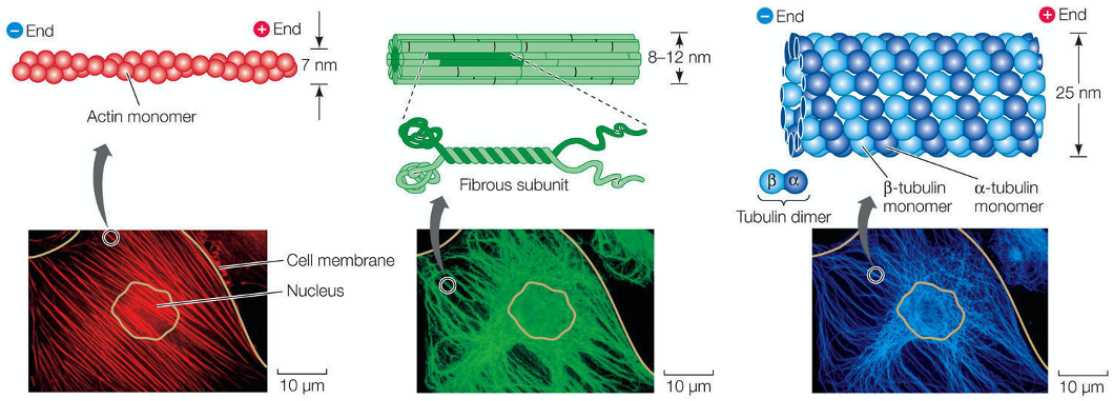

Figure 2.9: **Components of the cellular cytoskeleton.** From left to right, actin filaments, intermediate filaments, and microtubules. The upper half of the panel schematises the filaments and the subunits composing them; the bottom half shows their distribution within a cell based on fluorescence microscopy. Actin filaments provide the cell with structure; intermediate filaments and microtubules often co-localise, the later of which depart from the primary MTOC adjacent to the nucleus. Courtesy of Vic Small, Austrian Academy of Sciences.

of three actin subunits that, once linked, hydrolyse bound ATP to stabilise the filament. This creates a slow degrading end -the pointed or (-) end- and a fast polymerising side where new G-actin is bound, the barbed or (+) end. In the cytoplasm, however, G-actin monomers are sequestered by proteins such as profilin and, when able to form dimers and trimers, hence polymerisation nuclei, these are unstable. Together, this encumbers the spontaneous formation of F-actin. Accordingly, the process requires the presence of nucleators [84], of which three major classes have been identified: the Arp2/3 complex, actin-binding domain nucleators like Spire [85], and formins [84].

The **Arp2/3 complex** is an assembly of seven proteins containing the actin related proteins (Arp) 2 and 3, with similar homology to actin. It is activated by Nucleation Promotion Factors (NPFs) like the Wiskott-Aldrich Syndrome protein (WASP), which exists in an auto-inhibited state until it is itself activated via Cdc42. Upon the interaction of the complex with WASP, a conformational change repositions the subunits into a filament-like disposition, thus allowing it to weakly interact with F-actin. This interaction strengthens when the WASP links to G-actin, which is then nucleated via the Arp2/3 actin homologues causing the branching of the actin filaments [86]. **Actin-binding domain nucleators** are also referred to as tandem WH2-domain-based nucleators. The WH2 domain is the WASP-Homology 2 domain, a sequence of 17 aminoacids participating in actin-subunit recruitment. Spire, for example, contains four WH2 domains that stabilize linear arrays of four actin subunits. Albeit this organisation seems suboptimal since its nucleation activity is lower than that of the Arp2/3 complex, tandem

WH2 nucleators can interact with other complexes and dimerise into parallel strands that present increased activity [84]. Due to a more fundamental relevance to the thesis, formins will be described in more detail below.

Formins

Formins are a large family of proteins that modulate cytoskeleton organisation by regulating actin and microtubule dynamics [13]. Formins are dimeric multi-domain proteins with varying architecture. However, they are mostly characterised by the formin-homology 1 (FH1) and 2 (FH2) domains. The FH1 domain is able to recruit actin in profilin-containing complexes via proline-rich motifs, whereas the FH2 domain forms a ring-like structure that surrounds the actin filament at the barbed end and elicits processive elongation. Therefore, unlike the Arp2/3 complex, which leads to branched organisations, formin nucleates linear filaments (Fig. 2.10). The C-terminal end of the FH2 domain, in addition, enhances nucleation by direct recruitment of actin monomers or other nucleation promoters [84]. An FH3 domain, less conserved and common, directs formins to specific intracellular locations.

Unlike other actin nucleating complexes, formins remain bound at the barbed ends of the filaments. Accordingly, they can prevent the action of capping proteins and therefore elicit both nucleation and elongation of actin filaments, the mechanism for which is not completely understood. The elongation process is believed to involve transient and alternating interactions between the two halves of the FH2 dimer ring and the two actin end-units of the filament. With this movement, the FH2 domain would undergo conformational changes, thus switching between an actin-accepting form and a closed state. It is also unclear whether within this motion, formins would slip over or rotate around the actin filaments [13]. Some formins are directly anchored to the cell membranes, which could limit their rotational capability. For this reason, alternative mechanisms have been proposed by which formins would follow a star-stepping mechanism or by which they would rotate in the direction opposite to the filament growth, hence reducing torsion strain [88].

Within the formin family, the Diaphanous-related formins (DRFs) are a major subgroup characterised, as shown in figure 2.11, by three domains: a C-terminal Diaphanous auto-regulatory domain (DAD), a Diaphanous inhibitory domain (DID), and an N-terminal GTPase-binding domain (GBD). The DID-DAD interaction leads to DRF inhibition, which is commonly released by the binding of Rho-like GTPases like Rho [14]

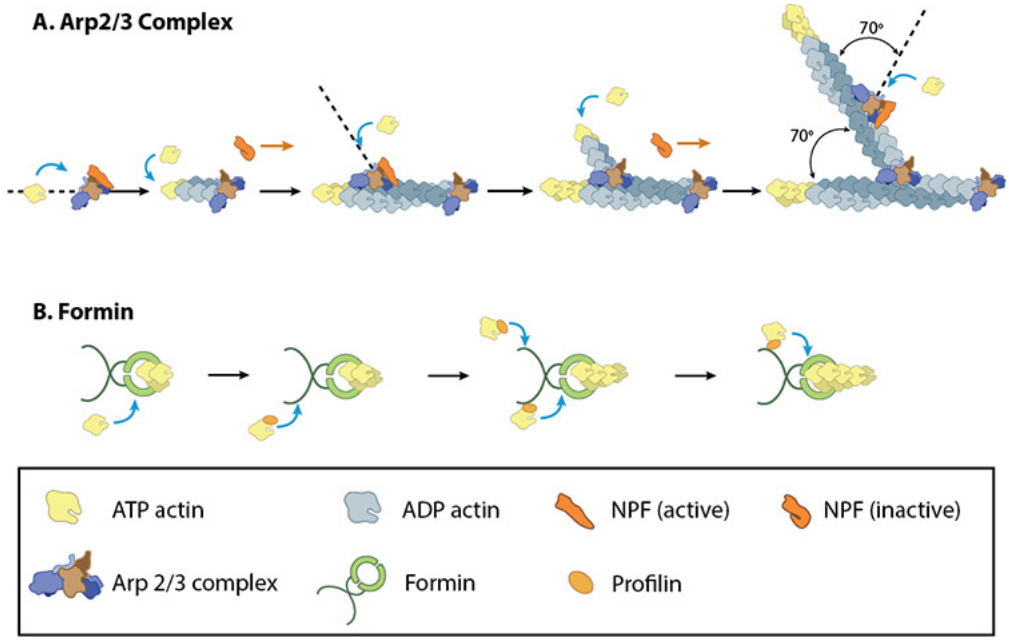

Figure 2.10: **Formin and Arp2/3 mediated actin polymerisation. A)** NPFs activate the Arp2/3 complex, which interacts with actin monomers and undergoes a conformational change that allows its association with pre-existing F-actin to promote nucleation of branched actin filaments. The complex remains at the minus end of the filament. **B)** Formin dimers recruit ATP-actin monomers via profilin interaction and promote filament elongation. The nucleated segment is stabilised by hydrolysis of ATP in the actin subunits. Formin remains associated to the barbed end of the filament. Reprinted with permission from [87] (CC BY 4.0).

and Ras [16]. Briefly, Rho GTPases are molecular switches that cycle between two conformational states in dependence to GTP/GDP association and hydrolysis. They participate in the regulation and coordination of several signal transduction pathways related to cytoskeletal organisation [15], and are therefore involved in cell adhesion, polarity, migration [90], contractility and cell-cell communication [91]. Rho -encompassing Rac and Cdc42- and Ras represent 2 of the 5 families in which the small GTPases can be classified [15].

DRFs comprise 10 of the 15 formin forms in mammals [13] and, with 10 isoforms (ForA to J), constitute the formin population of the model amoeba *Dictyostelium discoideum* [92]. Mesenchymal and *Dicty* cells represent the extremes of a broad spectra in cell migration: mesenchymal cells, like fibroblasts, advance slowly via strong cell-substrate interactions, protruding lamellipodia at the leading edge and prominent stress fiber formation; in contrast, amoeboid migration (also observed in cancer and immune cells) is based on weak substrate adhesion. Accordingly, it is fast and allows the cell to maintain a rounder shape, hence facilitating a more 3D-like migratory behavior in which pseudopods and blebs form the advancing front while myosin II-driven

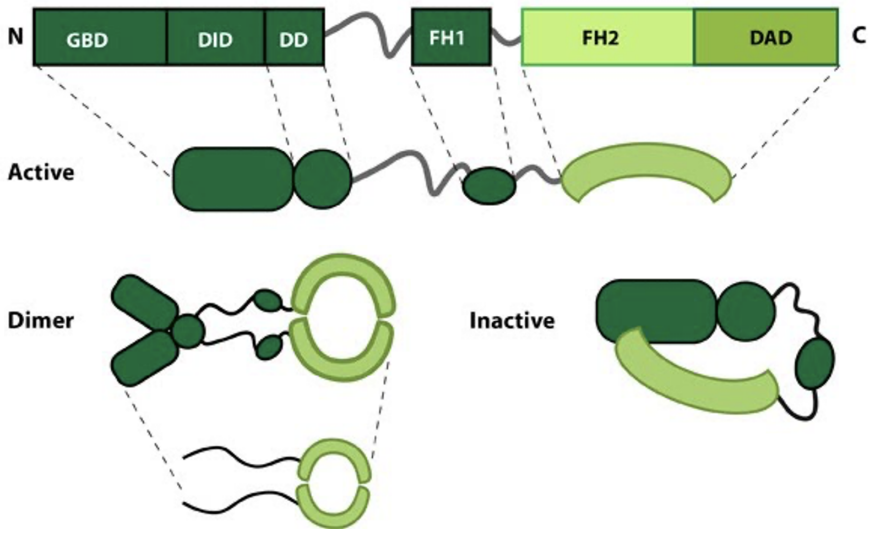

Figure 2.11: **Structure of Diaphanous-related formins.** In the active and dimerised formin configuration, the FH1 domain recruits actin-profilin dimers while the FH2 domain, which forms a ring-like structure, surrounds the actin filament and promotes its elongation. In its inactive form, the DID and DAD domains associate, resulting in formin inhibition. This interaction can be dissociated with the binding of Rho at the GTPase binding domain. Modified with permission from [89] (CC BY 4.0).

contractility dominates the rear [13, 92]. Despite these differences, and underlining the relevance of formins and their conservation through species, mesenchymal and *Dicty* cells present formin forms with related functionality. Accordingly, Diaphanous-related formin-1 (mDia1), mDia2 and mDia3 in mesenchymal cells respectively relate to ForA, ForH and ForE in *Dictyostelium discoideum*. In *Dicty*, ForA, ForH and ForE collaborate to ensure the integrity of the actin cellular cortex; ForA carries this function at the trailing edge of migrating cells and ForH and ForE localise at filopodia tips. While triple mutants devoid of these formins are unable to migrate, partial mutations induce a compensatory over-activation by other formins. In mammalian cells, very similar effects are observed: mouse melanoma mutants lacking mDia1 and mDia3 show defects in polarization and migration as a result of a less dense actin cytoskeleton. In addition, partial deletions lead to compensatory over-expression of the remaining formin [16, 93], reflecting the essential role of formins in normal cell behavior.

Actomyosin cortex

As described above, the cytoskeleton is a highly dynamic structure formed by filamentous elements such as actin, microtubules and intermediate filaments. However, it also

encloses a characteristic element that acts like a shell and provides the cell with control over its architecture: the actomyosin cortex (Fig. 2.12). The cortex is a densely cross-linked actin mesh that, by action of myosin II motors, presents a compliant and contractile behavior [9]. In addition, it is bound to the plasma membrane through several proteins including ezrin, radixin and moesin (ERM), and myosin I motors [10].

Fine control over the cortical behavior is provided by the myosin-mediated contraction but also by the tailoring of the mesh architecture in response to environmental and intracellular cues. Accordingly, a balance exists between the concurrent action of actin-polymerising factors like the Arp2/3 complex and formins (which promote branching, elongation and *de novo* synthesis of F-actin), and of capping proteins and actin-severing and disassembling factors. This organisation provides the actomyosin cortex with adaptable thickness and density, required for the proper functioning of the cortex during cell division, migration and adhesion, differentiation or external deformation [10, 11]. As an example, in the transition from weak to strong adhesion, the thickness of the cortices of MDCK II cells increases from 165 nm to 174 nm, whereas cortices of fibroblasts are over 2-fold thicker; cortical mesh sizes range between 20 and 250 nm [9].

Rheological properties of the actomyosin cortex

Given the importance of cortical adaptability, several models and methods have been developed to describe the viscoelastic behavior of the actomyosin cortex. To this purpose, the cortex has been generally described as a contractile shell surrounding an incompressible liquid, model that has been afterwards applied to the measurements obtained via atomic force microscopy [94, 95], parallel glass microplate compression [96], micropipette aspiration or numerical simulations [97], to obtain several parameters that have become of widespread use.

One of these parameters is the **Young's elastic modulus**, which reflects the cortex stiffness through the ratio of its deformability (or tensile stress) upon an applied tensile strain. Values have been found in an interval from 0.1 to 100 kPa. This wide range is consequence not only from the properties intrinsically different throughout a number of cell types, but also due to the conceptual and mathematical variations introduced by the models applied [98]. Another parameter is **cell fluidity**, characterised as a dimensionless coefficient ranging from 0, representing an ideal elastic solid, and 1, a newtonian fluid. Typical values for adherent cells fall between 0.2 and 0.4 [99, 100], albeit *in vitro* experiments on confluent MDCK II cells, artificial actin cortices and theoretical interpretation point to values of 0.5 [101, 102]. **Cortical prestress** -sometimes referred

to as cortical or active tension [97]-, has shown a wide range of values, from 0.4 to 25 mN/m. It mirrors the actin architecture and the membrane tension transmitted through myosin-mediated contraction. The **area compressibility modulus**, on the other hand, is the 2D elastic modulus of the cortex and describes the time-dependent resistance to area increase during deformation. It can be calculated based on the mesh size and thickness of the actin cortex.

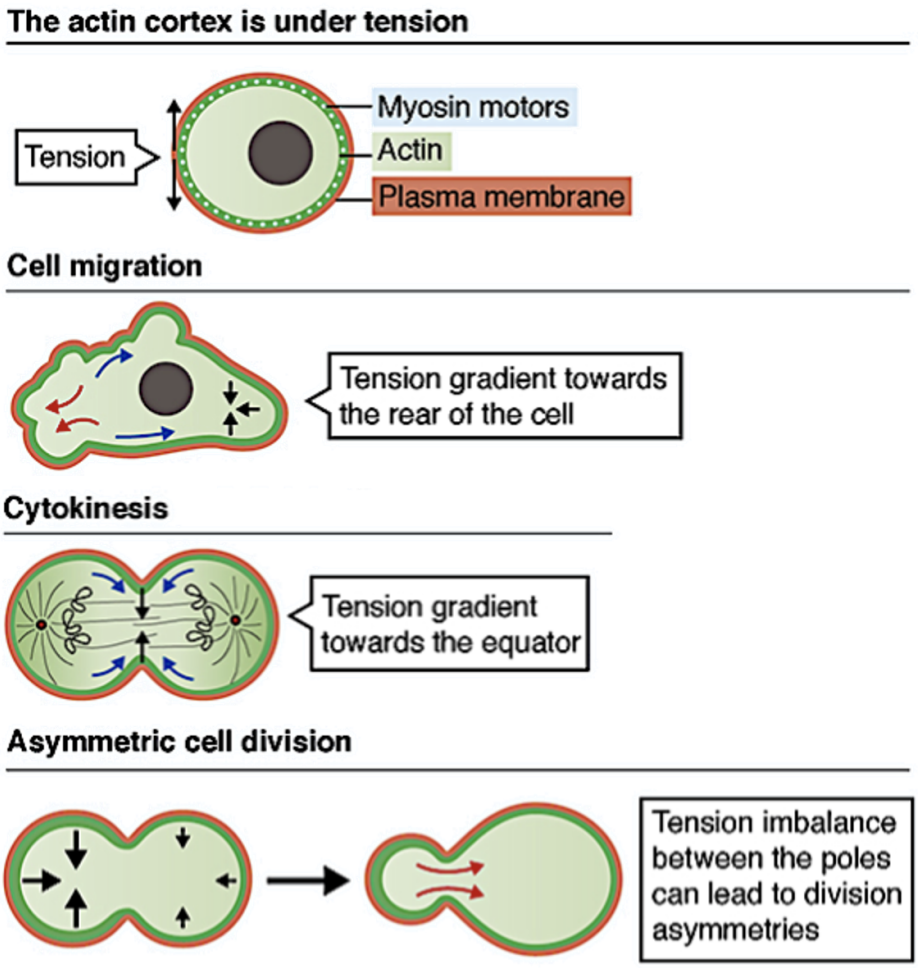

Figure 2.12: **Adaptations of the actomyosin cortex.** The actomyosin cortex is located underneath the plasma membrane and is formed by an actin mesh enriched with myosin motors. In normal conditions, the cortex provides structure to the cell and generates prestress via its contraction. To carry cell functions, the cortex needs to adapt tension gradients: during cell migration, the tension is larger at the rear end to promote cell contraction; during cell division, it is localised at the equator to facilitate cytokinesis. Asymmetric distributions of the tension gradient lead to asymmetric cell division. Reprinted with permission from [10] (CC BY 3.0).

2.4.2 Cellular adhesion

Cell adhesion is key to cell survival, as it provides communication with the surrounding microenvironment and neighbouring cells. Cell-substrate adhesion of spreading and migrating cells starts with the formation of a protrusion at the front edge, the lamellipodium. In this region, actin polymerisation is highly active and forms branched architectures via the action of the Arp2/3 complex. Under the umbrella of this structure, the first cell-substrate interactions are established via nascent adhesions (NAds), which are small and dot-like. However, they involve several molecules including integrins, actin-linking molecules like vimentin, and the signaling focal adhesion kinase (FAK). Amongst others, vimentin and FAK present phosphorylated residues that can therefore promote additional signaling processes. NAds have relatively short lifetimes ($\sim$ 1 min) depending on the migratory speed of the cells: the more distal and rear sides of the lamellipodium's front undergo actin depolymerisation and therefore, when the lamellipodium advances and the nascent adhesions enter the degradation area, they are either disassembled or enter a maturation process to become focal complexes (FCs). FCs are larger and present non-muscle myosin II dependence, but like NAds, are transient. With the advancement of the lamellipodium, FCs grow and mature into focal adhesions (FAs). As the number of FAs increases, they slow down the movement of the lamellipodia through the action of the myosin motors. Finally, the endpoint of the adhesion maturation is reached with the formation of fibrillar adhesions, which are associated to bundles of actin filaments and present lifetimes of several hours [103, 104].

Integrins

NAds represent a first cell-substrate interaction that is established through the formation of integrin-ECM contacts. Integrins are heterodimers formed by α and β units that form two-legged conjugates. They are regarded as promiscuous due to their ability to bind to several ligands, which enables them to sense cues in the cellular environment and initiate a number of cell functions in response, from proliferation to migration. In general, they target the ECM via RGD moieties, laminin and collagen [104, 105].

To form NAds, integrins must be first activated through a conformational change. This can happen via an outside-in or inside-out mechanism. Within the former, activation is caused due to the binding of transmembrane integrins to extracellular ligands or by strong membrane deformations, followed by the binding of stabilising adaptors to the cytoplasmatic tail. Within the latter, cytoplasmatic factors like talin cause integrin activation for the binding to extracellular ligands. The affinity between integrins and ligands is also promoted upon integrin clustering, given when several integrins bind poly-

valent ligands or through cytoskeletal re-organisation. Clustering allows NAds to grow into bigger adhesion points and is part of their maturation process. After integrins have clustered, the adaptor protein tensin and FAK are recruited, followed by vinculin, talin, paxillin, kindlin and α-actinin [105, 106]. The association of the cluster and the local tension induce phosphorylation events causing the downstream activation of Rho-like GTPases like Cdc42 and Rac [105] which, as schematised in figure 2.13, promotes actin polymerisation.

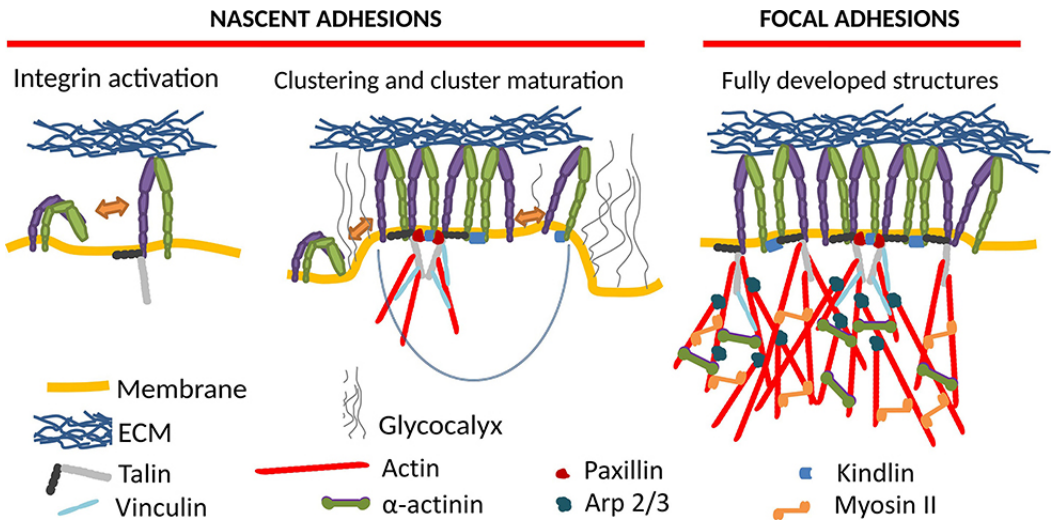

Figure 2.13: **Integrin-mediated adhesion.** The formation of nascent adhesions requires initial activation of integrins, upon which they can interact with their ligands. Upon binding, a number of factors are recruited, leading to actin polymerisation and clustering. The maturation process eventually leads to the formation of robust focal adhesions. Reprinted from [103] with permission from Frontiers in Physiology (CC BY).

The process by which cells can detect and adapt to the biophysical properties of the microenvironment is called mechanotransduction. Through integrin-mediated adhesions, a mechanical cross-talk is established between the viscoelasticity of the ECM and the tension within the actin filaments of the cell. The transmission of the resulting forces can regulate rapid and long-term responses through the activation of signaling cascades [107]. To give an example in the frame of cell adhesion and motility, integrin association to high concentrations of fibronectin -abundant, for example, in wounds [80]- inhibits cell polarisation and formation of membrane protrusions to cease migration in neutrophils upon their recruitment [108].

Cadherins

Cadherins are transmembrane glycoproteins that form adherent junctions through Ca^{2+}-mediated self-association. Once the cell-cell contact is formed, however, the protein also acts as an anchoring point for actin filaments through the binding of catenin proteins (Fig. 2.14). In addition, cadherins are tightly related to signaling cascades with specificity to the cadherin and cell types. Accordingly, the formation of cadherin-mediated cell-cell contacts can lead to the activation or inhibition of Rho, Rac and Cdc42 GTPases, with consequences from differentiation to cell migration [109].

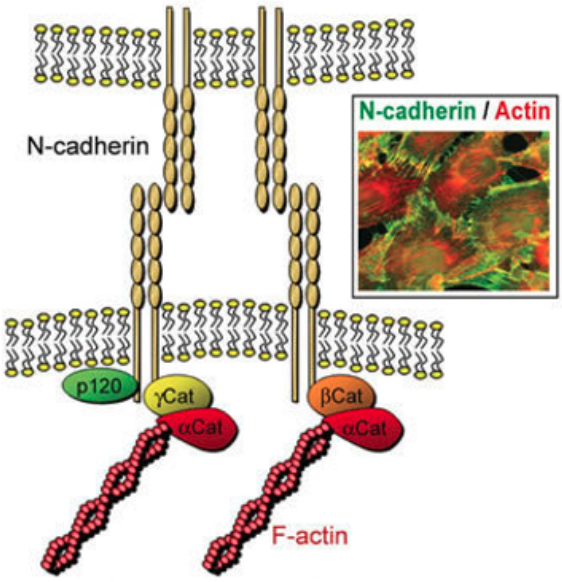

Figure 2.14: **Cadherin-mediated adhesion.** Cadherins form cell-cell contacts and associate with actin filaments through the presence of several catenin forms (α-, β-, γ-Cat and p120). Inlet: fluorescence micrograph of mesenchymal cells stained for N-cadherin (green), located at the cell periphery, and actin (red). Modified from [109] with permission from Springer Nature.

2.4.3 Cellular migration

Cell migration is initiated by a number of cues including chemotactic or electrochemical gradients, ECM composition, topography and fluid flows. For most eukaryotic cells, migration starts with the polarisation of the cellular body, which is the elongation towards the origin of the cue, and the forward protrusion of the cell membrane in the form of lamellipodia and filopodia. Similar to lamellipodia, filopodia are protrusions at the periphery of the cell, typically induced via Cdc42, that are composed of F-actin bundles. However, instead of forming a front, they are individual structures (Fig. 2.15). Both

lamellipodia and filopodia, and the signals derived from the formation and maturation of adhesions, influence cytoskeletal organisation via actin polymerisation; at the same time, the cytoskeletal architecture influences the assembly and disassembly of adhesions [23].

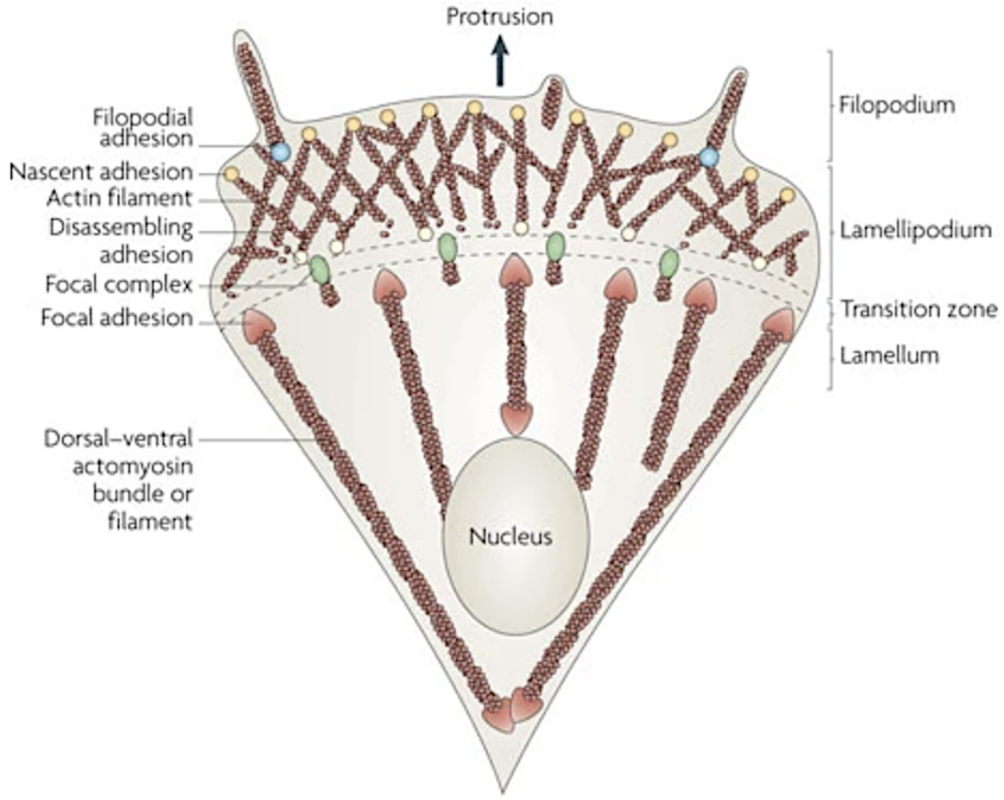

Figure 2.15: **Cell migration.** During the process, protrusions are formed at the advancing edge in the shape of filopodia and lamellipodia. In the latter, nascent adhesions are established, which can either disassemble or maturate once they enter the lamellum. Mature adhesions are stronger and larger, bundling several actin filaments in which myosin motors can induce force exertion via contraction. Modified from [23] with permission from Springer Nature.

At the advancing front, adhesions are under the retrograde tension exerted by the membrane resistance at the leading edge, and by the action of myosin motors on those focal contacts or adhesions under maturation at the lamellum, the region behind the lamellipodia. Accordingly, a competition exists between bidirectional forces that determines the advancement of the cell. For migration to be possible, the adhesions at the rear of the cell must disassemble so that the trailing edge can retract [23]. In fact, during cell migration, cortical tension is higher at the back of the cell to power cell body retraction [10]. Adhesion disassembly is associated with an apparent sliding of

the adhesions followed by their dispersal. This sliding action involves large numbers of integrins with fast turnover, suggesting that the anchoring point is constantly renewed in the direction of movement so that the global intracellular structure of the adhesion can slide with the cell [110]. Such behavior could be linked to the observation that migrating cells sometimes leave integrins behind, but not their cytoplasmatic components [111]. Besides this mechanism, proteases like calpain, which are Ca^{2+}-activated, have talin and the cytoplasmatic domain of the integrin β subunits as substrate, and therefore act as direct mediators of adhesion disassembly in retracting regions [23].

2.5 Single-cell force spectroscopy

2.5.1 The Atomic Force Microscope

Atomic force microscopy was initially developed as an improvement to the scanning tunnelling microscope (STM) in order to make the imaging of non-conducting samples accessible [112]. However, it was soon identified as a powerful tool in the biophysics field: not only the AFM presented enhanced imaging resolution in the native biological state of samples, thus minimising sample preparation and related artifacts [113], but its non-imaging operational mode opened up access to the structural, mechanical and chemical study of even the smaller molecules.

All this became possible due to the working principle of the AFM, which relies on the use of the cantilever: a very small tip suspended on a very soft spring that is actuated by a piezoelectric element allowing its relative motion with sub-Angstrom accuracy [114]. Approaching a sample with a cantilever causes the cantilever's deflection. As shown in figure 2.16, this generates a change in the optical path of a laser beam directed to its surface that is captured by a four-segment photodetector. The corresponding electrical signal is then translated into deflection values, and the information is used to regulate the cantilever's displacement via a feedback loop [115]. This setup allows the device to access forces in the pico-Newton domain, thus within the range of the forces necessary to separate ligand-receptor pairs (exemplary table shown elsewhere [116]).

2.5.2 AFM-based sample characterisation

AFM strategies are classically divided into contact, non-contact and tapping modes. In contact mode, the cantilever is in close vicinity with the surface of the sample. By dragging the tip over its surface while a feedback loops adjusts the cantilever's height to maintain constant deflection, studies on friction or conductive forces can be performed.

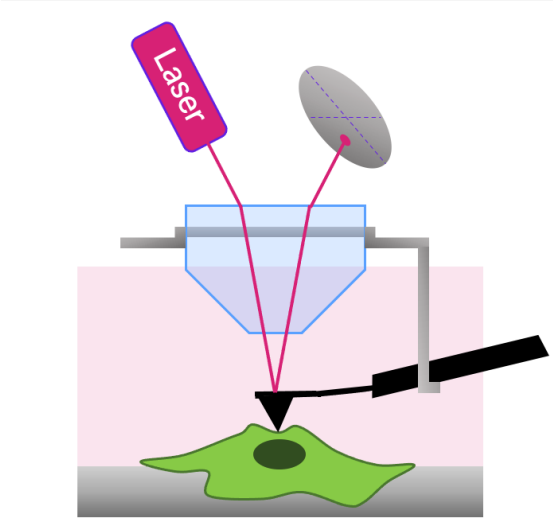

Figure 2.16: **Working principle of the AFM.** The AFM allows the characterisation of samples in solution, hence emulating its native state. When the cantilever probe approaches the sample, the cantilever is deflected, which causes a change in the optical path of a laser directed to its surface. The displacement of the incident beam on a photodiode receptor is translated into cantilever deflection, information used in a feedback loop to control the cantilever's position. Based on [115].

However, given the fragility of the AFM probes, this mode results dangerous for samples that are not specially planar. To overcome this, the non-contact mode maintains the cantilever's tip hovering about 5 - 15 nm above the sample's surface. Maintaining the oscillation amplitude via the feedback loop, the mapping of the surface can be performed with reduced risk. The tapping mode, alternatively, represents a compromise between the two first modes: the cantilever oscillates while the tip makes repulsive contact with the surface of the sample at the lowest oscillating point, which mitigates damaging lateral forces. In addition, it causes less stress to the sample, so it is specially suitable for the imaging of molecules that are non-covalenty attach to the surface [117].

AFM force curves

In this thesis, the interest lays on the use of the AFM to access the forces generated by cells as a result of their viscoelastic properties. Accordingly, the AFM is operated in contact mode. However, upon approaching the sample, the cantilever does not displace in the x- and y-directions, which would lead to the mapping of the region. Instead, force curves are obtained by lowering the cantilever towards the sample at constant velocity until its deflection indicates that a target force has been reached. At this point, the cantilever is retracted.

This is reflected in figure 2.17, where exemplary curves on a hard substrate and a cell are compared. On hard and homogeneous substrates, the force -or deflection- follows a linear trend with the cantilever's displacement from the moment it gets in contact with the sample. In contrast, when probing cells, the hysteresis in the curvature of the force-distance plot reflects the viscoelastic properties of the biological sample, whereas the snap on/off events contain information on the affinity and adhesive forces between sample and cantilever.

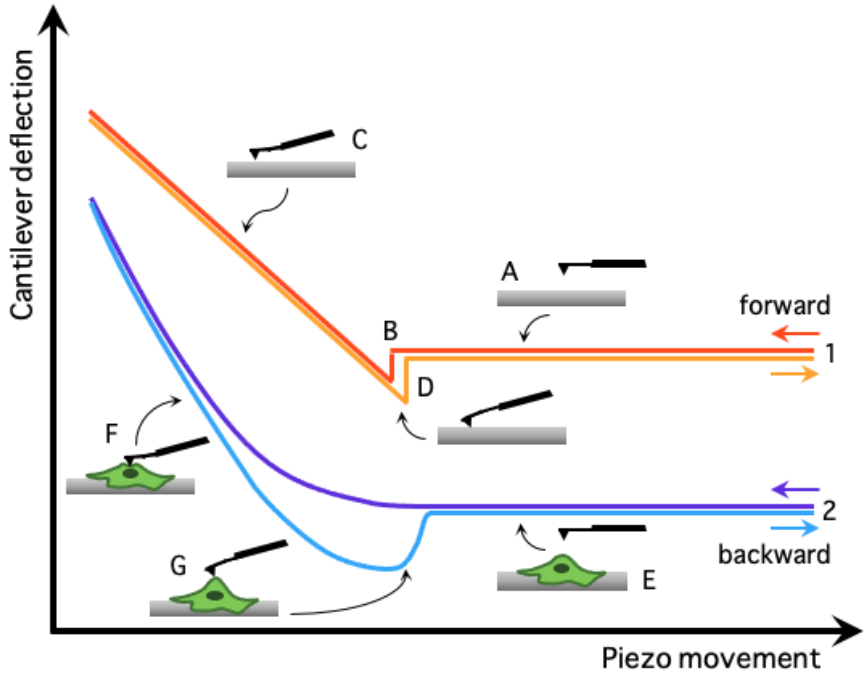

Figure 2.17: **Exemplary AFM force curves. 1)** When the cantilever approaches a hard sample (A), no deflection is measured until it starts interacting with the surface of the sample and the tip *snaps on* onto it (B). If the approaching continues and the sample is homogeneous, a linear increase in deflection is detected (C) until a set-point force or deflection are reached, upon which the measurement proceeds with the retraction of the cantilever. The cantilever will remain attached to the surface until the force deflecting the cantilever exceeds the attractive forces between cantilever and sample; at this point, the cantilever *snaps off* (D) and deflection returns to baseline values. Based on [115]. **2)** On soft surfaces, the operation of the cantilever follows the same steps. However, since cells are relatively soft samples with inherent inhomogeneities and viscoelastic properties, the deflection-displacement curves show non-linearities (F) due to force dissipation and cellular adaptations. During retraction, adhesive forces may contribute to the delay of the snap off event (G), after which the baseline values are recovered (E).

Compression-relaxation force curves are a specific type of AFM-based sample probing. In their acquisition, typical cantilever actuation is followed, with the difference that upon reaching the target force (compression), the cantilever remains immobile in

position for a short dwell time duration before being retrieved (relaxation). For the research presented in this thesis, tipless cantilevers are mostly used to provide a parallel plate-like compression of the cells (Fig. 2.18).

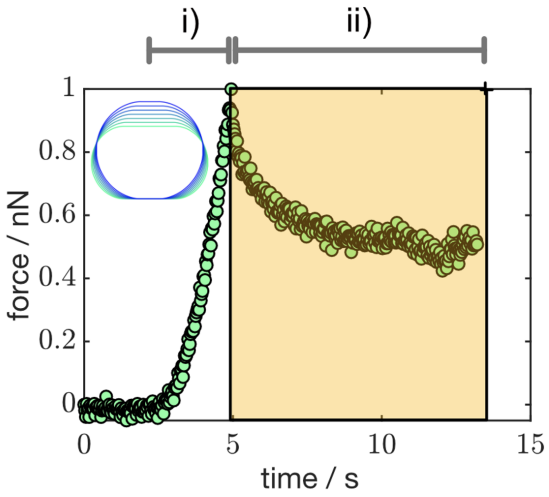

Figure 2.18: **Compression-relaxation force curve.** In the time course of the AFM-based measurement, cellular compression (i) is followed by relaxation (ii), during which the cantilever is maintained in position sandwiching the cell in a parallel plate fashion. The inlet reflects the progression of the cellular geometry during compression (from dark blue to light green). Courtesy of Andreas Janshoff, University of Göttingen.

Figure 2.19 shows that during the probing of a sample, the cantilever's deflection (δ) is smaller than the displacement z recorded based on the piezoelectric actuation. This is caused by the indentation of the sample, of depth h. Accordingly: $z = \delta + h$. To retrieve h, the deflection of the cantilever can be subtracted from z upon its calculation following Hooke's law, where k denotes the cantilever's spring constant:

$$F = k\delta \tag{2.1}$$

Cantilever calibration

To accurately convert the photodetector's signal into quantitative values of force, the cantilever must be first calibrated in order to determine the distance that is actually deflected given a change in the photodetector's voltage. Nominative values are provided by the manufacturer based on the geometry and Young's modulus of the cantilever and its material. However, variations during the production process can cause divergences. In addition, calibration is also affected by the optical path that the detection laser follows

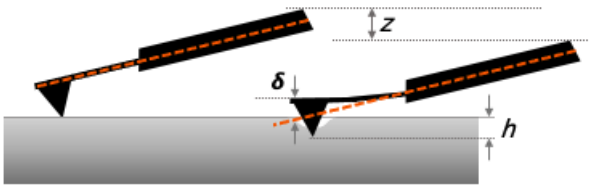

Figure 2.19: **Sample indentation in AFM measurements.** Upon entering in contact with the surface (left), the progressive lowering of the cantilever into the sample (right) for a distance z causes, simultaneously, cantilever deflection δ and sample indentation h. Based on [115].

within the AFM, sensitive to the refractive index of the immersion medium. Therefore, the instrument must be calibrated at the start of an experiment.

Several methods exist for carrying out this process. Here, the thermal noise method is applied [118]: the fluctuations of the cantilever caused by its kinetic energy at a given temperature are plotted as a function of frequency. The greatest amplitude in the resulting thermal noise spectrum indicates the resonance frequency of the cantilever, which depends on its spring constant and follows a Lorentzian shape. The area below the peak is a measure of the power of the cantilever's fluctuations; given that the integral of the power spectrum equals the mean square of the fluctuations in the time series, the spring constant k can be determined according to the following equation [119], where $k_B T$ reflects the energy value through Boltzmann's constant, and P is the area of the power spectrum corresponding to the thermal fluctuations:

$$k = k_B T / P \tag{2.2}$$

2.5.3 Modeling compression-relaxation curves

To be able to access the rheological properties of cells from compression-relaxation measurements, a suitable model is necessary. In this thesis, the Evans model is applied [9]. Before proceeding to its description, however, the Hertz model will be explained as a well-established reference.

The Hertz Model

The hertzian model allows the determination of the Young's modulus of a sample (E), which defines the relationship between an applied tensile/compressive stress (σ) and the resulting axial strain (ε). The equation to be used in the calculation depends on the geometry of the indenter, as the Hertz model considers the contact area between

sample and indenter. However, a generalized force-indentation relation exists based on Sneddon's formalism [120, 121]:

$$F(\delta) = \alpha\, E\, \delta^{\beta} \tag{2.3}$$

Here, δ is the indentation depth; α and β reflect the geometry of the indenter and the sample's Poisson's ratio (values for typical geometries can be found elsewhere [122]). In order to apply eq. 2.3, the system must comply with some assumptions: (1) the sample is approximated as an isotropic and linear elastic solid that expands, infinitely, in a half-space, (2) the indenter is not deformable and (3) there are no additional interactions between sample and indenter. To adhere to the first assumption, the Poisson's ratio is set to 0.5, characteristic of an incompressible rubber-like material elastically deformable at small strains. Upon such considerations, E can be obtained as a fit parameter in the fitting of force-indentation curves following the expression above.

The Evans Model

The Evans model aims to describe the time-dependent relaxation and deformation of the cellular cortex upon the determination of the contractility and power law values that correspond to such behaviour, based on time-independent prestress. The viscoelastic model is presented and explained at length in "Prestress and area compressibility of actin cortices determine the viscoelastic response of living cells" [9]. Here, the fundamentals will be introduced.

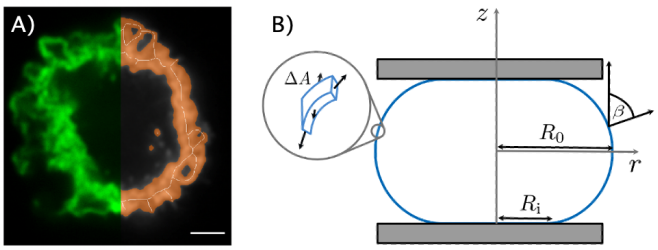

Figure 2.20: **Actomyosin cortex as a thin shell. A)**. Actomyosin cortex of a non-spread fibroblast. The left side shows a stimulated emission depletion (STED) micrograph (actin in green) and the right side the corresponding reconstruction (brown). White lines indicate the center contour. Scale bar: 500 nm. **B)** Parametrisation of the actomyosin cortex upon compression between parallel plates. In the schematics, R_0 and R_i respectively indicate the equatorial and contact radii. ΔA reflects the interpretation of the cortex as a minimal surface of constant curvature; β is the angle between the vertical axis and the normal at the cell surface. Adapted with permission from [9]; © 2020 by the American Physical Society.

The structure of the cellular actomyosin cortex is that of a thin shell (Fig. 2.20). Based on microscopy images, it has a thickness of around 400 nm for fibroblasts. Due to the thin-sheet structure of the cortex, its bending and shearing contributions -both dependent on the material's cross section- can be neglected. Therefore, the cortex resists deformation only by its prestress and area compressibility modulus. During indentation experiments, the volume of the cell is constant [123]. Even assuming typical hydraulic permeability values, no volume changes take place during the experimental time scales. Upon this consideration, the total force f is axially balanced at the equator of the cell and can be determined as the difference of pressure acting on the contact surface:

$$f = \Delta P \pi R_i^2 = \frac{2\pi R_0 R_i^2}{R_0^2 - R_i^2}(T_0 + K_A \alpha) \tag{2.4}$$

R_0 and R_i are, according to figure 2.20, the equatorial and contact radii of the compressed cell; α is the areal strain $\Delta A/A_0$. The difference of pressure ΔP is obtained from considering that, in mechanical equilibrium, the function describing the constant curvature of the cell (λ) is equivalent to the pressure difference across the surface divided by the isotropic tension (T):

$$\lambda = \frac{\Delta P}{T} \tag{2.5}$$

Such expression, where $T = T_0 + K_A\alpha$, can be divided into the meridional and circumferential components of the curvature and re-written as a function of the cell radius (r) and the angle with the normal to the cell surface (γ; β in Fig. 2.20), $u(r) = sin\gamma$. By applying the boundary conditions that at the equator $u(r = R_0) = 1$ and at the contact region with the parallel plate $u(r = R_i) = 0$, equation 2.5 eventually leads to:

$$\Delta P = \frac{2R_0}{(R_0^2 - R_i^2)} \tag{2.6}$$

Going back to equation 2.4, the expression can be transcribed into a non-dimensional form by using the generic shape function $g(\xi)$, where $\xi = z_p/R_c$ with z_p the distance between parallel plates and R_c the radius of the cell in suspension. Accordingly:

$$f = R_c(T_0 + K_A\alpha)g(\xi) \tag{2.7}$$

The advantage that this poses is that $g(\xi)$ and $\alpha(\xi)$ can be approximated by polynomials to obtain analytical solutions that only need to be computed once. These solutions build up to a general expression for the restoring force during parallel-plate compression that is suitable both for the compression ($0 < t < t_m$; $s = t$) and relaxation ($t > t_m$; $s = t_m$ and $\dot{a} = 0$) intervals:

$$f = g(\xi) R_c \left(T_0 + \int_0^s \tilde{K}_A \left(t - \tau \right) \frac{\partial \, \alpha(\tau)}{\partial \tau} \, d\tau \right) \tag{2.8}$$

The integral can then be solved by using $\xi \approx v_0 t / R_c$, where v_0 is the cell compression velocity, and, based on the broad distribution of relaxation times that can be observed on the cortex, by assuming the power law behavior $\tilde{K}_A = K_A (t/t_0)^{-\beta}$; t_0 is a scaling parameter. Accordingly, by applying equation 2.8 to the compression-relaxation curves measured with the AFM, the Evans model gives access to T_0, K_A and β. The same mathematical pipeline can be applied to describe the indentation of different cellular geometries, like capped spheres reflecting the geometry of confluent and adherent cells, as long as rotational symmetry can be assumed.

Figure 2.21 shows the impact of prestress, area compressibility modulus and cortex fluidity on compression-relaxation curves. At low indentation depth, prestress leads the cortical response, while at larger strain, the area compressibility modulus dominates. Increasing K_A impacts the compression at larger strain and increases the amount of dissipated energy during relaxation. Finally, increasing β leads to a larger slope during compression and a faster drop of the force in the relaxation.

2.6 Impedance-based wound healing assays

2.6.1 Classical wound healing assays *in vitro*

Initial work in the field of wound healing research made use of mechanical wounding approaches, such as the scratch assay, due to the simplicity and accessibility of the required materials. For this reason, it prevails to-date. The assay consists on scratching part of a pre-formed cellular layer with a pipette tip, a surgical knife, or the likes, to thereafter analyse the recolonisation process. The manual application of the wound rests reproducibility between experiments. For this reason, stamping assays and variations like thermomechanical damaging were developed to overcome the drawbacks of the scratch assay [124] and provide flexibility in wound size and geometry.

Depending on the time of interference with the cell layer, experiments can mimic the formation of a wound or lead to the time-controlled expansion of the surface available for cell colonisation. For the former, a pre-existing cellular layer must be damaged, like in the case of the scratch assay (Fig. 2.22), so that the chemical signals associated to cell death are released, thus involving the pro-inflammatory stress signals TGF-β and TNF-α [125]. For the latter, a space is made inaccessible during the formation of the

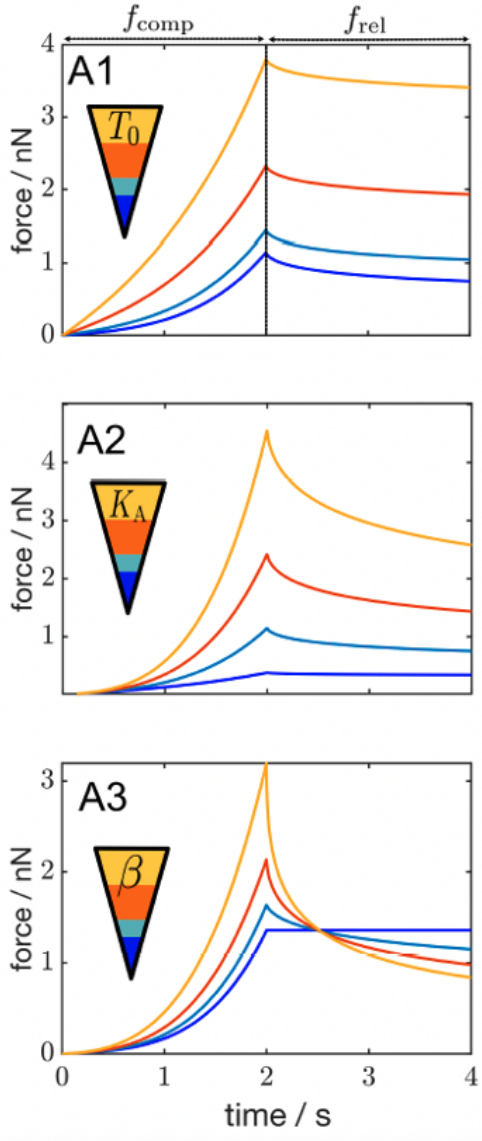

Figure 2.21: **Impact of the cortical parameters on force curves.** Computation of compression-relaxation curves based on the modification of T_0, K_A and β. Prestress mirrors the actin architecture and the membrane tension transmitted through their interaction; area compressibility modulus, the 2D elastic modulus of the cortex, reflects its time-dependent resistance to area increase and therefore, to deformation. β characterises the shell's fluidity. **A1)** Result of varying T_0 (0.1, 0.2, 0.5 and 1 mN/m) with constant K_A of 0.1 N/m and β of 0.3. **A2)** Result of varying K_A (0.01, 0.1, 0.25 and 0.5 N/m) with constant T_0 of 0.1 mN/m and β of 0.3. **A3)** Result of varying β (0, 0.2, 0.4 and 0.6) with constant T_0 of 0.05 mN/m and K_A of 0.2 N/m. With increasing strain, the dominating factor on cortex response transitions from prestress to area compressibility modulus. Reprinted with permission from [9]; © 2020 by the American Physical Society.

cell layer, for example via the use of a stamp or an electric field, and the obstacle is then removed to expose the void to be colonised. This is the case of the barrier assay, where gap closure is hence carried in the absence of paracrine signalling factors related to cell death [126].

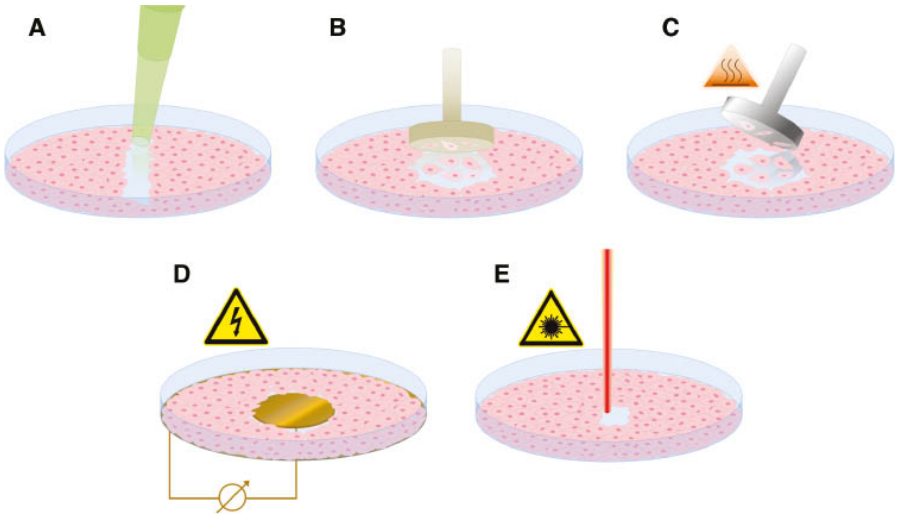

Figure 2.22: ***In vitro* wound healing assays. A)** Classical scratch assay. **B)** Stamp assay with **C)** thermal wounding. **D)** Electrical wounding. **E)** Laser ablation or optical wounding. Reprinted from [124] with permission from De Gruyter.

2.6.2 Electrical Cell-substrate Impedance Sensing

Covering a range of gap geometries and sizes, and accommodating the wound and barrier assays in one single device, the Electric Cell-substrate Impedance Sensing (ECIS) is a well-established and label-free technique that allows the real-time study of cellular dynamics. Due to their membrane structure, cells naturally present insulating properties against the free flow of electrons. Accordingly, when colonising and spreading over electrodes embedded in culture dishes through which a small AC field is applied, cells interfere with the electric flow (Fig. 2.23) generating a characteristic complex impedance (Z) that can be measured as a function of frequency. This conforms the working principle of the ECIS.

Adjusting the AC field's amplitude and frequency, as well as pulse duration, enables the switch between a passive and non-invasive mode that allows monitoring cell activity through the recording of its characteristic Z, and an active mode at high frequencies and amplitudes in which the cells on the electrodes are damaged and a wound is created

(Fig. 2.23). Alternatively, in the so-called electric fence approach, the high intensity AC field is applied before the cellular monolayer is formed, which acts as an electric barrier against their expansion. In this thesis the focus lays on ECIS-based wounding; more information on the electric fence experimental can be found elsewhere [27, 127]. In the monitoring mode, a weak current (< 1 µA) of relatively low cell specific frequency (from 1 to 40 kHz) is applied between the working and reference electrodes. Under these parameters, the cell membrane circumscribes the current to flow beneath and in-between cells in a non-invasive way [128]. When the amplitude is increased to the order of milliamperes and the frequency > 40 KHz, the current couples capacitively through the cell membranes causing electroporation. If the pulse duration is long enough (in the order of seconds to minutes), the damage of the membrane is irreversible and cell death occurs in the area constricted by the electrode's surface [129].

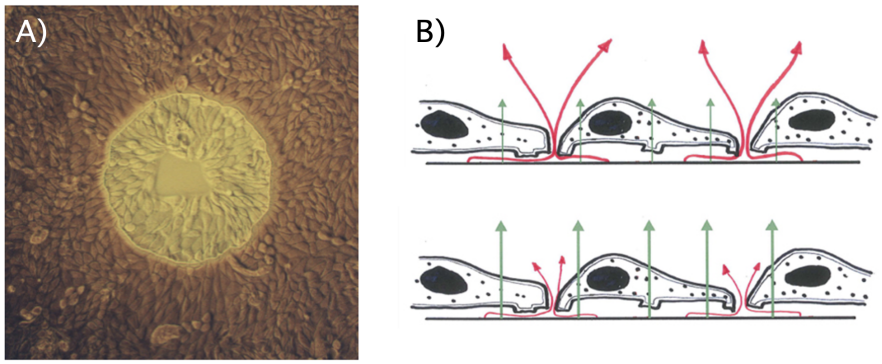

Figure 2.23: **ECIS working principle. A)** Phase contrast view of MDCK II cells repopulating a 250-µm electrode upon wounding. **B)** Schematics of the electric flow directionality during the passive (top) and active (bottom) ECIS modes. In the former, the current is mainly constrained by the cell membranes and confined under and between cells; in the latter, it couples capacitively through the cell membranes causing electroporation and cell death. Courtesy of Applied BioPhysics.

By analysing the impedance time courses resulting from the cell coverage of electrodes, enclosed information on both collective dynamics and biological condition can be retrieved. Collective dynamics reflect gap closure mechanisms in terms of recovery half time ($t_{1/2}$) and recovery rate (R), both obtained upon the fitting of the real part of the impedance to a sigmoidal function. Parameters relating to cellular condition and cell layer integrity, in contrast, provide insights on the changes and stress that cells undergo in the wound-healing process. These parameters are, specifically, the membrane capacitance (C_m), the barrier resistance (R_b) and α which, in order, reflect the average capacitance of the apical and basal cell membranes, the junctional resistance between

cells, and the inverted distance between the substrate and the basal cell membrane. In order to retrieve them, the impedance data needs to be fitted to an equivalent electrical circuit modeling the biological system.

2.6.3 The Lo-Ferrier model

Since the ECIS fundamental methodology was first described by Giaever and Keese in 1984 [130], several models of equivalent electric circuits have been developed with varying degrees of complexity [131, 132, 133]. Initial work regarded cells as disks. However, the need to more accurately describe the cellular geometry was already acknowledged [128]. To this purpose, Lo and Ferrier defined a cell as a rectangular box with two half disks attached at each end. Accordingly, the impedance was modeled as the sum of the contributions from the separate geometries [25], which led to the following definition:

$$\frac{1}{Z_c} = \frac{1}{Z_n + Z_m}\left[1 + \frac{LW}{LW + \frac{\pi W^2}{4}} \cdot \frac{\frac{2Z_m}{Z_n}}{\gamma W coth\left(\frac{\gamma W}{2}\right) + 2R_b^{rec}\left(\frac{1}{Z_n} + \frac{1}{Z_m}\right)} + \frac{\frac{\pi W^2}{4}}{LW + \frac{\pi W^2}{4}} \cdot \frac{\frac{2Z_m}{Z_n}}{\frac{\gamma W}{2}\frac{\left(\frac{I_0 \gamma W}{2}\right)}{\left(\frac{I_1 \gamma W}{2}\right)} + 2R_b^{disk}\left(\frac{1}{Z_n} + \frac{1}{Z_m}\right)}\right] \tag{2.9}$$

The complex impedances Z_n and Z_m refer, respectively, to the cell-free electrode, which is modelled as a constant phase element (CPE), and to the characteristic impedance of the covered electrode. The cell shape is defined upon typical length and width values

introduced via L and W. To describe the impedance through the edges of the cell body, hence two half disks, I_0 and I_1 are modified first kind Bessel functions of order 0 and 1 that portray the wave propagation within a drumhead. Other relevant properties of the system like the resistivity of the bulk cell culture medium (ρ) and the height between the substrate and the basal cell membrane (h) are introduced with γ:

$$\gamma = \left[\frac{\rho}{h}\left(\frac{1}{Z_n} + \frac{1}{Z_m}\right)\right]^{\frac{1}{2}} \tag{2.10}$$

From equation 2.9, C_m can be retrieved from the membrane impedance Z_m following expression 2.11. R_b accounts for the geometrical description of the cells based on the rectangle (eq. 2.12) and disk (eq. 2.13) shapes. Finally, α is inversely proportional to h (eq. 2.14):

$$Z_m = \frac{1}{i\omega C_m} \tag{2.11}$$

$$R_b^{rec} = \frac{\frac{4L}{W} + 2\pi}{\frac{4L}{W} + \pi} R_b \tag{2.12}$$

$$R_b^{disk} = \frac{\frac{2L}{W} + \pi}{\frac{4L}{W} + \pi} R_b \tag{2.13}$$

$$\alpha = \frac{\gamma W}{2}\left(\frac{1}{Z_n} + \frac{1}{Z_m}\right)^{-\frac{1}{2}} = \frac{1}{2} W \left(\frac{\rho}{h}\right)^{\frac{1}{2}} \tag{2.14}$$

To retrieve the parameters, the impedance time course is fitted using an iterative custom written MATLAB (MathWorks, MA, USA) algorithm based on least square analysis. However, the Lo-Ferrier model assumes a cell-covered electrode. Accordingly, it cannot be applied immediately after wounding or on partially re-populated electrodes. Furthermore, the fitting needs to be applied in discrete time intervals where the impedance is quasi-stationary so that average values can be calculated. Therefore, pre-wounding (20-23 h upon cell seeding) and post-wounding intervals at 45-48 h and 69-72 h are used.

2.6.4 Cellular micromotions

Cellular micromotions are tiny height fluctuations of the ventral membranes associated to cellular viability and metabolic activity [28, 134] that can be recorded with the ECIS. Their analysis requires transforming the frequency time courses into power spectral densities, and subjecting the micromotions to the study of long-term correlations through detrended fluctuation analysis (DFA) and computation of the variance in the noise of the impedance signals [29].

By treating a signal such as the impedance measurement as a statistical average of its frequency content, hence a power spectral density (PSD), periodical events like the beating of cardiomyocytes can be detected through peaks in the log-log representation of the PSD [26]. In the absence of periodic events, the PSD slope (S_{PSD}) itself characterises the source of the signal with enough sensitivity to differentiate between cancerous and normal cells [134, 135]. Biological noise is characterised by a non-zero linear slope of $1/f$ with the frequency f; in contrast, while white noise is independent of frequency and therefore originates a horizontal slope, Brownian motion follows a $1/f^2$ power law [136]. The PSD is obtained upon applying a fast Fourier transformation (FFT) to the fluctuating time series. On the other hand, detrended fluctuation analysis requires, according to Peng *et. al* [137, 138], the removal of the linear trend inherent to the raw data (hence, detrended). Variance, which is a measure of the amplitude of the signal fluctuations, is then calculated as the difference between the original and detrended data. This comparison can be done using data intervals, or boxes, of different length. By plotting the variance against the length of the boxes in a log-log plot, the resulting slope (α_{DFA}) provides insights on any long-term correlations ($\alpha_{DFA} > 0.5$) or strong correlations ($\alpha_{DFA} > 1$) within the signal [29].

Chapter 3

Materials and methods

In this chapter, the experimental practice is described with the aim to illustrate how the observations reported and discussed in this thesis were obtained, and to allow the repetition by the reader to whom it may be of interest.

3.1 Cell culture

3T3 fibroblasts are one of the most relevant cell lines used in wound healing research since their introduction in 1963 by G. Todaro and H. Green [139]. The isolation of the cell line was later repeated by G. Todaro on Swiss mouse embryo at the National Cancer Institute in Bethesda, part of the National Institutes of Health (NIH), thus originating NIH-3T3 fibroblasts. Obtained from the American Type Culture Collection (ATCC; Manassas, VI, USA), the NIH line was used throughout the experimental herein reported.

Upon arrival in a cryotube, cells were warmed in a water bath (37 °C) until ice crystals were dissolved. Contents were then transferred to a centrifuge tube with 9 mL of pre-warmed fibroblast (Fb) medium: Dulbecco's modified Eagle's medium (DMEM; Lonza; Verviers, Belgium) with 10 % fetal bovine serum (FBS; Biowest; Nuaillé, France), 1 % L-Glutamine (Lonza), and 1 % penicillin/streptomycin (Biowest). Next, the tube was centrifuged (1000 rpm for 5 min at 4 °C) and the pellet resuspended in 1 mL of fresh Fb medium. Cell density was determined using a Blaubrand Neubauer chamber (Marienfeld, Germany) and cells were seeded in a T25 flask, pre-coated with 0.1 % gelatin, containing 9 mL of fresh Fb medium.

In describing the expansion of 3T3 cells *in vitro*, their name sets a guideline: 3T3 stands for '3-day transfer, inoculum of $3{\cdot}10^5$ cells' for a 20 cm^2 dish [139, 140]. The immortalised cells were seeded accordingly in T25 flasks and cultured in Fb medium at 37 °C in a humidified incubator with 5 % CO_2. When approaching confluence but still

in the exponential growth phase, cells were trypsinized (Trypsin-EDTA 0.5 %/0.2 %; Sigma Aldrich; St. Louis, MA, USA) at 37 °C for 5 min, centrifuged (1000 rpm for 5 min), and resuspended after counting them in a Blaubrand Neubauer chamber in order to be sub-cultured in fresh flasks to avoid contact inhibition effects [141]. Adherent cells grow as a monolayer; confluent fibroblast monolayers yield around 40 000 cells/cm^2.

When preparing cells for an experiment, the same trypsinization process was followed. Upon centrifugation, however, cells were resuspended in the media required by the experiment, as detailed in the respective methods sections.

Cell culture was performed in the cell lab of the Max-Planck-Institute for Dynamics and Self-organisation in cooperation with the cell culture facility of the Department of Physical Chemistry at the Georg-August-Universität Göttingen.

3.1.1 3T3 clones with formin modulation

3T3 clones with formin modulations were provided by Prof. Dr. Jan Faix's group at the Medizinische Hochschule Hanover. Upon arrival, clones were immediately centrifuged (5 minutes, 4 °C, 1000 rpm). The pellet was then resuspended in 10 mL of fresh Fb medium and transferred to culture flasks to proceed with their culture as with wild type Fbs, hence at 37 °C in a humidified incubator with 5 % CO_2. Periodic sub-culture was performed to prevent confluence-related contact inhibition phenomena.

Inactivation of Diaph1 and Diaph3 genes to obtain NIH 3T3 fibroblasts with individual and simultaneous deletions of mDia1 and mDia3 was achieved, as previously described by the group, based on adoption of CRISPR/Cas9 technology followed by deletion verification via immunoblotting [142].

Briefly, the online prediction platform CCTop (crispr.cos.uni-heidelberg.de) was used to obtain suitable guides for the CRISPR/Cas procedure. Corresponding oligonucleotide DNA duplexes encoding the guide RNA were then inserted into the plasmid pSpCas9(BB)-2A-Puro from Addgene (Watertown, MA, US; plasmid #62988), with which cells were transfected. Successfully modified cells were selected via exposure to puromycin and thereafter amplified.

3.2 SCFS rheological characterisation

Single-cell force spectroscopy measurements were carried in an MFP-3D AFM (Asylum Research; Santa Barbara, US) equipped with an extended z-scanner (40 µm nominal range). The setup was mounted on a bright field IX71 Olympus microscope (Shinjuku City, Tokyo, Japan) with 10x (UPlanFI, Numerical Aperture (NA) = 0.30) and 40x (LUCPlanFLN, NA = 0.6) Olympus objectives, connected to a Zyla sCMOS camera (Andor; Belfast, UK). The whole setup was located inside a TMC Vibration Control chamber (Ametek; Berwyn, PA, US) over an active vibration isolation module (Accurion GmbH; Göttingen, Germany). Force measurements were carried using untreated, tipless Arrow$^{\text{TM}}$ TL2 cantilevers (NanoWorld; Neuchâtel, Switzerland; nominal spring constant (k_c) = 0.03 N/m) (Fig. 3.1).

Measurements were done on single cells. To make them accessible to the cantilever once seeded on the substrates (9 - 20 cm^2), cell suspensions had to be diluted in DMEM to a concentration of 300.000 cells/mL. Media was not supplemented with serum or hydrogen carbonate for pH stabilisation in order to avoid non-specific interactions that could cause drifts in the deflection. For this reason, cells could be maintained for an average time of 3 to 4 h, after which they started to incur into apoptosis. Accordingly, experiments were stopped before reaching this stage.

During measurements, cells were also maintained at 37 °C with an Environmental Controller (Asylum Research) using two different setups: the first one consisted of a BioHeater holder (Asylum Research) that sandwiched glass substrates against the AFM head, thus forming a closed space; the second one was based on the use of a Petri Dish Heater (Asylum Research) that sandwiched the Petri dishes (#351006; Falcon - Neta Scientific, Hainesport, NJ, US) used as substrate against the AFM head (Fig. 3.1). The BioHeater setup required the consumption of less material (by employing glass disks, it avoided single-use, plastic-based cellular culture dishes and, in addition, needed less volume of media and cell suspension), but was more prone to temperature drifts, mechanical damage of both the substrate's coating and the cantilever holder, and to cavitation. The Petri Dish Heater, in comparison, required more volume of solutions and was slower in regulating the temperature of the system. However, the heating was more stable over time and volume, and it was easier to handle.

Experimentally, measurements started by readying the setup with a bare, cell-free substrate submerged in media, and by bringing the system to 37 °C. Upon placing the cantilever in its holder, its position and rotation were adjusted through the sum and deflection feedback loops, which respectively indicate the total amount of light and the

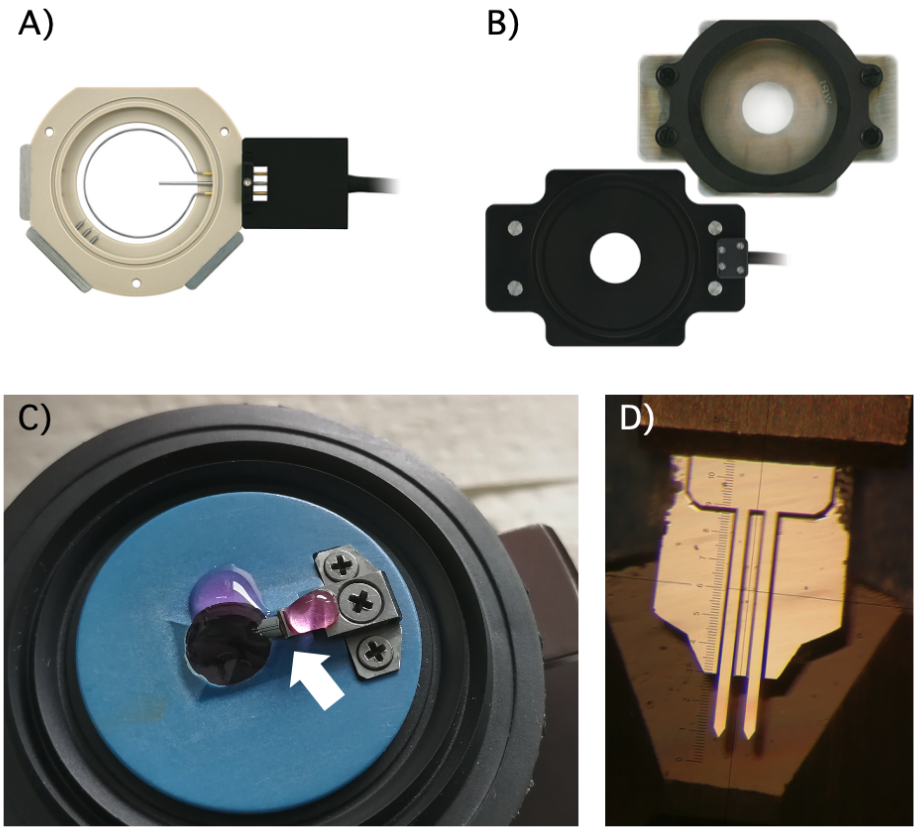

Figure 3.1: **AFM sample holder setup. A)** BioHeater system. Glass substrates are placed at the center of the holder from below, and fastened with a ring that is screwed against the body of the BioHeater. Media and cells are then added from above and their temperature regulated via the metal ring circumscribing the sample space. **B)** Petri Dish Holder (above) and Heater (below). Petri dishes are clamped against the supports with the black fastener shown in the non-heating holder, which is magnetically attached via the four magnets visible in the heater system (silver circles). The gap at the center allows access to the samples. Images provided by Applied Biophysics. **C)** Cantilever (arrow) clamped to the adapter of the AFM head over the prism that determines the light path of the laser. The fluid-retaining black membrane around the blue holder forms a closed space for the sample once it is sandwiched against the sample holders. Adding a drop of media over the cantilever helps prevent the appearance of bubbles once it is submerged in the media covering the sample. **D)** Detail of a cantilever (Arrow^{TM} TL2) clamped to the AFM support and hovering over the polished surface of the prism. The sides of the cantilever close to the clamping edge are notched due to its manipulation with tweezers, which has no effect on the AFM measurement as long as there is no debris attached to the free standing cantilever tips.

laser's beam position on the detector with respect to its center. The cantilever's spring constant was then validated following the thermal noise method [118]. Subsequently, AFM calibration was performed by approaching the substrate and removing bimetallic or thermal drifts using the resulting force curve as a reference. Cells were then resuspended and dispersed on the substrate. Temperature was re-adjusted to 37 °C and the whole chamber left to acclimatise for 30 min while cells settled and adhered to the substrate.

To obtain compression-relaxation curves, single cells were located through the microscope. After taking a micrograph from which the uncompressed cell radius could be later determined (Fig. 3.2.A), a series of force curves was obtained under the parameters of interest. As depicted in figure 3.2, **compression** started with the cantilever's approach to the cell at a minimally invasive speed of 1 µm/s until a target force of 1 - 2 nN, providing a compromise between contact formation and small cellular deformation, was reached. At this stage, the measurement of the **relaxation** caused by the cortical cellular adaptations proceeded with the maintenance of the cantilever's position for a dwell time of 5 seconds, after which it was withdrawn at the initial speed. For validation purposes, other combinations of speeds (1, 2.5, 5, 10 µm/s) and forces (1, 2, 5, 10 nN) were tested as specified in Chapter 5.

On a normal experimental day, force curves were obtained on an average of 8 cells with a maximum of 5 to 10 repetitions per cell to avoid cellular adaptations to the external load while ensuring the measurement of enough force curve repetitions. At least two measurement days were dedicated to each experimental category.

Substrate preparation

As mentioned above, two types of substrates (glass disks and synthetic Petri dishes) were used based on the requirements of the sample heater system employed. The preparation of the substrates was however independent of the setup, and conditioned only by the experimental requirements on cellular adhesion. Three states were distinguished: strong adhesion (i), strong adhesion reduction (ii), and weak adhesion (iii).

In order to measure **strongly adherent cells (i)**, substrates were functionalised with fibronectin: on the day of the experimental, substrates were exposed to oxygen plasma for 30 s and then coated with 0.5% fibronectin solution for 1 h at 37 °C. After incubation, functionalised substrates were rinsed with PBS and stored until the AFM measurement.

To achieve **strongly reduced cellular adhesion (ii)**, substrates coated with polyethylenglycol (PEG) were used instead [9]. In summary, PEGylation started with the cleaning of glass substrates with water and ethanol. After letting them air dry,

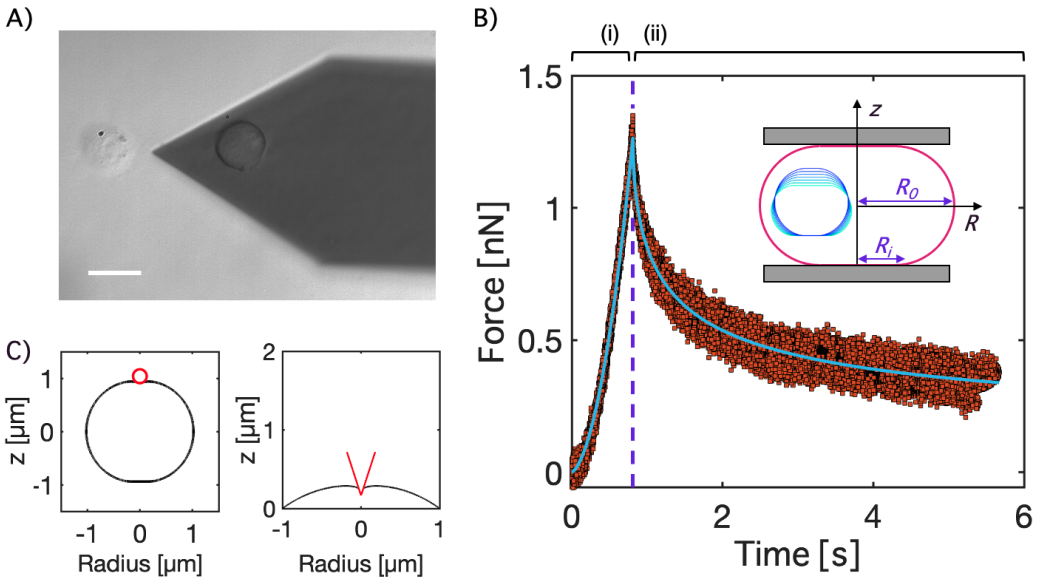

Figure 3.2: **Tip geometries in the acquisition of a compression-relaxation force curve. A)** Micrograph of a weakly adherent cell, thus round, pressed under a tipless cantilever, and of a strongly adherent cell in front of it with a more diffuse contour. Scale bar: 25 µm. **B)** Exemplary force curve (orange dots) obtained on a weakly adherent Fb fitted to the Evans model (blue line). The purple dotted line separates the compression (i) and relaxation (ii) regimes of the force measurement. The inlet shows the geometry of the cell upon the compression between parallel plates; the complete time progression from an uncompressed to a fully compressed cell is indicated by the blue schematics. **C)** Geometries of a weakly adherent cell indented by a colloidal cantilever (left panel), and of a strongly adherent cell, with capped geometry, indented by a pyramidal tip. Indentation is in both cases of 15 % of the total cell radius.

they were consequently exposed for 10 s to oxygen plasma, and for 30 min at 77 °C to 3-(trimethoxysilyl) propyl methacrylate vapor (Sigma Aldrich), which contains trialkoxy groups that can hydrolyze in aqueous environments to form hydroxyl groups that condensate with those present on the activated glass surface. A 30 % polyethylene glycol diacrylate (PEG-DA) pre-polymer solution was then dispensed onto the center of the glass substrate and formed into a thin layer by squeezing it with an untreated cover glass. The pre-polymer solution contained an UV sensitive photo-initiator that crosslinked PEG-DA molecules via acrylate groups, converting the PEG-DA into a PEG gel via exposure to 2.19 J/cm^2 of 365 nm UV radiation for 60 s. Afterwards the top cover glass was removed, leaving a 4 µm thick layer of covalently bound PEG.

Weak cellular adhesion (iii) was achieved on bare glass substrates and via RGD inoculation (Sigma Aldrich; #A8052). In this case, upon cell addition, cells were allowed to settle for only 10 min, after which soluble RGD was added to a 1 mM concentration and left for the duration of the measurements.

Use of myosin II activity-modulating drugs and formin family inhibitor

Beyond cell adhesion, cell mechanics were also modulated via exposure to small molecules [143]. Actomyosin dynamics were modified through inoculation of **calyculin A**, a protein phosphatase inhibitor that promotes myosin II processivity (Sigma Aldrich; #C5552) [144], and **blebbistatin**, an ATPase that stalls the motor's activity (MilliporeSigma, Burlington, MA, US; #203389) [145] (Fig. 3.3). Both were applied immediately after cell addition, calyculin A at a concentration of 0.1 µM and blebbistatin at a concentration of 10 µM. After 30 min incubation, the media was refreshed and measurements started.

To better describe the functions of the formins mDia1 and mDia3, the small molecule inhibitor of formin FH2 domain (**SMIFH2**; MilliporeSigma; #344092) was employed to globally suppress the activity of formins in wild type Fbs [24]. Once cells had settled for 30 min upon their addition, SMIFH2 was inoculated at a 10 µM concentration. Measurements were started 5 min after inoculation. To prevent cortical contractility and re-organisation, cell fixation was performed by treating the samples with 0.5 % glutaraldehyde (**GDA**; Sigma Aldrich) in PBS for 10 min at room temperature. Samples were then rinsed with PBS and mounted to the AFM submerged in cell media for the acquisition of force curves.

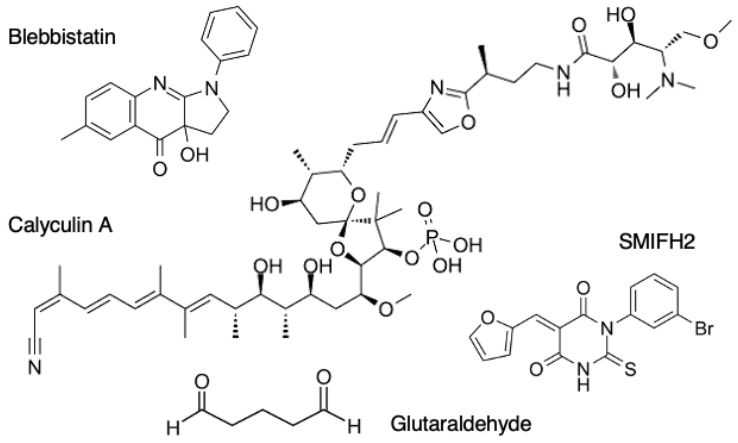

Figure 3.3: **Molecular structures of myosin II and formin activity-altering drugs.** Blebbistatin blocks myosin II heads by forming a complex with low actin affinity [144], whereas calyculin A prevents myosin-light-chain phosphatases from dephosphorylating myosin regulatory light chains, hence rendering myosin II motors hyperactive [66, 145]. SMIFH2 acts as a general formin inhibitor by targeting the highly conserved FH2 domain [24]. Glutaraldehyde presents carbonyl (–CHO) groups that allow amine condensation via Mannich reactions, rendering the drug an aggressive crosslinker. Produced in ChemSketch™.

3.2.1 Application of the Evans model

Force compression-relaxation curves were analysed following the viscoelastic Evans model, described in Chapter 2, using a routine implemented in MATLAB by Prof. Dr. Andreas Janshoff.

Two versions of this model exist; for simplicity, they will be referred to as the individual (IF) and serial fitting (SF) routines. Both required the introduction of the cell radius. To determine it, ImageJ (Rasband, W.S. - NIH, Bethesda, MD, USA) [146] was employed on the bright field micrographs obtained for each cell subjected to compression-relaxation measurements (Fig. 3.2): upon setting the scale based on the known width of the cantilever (100 µm), cell diameter was determined using the Straight tool. Furthermore, both versions required conversion of the MFP files into ASCII format, achieved using a custom Python script.

The **SF routine** included three sub-routines. The first one was applied individually to each measurement file to obtain the interval for fitting: first, the general baseline was removed; then, an initial fitting interval comprising baseline and the compression-relaxation region was selected, from which the hydrodynamic drift was corrected. The contact point was indicated manually or selected from an automatic calculation, which delimited the final fitting interval (Fig. 3.4). The second sub-routine calculated the geometry of the cell under compression to then be applied in series to a set of measurements, hence providing a fast determination of the parameters T_0, K_A and β, with the requirement that they were obtained under the same experimental conditions. Accordingly, information on the experiment type had to be provided regarding 1) dwell time after reaching the target force upon compression; 2) cellular geometry, based on weak (spherical) or strong (capped) adhesion force; and 3) type of indenter, differentiating between tipless (parallel plate), spherical and conical cantilever tips. Once the cell-cantilever contact geometry was resolved, the cell radius and the approaching-retracting cantilever velocity were introduced. Each individual file was then processed in series to calculate the parameters of interest based on the geometry of the indented cell. The last sub-routine collected and displayed all individual fits in a category (which allowed to detect and discard any misfits), and determined the mean and SD values for T_0, K_A and β, thereby creating the corresponding violin plots.

The **IF routine** combined only sub-routines 1 and 2. Accordingly, the contact geometry was calculated for each force measurement, hence slowing the process. In addition it could not automatically determine the contact point.

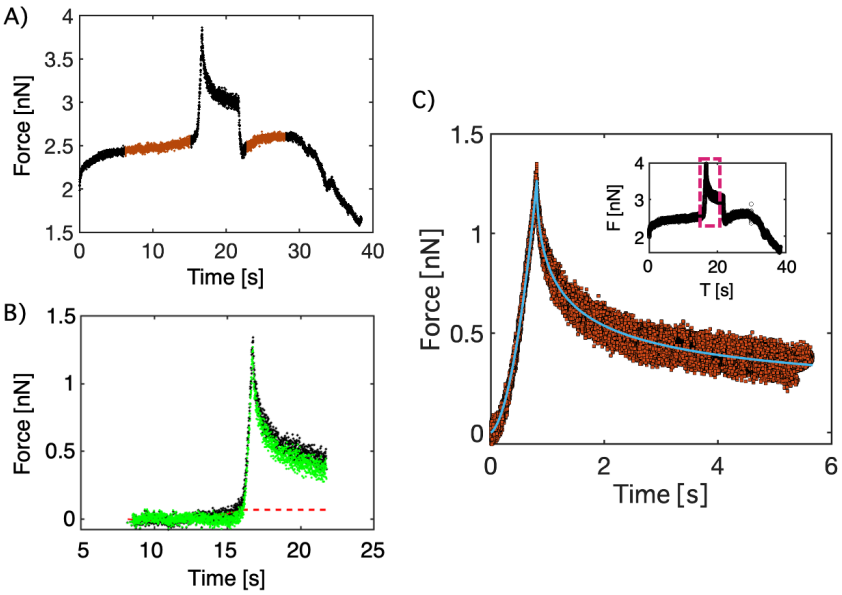

Figure 3.4: **Processing of AFM force measurements to obtain fitting intervals. A)** Integral force curve obtained during a compression-relaxation experiment. The baseline selection is highlighted in orange, incidentally encasing the interval in which contact between cell and cantilever is maintained. The region containing the compression-relaxation phase, together with a section of baseline, are selected leading to **B)**, where the hydrodynamic correction is shown in green. **C)** The selection of the contact point determines the final interval (orange dots) to be fitted to the Evans model (blue line). The inlet shows the corresponding region (pink frame) within the original, pre-processed force measurement.

3.3 ECIS-based acquisition of cellular impedance spectra

Time resolved cellular impedance spectra were acquired using the ECIS ZΘ setup (Applied BioPhysics Inc, Troy, NY, USA) and its associated software by Applied BioPhysics Inc. As shown in figure 3.5, the setup included a 16 Well Station -with capacity for 2 chips containing 8 culture wells each- that could be placed inside the incubator at 37°C and 5 % CO_2 throughout the duration of the experiment.

3.3.1 Pre-experimental considerations

To perform the ECIS experimental, the elements of the setup hereafter described were predefined in order to guarantee consistency and significance, including: cellular seeding

Figure 3.5: **ECIS setup.** The acquisition device includes a chip holder (pink box) with capacity to encase two chip arrays. The 8W1E chip (yellow box) presents 8 wells with a central working electrode (blue arrow), where the bright, central spot is the exposed surface (⌀ 250 µm), and a larger counter electrode (yellow arrow). The blue box schematic reflects the current flow during impedance monitoring, when it is confined under and between cells (red arrows), and during wounding, when larger currents are created (green arrows) that cause poration of the cell membranes, thus leading to cell death. Images courtesy of Applied BioPhysics.

density, substrate functionalisation for an optimal interaction with cells, and determination of an optimal frequency of acquisition.

Cellular seeding density

For ECIS experiments, cells were kept in DMEM complemented with 10% FBS and 1% L-Glutamine in HEPES buffer. Samples were prepared at a concentration of $2{\cdot}10^5$ cells per well which, with an electrode area of 0.042 mm^2 but a total substrate area of 0.8 cm^2, corresponded to a cell density of $2.5{\cdot}10^5$ cells/cm^2. This concentration was adjusted for an optimal growth based on the results of J. Rother *et al.*, who analysed the impedance time courses of primary rat cardiomyocyte and fibroblast co-cultures with different cell concentrations and percentages. As shown in figure 3.6, they observed that maximum Z_{real} values in a Plateau phase correlated to cells reaching confluence. While exceedingly low seeding densities presented low maximum impedance values that linearly increased with time, exceedingly high concentrations showed a Plateau phase that, at very high cell numbers, was followed by a drop in impedance as a consequence of accelerated medium consumption and contact inhibition, which prevents cell growth and causes delayed expression of quickly degraded cell-cell contacts [147].

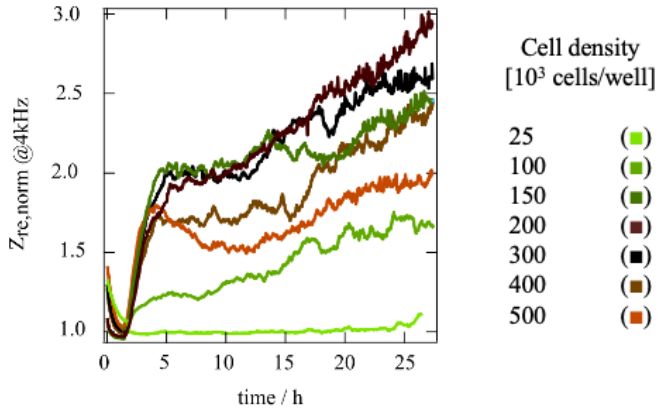

Figure 3.6: **Optimisation of cell seeding density for ECIS experiments.** Normalised Z_{real} time courses obtained at a frequency of 4 KHz for CM primary monocultures prepared with different seeding densities. Optimal seeding density for maximal Z_{real} values was found at 200 000 cells per well. Adapted with permission from [147].

Substrate functionalisation

Generally, experiments were performed using 8W1E chips (ECIS Cul-tureware^{TM}, ibidi®, Fitchburg, WI, USA) presenting, in each of the 8 wells, an active electrode of 250 µm in diameter (0.049 mm^2) and a significantly larger counter electrode. In order to test the influence of wound area in cellular recovery dynamics, custom chips were employed. These differed by presenting pairs of wells, each with active electrodes of 31, 63, 127 or 255 µm in diameter. Both chip types were based on a polyethylene terephthalate (PET) substrate of 0.25 mm in thickness, and an insulating layer of 500 nm.

On the measurement starting day, the wells of 2 chips were functionalised with a combination of gelatin (0,002%) and fibronectin (0,5%) for 1h at 37°C. This combination, which provides a compromise between substrate elasticity and binding site density, was based on previous work (Fig. 3.7) [26, 147]. After washing off the excess coating with PBS, the wells were filled with 500 µL of culture medium and placed in the incubator for acclimatisation and stable baseline acquisition until the experiment could start.

Frequencies for optimal SNR acquisition and wounding

For the measurement of frequency-dependent impedance spectra over time, the ECIS counts with a series of 11 discrete acquisition frequencies spanning from 62.5 Hz to 64 KHz (62.5, 125, 250, 500, 1000, 2000, 4000, 8000, 16000, 32000, 64000 Hz). Within this range, an optimal frequency can yield a maximal sample-to-noise ratio (SNR). This

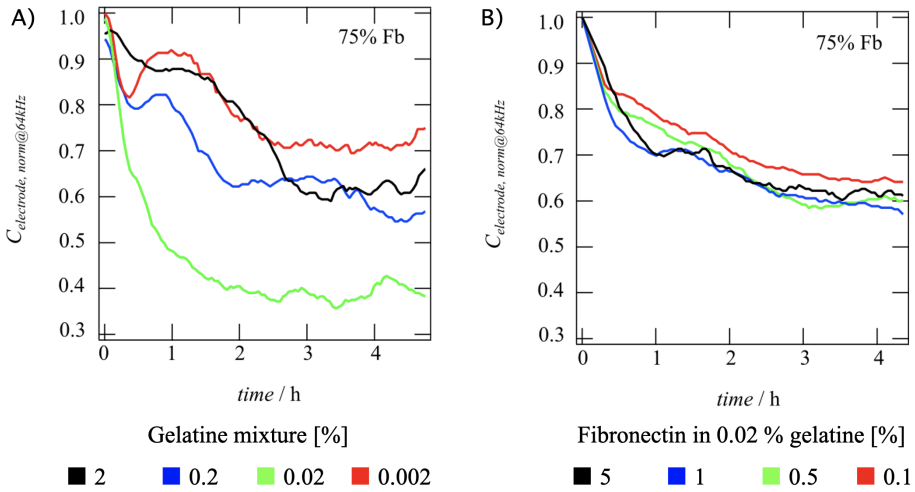

Figure 3.7: **Optimisation of substrate functionalisation for ECIS experiments.** Normalised capacitance (Z_{im}) obtained at a frequency of 64 KHz for co-cultures of primary CMs and Fbs at a ratio of 25 %/ 75 %, respectively. **A)** Functionalisation with various gelatin mixtures. **B)** Functionalisation with 0.02 % gelatin and various fibronectin concentrations. Adapted with permission from [147].

f_{SNR} is relevant for the analysis of amplitude sensitive measurement types such as the recording of micromotions, in which the high acquisition rate requires the selection of a specific acquisition frequency, and thus relies on a well selected impedance amplitude regime.

To determine f_{SNR}, the impedance of the cell-covered electrode was normalised with respect to the impedance of the free (thus electrolyte-covered) electrode. By plotting Z_{real} against the frequency of acquisition, a Gaussian-shaped peak centered on the frequency with the best signal to noise ratio was revealed (Fig. 3.8).

For NIH 3T3 monolayers on electrodes of 250 µm in diameter, an optimal frequency of 8 KHz was found. The optimal frequency is dependent on the cell density and on the functionalisation of the electrode, but also on the size of the electrode, the cell type and the media composition. Accordingly, it is specific to the experiment and any changes in the setup will cause shifts in the amplitude and frequency of the peak. For the f_{SNR} characteristic of other combinations of cell type and electrode diameter, refer to Table 3.1, provided by L. Mamoyan [148].

In the standard monitoring mode, the electric field employed presented an amplitude in the order of microamperes and resulted non-invasive to cells. However, the ECIS allows to modulate the strength of the electric field to milliampere amplitudes in order to cause wounds via permanent cell membrane permeabilisation. In this work, a 2 min pulse of

high frequency (10 KHz) and amplitude (1.8 mA) was applied for this purpose. These parameters were based on previously reported optimisation work in which different pulse intervals and AC amplitudes and frequencies were tested [26], and that was reproduced and confirmed for the cell type and conditions of this work [149].

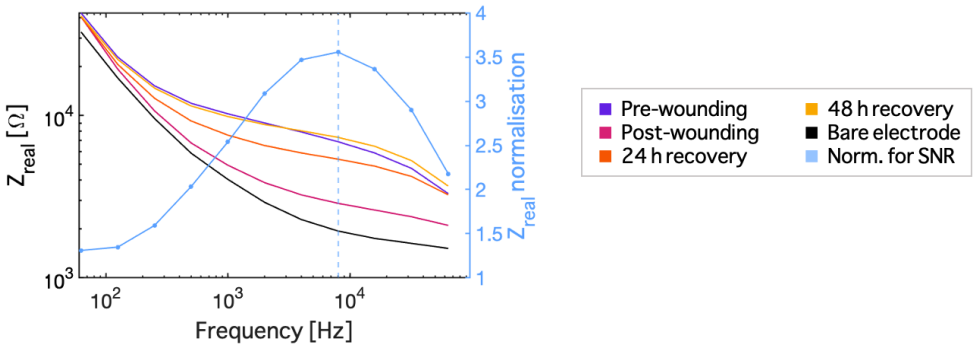

Figure 3.8: **Determination of f_{SNR} for the ECIS-based acquisition and analysis of impedance spectra.** Left axis: Z_{real} of NIH 3T3 WT fibroblasts obtained at the discrete frequencies composing the acquisition spectra. Impedance measurements were performed upon monolayer formation (pre-wounding) and during recovery after wound formation (see colored legend). Post-wounding impedance levels approach that of a bare electrode; after 48 h of recovery, impedance approximates that of the pre-wounding stage. Right axis: Z_{real} pre-wounding values normalised with respect to those of the bare electrode. As indicated by the dotted line, the 8 kHz frequency showcases the biggest change in impedance, thus yielding the best SNR for the specific experimental conditions.

Table 3.1: **Optimal ECIS frequencies of acquisition**. Optimal frequencies (KHz) are specific to the setup and accordingly vary, amongst others, with cell type and electrode size. With decreasing diameter, the optimal frequency increases due to the constriction resistance. Data courtesy of L. Mamoyan [148].

Electrode size [µm]	Frequency [kHz] corresponding to: WT	mDia1	mDia3	dKo
250	8	4	2	8
127	8	8	16	8
63	16	8	8	8
31	16	16	2	16

3.3.2 Impedance-based wound healing assays

The wounding and recovery of various samples was monitored based on the recording of their characteristic impedance over time. To this purpose, the ECIS was employed using

the multiple frequency over time (MFT) mode, in which 11 discrete frequencies ranging from 62.5 Hz to 64 KHz (62.5, 125, 250, 500, 1000, 2000, 4000, 8000,16000, 32000, 64000 Hz) were applied in sequential order. The resulting spectra -obtained sequentially through the experimental wells- presented a sampling rate of 2.6 min^{-1}.

Prior to starting an experiment, the materials -including pre-functionalised ECIS chips, cells and media- were placed in the incubator to allow adjustment to 37°C. Once equilibrated, the chips were placed in their holder and the ECIS measurement was started with the acquisition of a cell-free impedance baseline, for at least 30 min, in order to provide reference for the bare electrode. Subsequently, typical experiments continued over the course of 4 to 5 days following the steps here described and denoted as 1 through 5 in the exemplary figure 3.9: **Cell seeding (1)** was performed immediately after stable baseline acquisition with the inoculation of 100 µL of cell suspension at 10^6 cells/mL per well. To work always with a constant volume of 500 µL per well, the same volume was removed right before the inoculation took place. After 24 h, impedance presented a Plateau that indicated a contact inhibited **quasi-stationary state of cell growth (2)**. At this point, **wounding (3)** was initiated by the application of a 1800 µA current at 100 kHz for 120 - 240 s through the working electrodes. Dead cells and debris were then removed by thoroughly washing the wells twice with 500 µL of medium before adding 500 µL of fresh solution. This step required special attention in order to prevent the damage of the insulating layer of the ECIS chip as well as of the leftover living cell layer, and yet achieve a successful clearance of the electrode's surface. Finally, the **recovery progress (4)** was monitored over the following 2-3 days until the impedance values showed **recovery (5)** by reaching or exceeding the pre-wounding level. Until terminating the experiment, cells were fed every 24 h with fresh culture medium.

Impedance recording under the influence of the formin inhibitor SMIFH2

Taking the process described above as the basic protocol, ECIS-based impedance measurements were also combined with the use of the small molecule inhibitor of the FH2 formin domain SMIFH2 (Sigma-Aldrich, St. Louis, MO, USA; 344092). The versatility of the ECIS allows the continuous or pulsed application of a drug at any time point to assess its influence on cellular micromotions, cell-cell connectivity or electrode coverage dynamics. However, only two approaches were relevant to this work. The first one consisted on the application of the drug right after wounding: after washing off cellular debris, 500 µL of the solution containing SMIFH2 at the desired concentration were added. After 30 min of incubation, the samples were washed twice with fresh media, and left in 500 µL of fresh media to proceed with the measurement. The other

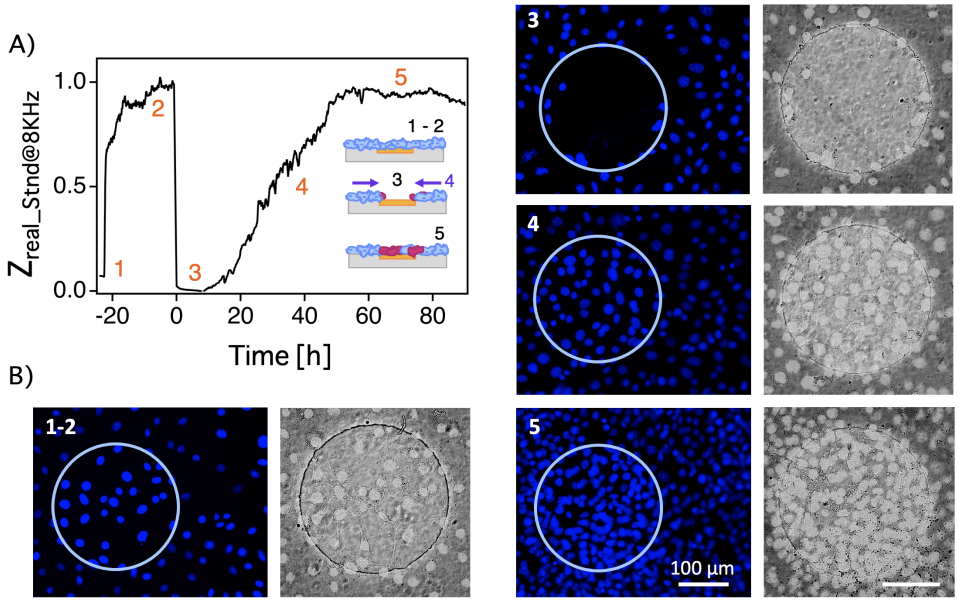

Figure 3.9: **ECIS-based wound healing assay. A)** Typical time course evolution of the Z_{real} of NIH 3T3 WT fibroblasts, standardised and obtained at a frequency of 8 KHz. Numbers (in orange) correspond to the inlet schematics reflecting the experimental steps: fibroblasts (blue cells) are seeded (1) and allowed to form a monolayer (2), point at which they are wounded (3) and allowed to recover (4), through FMT progression (pink cells), until pre-wounding values are observed (5). **B)** Fluorescence (left) and bright field (right) micrographs of WT fibroblasts (nuclei in blue) cultured on ⌀ 250 µm electrodes. Numbers (top left corner) correspond to the schematics in panel A.

approach consisted on exposure of healthy monolayers to SMIFH2: 24 h after initiating the experiment, wounding was not performed. Instead, the media was substituted with the solution containing SMIFH2 at the desired concentration. After 30 min incubation, the media was refreshed and the experiment continued. SMIFH2 dilutions in culture media were always prepared fresh on the day of addition. Upon purchase, stock solution was solved in dimethyl sulfoxide (DMSO) at a concentration of 50 mg/ml (133 mM), and stored at -20 °C for up to 3 months as recommended by the manufacturer. Once thawed, consecutive dilutions to achieve the concentrations of interest -detailed in Chapter 6- were prepared in sterilised PBS in at least two steps.

3.3.3 Analysis of impedance spectra

Standardisation of impedance time courses

Standardising the ECIS data prior to its analysis atoned for the inherent variability in the electrical properties of the electrodes within a chip, and in the impedance spectra

resulting from the passive electrical properties of cells. Accordingly, it was specially relevant for the comparison of recovery time courses obtained on different samples. Following the expression in eq. 3.1, where $\langle M \rangle$ and $\langle N \rangle$ are the cell-covered and cell-free impedance levels measured at the optimal frequency, respectively, the impedance time course ($z(t)$) was standardised ($S(t)$) between 0, reflecting the minimum impedance after wounding -thus corresponding to the initial electrode impedance before cell inoculum- and 1, the maximum impedance of the pre-wounded, healthy cellular monolayer.

$$S(t) = \frac{z(t) - \langle N \rangle}{\langle M \rangle - \langle N \rangle} \tag{3.1}$$

Sigmoidal evolution in recovery curves

In order to compare the recovery rates between samples, a sigmoidal fit was applied to the previously standardised impedance time courses. As shown in figure 3.10, the fit described by equation 3.2 was applied in the time interval defined between the wounding and recovery stages, i.e. taking A_{max} and A_0 as the pre-wounding and post-wounding impedance values, respectively. By applying the sigmoidal fit, the recovery half time ($t_{1/2}$) and the impedance rise rate (R), also referred to as the recovery rate, were retrieved.

$$y(t) = \frac{A_{max}}{1 + \exp\left(-\frac{t - t_{1/2}}{R}\right)} - A_0 \tag{3.2}$$

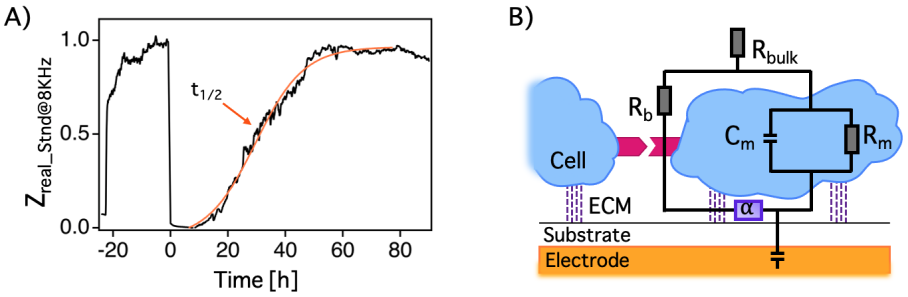

Figure 3.10: **Analysis of ECIS-based wound recovery measurements. A)** Standardised impedance time course subjected to a sigmodal fit; $t_{1/2}$ is indicated. **B)** Schematic electric circuit based on the Lo-Ferrier model for a cell layer cultured on a gold electrode. The passive electrical properties junctional resistance (R_b), the cell-substrate distance sensitive parameter α, and membrane capacitance (C_m) are highlighted. R_m refers to the cellular membrane resistance and R_{bulk} to that of the media. Based on [25, 150].

Lo-Ferrier equivalent electric circuit

The passive electrical properties of the cell layer such as R_b, C_m and α -which describe the cell-cell connectivity, membrane capacitance, and cell-substrate distance, respectively-, can be determined upon fitting impedance spectra to an equivalent electric circuit model reflecting the cell-electrode system as a monolayer of particles of defined geometry (Fig. 3.10), as defined by Lo and Ferrier [25].

To apply the fit, segments of 2-3 h at relevant experimental time points were selected from the impedance spectra, which spanned over the duration of 4 to 5 days, using a Python-based routine. These were at 21, 45 and 69 h upon starting the experiment, thus reflecting pre-wounding, 24 and 48 h of recovery. Each of the split files was then independently fitted to an iterative custom written MATLAB (MathWorks, MA, USA) algorithm based on least square analysis of the Lo-Ferrier's model. The routine required the introduction of initial guess values for R_b, C_m and α, and the introduction of pre-defined values for the series of parameters described in table 3.2.

Table 3.2: **Parameters required for the ECIS Lo & Ferrier model**. Parameters for the fitting routine based on the Lo-Ferrier model implemented in MATLAB; the values specified are characteristic of the system, thus employed during data analysis and kept constant. R_b, C_m and α, marked with *, are guess values that have to be adjusted specifically for each experimental curve until a proper fit is achieved.

Parameter	Description	Typical magnitude
R_b (*)	Cell-cell barrier resistance	1 – 15 [Ω cm^2]
C_m (*)	Cell membrane capacitance	10^{-7} - 10^{-6} [F cm^{-2}]
α (*)	Parameter reflecting cell-substrate height	0.1 – 0.9 [$\Omega^{1/2}$ cm]
r	Electrode radius	$125 \cdot 10^{-4}$ [cm]
W	Width of the cells	$22 \cdot 10^{-4}$ [cm]
L	Length of the cells	$46 \cdot 10^{-4}$ [cm]
ρ	Electrolyte resistivity	54 [Ωcm]
R_{cons}	Constriction resistance	$\rho \cdot 0.25A/r$ [Ω cm^2]
A	Electrode area	πr^2
C_n	Bare electrode capacitance	$9.4 \cdot 10^{-5}$ [F cm^{-2}]
n	Exponent for the calculation of capacitive contribution	0.75
ω	Angular frequency	$2\pi f$

3.4 Acquisition of cellular micromotions

Recording of cellular micromotions was performed using the Rapid Time Collection (RTC) mode of the ECIS ZΘ device. In this setup, impedance was recorded for a minimum of 2 min per sample at 8 KHz -the optimal frequency- and 28 pps, the maximal resolution given by the technical capabilities of the device. To avoid thermal drifts and to minimize registration of non-stationary cellular activity, the measurements were performed right before wounding and, during recovery, at intervals of 24 h always before refreshing cell media.

3.4.1 Analysis of cellular fluctuations via PSD, variance and DFA

Fluctuations derived of the biological and metabolic activity were studied using a custom MATLAB routine that allowed its analysis based on power spectral density in parallel to detrended fluctuation and variance analysis, as shown in figure 3.11.

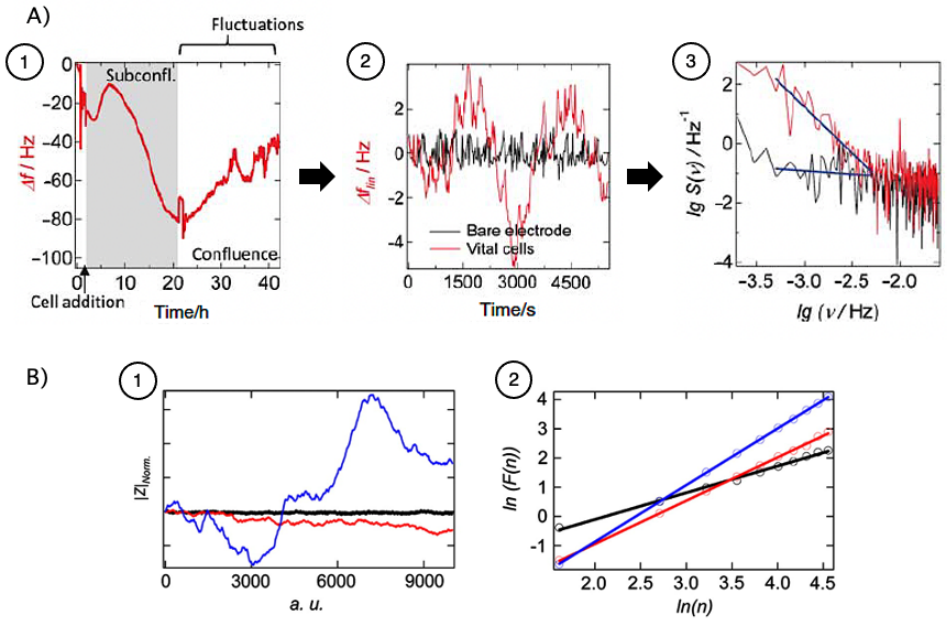

Figure 3.11: **Micromotion analysis. A)** Time-resolved frequency courses (1) are normalised with respect to their linear trend and subjected to FFT (2). The slopes of the resulting PSD spectra (3) are a measure of cell vitality. Adapted from [151] with permission of Informa UK Limited, trading as Taylor & Francis Group; © 2010. **B)** Time series of white noise (black), Brownian (red) and biological (blue) fluctuations (1) are normalised with respect to their linear trend. Once detrended, variance is calculated and represented in a ln-ln plot against the length of boxes n (2). The slopes of the linear fits (α_{DFA}) are indicative of long-term memory: $\alpha_{DFA} > 0.5$ and > 1 for correlation and high correlation, respectively. Adapted from [29] with permission from Elsevier B.V; © 2011.

Power spectral density-based analysis was initiated with the normalisation of the measurement against the linear or polynomial fit that better reflected its general temporal evolution. Once the general drift or offset was removed, an FFT was applied to the time-resolved data using a sliding box of 2K points and an overlap of half a window. By plotting the resulting spectra against the frequency in a log-log graph, the power law behaviour, reflected as the PSD slope, was determined in the linear frequency regime between 2 and 3.5 Hz, known to reflect the regime expected for (net vertical) collective cellular migration [29].

Detrended fluctuation analysis and calculation of the variance in the noise of the impedance signal started as well with the subtraction of the general trend. Next, the data was subdivided in non-overlapping boxes of length n. The local trend within the box was calculated using a linear least-squares fit, and variance was determined as the root-mean-square deviation between the original data and the linear fit. For DFA, the process was repeated with boxes of different n size. The corresponding variances were represented against n in a log-log plot, which resulted in a linear trend indicating statistical self-affinity according to $var(n) \propto \Pi^{\alpha}$, where α (α_{DFA}) was the slope of the plot calculated upon least-squares fitting.

3.5 Immunofluorescence

Immunostained micrographs are highly relevant to this work in order to complement the information obtained from the ECIS-derived impedance measurements regarding cell migration and phenotypic adaptations through the FMT. To characterise the former, samples were fixated right before and after wounding, and at 3, 6, 10 and 17 h of recovery. To detect migratory patterns, F-actin and myosin were respectively stained via phalloidin- and antibody-based fluorescent labeling (Fig. 3.12). To identify the stages of FMT progression, samples were fixated at the pre-wounding stage, and then at 24 and 48 h of recovery. In this case, the staining targeted α-SMA and connexin-43, as they are expressed by the myofibroblast phenotype (Fig. 3.13). In both cases, nuclear staining with DAPI was performed as a control and to identify individual cells. The details on the labels used for staining are detailed in table 3.3 (page 70).

Sample preparation started by washing the cells twice with PBS, followed by a 10 min incubation at room temperature with paraformaldehyde (PFA) 4%. Samples were then washed thrice with PBS and stored at 4°C until immunostaining could be performed. In some cases, ECIS chips were fixated only partially while the experimental was allowed

to proceeded in neighbouring sample wells. In this case, the PFA 4% incubation was done at 37°C and fixated wells were filled with PBS until the experiment ended and the process could continue at whole chip level.

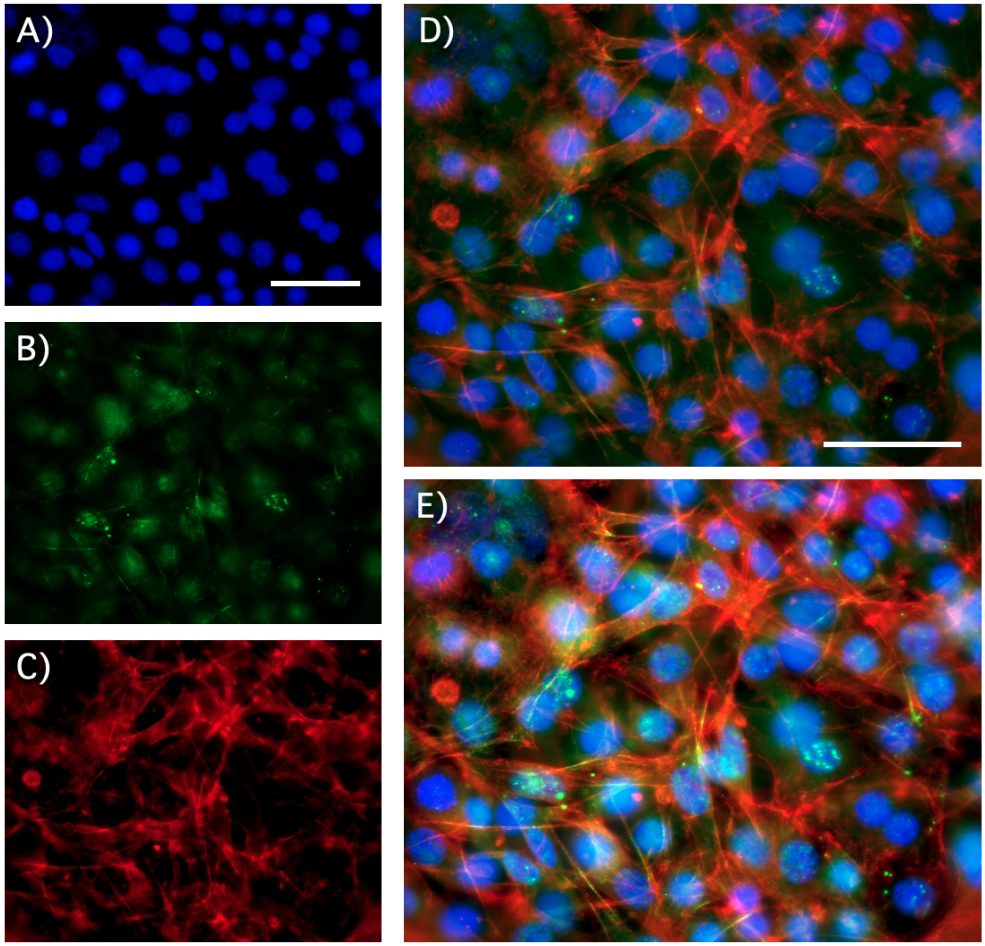

Figure 3.12: **Fluorescence staining of the actomyosin distribution in fibroblasts.** Fluorescent labels show **A)** cellular nuclei, **B)** myosin II and **C)** actin, highly involved in cell migration (see Table 3.3 for details on the fluorescent labels). Individual micrographs are obtained for each fluorochrome-labeled cellular component of interest. **D)** Upon overlaying the micrographs, the composite image has to be optimised to properly highlight the relevant features (**E**). Scale bars: 50 µm.

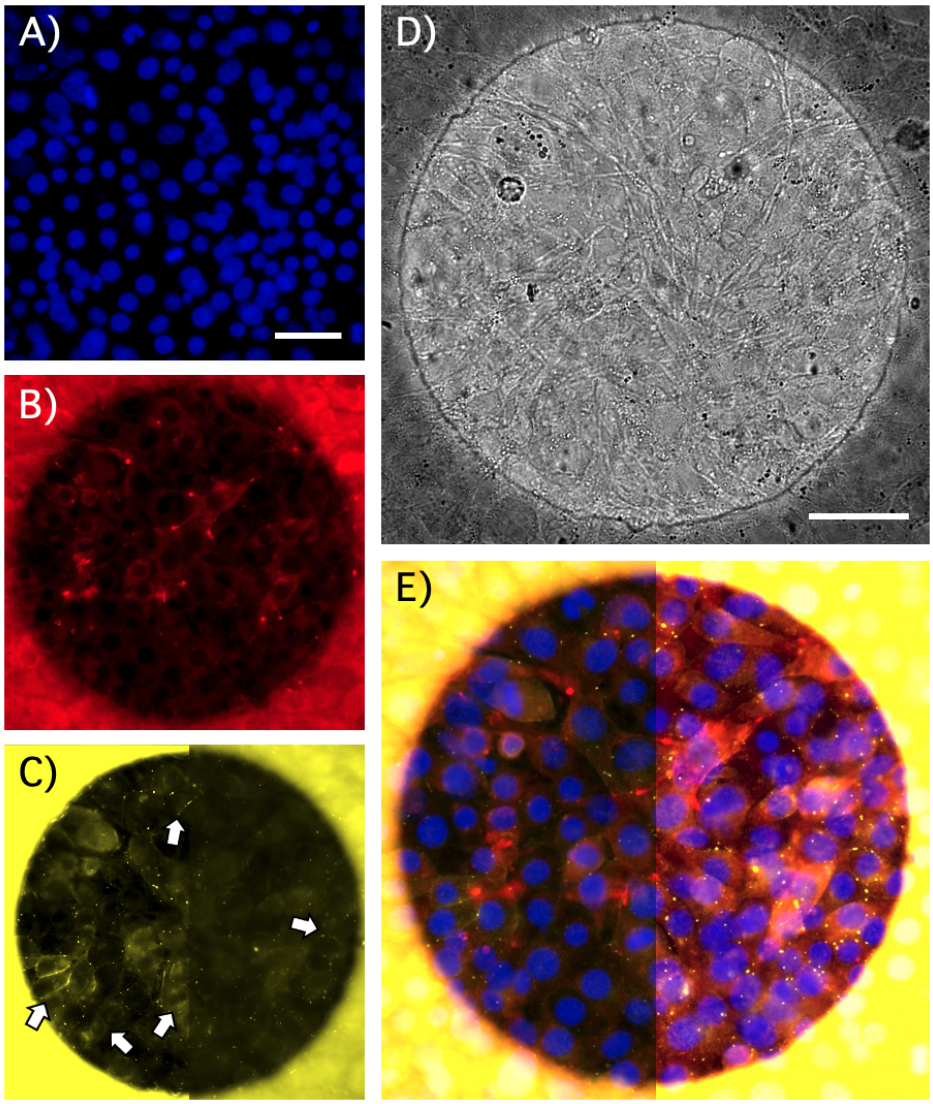

Figure 3.13: **Fluorescence staining of FMT progression markers.** Exemplary micrographs of WT NIH 3T3 fibroblasts for the identification of FMT progression 24 h after wounding. Fluorescent labels show **A)** cellular nuclei, **B)** ∝–SMA and **C)** connexin-43 (see Table 3.3 for details on the fluorescent labels). The photoresist layer covering the substrate of the ECIS culture chips presents auto-fluorescence, specially when exposed to excitation wavelengths in the range of 540-570 nm [152]. To allow the proper identification of the cellular features labelled with fluorochromes excited within this range, as it is the case of Cx43, saturation of the photoresist region may result necessary: cell-cell contacts, indicated by the intercellular expression of Cx43 (arrows in panel C), are easily detected upon saturation (left side) of the photoresist background, unlike in the non-saturated (right side) micrographs. **D)** Bright field micrograph of a 250 µm wide electrode. **E)** Micrograph of the same region obtained upon merging the three fluorescently labelled channels shown from A to C. The left side of the micrograph is optimized through the adjustment of contrast and brightness while preventing saturation; the right side shows optimization upon incurring saturation of the photoresist region. Scale bars: 50 µm.

Immunostaining proceeded with a 10 min incubation at 37°C with permeabilization solution (0.1% Triton-X 100 in PBS), followed by a 30 min incubation in blocking solution (5% FCS in 0.02% Tween-20 in PBS) in order to saturate nonspecific binding sites. Samples were washed 2-3 times with PBS after each step, and afterwards stained by sequentially exposing the cells to the primary and secondary antibodies of interest for 60 min each, with three intermediate washing steps of 5 min with PBS. The details of the solutions -all of them prepared in 1% BSA in PBS- and antibody combinations can be found in table 3.3 (page 70). Note that the staining of F-actin was not based on the use of antibodies but on the use of phalloidin, which inserts itself between actin monomers in a filament, thus locking them together. Accordingly, it could be applied in combination with the secondary anti-myosin antibody. For the staining of the cellular nuclei, cells were incubated with DAPI (4,6 diamidino-2-phenyindole) for only 1 min. In order to prevent photobleaching of the fluorochromes, sample manipulation was continued in the dark from the moment the first secondary antibody was used. After staining the samples, they were stored in PBS at 4°C.

Imaging was achieved using Olympus equipment: a custom BX53M microscope with extended z-range in combination with a U-CMAD3 camera, and the associated software cellSens. The wells within ECIS chips enclose a large culture area compared to the exposed surface of the electrodes. To locate them, small magnification objectives -all from Olympus- were used to locate them in the sample by exploiting the auto-fluorescence of the photoresist layer, specifically: water-immersion 10x (UMPLFLN10XW; numerical aperture (NA) = 0.3) and 20x (UMPLF-LN20XW, NA = 0.5). Once the exposed areas of the electrodes were located, larger magnification objectives were employed for image acquisition: 20x, 40x (LUMPLFLN40XW, NA = 0.8) and 60x (LUMPLF-LN60XW, NA = 1.0). Such setup required the removal of the plastic well delimiters of the ECIS chips (0.5 cm high) in order to get within the range of focus.

ImageJ was adopted during image processing: first, the different channels were merged and consequently, color balance, brightness and contrast were adjusted to better showcase the features of the images. As shown in figure 3.14, brightness is a measure of the global intensity of the micrograph; contrast indicates the range of brightness, from lightest to darkest.

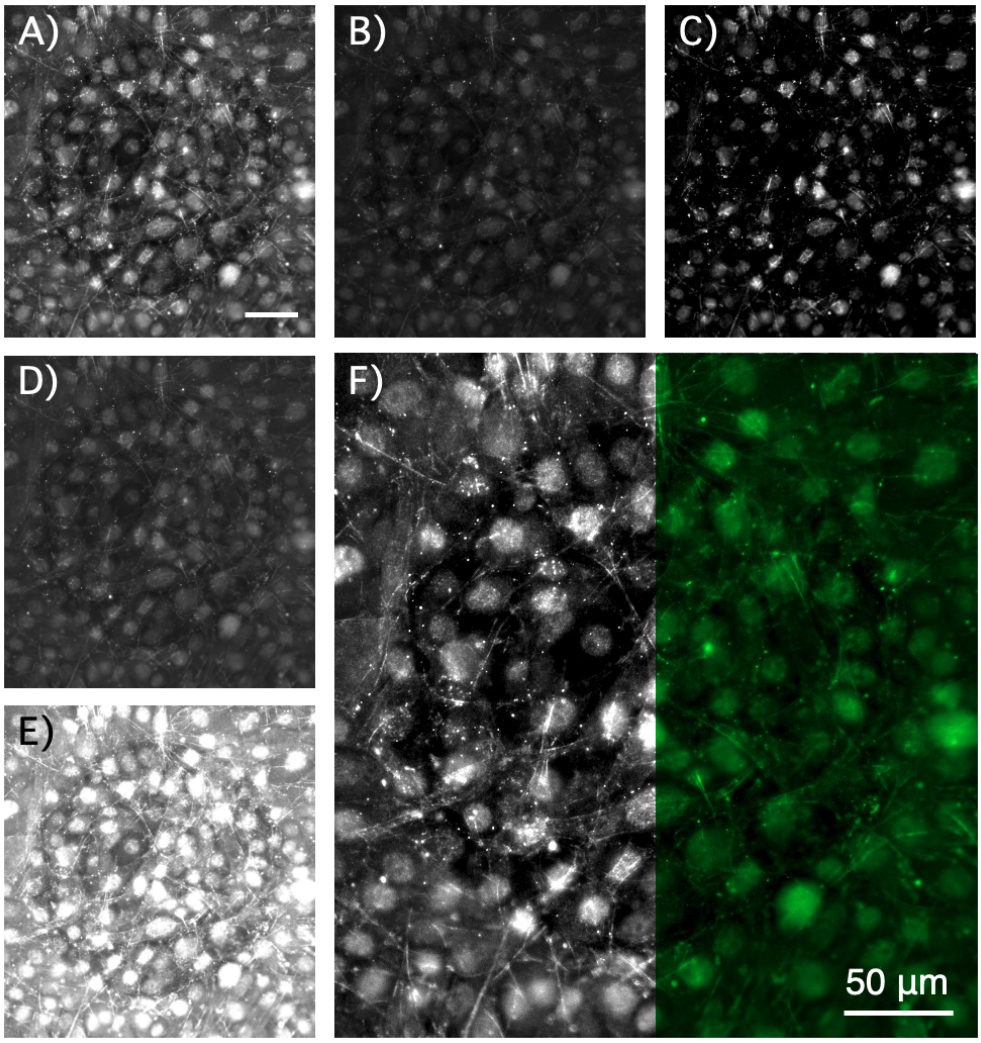

Figure 3.14: **Acquisition of a compression-relaxation force curve. A)** Micrograph of a WT NIH 3T3 fibroblast monolayer with immunolabeled myosin expression as obtained with the BX53M Olympus microscope upon adjusting the exposure time and intensity of the light source through the associated cellSens software. **B-C)** Effect of lowering (B) and increasing (C) image contrast using the ImageJ software. **D-E)** Effect of lowering (D) and increasing (E) image brightness using the imageJ software. **F)** Micrograph presented in A) after optimising image contrast and brightness in order to highlight the myosin distribution within the cell monolayer. The left half of the micrograph is presented in grey-scale; the right half is artificially tinted to allow the simultaneous presentation of multiple biological immuno-labelled components in a single micrograph. Scale bars: 50 µm.

Table 3.3: **Immunostaining materials**. Specification of the solutions and antibodies used, classified according to the cellular component they targeted. The concentrations yielding an optimal staining are listed.

Target		Solution	Concentration
Cell migration	Myosin	**1° Ab**: Phospho-myosin light chain 2, from Cell signaling Technology (Danvers, Ma, USA) (antibody #3674S)	1:130
		2° Ab: Goat anti-rabbit IgG Alexa Fluor 488, from Thermo Fisher Scientific (Waltham, MA, USA) (A-11008)	4 µg/mL
	F-actin	Phalloidin-iFluor 555, from Abcam (Cambridge, UK) (ab176756)	1:780
FMT progression	α-SMA	**1° Ab:** Monoclonal anti-actin α-smooth muscle, from Sigma-Aldrich (St. Louis, MO, USA) (A2547)	1:400
		2° Ab: Atto 633, from Sigma-Aldrich (78102)	1:240
	C-43	**1° Ab:** Anti-connexin 43, from Abcam (ab219493)	1:100
		2° Ab: Alexa Fluor 555, from Abcam (ab150130)	1:300
	Vimentin	**1° Ab:** Recombinant anti-vimentin cytoskeleton marker, from Abcam (ab92547)	1:200
		2° Ab: Alexa Fluor 488, from Thermo Fisher Scientific (A-11008)	1:240
Nuclei		DAPI, from Sigma-Aldrich (D9542)	1 µg/mL

3.6 Statistical analysis

Statistical significance of the differences between experimental data groups was assessed using the two-sample test routine of IgorPro (Wavemetrics, Portland, OR, USA), mostly based on the Wilcoxon rank-sum test or the T-test. The routine started with the introduction of the p-value (0.05, 0.01 or 0.001) of interest. Next, a series of tests were used to determine whether the inputs were normally distributed random samples. First, the Runs Test was applied individually to each sample in order to determine if they were randomly distributed, thus revealing any variables with data patterns. This was complemented with the Kolmogorow-Smirnow (KS) and the Jarque–Bera (JB) tests. The former determined whether it was probable that the two sets of data were drawn from the same probability distribution. The latter tested if the data sets had the skewness (symmetry) and kurtosis (heaviness of the distribution tails) of a normal distribution. If the conclusion of these tests was that the inputs were normally distributed random samples, the routine continued by determining if their variances were equivalent. If they were equal, the T-test was applied; if not, or if the previous hypothesis that the inputs were normally distributed random samples was rejected, the routine ended with the Wilcoxon rank-sum test instead.

To illustrate the statistical differences within the results of this thesis, [*] refers to a p-value of the applied test of $p < 0.05$, [**] to $p < 0.01$, and [***] to < 0.001. To illustrate the size of the samples, n refers to the number of AFM force-curves or to the number of ECIS impedance time courses within a category, m to the number of experimental days, and c to the number of cells tested in AFM experiments.

Graphics and figures are based on a color palette adapted for colorblindness [153].

Part II

Experimental Research

Chapter 4

Rheological characterization of the actomyosin cortex

As previously described, the cortex is formed by a mesh of compliant but contractile actin fibers that result in a composite shell. The contraction of the mesh, regulated by motor proteins, provides resistance against deformation and thus, a measurable prestress. At the same time, the power law coefficient β defines the degree of fluidity and energy dissipation in a deformation process. Accordingly, in order to closely characterise the rheological properties of the actomyosin cortex, a viscoelastic model is necessary that correlates the fluidity observed in deformation-relaxation experiments and the cellular prestress. In this chapter, such model -the Evans model [9], which describes the cell as a liquid droplet and thus as a viscous fluid with a constant cortical tension following the so-called liquid-drop model [154, 155, 156]- is applied in order to characterise the rheological properties of weakly adherent fibroblasts, and to asses how these are influenced by the activity of cortex-regulating motor proteins. In doing so, experimental limitations of the model are also determined.

Part of the results herein presented are published in *Physical Review Letters* under the title: Prestress and Area Compressibility of Actin Cortices Determine the Viscoelastic Response of Living Cells [9].

4.1 Results

4.1.1 Applying the Evans model

Initial experiments to validate the Evans model were performed on weakly adherent WT fibroblasts. Accordingly, cells were cultured on glass and PEGylated substrates,

and tested under standard conditions: set-point force of 1 nN and probing velocity of 1 μm/s. In order to validate the Evans model, two processing routines were applied. To assess whether the semi-automated version allowed the proper determination of the rheological parameters of interest, the same set of force curves was analysed using both the individual (IF) and serial (SF) fitting routines.

This is reflected in figure 4.1. When comparing T_0, K_A and β for cells on the same substrate, no significant difference was found as a result of applying either of the two protocols. However, β values presented a slight, non-significant deviation: the mean and median of the distribution obtained from cells on glass were marginally higher when determined by the SF. Despite both substrates leading to weak cellular adhesion -strongly reduced in the case of PEGylated surfaces, and only mildly reduced on glass-, rheological parameters significantly differed, with fibroblasts showing increased prestress and fluidity on the former. K_A values showed an increased variability compared to T_0 and β, but with no discernible substrate or routine-dependent trend. It is noteworthy that the pool of force curves obtained on PEGylated substrates that was analysed with the IF was smaller because the experimental category was expanded only after performing the evaluation.

The individual fitting routine applied, simultaneously, both the Evans and Hertz models. As exemplary shown in figure 4.2, the Evans model was able to describe the force curve more accurately. This was specially noticeable at the onset of both compression and relaxation, where the force curve was respectively under- and over-represented by the Hertz model. As indicated in the same figure, such deviation resulted in distinct β values based on the model applied: on the same force curve, the Evans model showed increased fluidity with respect to the Hertz model.

Hereafter, the serial fitting routine of the Evans model was employed in the AFM measurements presented unless otherwise specified.

4.1.2 Experimental and analytical parameters influencing the Evans model

In the validation process of the Evans model, several experimental parameters were tested in order to determine their influence on the measured rheological values. These included the approach velocity of the cantilever (constant throughout the individual measurements), the set-point compression force, and the geometry of the cantilever's tip. However, other parameters that became relevant during the analytical application of the Evans model, such as the indentation percentage, the radius of the cell, or the

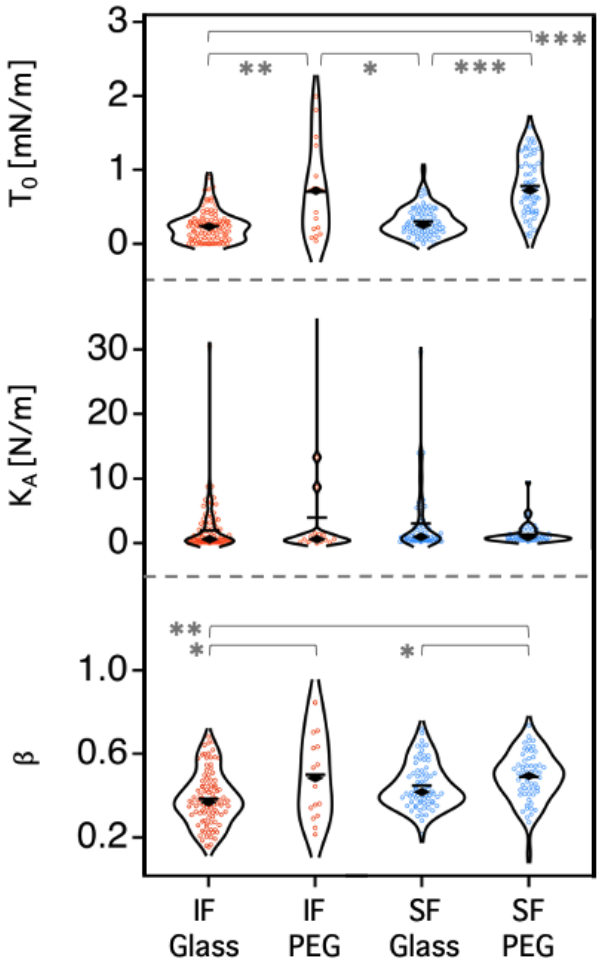

Figure 4.1: **Comparison of the rheological parameters obtained upon applying the Evans model through the individual and serial fitting routines.** T_0, K_A and β values are obtained from WT cells cultured on either glass or PEGylated substrates (1 µm/s and 1 nN) following the individual (■; $c_{glass} = 21$, $n = 99$; $c_{PEG} = 7$, $n = 17$) and serial (■; $c_{glass} = 17$, $n = 74$; $c_{PEG} = 24$, $n = 60$) fitting routines. Within the same substrate type, no significant difference is found as a result of applying the different processing protocols; cells on glass, thus with higher adhesion strength, present a lower prestress and fluidity than cells on PEG, as captured by both fitting implementations ([*] for $\alpha < 0.05$, [**] for $\alpha < 0.01$, and [***] for $\alpha < 0.001$; mean and median are respectively indicated with - and ⬥).

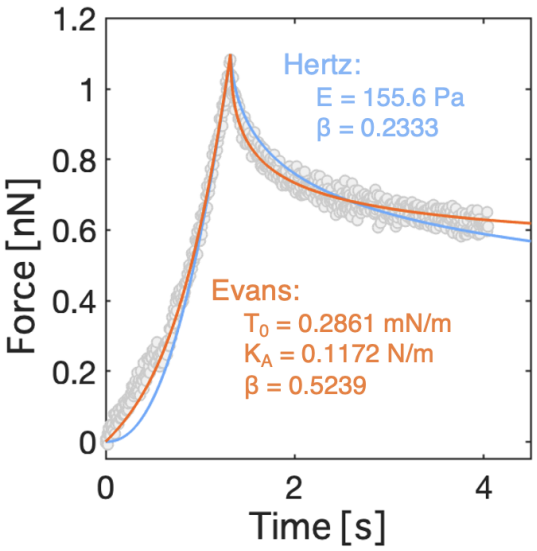

Figure 4.2: **Comparison of the force-curve fits obtained upon applying the Evans and Hertz models.** Both fits are used to describe the same compression-relaxation curve (grey circles), obtained on a WT fibroblast on glass substrate (1 µm/s and 1 nN). Comparatively, the Evans model (■) leads to a more accurate description of the force curve, both under low stress and at the start of the relaxation. The rheological parameters derived of both fits are indicated; the fluidity captured by the Evans model results higher than that determined by the Hertz model (■).

contact point during the approximation of the cantilever, also influenced the result of the calculation of T_0, K_A and β. Accordingly, in this section they will be explored.

In order to determine the optimal **cantilever's approach velocity**, thus least influential to the measurement of the cortical parameters, different velocities were tested on weakly adherent cells on glass substrates. To this purpose, each cell was serially measured through a range of approach velocities -namely 1, 2, 5 and 10 µm/s- using a constant set-point force of 1 nN. Figure 4.3.A shows the resulting T_0, K_A and β values. Both prestress and area compressibility showed a decreasing trend with increasing cantilever velocity. This became statistically significant between the approaching velocities of 2 and 5 µm/s, thus creating a threshold between *low* (1 - 2 µm/s) and *high* (5 - 10 µm/s) velocities that hints at a possible active cellular response to fast deformations, hence suggesting that high velocities should be avoided. The coefficient β, however, only showed increased fluidity at the highest velocity tested, 10 µm/s, presenting a significant difference compared to that obtained at 5 µm/s.

Figure 4.3.B shows exemplary force curves measured using the different test velocities (data points indicated with circles), and their corresponding fits upon applying

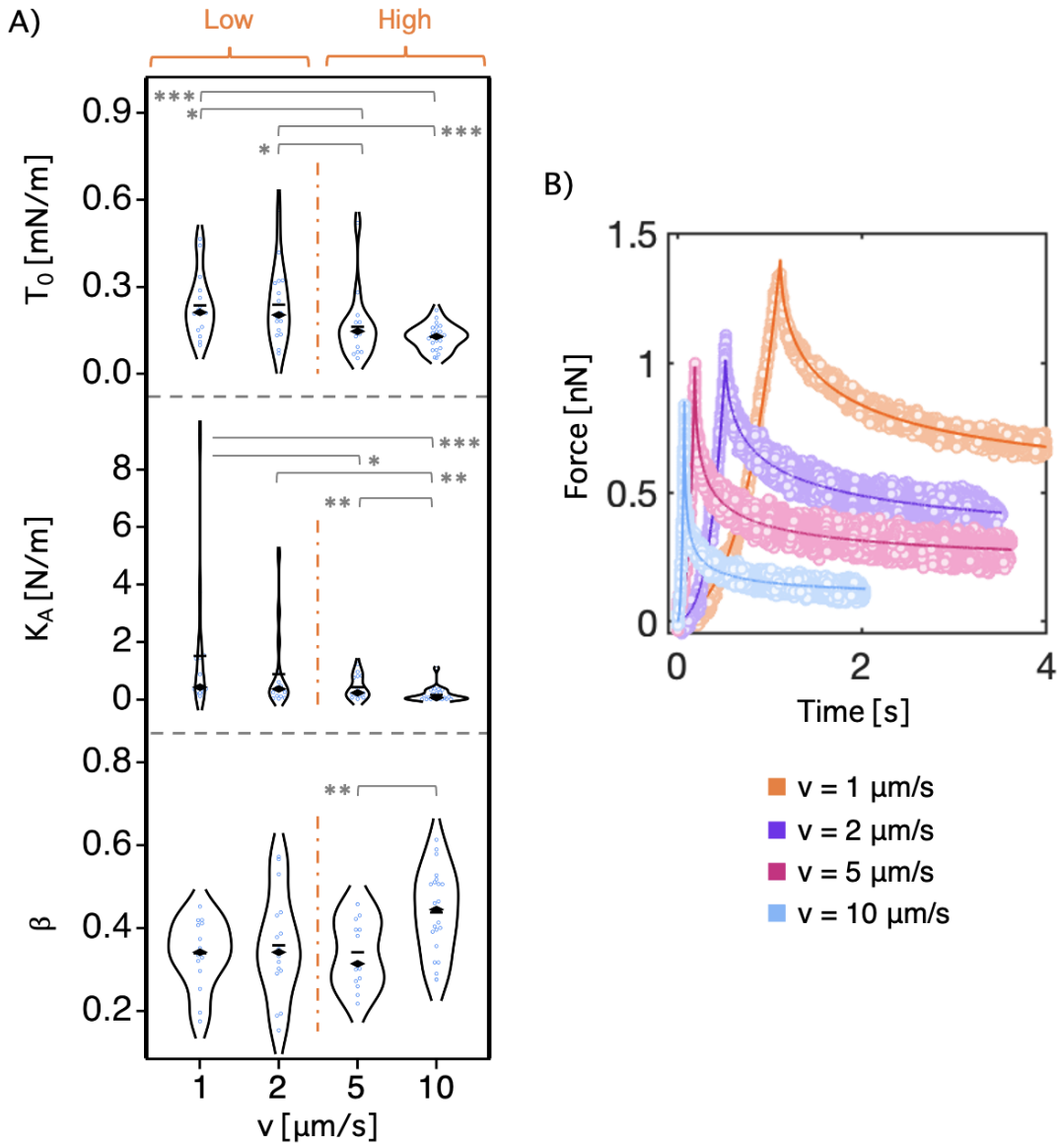

Figure 4.3: **Influence of the cantilever's approach velocity on the determination of cortical parameters. A)** Comparison of T_0, K_A and β parameters obtained upon applying the same compression (set-point force of 1 nN) at different velocities ($n_{1\mu m/s} = 15$, $n_{2\mu m/s} = 16$, $n_{5\mu m/s} = 15$, $n_{10\mu m/s} = 23$) on WT Fbs on glass substrates. Invasivity of the measurement increases with the cantilever's approach velocity: as indicated by the decrease in T_0 and K_A, and simultaneous increase in fluidity, approach velocities of 5 - 10 µm/s may trigger cortical adaptations, hence differentiating between *low* (optimal) and *high* velocities (discontinuous orange line). Changes in β become significant only at the higher approach velocity of 10 µm/s. Significance denoted with [*] for $\alpha < 0.05$, [**] for $\alpha < 0.01$, and [***] for $\alpha < 0.001$; mean and median are respectively indicated with **-** and ⬥. **B)** Compression-relaxation force curves obtained at different velocities and their corresponding fits (solid lines). All exemplary measurements were performed consecutively on the same cell.

the Evans model (solid lines). All curves belong to the same cell. Even though with increasing approach velocity a decreasing trend in the apparent force set-point was visible, all measurements were performed using a constant target force of 1 nN. At high velocities, the shape of the compression curve became more linear, thus loosing the characteristic gradual increase of standard AFM-based force-curves obtained on soft matter like cells. Simultaneously, immediately at the onset of relaxation, the curvature became more accentuated due to a fast and steep decline in the force measured. Despite these differences in the shapes of the force-curves, the Evans model was able to capture their outlines throughout the entire interval of velocities tested.

The influence of the **set-point contact force** on the cortex rheology was determined in a similar manner: force set-points of 1, 2, 5 and 10 nN were tested on weakly adherent WT fibroblasts, both on glass and on PEG substrates. In this case, measurements performed under approach velocities of 0.5, 1, 1.5 and 2 μm/s were pooled together as, in order to optimally record the force curves, adjustment of this parameter was experimentally necessary. As proven above, however, this range of velocities resulted non-invasive and caused no significant differences in the measurements.

Figure 4.4 shows the evolution of T_0, K_A and β under the aforementioned conditions. In general, cells on PEGylated surfaces showed increased prestress and fluidity than cells on glass throughout the tested experimental conditions. On glass substrates, the use of larger force set-points correlated to a statistically significant increase in the measured prestress. This trend was also observed on PEG, with the difference that the measurements performed at 2 nN showed a lower T_0 than those performed both at lower and higher forces. The area compressibility modulus, on the other hand, decreased with higher compression forces on both substrates. On glass, the trend became statistically relevant only when comparing the K_A values obtained under higher stress to the rest of experimental groups. In contrast, measurements on PEGylated substrates indicated that the area compressibility modulus already differed significantly amongst the closer experimental groups. Finally, regardless of the type of substrate, fluidity increased non-linearly upon cell compression at higher forces, leading to a stabilisation of β values close to a 0.6 coefficient.

To illustrate the effect of the force set-point on the compression-relaxation measurements, exemplary force curves are shown in Fig. 4.5. Both on glass and PEG substrates, the Evans model was able to globally capture the evolution of the force curves. However, beyond the set-point of 5 nN, an under-estimation of the force trend was visible in the modelled data at the onset of both compression and relaxation.

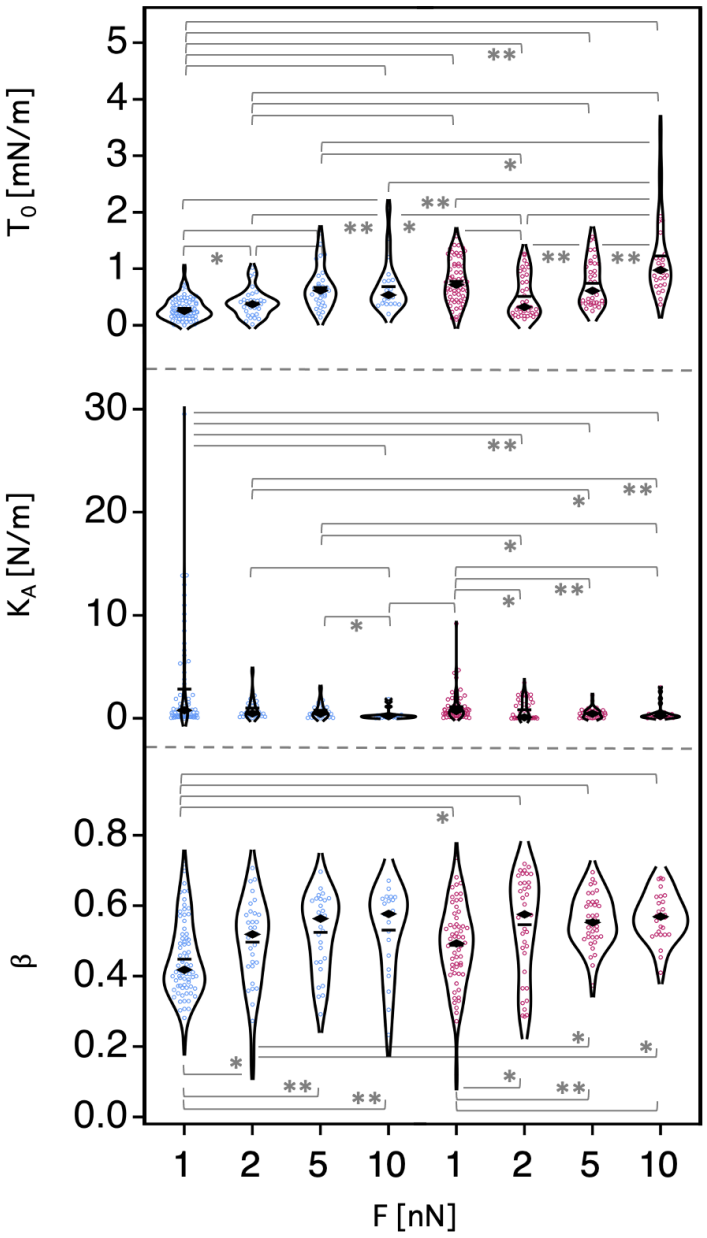

Figure 4.4: **Cortical response to the compression force.** T_0, K_A and β of WT fibroblasts on glass (■; $n_{1\text{-}10nN} \geqslant 21$) or PEG (■; $n_{1\text{-}10nN} \geqslant 28$) substrates, approached at 1 µm/s with different set-point forces. On glass substrates, cortical prestress and fluidity increase with the loading force. The same trend is generally observed on PEG substrates, with a deviation for a force of 2 nN. K_A values decrease with increasing load force. Significance denoted with [*] for $\alpha < 0.05$ and [**] for $\alpha < 0.01$; for simplicity of the plot, significance corresponding to [***] ($\alpha < 0.001$) is only indicated with brackets. Mean and median are respectively indicated with - and ◆.

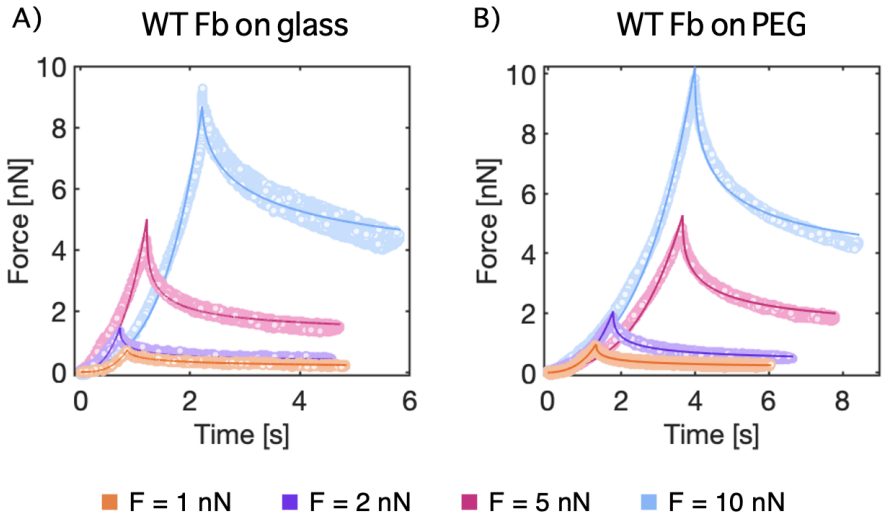

Figure 4.5: **Compression-relaxation force curves under different loads. A)** Exemplary measurements performed on the same WT fibroblast cell on glass at 1 µm/s and different set-point loads according to the legend. Curves denote measured data points (circles) and their corresponding fit based on the Evans model (solid line). **B)** Equivalent results, obtained from a cell on a PEGylated substrate at 0.5 µm/s and same interval of set-point forces.

The **geometry of the cantilever's tip** as experimental parameter was also tested as part of the validation process of the Evans model. However, only few experiments were performed on fibroblasts, resulting in low statistical relevance. For this reason, instead of determining whether the tip geometry has an influence on the measurement of the cortical parameters, the interest lays on the application of the Evans model and the error that the indentation percentage, which reflects the ratio of cellular deformation with respect to the cell radius, may introduce to the fitting routine.

Accordingly, three force curves measured on the same cell with pyramidal cantilevers were fitted to the Evans model using several indentation percentages: 7, 10, 13, 16, 20, 50 and 100 %. The averaged results for T_0, K_A and β are plotted in figure 4.6.A. No significant deviations were visible within the parameters determined under typical indentation values, ranging from 7 to 16 %. However, with indentation percentages beyond 20 %, hence reflecting a large cellular deformation, a divergent trend appeared. Therefore, indentation beyond 20 % of the cellular radius are not recommended. Figure 4.6.B illustrates the deformation of weakly adherent cells upon contact with pyramidal cantilever at different indentation percentages.

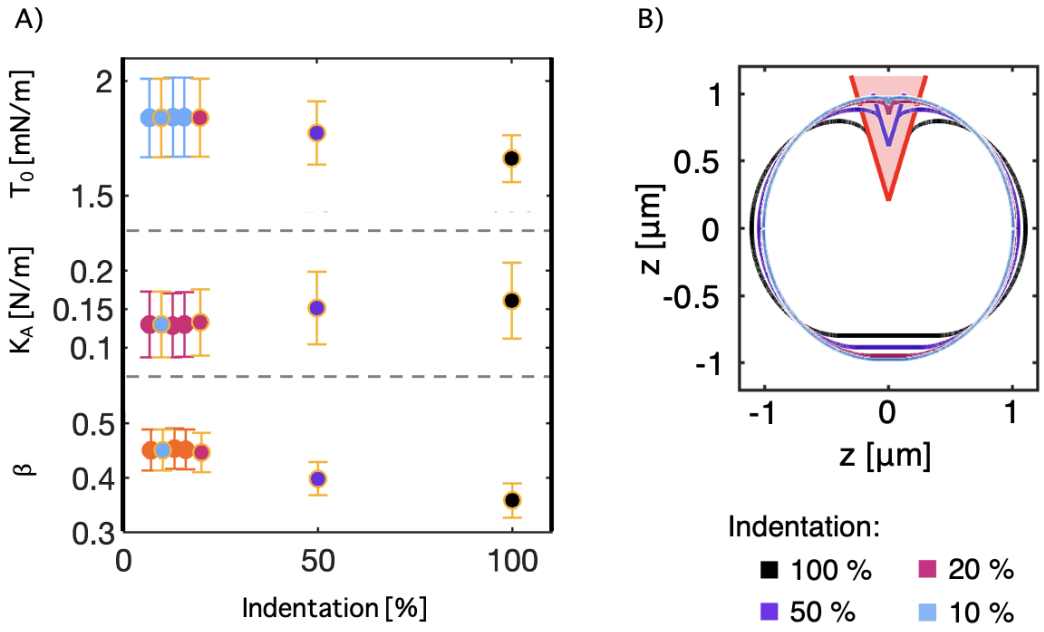

Figure 4.6: **Influence of the indentation percentage in the application of the Evans model. A)** T_0, K_A and β as calculated with varying indentation percentages. The individual data points reflect the mean and standard deviation obtained upon averaging the parameters retrieved from three force curves performed on the same WT cell (PEG substrate and standard conditions). Indentation values beyond 20 % cause a deviation in the calculation of T_0, K_A and β, and are therefore not recommended. **B)** Schematics reflecting the geometrical deformation of a weakly adherent cell probed by a pyramidal cantilever (red shadow) with different indentation depths. Cellular indentation causes simultaneous deformation at the substrate and cantilever interfaces: with a normalised radius (1 µm), an indentation of 100 % causes a deformation depth of 0.75 µm by the cantilever and a flattening of 0.25 µm (z direction) by the substrate. The geometries depicted in B) correspond to the data points framed in yellow in A) according to the color legend.

In order to apply the Evans model, the **radius of the cell** must be provided. However, cells are seldom perfectly circular in their contact area to the substrate. Accordingly, depending on how the cell diameter is drawn, its value may present a relatively large variability. This is exemplified in figure 4.7, where the influence of the radius in the determination of T_0, K_A and β is evaluated. While T_0 and β showed a relatively low variability with the radius even upon duplication of the real length, K_A showed a strong dependence: an increase of 2.5 µm in the cell radius resulted, approximately, in a two-fold increase in K_A.

Finally, the importance of the **contact point** -between cell and cantilever- in the final calculation of T_0, K_A and β was explored. To this purpose, the same compression-

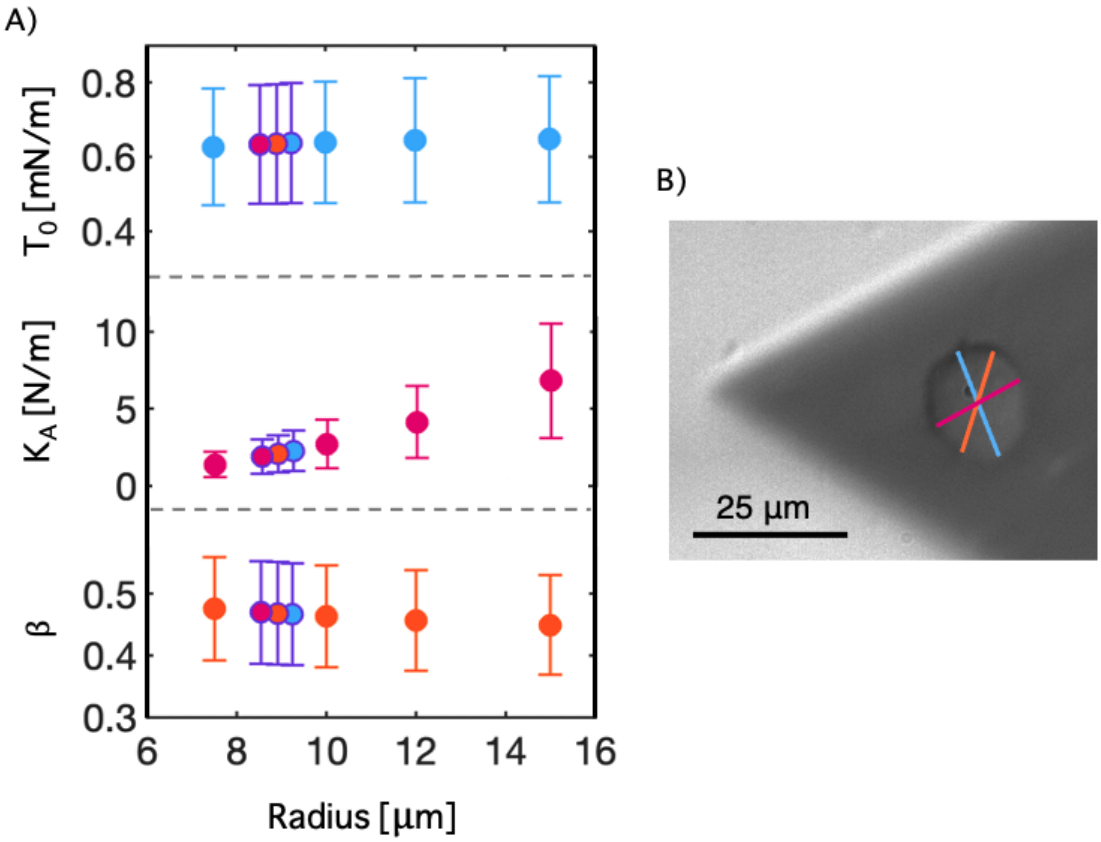

Figure 4.7: **Influence of the cell radius value in validating the Evans model. A)** T_0, K_A and β as calculated with varying cellular radii. The individual data points reflect the mean and standard deviations obtained upon averaging the parameters retrieved from three force curves performed on the same WT cell on glass substrate and under standard conditions. The values indicated with a purple frame correspond to the radii depicted in **B**: 8.55, 8.91 and 9.25 µm. K_A doubles with an increase in radius of 2.5 µm, highlighting the importance of maintaining consistency when measuring the cellular radii.

relaxation curve was fitted to the Evans model using different manually selected contact points, as illustrated in figure 4.8, and the corresponding calculations of the rheological parameters were compared (table 4.1). Despite using different contact points -all of them in a region where they could be reasonably selected during the processing of the force curves-, the Evans-fitted data showed comparable trends. Divergences were mostly localised immediately at the onset of compression, and slight deviations were present at the beginning and towards the end of the relaxation interval. Taking into account the values in table 4.1, the use of different reasonable contact points had a small influence.

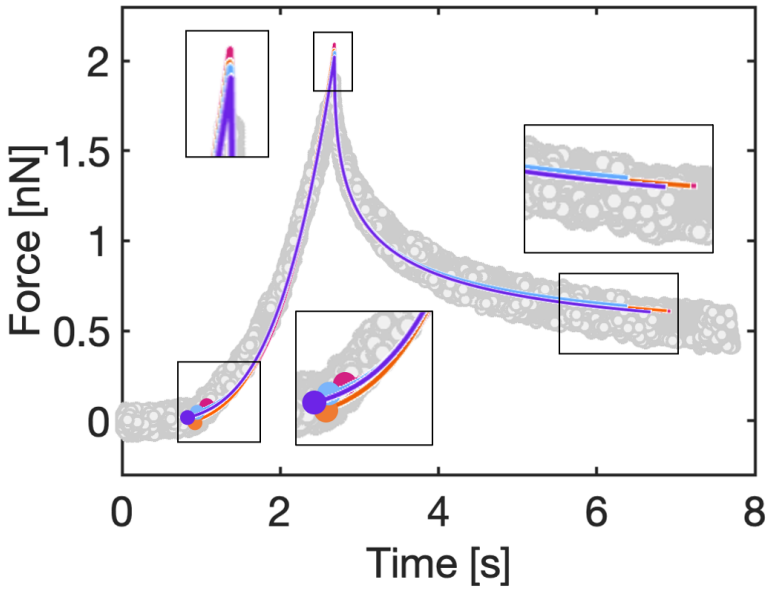

Figure 4.8: **Influence of the contact point in the application of the Evans model.** The same compression-relaxation force curve, obtained on a WT Fb on PEGylated substrate at 1 µm/s and 2 nN, is fitted to the Evans model using different contact points (colored dots). The corresponding fitted trends are indicated using the same color legend. Insets aim to highlight regions with visible variability.

Table 4.1: **Rheological parameters as affected by the contact point.** Values correspond to the force curve in Fig. 4.8, fitted to the Evans model using different contact points (same legend). The averaged values (Av) and standard deviation (SD) are indicated to illustrate the deviation caused by the use of different contact points.

Contact point	T_0 [mN/m]	K_A [N/m]	β
■	0.226	0.571	0.570
■	0.251	0.837	0.586
■	0.260	0.650	0.583
■	0.296	0.607	0.590
Av ± SD	0.259 ± 0.029	0.666 ± 0.118	0.582 ± 0.009

4.1.3 Influence of the myosin II activity in the rheology of the actomyosin cortex of weakly adherent cells

The contraction of the actomyosin cortex is regulated by the action of motor proteins such as non-muscle myosin II. Accordingly, alterations in motor activity should transmit to the prestress. This was tested by the exposure of cells to two small molecules that interfere with myosin II activity: calyculin A and blebbistatin. The former is a protein phosphatase inhibitor that prevents the dephosphorylation of the myosin regulatory light chains (RLCs). In the dephosphorylated form, RLCs induce myosin inactivation. Accordingly, calyculin A leads to hyperactivation of myosin II motors [66, 145]. In contrast, blebbistatin is an ATPase that stalls the motor's activity by blocking myosin II heads through the formation of a complex with low affinity for actin [144]. Cortical parameters obtained upon exposure to these drugs are shown in figure 4.9, where the effect of the fixating agent GDA is also displayed as a reference since, due to its cross-linking activity of aldehyde groups, it indirectly inhibits contractility and motility by stiffening the cell membrane.

Fibroblasts became stiffer upon exposure to calyculin A, as shown by an increase in T_0 and K_A that was accompanied by a decrease in fluidity. In contrast, exposing cells to blebbistatin led to a very small decrease in prestress compared to the untreated fibroblasts. The mean of the distributions in the violin plots of Fig. 4.9 are detailed in table 4.2. Fixation of the cytoskeleton by GDA-based cross-linking led to a drastic stiffening of the cell as reflected by the elevated prestress and decreased cortex fluidity. Upon exposure to calyculin A and GDA, fibroblasts present a similar area compressibility modulus, suggesting that the activity of hyperactive myosin motors generates a cortex with high resistance to compression-extension changes, similar to the effect of a stiff and cross-linked cellular membrane.

In figure 4.9, exemplary curves showing the effect of the different small molecules are also presented. The use of GDA or calyculin A, which led to a stiffening of the cortex, caused a more linear compression compared to the classic force curves obtained from untreated cells. The decrease in fluidity was also observed in the relaxation region of the curve, where a smaller and more horizontal drop in the measured force was observed. Comparing the same reference force curve to the result of adding blebbistatin to the media showed a minor variation, mostly localised at the onset of compression and relaxation, with an increase of the curvature, thus indicating K_A adaptation.

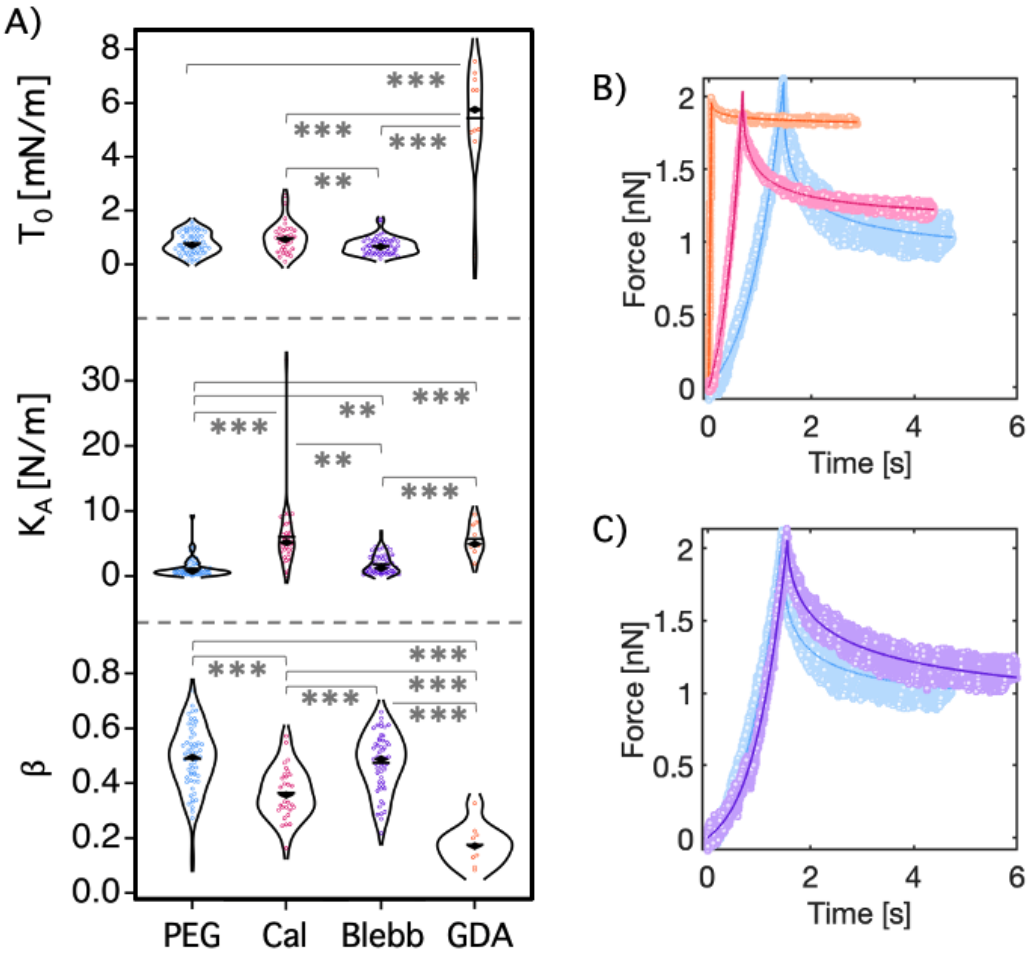

Figure 4.9: **Influence of the myosin II activity on the rheology of the cortex. A)** T_0, K_A and β of WT fibroblasts on PEGylated substrates. Comparison is done between untreated cells ($n = 61$) and fibroblasts exposed to blebbistatin ($n = 104$), which does not cause a significant difference, and calyculin A ($n = 100$) and GDA ($n = 10$), which leads to the stiffening of the cortex (significance denoted with [*] for $\alpha < 0.05$, [**] for $\alpha < 0.01$, and [***] for $\alpha < 0.001$; mean and median are respectively indicated with **-** and ⬥). **B)** Exemplary force curves showing the cortex stiffening caused by exposure to calyculin A (■) and GDA (■). Untreated cells (■) are kept as a reference in **C)** where they are compared to blebbistatin-treated fibroblasts (■).

Table 4.2: **Influence of the myosin II activity on the rheological parameters**. The table reflects the mean and SD values of the distributions in the violin plots of Fig. 4.9 for WT Fbs on PEGylated substrates (reference values) and cells exposed to calyculin A, blebbistatin and GDA.

Condition	T_0 [mN/m]	K_A [N/m]	β
WT ■	0.779 ± 0.385	1.14 ± 1.47	0.488 ± 0.117
Cal ■	0.967 ± 0.550	6.01 ± 5.61	0.366 ± 0.090
Blebb ■	0.680 ± 0.307	1.76 ± 1.48	0.475 ± 0.105
GDA ■	5.43 ± 2.08	5.66 ± 2.31	0.175 ± 0.071

4.2 Discussion

The Evans model is a robust tool in the characterisation of the cellular cortex. Through a range of experimental conditions, even upon cortical perturbance through the exposure of drugs like blebbistatin or calyculin A, it is able to successfully relate the cortical prestress to the fluidity of the cell, and determine T_0, K_A and β. However, as all models, it presents experimental considerations beyond which its accuracy may decrease, such as the implementation of different fitting routines and the introduction of batch-processing, experimental parameters like approach velocity or set-point force, and analytical parameters like the cell radius, indentation percentage or contact point.

Hereafter, a consistent methodology, optimised based on the experimental and analytical limitations of the Evans model, will be defined. Upon this, the cortical response to the exposure of blebbistatin, calyculin A and GDA will be discussed.

4.2.1 Comparison of the fitting routines implemented for the analysis of force curves based on the Evans model

To provide coherence in the presentation and discussion of results throughout this thesis, one of the two fitting routines existing in the application of the Evans model had to be determined as the standard protocol. This was relevant due to two main reasons: 1) the processing of force curves is time consuming (both for the IF and SF), so repetition should be avoided when possible; 2) the process itself should have no influence on the results, but to reduce possible sources of uncertainty during evaluation, compared data sets should be acquired using the same protocol.

As shown in figure 4.1, applying either of the IF or SF to the same experimental group did not lead to significant differences, albeit slight deviations amongst the mean

and median values may appear. In addition, the distribution shown by the violin plots on glass substrates was mostly preserved between fitting routines for all three parameters of interest; on PEGylated substrates, comparison was restricted due to the difference in sample sizes. Accordingly, the use of the IF or SF did not influence the results of applying the Evans model and the decision was therefore based on the practical advantages that either of the fitting routines may have presented during the processing of the force curves. In this regard, both followed the same general process: each force measurement had to be individually processed in order to remove drifts and drag-related artifacts from the baseline, the interval to be fitted had to be manually selected, and the contact point indicated. The difference laid on the fact that the individual fitting routine calculated the geometry of the compressed cell for each file, whereas the serial routine determined the geometry once and then applied it to serially process a group of files. The SF was therefore faster and more convenient as, in addition, allowed the quick visualisation, and therefore comparison, of the force curves of an experimental category. Considering these advantages, the serial fitting routine was established as the standard protocol and the results presented in this thesis were obtained upon its application unless otherwise specified.

4.2.2 Experimental and analytical constraints of the Evans model

Originally, the SF was developed for the batch-processing of force curves with the aim to simultaneously analyse all the measurements belonging to an experimental category. However, some experimental limitations had to be considered in this regard.

As observed in Fig. 4.3, the use of low **approach and retraction velocities** (1 - 2 μm/s) in the measurement of force curves did not lead to differences in the resulting rheological parameters. This was not the case for moderate (5 μm/s) or high (10 μm/s) velocities, which led to the sensing of significantly more pliant cortices, thus suggesting a fast adaptation to prevent membrane rupture.

This indicates that experimental cantilever velocities should be limited to $\leqslant 2$ μm/s, which is also required in order to avoid artifacts due to the presence of hydrodynamic drag forces. These forces, which appear as a result of the viscous friction between the cantilever and the liquid media in which the measurements are performed, show a linear dependence with the speed of the cantilever [157]. Accordingly, they are negligible only at low speeds. In addition, the presence of drag forces in the characterisation of weakly adherent single cells may cause their displacement out of the compression area during the approach phase. This is specially relevant during parallel plate compression with

cantilevers of rectangular beam, as this geometry provides higher drag forces than for triangular cantilevers [158].

The use of varying **set-point forces**, as illustrated in Fig. 4.4, led to important variations in the rheology of the actin cortices. By increasing the compression force, a cortical modulation may be triggered in order to resist or adapt to the increasing external load. Simultaneously, deeper regions of the cellular body may be probed, hence registering contributions from the cellular organelles in the resulting force curves. For cells on glass substrates, already within a difference of 1 nN in the set-point force, significant differences ($\alpha = 0.05$) were observed in T_0 and β. This highlights the importance of delimiting the experimental conditions to low forces, specifically below 2 nN. In the case that adjustment of this parameter is experimentally necessary for the optimal recording of the force curves, attention needs to be put on any analytical deviations that may come from pooling data acquired under different set-point forces.

Interestingly, both on glass and PEGylated substrates, cell fluidity showed a plateau in the coefficient β with increasing set-point forces, whereas prestress preserved a linear trend. This suggests that once fluidity cannot increase anymore, prestress rises to prevent further cellular deformation. The saturation regime should be avoided to allow detection of cortical adaptations through the three parameters of interest T_0, K_A and β.

As discussed by Cordes *et al.*, and demonstrated by indenting MDCK II cells with conical and colloidal cantilever tips of various sizes, the Evans model is independent of the indenter geometry [9]. Here, the focus lies on determining the influence that the **indentation percentage**, parameter required during the application of the Evans model, has on the calculation of T_0, K_A and β . The indentation value is tied to the set-point force and is determined as the indentation depth with respect to height of the cell. In the AFM setup here used, only the top view of the cell was accessible, meaning that the indentation distance could not be optically determined. Alternatively, indentation can be calculated from the cantilever's z-displacement and Hooke's law (eq. 2.1). However, in this process, the cantilever's deflection needs to be known, and this value may be affected by drifts in the baseline. Accordingly, for a proper evaluation of the rheological results, it is important to determine whether they may be affected by deviations in the indentation values. As shown in figure 4.6, T_0, K_A and β were only significantly distorted with indentation percentages beyond 20 %. Larger indentations correlate to set-point forces beyond those used in this thesis, establishing a limit that albeit more relevant for the general handling of force indentation experiments, is also important for the consistent application of the Evans model.

Two other analytical parameters were tested: the cell radius and the contact point. Regarding **cell size**, figure 4.7 shows the importance of consistency in determining cellular radii, specially involving K_A. As a simple approach, variability in T_0, K_A and β can be reduced by systematically drawing the cell diameter through the longest, shortest, or averaged diameter. Considering the batch-processing feature of the SF routine, the radius is introduced for the general calculation of the geometry of the compressed cell and is thereafter serially applied to the grouped measurements. Accordingly, only cells with comparable radii should be processed together. Seeking consistency in the determination of the **contact point** between cell and cantilever is also important, albeit its influence is considerably smaller than that of the cell radius. This becomes challenging when testing different experimental conditions because force measurements may present different curvatures at the onset of compression as reflected in figure 4.5, where the misalignment between force curves is partially due to a lack in consistency in contact point indication. The implementation of an improved and automatic sub-routine could therefore reduce the variability associated to contact point selection by optimally determining its location.

In the application of the Evans model, a compromise between minimal invasivity and cell-cantilever contact formation -especially challenging for weak adhesiveness- must be reached. Based on the results above, these *standard* conditions are defined by low approach velocities ($\leqslant$ 2 µm/s) and set-point forces ($\leqslant$ 2 nN), which also relate to low indentation percentages ($\leqslant$ 20 %). In addition, to limit variability during the systematic analysis of force curves, specially in K_A, consistency is required in the indication of cell radius and contact point.

4.2.3 Comparison of the Evans and Hertz models

Experimentally, the validity of a viscoelastic model can be determined by testing whether it is independent of the geometry and size of the cantilever's tip. Based on this principle, Cordes *et al.* validated the Evans model by indenting confluent MDCK II cells with probes of different size and geometry. Simultaneously, they observed that the Young's moduli obtained upon applying the Hertz model to the same measurements decreased with increasing indenter size, and varied according to its geometry [9]. This poses a constraint in the application of the Hertz model, as different geometries are optimal for different applications: while pyramidal tips provide high resolution in the mapping of topographies and elastic moduli of samples, colloidal tips provide a larger contact

surface, thus limiting the risk of cell damage by distributing forces [159].

Furthermore, figure 4.2 shows how the Hertz model was unable to accurately describe the force curves especially at low strain, where the prestress dominates, and directly at the onset of relaxation. More importantly, as shown in the same figure, the Evans model led to fluidity coefficient β values that are larger than those determined by the Hertz model. Theoretical approximations to *in vitro* experiments on reconstituted bio-networks indicate that the relaxation times of transiently cross-linked actin networks correspond to β coefficients of 0.5. Accordingly, the Evans model provides fluidity values closer to these observations in comparison to the β coefficient of 0.2 reported in the bibliography for living cells, characteristic of glassy dynamics [102].

In conclusion, the Evans model is able to more accurately determine the rheological properties of the actomyosin cortex by relating the cellular prestress to its fluidity. Using standard experimental conditions and maintaining coherence in the analytical processing of the force measurements, the Evans model consistently describes the compression-relaxation phases of the force curve over the entire duration of the measurement.

4.2.4 Influence of the myosin II motor activity on the rheology of the actomyosin cortex

The cellular response to deformation is considered to be predominantly controlled by the structure of the actin mesh and by the network of non-muscle myosin II motors conforming the actomyosin cortex [10] [160]. This hypothesis is further supported by the findings in the viscoelastic characterisation of *ex vivo* isolated apical cell membranes on porous substrates, which show that activation of myosin II motors leads to a behaviour closer to that of living cells [101]. Calyculin A and blebbistatin are small molecules known to modify the activity of myosin II motors. While the former increases motor processivity [66, 145] and is therefore expected to generate higher prestress at the expense of fluidity, the latter stalls myosin II activity [144], thus promoting increased fluidity due to the loss of transient actin cross-links.

Observing figure 4.9, the effect of exposure to calyculin A was in agreement with the aforementioned. However, the use of blebbistatin did not induce a significant effect -but at least a trend- with respect to untreated cells. In comparison, equivalent experiments on MDCK II cells by Cordes *et al.* show a clear change in the behaviour of the cortex upon exposure to the same drugs [9]. This suggests that fibroblast could be more resistant than MDCK II cells to the effect of drugs that alter the regulation of the actomyosin cortex, which is not unreasonable given the important structural function

that fibroblasts perform in the tissue. Cellular polarity or cortical thickness may play an important role in determining cortical sensitivity. In this regard, stimulated emission depletion (STED) images have shown that weakly adherent fibroblasts present a cortex with an average thickness of ∼400 nm, whereas for MDCK II cells, the thickness is of ∼160 nm [9]. Such difference may reduce the sensitivity to blebbistatin and calyculin A in fibroblasts. The use of GDA, which generates solid-like shells by protein cross-linking, caused a drastic stiffening of the actomyosin cortex on both cell types. Interestingly, the resulting area compressibility modulus was comparable to that of fibroblasts exposed to calyculin A (Fig. 4.9), indicating that the cross-linking of the membrane and the over-activated contraction of the actin shell lead to a similar resistance to the increase of cellular surface.

Given the changes induced in the cellular rheology upon alteration of the activity of non-muscle myosin II motors, it is further supported that the cellular response to external stress is governed by the interplay between the components of the actomyosin cortex.

Conclusions

In conclusion, a clear standard methodology has been described in this chapter for the application of the Evans model to compression-relaxation force curves obtained on single cells. As a result, prestress, area compressibility modulus and fluidity, parameters describing the rheological properties of the actomyosin cortex, can be accurately determined. By using this model, the influences on cortical dynamics of blebbistatin and calyculin A, which alter the activity of non-muscle myosin II motors, and of GDA, which causes protein cross-linking, have been analysed, offering further proof that the cortical response to deformation is predominantly regulated by the activity of myosin II motors.

Chapter 5

Influence of formins on the actomyosin cortex throughout cellular adhesion

In the previous chapter, the Evans model and its robustness were validated in the context of rheologically characterising the actomyosin cortex of weakly adherent fibroblasts. However, the rounding of cells is rather constrained to specific stages of the cell cycle such as mitosis [161], cell death [162], or tissue developmental events [163]. Even in cell migration, despite lifting from the substrate [164], cells maintain a non-globular but polarised shape with an elongated body showing leading and trailing edges [165]. Therefore, in the exercise of characterising the actomyosin cortex, the study of strongly adherent cells becomes relevant. In this chapter, the relation between the degree of adhesion and the cortical properties of fibroblasts is determined. In addition, since changes in cellular shape correlate to the re-organisation and re-assembly of the actomyosin mesh [10], the influence of formin proteins, which participate in the nucleation and elongation of linear actin filaments, is assessed by comparing the properties of wild type fibroblasts to those of cells lacking mDia1, mDia3, or both isoforms.

5.1 Results

5.1.1 Actomyosin cortex adaptation with the degree of cell adhesion

In order to validate the Evans model, force measurements were obtained on cells cultured on archetypical substrates leading to weak and strongly reduced cellular adhesion. These

were, namely, glass and PEGylated surfaces which, as shown in figure 4.1 of Chapter 5, already led to considerably different cortical prestress and fluidity. Cell adhesion is largely governed by the interaction between integrins and proteins located at the extracellular matrix [166]. One of the most relevant recognition motifs for such ligand-receptor interplay is the Arg-Gly-Asp (RGD) peptide. Accordingly, the use of soluble RGD in culture prevents the cell-substrate interaction by blocking the integrin receptors, whereas when functionalised onto a surface, the motif promotes cell adhesion [167]. This is precisely what naturally occurs with fibronectin, a major ECM component rich in RGD amino acid sequences that thus promotes cellular adhesion and spreading [168].

Therefore, in order to compare the rheological properties of cells presenting different degrees of adhesion, the use of soluble RGD peptides and fibronectin-coated substrates was added to the use of bare glass and PEGylated surfaces already employed in Chapter 4. This is reflected in figure 5.1 and the corresponding table 5.1.

As shown, weakly adherent cells showcased a broad distribution of prestress values that encompassed that of strongly adherent cells as well. Within weakly adherent cells, which led to lower T_0 values, the addition of adhesion-inhibiting RGD caused a slight increase, albeit non-statistically significant. A similar trend was reflected in the fluidity values, being those observed on strongly adherent cells equivalent to those on glass. The area compressibility modulus showed a progressive increase with adhesion strength; highest values where therefore observed for strongly adherent fibroblasts, and lowest for cells on PEGylated substrates.

Table 5.1: **Influence of the degree of cellular adhesion on cortical parameters**. The table shows the mean and SD of the distributions of Fig. 5.1 for WT fibroblasts presenting different degrees of cell adhesion according to the seeding conditions employed.

Substrate	T_0 [mN/m]	K_A [N/m]	β
PEG	0.779 ± 0.385	1.13 ± 1.47	0.488 ± 0.117
Glass + sRGD 1 mM	0.324 ± 0.260	1.58 ± 2.25	0.453 ± 0.088
Glass	0.297 ± 0.192	2.83 ± 4.81	0.448 ± 0.107
Fibr	0.429 ± 0.200	4.05 ± 8.08	0.446 ± 0.115

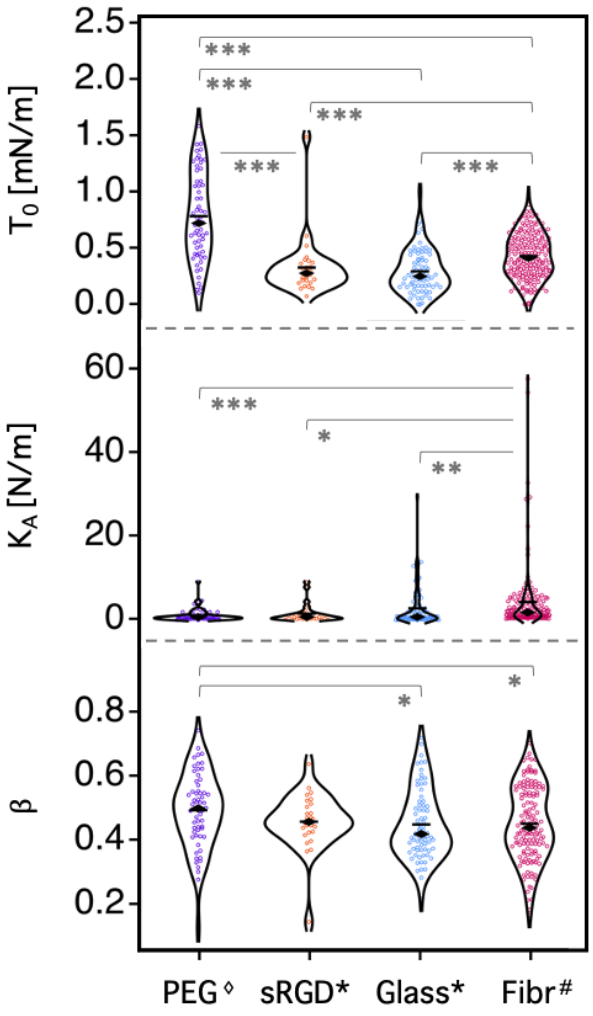

Figure 5.1: **Dependence of cortical properties on the degree of cellular adhesion.** Comparison of T_0, K_A and β parameters obtained on cells cultured on substrates leading to increasing degree of adhesion. From left to right, ranging from strongly reduced ($\diamond$) to weak (*) and finally to strongly increased (#) adhesion. Prestress values span over an interval delimited at the low end by those obtained on glass -with or without RGD- and those obtained on PEGylated substrates. Within weakly adherent cells, fluidity of cells on glass increases upon 1 mM RGD addition and is higher for Fbs on PEGylated substrates. Strongly adherent Fbs show fluidity values similar to those of cells on glass; compared to weakly adherent cells, they present intermediate prestress and a higher area compressibility modulus. Significance denoted with [*] for $\alpha < 0.05$, [**] for $\alpha < 0.01$, and [***] for $\alpha < 0.001$; mean and median are respectively indicated with **-** and $\blacklozenge$. All measurements were performed at standard conditions of 1 nN force and 1 µm/s; $n_{Glass} = 74$, $n_{RGD} = 27$, $n_{PEG} = 60$, $n_{Fibr} = 141$.

5.1.2 Relevance of formins in cortex regulation of weakly adherent cells

To establish a reference for the study of the influence of formins on the properties of the actomyosin cortex, initial experiments compared the behavior of WT Fbs to that of double knock-out (dKo) cells -thus lacking the mDia1 and mDia3 isoforms- and of WT cells exposed to the general formin inhibitor SMIFH2. SMIFH2 targets the formin homology 2 (FH2) domain of formins, hence preventing their actin nucleating and filament elongating activity. The results of such comparison, performed under standard conditions on PEGylated substrates, are shown in figure 5.2. Upon formin inhibition, cortical prestress was drastically reduced. This applied to the two experimental conditions of dKo cells and WT cells exposed to SMIFH2. Regarding K_A and β, however, the two formin-modulated categories presented different behaviours: while dKo cells did not show significant differences with respect to WT untreated cells, fibroblasts exposed to SMIFH2 presented a significant increase in K_A and decrease in β.

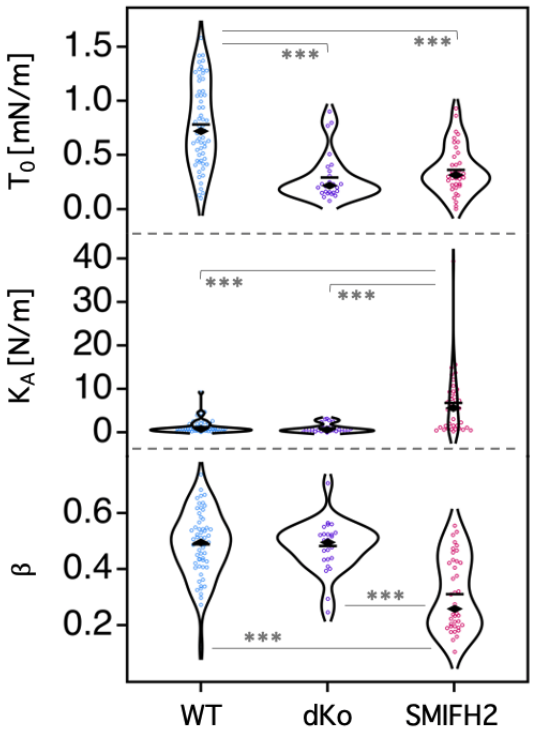

Figure 5.2: **Influence of formin-modulation on cortical properties.** Comparison of T_0, K_A and β parameters between WT fibroblasts and cells with modulated formin-activity, including dKo Fbs and WT cells exposed to SMIFH2. Prestress values decrease upon formin inhibition, but K_A and β only result affected by the exposure to SMIFH2. Significance denoted with [***] corresponds to $\alpha < 0.001$; mean and median are respectively indicated with - and ◆. Measurements were performed at standard conditions on PEGylated substrates; $n_{WT} = 60$, $n_{dKo} = 25$, $n_{SMIFH2} = 44$.

5.1.3 Influence of formin modulations in the adaptation of the actomyosin cortex of strongly adherent cells

Upon initiating the experimental on strongly adherent cells, the duration of the measurements was optimised to ensure that strong adhesion was fully established throughout the acquisition time. Accordingly, changes in the cortical parameters of the pool of cells measured in a day (9 to 10 per cell line) were qualitatively analysed as a function of time. To this purpose, for each cell tested, the resulting T_0, K_A and β values were averaged and presented against their acquisition time in figure 5.3.

For each parameter and cell line, the general trend was determined based on least square analysis. As a result, a linear regression was calculated for each experimental condition, collected in table 5.2. Cell fluidity remained relatively stable (small slope compared to initial value) for the duration of the experiment, showing small differences in the temporal trend between cell lines. In contrast, prestress and area compressibility modulus showed a higher variability in time with different trends for WT, mDia3 and mDia1-lacking cells; prestress of mDia3 showed a higher increase rate, albeit measurements were performed in a shorter time interval. Given the linear trends identified upon qualitative analysis, measurements on strongly adherent fibroblasts were performed during a 2 h interval in an attempt to maintain reduced but consistent distributions of T_0, K_A and β, and initiated 30 min after cell seeding (1 h upon preparation of the cell suspension) to ensure cellular spreading.

Table 5.2: **Linear fits describing the temporal evolution of the rheological parameters of adherent cells**. The equations of the linear fits representing the temporal evolutions of the parameters showcased in Fig. 5.3 are shown. Time in hours.

Cell type	$T_0(t)$ [mN/m]	$K_A(t)$ [N/m]	$\beta(t)$
WT	$0.350 + 0.065t$	$4.339 - 0.419t$	$0.585 - 0.033t$
mDia1	$0.228 + 0.103t$	$0.317 + 0.331t$	$0.726 - 0.073t$
mDia3	$0.113 + 0.292t$	$0.932 + 0.335t$	$0.605 - 0.039t$
dKo	$0.143 + 0.117t$	$3.261 + 0.320t$	$0.563 - 0.042t$

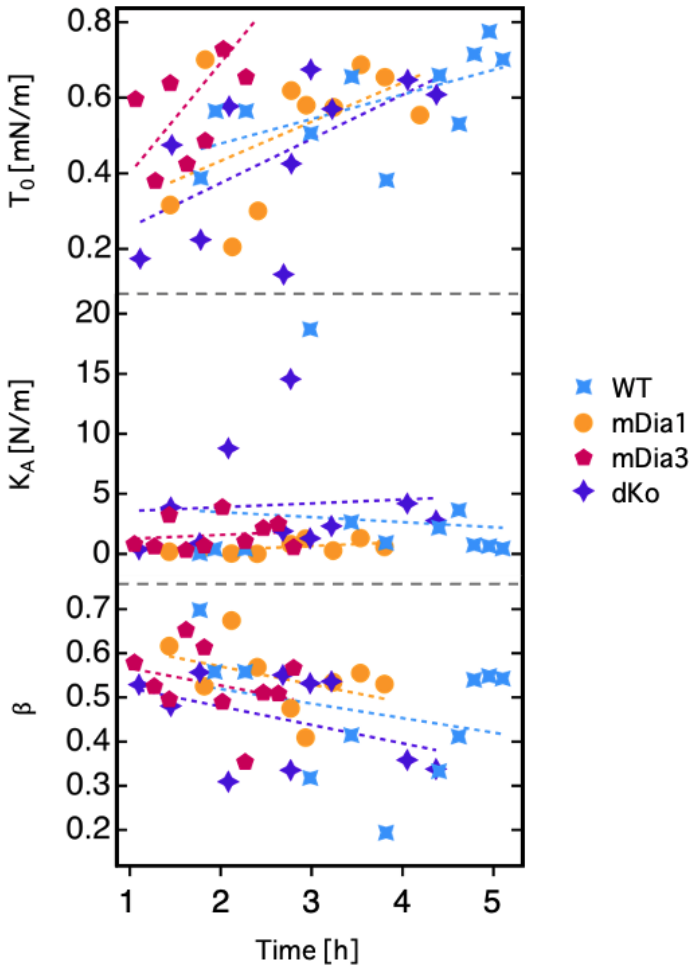

Figure 5.3: **Temporal evolution of the cortical properties of adherent cells.** Each marker represents the averaged values measured on a single cell (see legend for the cell line). To better illustrate the temporal changes, a linear fit is provided for each data set (dotted lines). Time of 0 h corresponds to the preparation of cell suspension; within the first hour, cells are transported and seeded to the AFM substrates.

The rheological parameters of strongly adherent WT, mDia1, mDia3 and dKo fibroblasts are shown in figure 5.4. Prestress values were lower for WT cells and increased, in this order, for mDia3, mDia1 and dKo cells. Between WT and mDia3 Fbs, however, differences resulted non-statistically significant. Fluidity of the two single knock-outs was also higher than for WT, but in this case, both comparisons resulted statistically significant. In contrast, fluidity of WT and dKo Fbs remained comparable. The trend in β was inversely reflected in K_A: higher moduli were found for WT and dKo Fbs, and lower K_A was found for mDia1 cells.

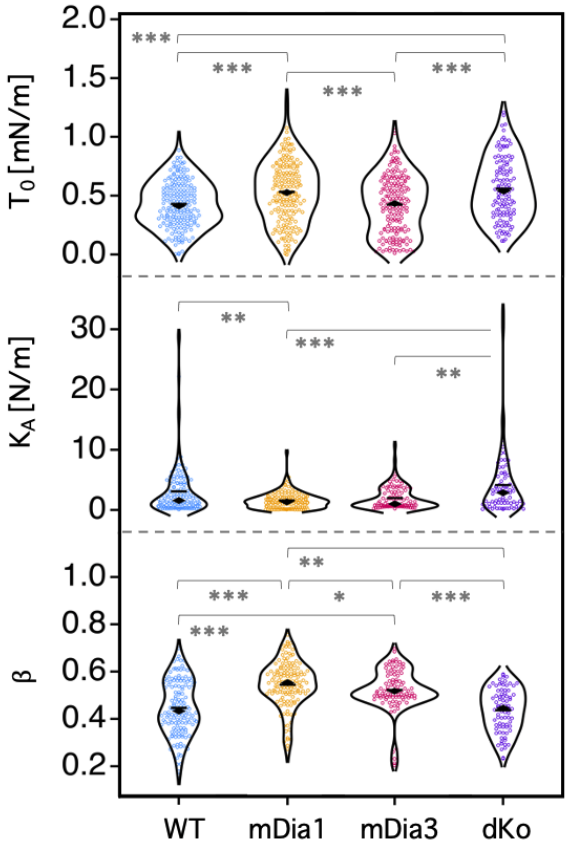

Figure 5.4: **Cortical properties of strongly adherent cells with different formin modulations.** Cellular prestress is lower on WT and mDia3 Fbs, and increases for mDia1 and dKo cells. K_A and β show mirrored trends: cellular fluidity is lower on WT and dKo cells, with very similar values, and higher for mDia1; the contrary is observed for K_A. Significance is denoted with [*] for $\alpha < 0.05$, [**] for $\alpha < 0.01$, and [***] for $\alpha < 0.001$; mean and median are respectively indicated with - and ◆. $n_{WT} = 140$, $n_{mDia1} = 138$, $n_{mDia3} = 99$, $n_{dKo} = 80$.

5.2 Discussion

5.2.1 Cortical parameters in relation to the degree of cell adhesion

Throughout their lifespan, cells *in vivo* regulate adhesion according to their biological needs as an intrinsic part of their natural behavior: during tissue formation or mitosis, cells become round at the expense of their attachment to the substrate and neighboring cells. In addition, strongly adherent cells lift from the surface in order to display directed migration towards or away from a myriad of cues. Incidentally, the wound healing process

leads to the expression of an important number of chemical cues, like pro-inflammatory cytokines, ECM components or TGF-β, that dictate migration through chemotaxis [169].

To understand various dynamical or non-lineal processes, the use of different substrates and chemical cues to regulate cellular adhesion *in vitro* has become a common practice in the field of biophysics. In this thesis, PEGylated substrates, glass surfaces, and fibronectin-coated supports were used to promote, respectively, highly reduced, weak, and strong cellular adhesion, thus mimicking the complexity of three stages within the adhesion process. Additionally, cells cultured on glass were also exposed to soluble RGD (Fig. 5.1), which led to cortical properties that fell between those of weakly adherent cells, thus on glass, and those with strongly reduced adhesion, hence on PEG (Table 5.1). The use of soluble RGD at concentrations close to 1 mM has been shown to extensively prevent cellular adhesion [170], whereas higher concentrations of 2 mM have completely prevented it [171]. Accordingly, results upon RGD addition showed an increased reduction of cellular adhesion with respect to cells on glass.

Based on the influence of the culture surface, results indicate that upon establishing the first interactions with the substrate (transition from PEG to glass in Fig. 5.1), fibroblasts underwent a significant relaxation of the cortical prestress and a decrease in fluidity. Upon spreading (glass to fibronectin in Fig. 5.1), the cortex stiffened up considerably but fluidity was maintained. Throughout the process, K_A consistently increased with the adhesion strength.

In order to understand these adaptations, it is important to consider that in spreading fibroblasts, membrane surface can increase up to 80 % with the doubling of the cell-substrate contact area [172]. Such a substantial change demands a stringent regulation of the cellular architecture in order to avoid the rupture of the plasma membrane: in the absence of reservoirs and depending on its composition, membrane integrity cannot be maintained beyond ∼3-5 % dilation of its initial area [173].

The plasma membrane is known to be linked to the actomyosin cortex through several proteins including ezrin, radixin and moesin (ERM), and myosin-I motors [10, 11]. These tethers determine the membrane-to-cortex distance to the scale of single actin nucleators, which also provides control over formin activity [174]. Accordingly, an active interplay can be expected between the membrane and the actomyosin cortex. In fact, rather than a passive physical scaffold hosting actin polymerization, the membrane may act as an effective regulator of cell spreading: lateral protrusions are reversely sacrificed for the directional stretching of epithelial cells [175]; moreover, reduction of membrane tension, disruption of the actomyosin cortex, or loss of its molecular linkers to the cell membrane promote formation of lamellipodia and blebs [176, 177].

Physically describing this interplay, the cortical prestress (T_0) encapsulates cortical (T_c) and membrane (T_t) tensions according to:

$$T_0 = T_c + T_t \tag{5.1}$$

At the same time, T_t arises from in-plane tension due to membrane inextensibility, and from the tension generated by the membrane-cortex attachment sites. Using AFM-based tether pulling experiments, Pietuch and Janshoff [178] described the cortical adaptations of spreading epithelial MDCK II cells through the characterisation of T_c, T_t and the apparent area compressibility modulus ($\tilde{K}_A$). In contrast to the area compressibility modulus (K_A) used in this thesis, $\tilde{K}_A$ accounts for wrinkles and membrane folds that constitute a *real* surface area larger than the geometrical one.

For MDCK II cells it was thus found that upon initial contact with the substrate, cells remained very round and presented high stiffness. Immediately after (next 5-10 min), T_c, T_t and $\tilde{K}_A$ showed a decrease. Simultaneously, the membrane protrusions that would establish the initial substrate adhesion area were formed as a mechanism to restore T_0 upon the increase in available membrane (drop in T_t and $\tilde{K}_A$); at the same time, imaging of the basal cellular membrane showed disruption of the F-actin organisation, which facilitated the re-organisation and expansion of the cell. With increasing spreading, membrane reservoirs within the cell were consumed, thus leading to an increase and stabilisation, upon depletion, of $\tilde{K}_A$. At the same time, formation of stress fibers reinforcing a stable adhesion led to an increase in T_c and T_t [178].

When comparing these literature results, relevant for non-migratory epithelial states, to the observations reported in this thesis for WT fibroblasts, several parallels were found. Figure 5.1 shows that with increasing adhesion strength, T_0 underwent a significant drop followed by a strong increase, hence reflecting the same trend observed on MDCK II cells. Interestingly, while epithelial cultures showed a higher cortical tension after complete adhesion, prestress in fibroblasts was higher when the cells remained rounded upon the first contact with the substrate. Accordingly, strongly adherent fibroblasts could preserve higher adaptability in the cortical response than epithelial cells. Changes in β through the adhesion process showed a trend similar to T_0: upon initial adhesion, a significant decrease in fluidity was followed by an increase during cellular spreading. Even though at the final adhesion stage β was significantly lower than for cells on PEG, the fluidisation observed in the transition from weak to strong adhesion has also been recognised on MDCK II cells, in which the process has been identified as a possible mechanism to allow extensive cytoskeletal re-organisation and expansion while avoiding membrane rupture during lateral stretching [179].

Regarding K_A, a progressive rise in the resistance to increase the surface of fibroblasts was detected with the adhesion strength. In the transition from weak to strong adhesion, intracellular membrane reservoirs are depleted [177, 178] while the actin architecture is re-organised with the enrichment of the cortex and the formation of stress fibers stemming from newly formed focal adhesions. The stabilisation of the spread cytoskeleton thus correlates to increased K_A values, as observed in figure 5.1.

Overall, results indicate that in suspension, fibroblasts simultaneously present a high prestress and fluidity, and low K_A values, which provide the cell with a cohesive shell to maintain a globular structure, while preserving its adaptability to interact with the surroundings and establish contacts with a surface in order to initiate the adhesion process. At this stage, the cellular prestress relaxes to allow the adaptation of the actin architecture to transition from a globular to a capped cell shape. Simultaneously, blebs and protrusions are form to establish a first contact area between the cell and the substrate. This requires the consumption of the membrane reservoirs in the form of wrinkles and folds, which causes a small increase in K_A and a decrease in fluidity. With progressing adhesion and spreading, thus transitioning from weak to strong adhesions, fibroblasts fluidise which, in agreement with bibliographic sources, allow cells to tolerate extensive cytoskeletal re-organisation and expansion [177, 178, 179]. Once the expansion of the cell-substrate contact area is complete, likely linked to the depletion of intracellular membrane reservoirs [177, 178], enrichment of the cortex and higher levels of actin architecture, such as stress fibers, are synthesised, thus causing a progressive increase of cortical prestress and K_A until stabilisation of the cytoskeleton is achieved by the fully adherent cell.

5.2.2 Influence of formin modulation on the actomyosin cortex

As active regulators of the polymerization of actin filaments, formins represent an important element in the maintenance and regulation of the cellular cortical properties. As shown in figure 5.4, the absence of any formin isoform had a direct impact in T_0, K_A and β. These results are reproduced in figure 5.5 and table 5.3, where the measurements performed by V. Scheller on weakly adherent cells presenting equivalent formin modulations are included.

Original results on WT and dKo weakly adherent cells have already been presented in several figures throughout this and the previous chapters. However, to ensure coherence within the category of weak adhesion in figure 5.5, the measurements performed by V. Scheller on WT and dKo fibroblasts are presented instead. These results were

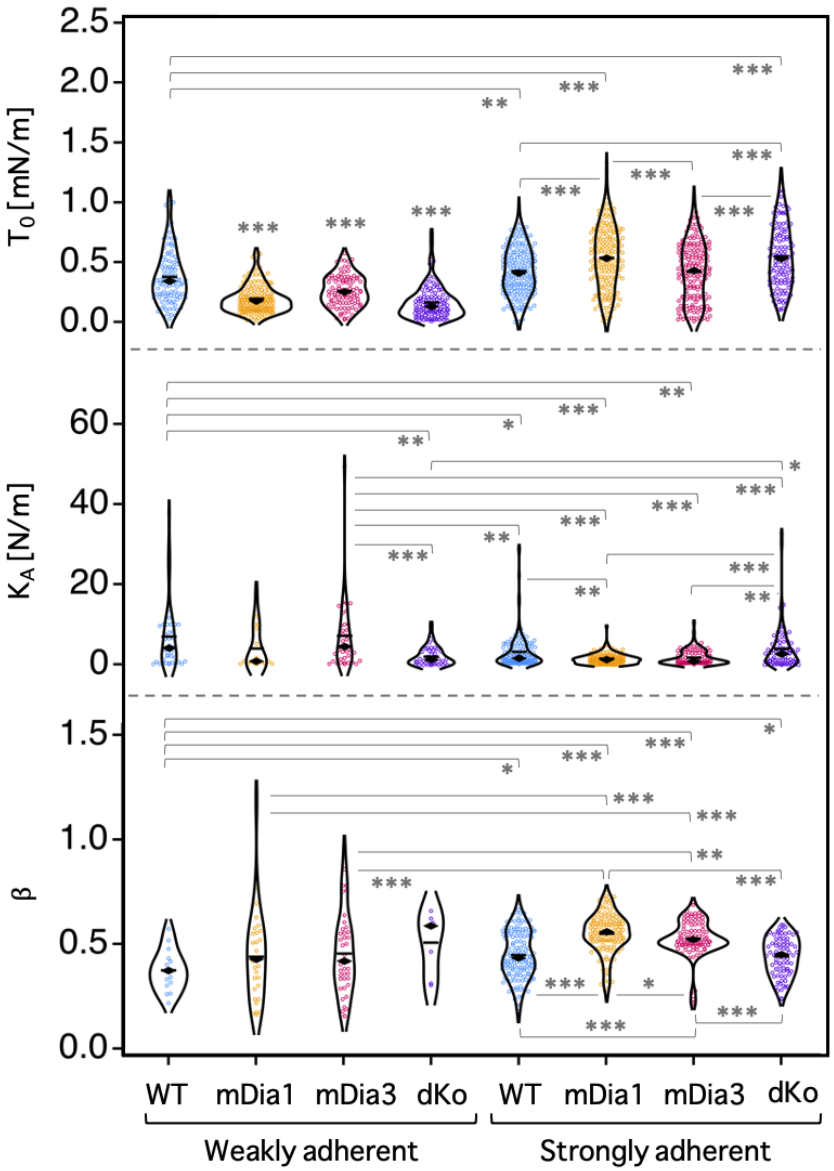

Figure 5.5: **Comparison of the cortical properties of weakly and strongly adherent cells with different formin modulations.** Through both degrees of cellular adhesion, cortical prestress increasingly deviates from WT behavior for mDia3, mDia1 and dKo cells. For weakly adherent cells, K_A follows the same trend, which results inverted in β. For adherent Fbs, fluidity increases for the single knock-outs, but not for dKo cells; the contrary is observed in K_A. Measurements on weakly adherent cells are provided by V. Scheller. Significance is denoted with [*] for $\alpha < 0.05$, [**] for $\alpha < 0.01$, and [***] for $\alpha < 0.001$; T_0 distributions of weakly adherent knock-out lines show statistically significant differences with all other categories corresponding to [***]. Mean and median are respectively indicated with **-** and ◆. For weakly adherent cells and in order of T_0, K_A and β: $n_{WT} = 104, 40, 15$; $n_{mDia1} = 171, 18, 30$; $n_{mDia3} = 96, 40, 42$; $n_{dKo} = 109, 42, 8$. For strongly adherent cells: $n_{WT} = 140$; $n_{mDia1} = 138$; $n_{mDia3} = 99$; $n_{dKo} = 80$.

also evaluated following a fitting routine preceding the ones employed in this thesis, but despite small variations, no major differences were found between the two sets of measurements. In agreement with figure 5.1 and albeit the wide distributions within experimental categories, a significant increase in cortical tension is observed between weak and strong adhesion.

Table 5.3: **Cortical parameters of weakly and strongly adherent cells with different formin modulations**. The mean and SD values of the distributions in the violin plots of Fig. 5.5 are indicated.

Cells		T_0 [mN/m]	K_A [N/m]	β
Weak	WT	0.377 ± 0.224	6.92 ± 8.60	0.373 ± 0.099
	mDia1	0.198 ± 0.115	3.91 ± 5.46	0.436 ± 0.217
	mDia3	0.257 ± 0.130	9.04 ± 15.0	0.451 ± 0.197
	dKo	0.158 ± 0.135	2.15 ± 2.31	0.504 ± 0.149
Strong	WT	0.429 ± 0.200	4.05 ± 8.08	0.446 ± 0.115
	mDia1	0.532 ± 0.262	1.51 ± 1.37	0.546 ± 0.099
	mDia3	0.450 ± 0.428	1.92 ± 1.87	0.523 ± 0.089
	dKo	0.559 ± 0.265	4.09 ± 5.55	0.438 ± 0.092

Within weakly adherent cells, the lack of any of the formins studied led to an increase in fluidity. While for single knock-out lines the increase was comparable, it was still lower than the increase observed for dKo fibroblasts. In contrast, cortical prestress and K_A presented a similar trend in which the biggest change with respect to WT behavior was given for dKo fibroblasts followed by mDia1. Accordingly, mDia3 cells showed the closest behavior to WT fibroblasts. Such trend, though mirrored, was also observed regarding cortical prestress on adherent cells since formin modulations led to higher values than for WT cells. On the other hand, while cellular fluidity increased for the single knock-outs, fluidity of dKo cells remained close to that of WT cells; K_A followed the reverse trend.

The properties of the actomyosin cortex thus resulted mostly impaired in the absence of mDia1, either as single knock-out or, even more significantly, as dKo, hence underlining the isoform's essential role in cortical maintenance and regulation. Even though a more extended discussion on the mDia1 and mDia3 functions will be provided in chapter 8, results on weakly adherent cells indicate that the absence of formins led to structurally deficient cortices that rendered the cells vulnerable to external deformation. Therefore, it could be expected that for strongly adherent fibroblasts, cortical deficiencies would be similarly reflected. Instead, results indicate that the prestress of strongly adherent cells was higher in the absence of formins.

Despite the clear impact that formin-nucleated actin filaments have in the rheological properties of the cortex, they constitute as little as 10 % of the total amount of fibers [180]. In the resulting mesh, isotropic and anisotropic regions coexist, simultaneously presenting both aligned and randomly oriented actin bundles [181]. Since myosin II motors move towards the plus end of actin filaments [182], the orientation of the actin mesh provides a balance between cortical contraction and relaxation.

In the absence of formins which, together with the Arp2/3 complex nucleate the bulk of the actin filaments, the cortical network consists mostly of branched structures [183]. Experimental simulations have shown than in such networks, the relaxation times are slower than for meshes rich in long (formin-nucleated) filaments due to the confinement of myosins between branches [184]. Accordingly, it is possible that in the absence of mDia1 and mDia3, a higher prestress is detected on strongly adherent fibroblasts due to the lack of long actin filaments relieving the contraction of branched structures. Furthermore, mDia1 and mDia3 are known to show compensatory activity in the lack of one or the other [16]. It is thus conceivable that in an adherent state, their absence triggers alternative mechanisms of actin polymerisation and contraction, beyond the involvement of the Arp2/3 complex, that reinforce the generation of a high prestress.

Experimentally, due the defective cortices of strongly adherent cell lines presenting formin knock-outs, higher prestress could also be measured due to the unforeseen contribution of cellular organelles. During the characterisation of the actomyosin cortex of weakly adherent fibroblasts, the AFM cantilever approaches the round cell from atop, which leads to a parallel plate-like compression. On strongly adherent cells, which show a capped or *fried egg* shape, the cantilever is instead directed to the area delimited between the cellular periphery and the nucleus, as this guarantees that the force sensed by the AFM is contributed by the cortex and not by the substrate or the nucleus itself. However, as shown in figure 5.6, knock-out fibroblasts present very flattened bodies with widespread morphologies. Accordingly, since there is no smooth transition between the nuclear area and the cellular lamellipodia, the identification of the optimal region for the acquisition of the force curves can result challenging. Furthermore, dKo cells show the spontaneous formation of transcellular macroapertures (TMs), which consist in tunnels traversing the cellular body and connecting the apical and dorsal membranes (Fig. 5.6); based on empirical observations, their formation is promoted by the stress generated during compression-relaxation measurements.

Due to this challenges, and favoring a compromise to ensure coherence between the measurements performed on strongly adherent WT, mDia1, mDia3 and dKo cells, the

force measurements were performed by directing the AFM cantilever towards the central region of the cell as shown in the schematics of figure 5.6. The cellular nucleus is highly anisotropic and presents a wide interval of Young's moduli in the order of 0.1 to 10^3 Pa [185], thus in the range of the modulus of actomyosin cortices as determined by the Hertz model (Fig. 4.2). Accordingly, due to defective cortices and to the experimental methodology, the prestress values measured on strongly adherent knock-out cell lines could present the rheological contributions of the cellular nuclei.

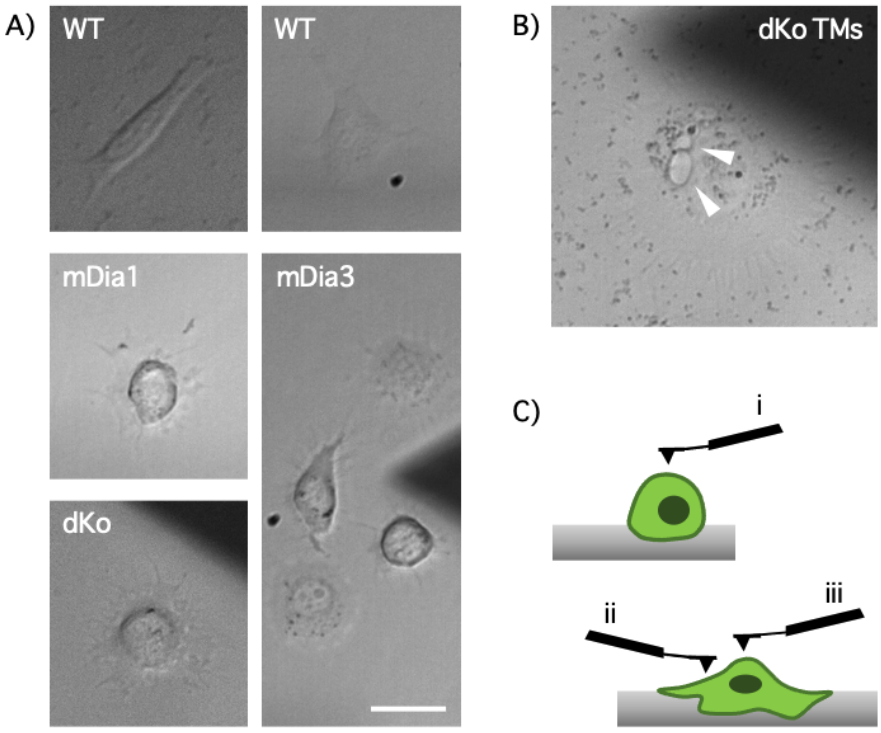

Figure 5.6: **Imaging and cantilever directionality during AFM measurements. A)** Bright field imaging of strongly adherent WT, mDia1, mDia3 and dKo Fbs on fibronectin-coated substrates. Images are not modified to reflect original experimental conditions: upon adhesion, knock-out Fbs flatten against the surface, often hampering their localisation. While mDia1 and dKo cells generally show a *fried egg* shape, mDia3 Fbs present larger morphological variability, sometimes retaining a polarised-like disposition. WT fibroblasts present elongated bodies, but are typically polarised with a spindle-like shape (right panel). **B)** Transcellular macroapertures on dKo Fbs (triangles). These tunnels are dynamic and are spontaneously formed and closed, albeit their appearance is seemingly promoted by the stress induced during probing. Scale bar of micrographs: 50 µm. **C)** Schematics reflecting the cantilever's approach towards the cell; albeit tipless cantilevers were experimentally used, they are schematised with a tip to better illustrate the cell-cantilever contact region. Round cells are approached from the top (i); to determine the cortical rheology on adherent cells, the cantilever should be directed to the region between cellular nucleus and lamellipodia (ii). Do to the morphology of adherent knock-out cells, consistency between measurements is achieved by probing the cells closer to the central region of the cell (iii).

5.2.3 Cortical properties upon SMIFH2-based formin inhibition

The use of SMIFH2, a known formin-inhibitor, was used to compare its effect to the behavior of WT and dKo cells on PEGylated substrates. As shown in figure 5.2, upon exposure to SMIFH2, the cortical properties of WT cells changed drastically with a relaxation of the prestress, an increase in K_A and a decrease in fluidity. In comparison, dKo cells only presented a decrease in prestress with respect to non-treated WT cells, but to a comparable level to that caused by the presence of SMIFH2. The differences between the behaviour of dKo cells and WT cells exposed to SMIFH2 could come from the fact that the inhibitor has a broad scope of effect beyond mDia1 and mDia3 inhibition. However, as recently discovered, SMIFH2 is also able to inhibit the activity of several forms of myosin [186]. Therefore, it is plausible that, in agreement with Chan *et al.* [187], the effect of SMIFH2 may have led to a decrease in cellular fluidity via the inhibition of myosin II activity, thus masking the formin inhibition.

Conclusions

Upon contact with a surface, fibroblasts in suspension undergo a relaxation of the prestress to allow the transition to a capped cellular geometry. Simultaneously, blebs and protrusions are formed, which establish a first contact area with the substrate. At this point, the cell fluidises to sustain the expansion of the cell membrane. Once the cellular spreading is complete, enrichment of the cortex and formation of stress fibers causes a progressive increase of the cortical prestress and K_A until stabilisation of the cytoskeleton is achieved by the fully adherent cell.

For mDia3, mDia1 and dKo cells, increasing defects in the architecture of the actomyosin cortex lead, in a weakly adherent state, to higher susceptibility to external deformation. For adherent fibroblasts, these defects are maintained. However, a prestress higher than that observed on WT cells is measured. In the absence of long actin filaments nucleated by formins, which provide a fine balance between compression and relaxation of the cortex, highly contracted branched actin filaments could lead to the high T_0 values measured. Furthermore, due to the widespread and planar morphology of knock-out fibroblasts and the resulting methodological adaptations in the acquisition of force-curves, prestress could include the rheological contributions of cellular organelles. In this case, the contribution would be larger with increasingly defective cortices, thus progressively higher for mDia3, mDia1 and dKo cells. The use of SMIH2, while it causes low prestress similar to that observed for dKo cells, also induces a decrease in fluidity, which could be caused by the off-scope inhibition of myosin II motor activity.

Chapter 6

Relevance of formins in wound healing

Until now, the focus of the research laid on the characterisation of the dynamics and regulation of the actomyosin cortex as a function of the degree of cell adhesion, and in relation to the role of mDia1 and mDia3.

In this chapter, the influence of the formins is analysed in regard to the collective kinetics of fibroblasts in the wound closure process. To this purpose, the WT and dKo cell lines are monitored during recovery upon injury using the Electric Cell-Substrate Impedance Sensing (ECIS) setup. Furthermore, results are compared to the effect of the general formin inhibitor SMIFH2, and to the behavior of single mDia1 and mDia3 knock-outs. The time resolved frequency spectra acquired with the ECIS are analysed based on the model developed by Lo & Ferrier in order to characterise the properties of the cell layer; micromotions resulting from the height fluctuations of the cellular basal membranes, which provide an indicator of cell vitality, are moreover studied. Finally, fluorescence microscopy is employed to correlate the findings with the morphological and phenotypical adaptations of the fibroblast cultures.

6.1 Results

6.1.1 FMT progression upon impedance-based wounding

The ECIS is a well-established and label-free technique that allows the real-time study of cellular dynamics based on the impedance spectra that the passive electrical properties of cells generate upon exposure to an electric field. In this chapter, the following methodology was employed to access the collective kinetics of fibroblast cultures during

recovery: when a fibroblast monolayer was formed 24 h upon cell seeding, a high amplitude and frequency electric pulse was applied in order to create a wound circumscribed to the surface of the working electrode embedded in the cultureware. Recovery was then monitored until impedance values returned at least to pre-wounding levels.

Upon wounding, certain physicochemical cues such as alterations of the ECM or the release of cytokines like TGF-β induce the fibroblast-to-myofibroblast (FMT) transition, which involves a phenotypical adaptation by which fibroblasts transiently become more mobile, express contractile cytoskeletal components such as α-SMA and, at longer time scales, produce cell-cell contacts. In order to confirm that the FMT took place after causing an impedance-based wound on fibroblasts monolayers, the presence of the adherent junction protein connexin-43 (Cx43) and α-SMA was assessed via immunofluorescence assays at relevant time points: before wounding, and at 24 and 48 h of recovery.

As shown in figure 6.1, in the pre-wounding stage (PW), expression of Cx43 was low and unspecific, mainly located close to the cell nucleus where it circulated between the endoplasmic reticulum and the Golgi apparatus as part of its synthesis process. However, already at the PW stage it was also visible between adjacent cells, albeit at low level, where gap junctions had been formed. During recovery, both the concentration and intercellular expression of Cx43 increased progressively in time. The same was observed for α-SMA which, although it could be already detected in the PW stage, both its expression and organisation in fibrillar structures became increased and ubiquitous throughout the re-colonised area as recovery advanced. The time-dependent increase of both markers was indicative of a progressing FMT. Nuclear staining showed occasional multilayer formation 48 h post-wounding, and increased cell density.

6.1.2 Recovery kinetics of WT and dKo fibroblasts upon impedance-based wounding

Impedance spectra were initially acquired on WT and dKo cells cultured on 250 µm wide electrodes. Figure 6.2 shows the averaged real part of the impedance time courses obtained following the ECIS-based methodology described above for both cell types.

As shown, WT fibroblasts recovered pre-wounding impedance values within the first 24 h of recovery, showing thereafter an overshoot that seemingly stabilised around 48 h after wounding (time = 70-80 h in Fig. 6.2). In contrast, fibroblasts with the double formin knock-out presented a significant delay. Upon applying a sigmoidal fit to the recovery interval of the real part of the impedance, the recovery half time $t_{1/2}$ of dKo cells indicated that recovery was delayed approximately 13 h with respect to WT cells: $t_{1/2}$(WT) = 15.07 h ± 4.56 and $t_{1/2}$(dKo) = 28.53 h ± 14.95.

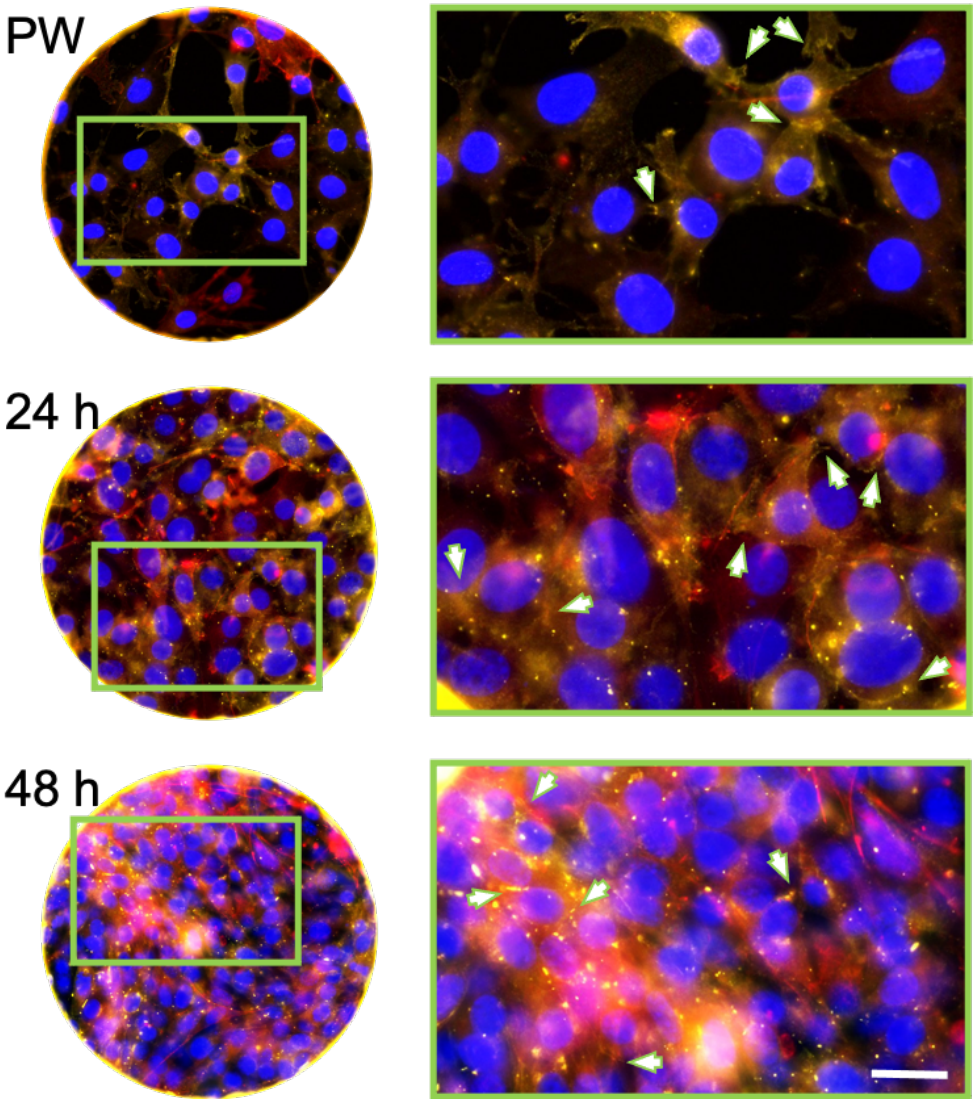

Figure 6.1: **FMT progression during wound recovery.** Micrographs showcase the expression of Cx43 (yellow) and α-SMA (red) in WT cells (nuclei in blue), spanning from a pre-wounding stage (PW) to 24 and 48 h of recovery. Left micrographs display the integral electrode surface (250 µm in diameter); green frames correspond to the magnifications on the left (scale: 25 µm). In the pre-wounding stage, Cx43 is mostly diffuse around the cell nucleus as it is synthesised but, as arrows indicate, it is also present between cells where gap junctions have been formed randomly at low level. During recovery, Cx43 is increasingly expressed and found between cells (arrows). Similarly, α-SMA expression progressively increases during recovery, for which the formation of fibrillar structures is also increasingly observed. Nuclear staining indicates that upon recovery, the cell layer has higher cell density and the size of the nucleus decreases. Occasional cell multilayer is also observed with overlapping nuclei.

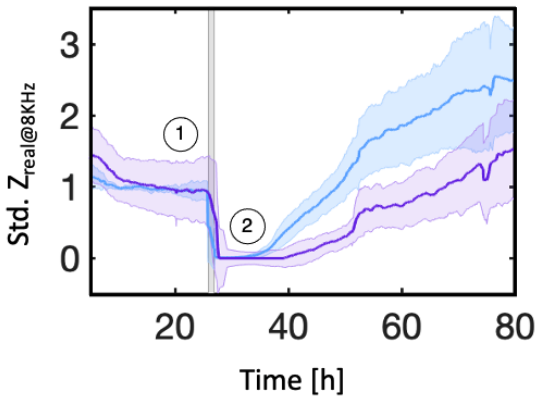

Figure 6.2: **Recovery time course of wounded WT and dKo fibroblasts.** The averaged real part of the impedance, acquired at the optimal frequency of 8 KHz, is standardised between the impedance values of the pre-wounded monolayer (1) and the cell-free electrode after wounding (2). Mean values (solid line) and standard deviations obtained from the averaging of 6 and 8 impedance courses gathered on 3 independent experiments are respectively presented for WT cells (■) and dKo fibroblasts (■). After monolayer formation, a high intensity and frequency pulse (1.8 mA at 10 kHz for 2 min) is applied in order to create a wound (grey area), upon which cells are allowed to repopulate the electrode and thus recover. DKo fibroblasts present a slower recovery, reaching pre-wounding values with a delay of approximately 13 h compared to WT fibroblasts.

In order to relate the recovery of impedance values to the actual cell-coverage of the electrode upon wounding, fluorescence micrographs were obtained during the first 24 h of recovery. Figure 6.3 depicts this process for WT fibroblasts by showcasing their intracellular distribution of actin filaments and myosin.

In the healthy and intact monolayer, actin filaments were clearly visible at the cellular peripheries, though a number of thinner filaments could also be seen forming mesh-like arrangements throughout the cellular bodies. Myosin was expressed at low basal levels and was diffusely distributed within the cells; dot-like aggregations were also associated to the nuclei. Right after wounding, a gap constrained to the surface of the working electrode (250 µm in diameter) and devoid of cells was observed, thus highlighting the efficiency of the impedance-based wounding process. Upon injury, the levels of myosin were immediately increased at the periphery of the wound and thin filaments became visible, often co-localised to the actin filaments. Within the first 6 h of recovery, a number of fibroblasts began the re-colonisation of the electrode with no apparent leading front or collective arrangement. Migration of individual cells progressed simultaneously with highly polarised and elongated bodies, and by transversely advancing from the wound periphery. In these cells, long myosin filaments could be seen along the polarised cellular body, thus parallel to the direction of migration. In com-

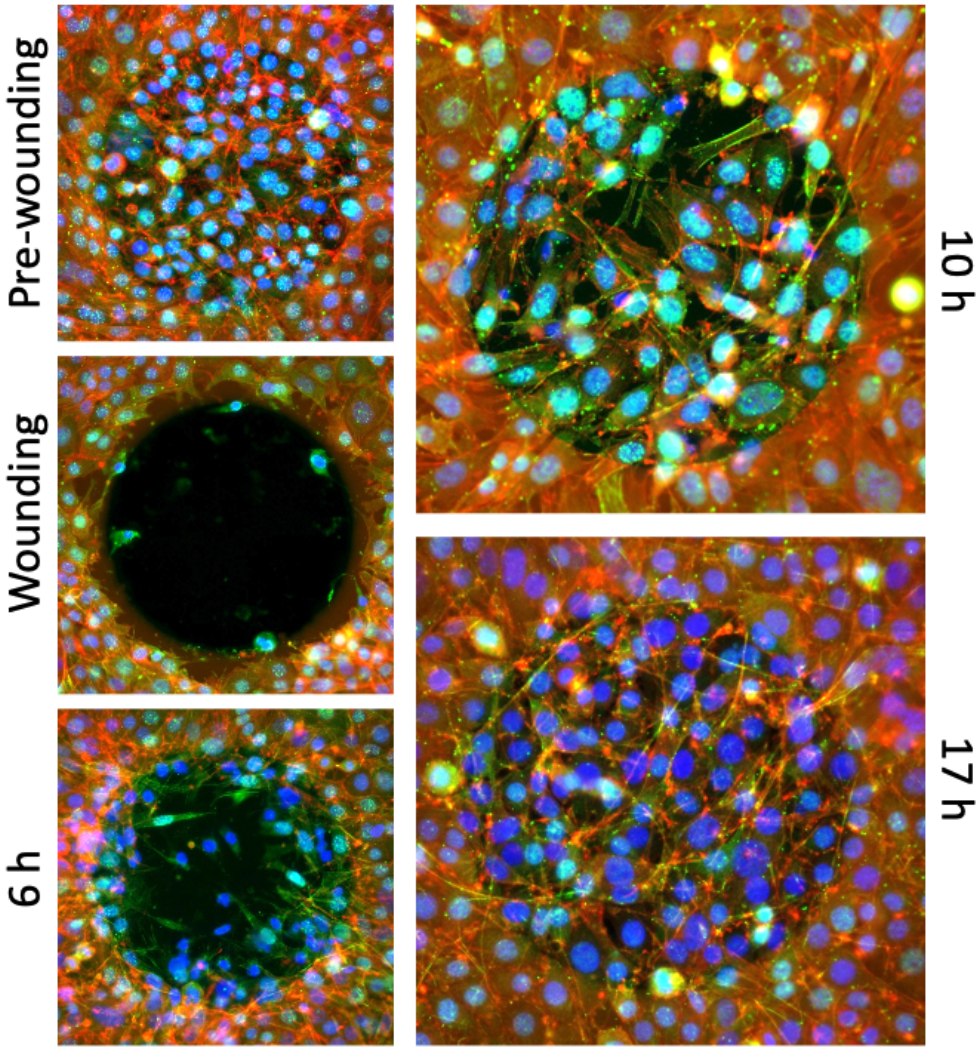

Figure 6.3: **Actomyosin distribution in WT cells during gap closure.** Micrographs showcase actin filaments (red) and myosin (green) distribution in WT cells (nuclei in blue) at different time points of the wounding and recovery process. Upon formation of a monolayer (pre-wounding) actin filaments are abundant at the cell periphery. Right after causing an impedance-based wound (time = 0h), the area delimited by the electrode surface (250 µm in diameter) is depleted from cells, which then start re-colonisation. 6 and 10 h after wounding, myosin is expressed in large amounts and myosin fibers are visible; actin is mostly located at the nascent adhesions and leading edge of advancing cells. After 17 h, the electrode surface is completely repopulated; myosin expression decreases and actin filaments, still highly concentrated in the growing adhesions points, become more common at the cell periphery.

parison, while actin filaments remained visible mostly at the cellular periphery, several discrete and dense actin aggregations appeared where cell-substrate adhesions were being formed. This distribution was also observed at the 10 h time point, when almost all the electrode surface was re-populated. Here, the number of actin focal points was increased and presented higher incidence closer to the areas of the electrode that remained depleted. After 17 h, the electrode was virtually re-colonised and the actin focal points became larger. In many cases filaments that followed the perimeter of the cellular body were also observed. Myosin concentration was decreased compared to the 6 and 10 h micrographs, but remained present in the form of filaments that often co-localised to the actin arrangements. Upon recovery, and in contrast with the pre-wounding monolayer, cellular overlapping could be occasionally detected.

The same analysis was applied to dKo cells in figure 6.4, where direct comparison is also established with the recovery of WT cells depicted in figure 6.3. Already in the pre-wounding stage, WT and dKo cells showed clear morphological differences: dKo fibroblasts spread over larger areas and formed less densely packed monolayers with gaps between neighbouring cells. In the cell-cell contacts between these gaps, actin aggregations were observed. Besides this, actin filaments were also present at the cellular periphery or as filamentous meshes throughout the cellular body. As in WT fibroblasts, myosin was expressed at low basal levels and appeared associated to the cellular nuclei. Upon wounding, dKo cells initiated the re-colonisation of the electrode by migrating towards the depleted surface with no clear leading cells or collective organisation. Similarly to WT fibroblasts, dKo cells became elongated. However, dKo cells showed a less predominant direction of polarisation with respect to the wound edge, and remained widespread. In this state, dense myosin fibers could be seen throughout the cellular bodies following two distinguishable organisations: fibers were either specially dense, straight and parallel, or thinner and following the curvature of the cellular morphology. Small intracellular voids within the actomyosin mesh were visible in some of the cells falling in the second category. Overall, and comparing both recovery time points, dKo cells presented a clear delay in the re-colonisation of the depleted electrode.

Regarding the voids observed in the cytoskeletal organisation of some dKo fibroblasts, these could reflect the formation of transcellular macroapertures (TMs). As described and shown in figure 5.6 of chapter 5, TMs consist in the spontaneous formation of tunnels connecting the dorsal and basal cellular membranes. Figure 6.5 highlights the appearance of these voids in a low density dKo cellular layer, where multinucleated fibroblasts and the widespread morphology characteristic of dKo cells can also be observed.

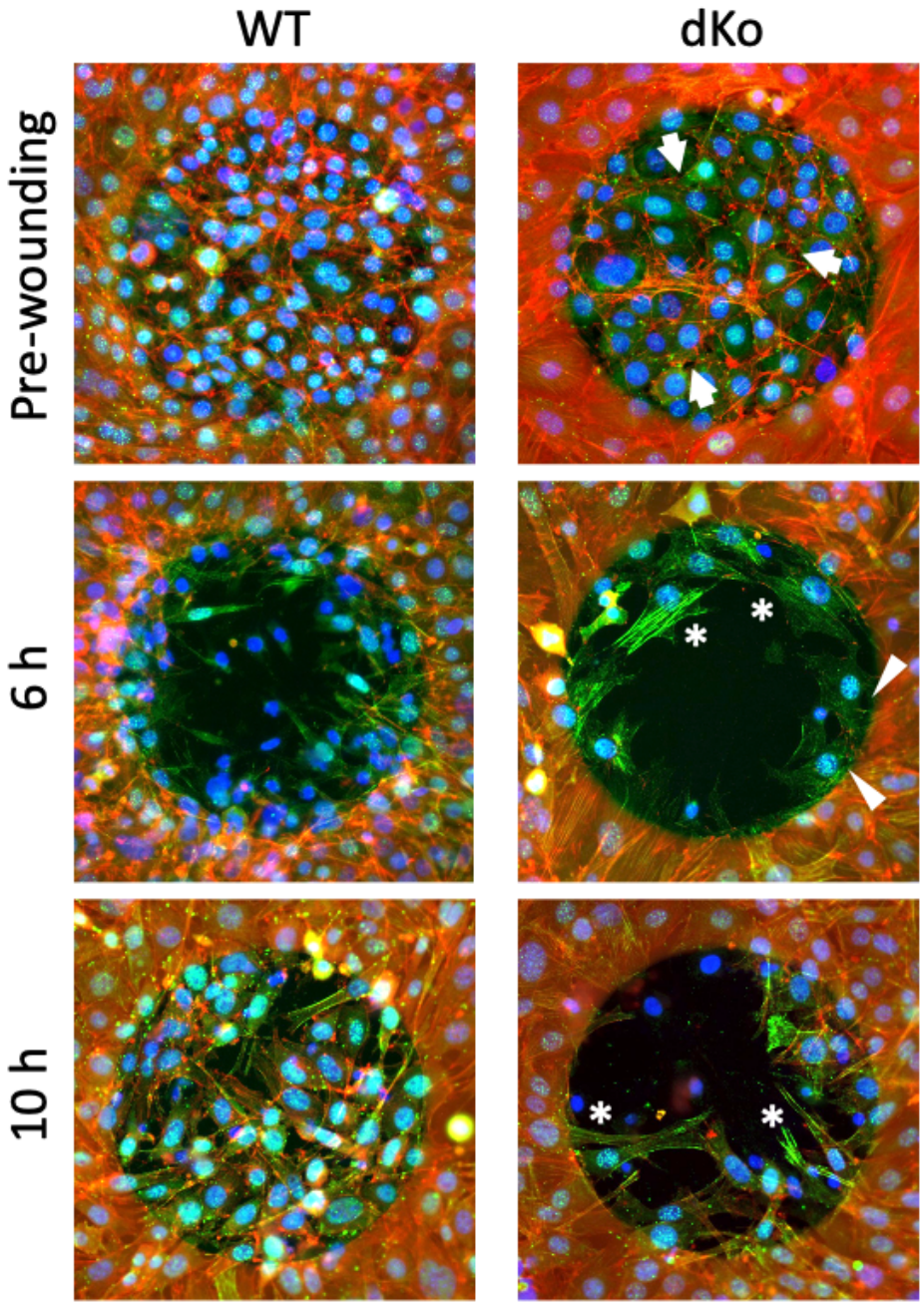

Figure 6.4: **Comparison of actomyosin distribution between WT and dKo cells during gap closure.** WT and dKo cells form distinct monolayers: dKo fibroblasts spread over larger areas and present gaps (arrows) between adjacent cells. During recovery, dKo cells show large and thick myosin fibers throughout the cellular body (asterisks) and, in some cases, gaps (triangles) in the fibrous cytoskeletal mesh. Upon wounding, both cell lines re-populate the gap via crawling in a direction perpendicular to its periphery, process in which dKo fibroblasts present a migratory delay with respect to WT fibroblasts. Staining: actin filaments (red), myosin (green) and nuclei (blue). Wound gap: 250 µm.

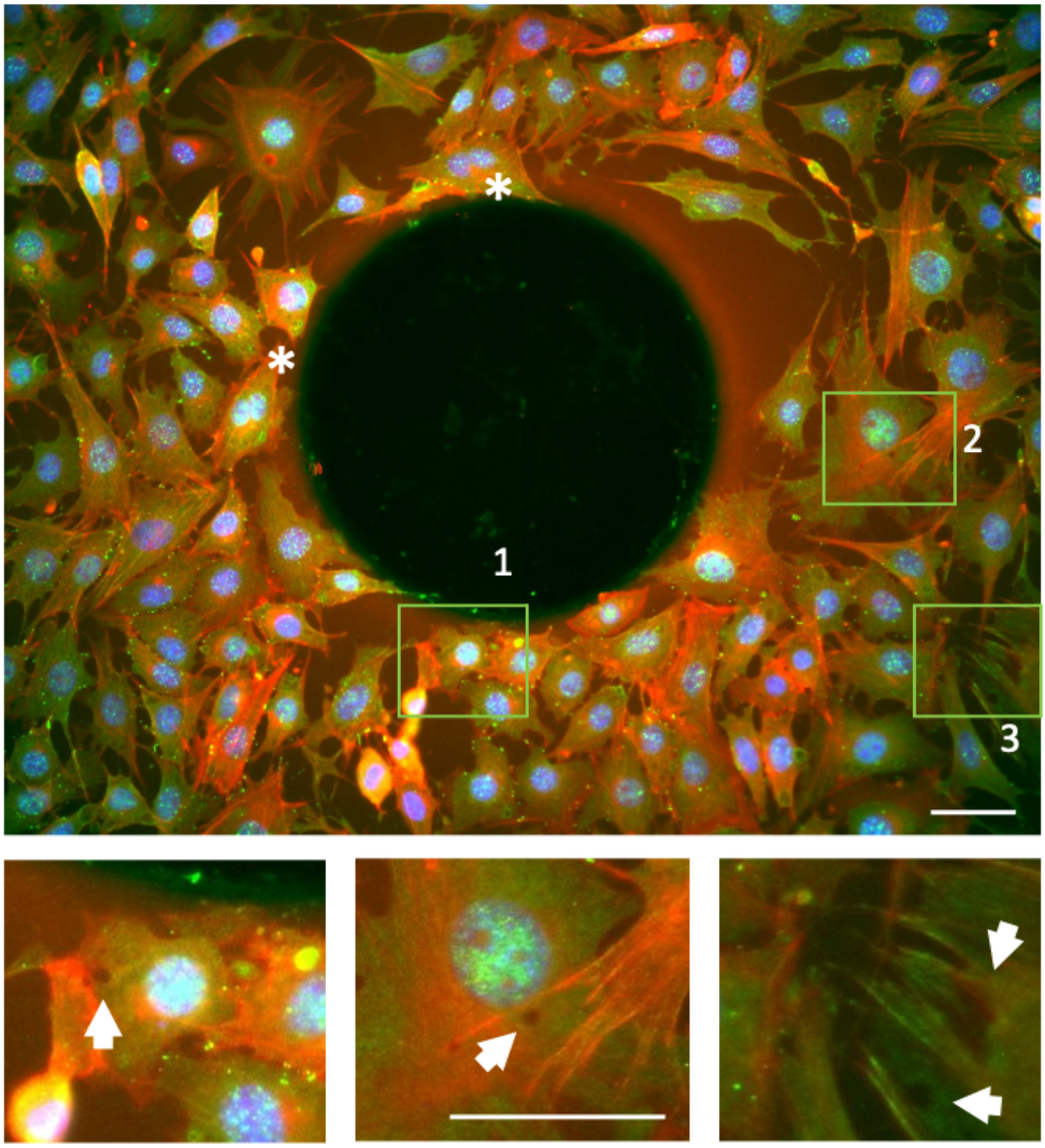

Figure 6.5: **Detection of transcellular macroapertures in immunofluorescently labelled dKo cells.** The distributions of actin filaments (red), myosin (green) and nuclei (blue) are indicated in a low seeding density dKo layer. Magnifications (corresponding from left to right to sections 1 to 3) highlight voids (arrows) in the actomyosin organisation of several cells. Inlet 1 (left) shows a small TM adjacent to two nascent voids. As shown in inlets 2 and 3, TMs can appear in different regions within the cellular body. Nascent voids are predominantly circular; as they grow in size, the regularity in the perimeter is lost (top arrow in inlet 3). Asterisks indicate multinucleated cells. Scale bars: 50 µm.

6.1.3 Recovery of layer integrity upon wounding of WT and dKo fibroblasts

To better understand the effect that the passive electrical properties of the cells caused on the time-resolved frequency spectra, these were analysed applying the Lo and Ferrier model [25]. This model describes the system using an equivalent electric circuit with specific parameters that relate to physiological elements and that can be quantified, namely: cell-cell connectivity, reflected by R_b; membrane capacitance, C_m, related to cell surface rigidity and membrane lipid composition; and cell-substrate distance, inversely proportional to α. The evolution of these parameters for control and wounded WT and dKo cultures is collected in figure 6.6. For simplicity, the pre-wounding (PW) values corresponding to the intact monolayers (24 h after cell seeding) are pooled together for the wounded and non-wounded categories since they represent the same experimental condition and are statistically equivalent. This is done, separately, both for WT and dKo fibroblasts. Furthermore, figure 6.6 only shows statistical significances between experimental categories obtained on the same cell line; the complete statistical comparison is shown in figures 1 and 2 of the supplementary information (SI; page 193).

The junctional resistance R_b represents cell-cell connectivity and, accordingly, is a measure for the expression of proteins restricting the ion flow through the intercellular cleft. As such, it reflects tight junctions and, at a lesser extent, adherent and gap connections. In this model system, no tight junctions are expressed, and R_b thus reflects a combination of the latter two. For WT control fibroblasts, R_b values increased progressively throughout the duration of the experiment as a result of monolayer maturation and formation of cell-cell contacts. On wounded samples, a drop in the resistance was found after 24 h of recovery; after 48 h, R_b increased over PW levels indicating recovery, but remained lower than for control cells at the same time point, hence pointing at delayed cell layer maturation. The same pattern was observed for dKo fibroblasts, with the difference that for equivalent conditions, the R_b values of dKo fibroblasts were consistently higher than for WT cells and presented broader distributions, which could hint at a tight relation between formin activity and formation of adherent and gap junctions.

The plasma membrane acts as a capacitor by providing a dielectric interface between the extracellular space and the cytoplasm, two electrolytic media. As such, its capacitance C_m depends on the surface area, sensitive to surface rigidity and membrane ruffling, and on the membrane's dielectric properties, determined by membrane composition. Accordingly, it is relevant in the regulation of resting potentials and in cellular stimulation. Generally following the inverted behaviour of R_b, C_m values of control WT and dKo fibroblasts progressively decreased with time throughout the experiment. The

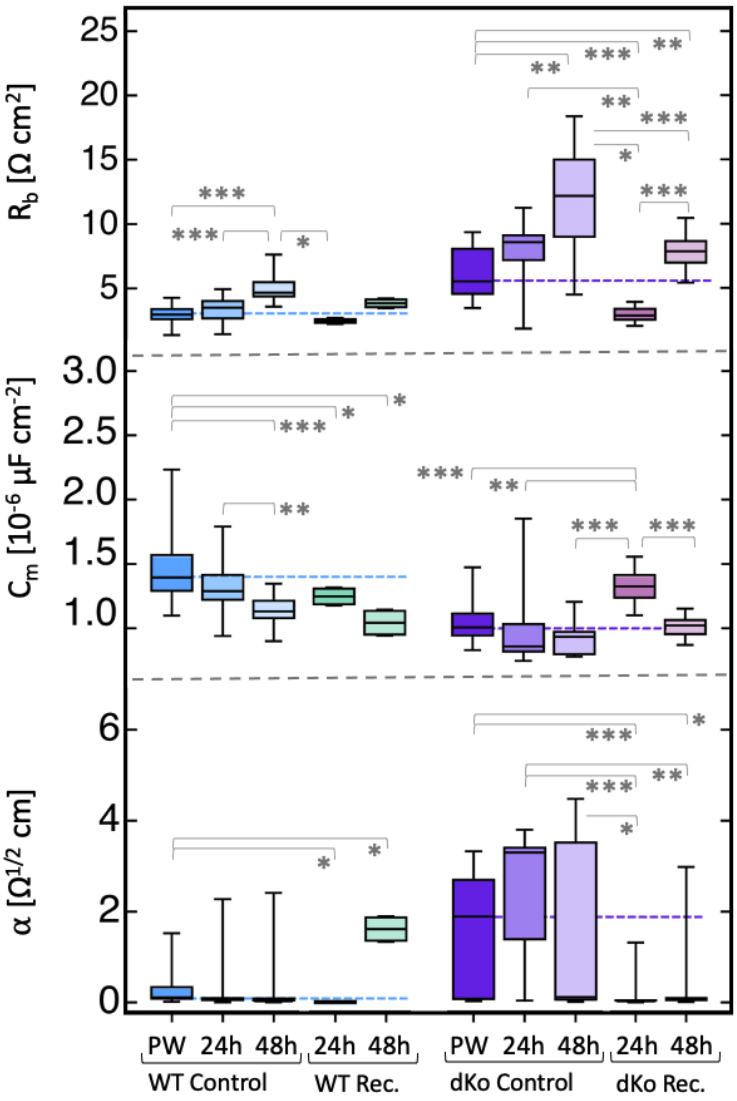

Figure 6.6: **Evolution of R_b, C_m and α of WT and dKo fibroblasts upon growth and recovery.** Parameters are obtained upon applying the Lo-Ferrier model to impedance time courses of control and wounded WT (■; n = 20, m = 14 and ■; n = 2, m = 2) and dKo cells (■; n = 7, m = 7 and ■; n = 33, m = 7). For control WT Fbs, R_b increases in time with respect to initial monolayer values (PW; dotted line). 24 h after wounding (t = 0 h), R_b is decreased and, 24 h later, PW values are recovered. DKo fibroblasts present the same pattern, but their characteristic R_b values are overall significantly higher than their equivalent WT categories. In control WT and dKo samples, C_m values decrease in time. Upon wounding, the same is observed for WT Fbs; in contrast, dKo present an increase in C_m that is later lowered to PW levels. Reflecting the inverted cell-substrate distance, α values present high variability. For control WT cells, α values decrease with time, whereas upon 48 h of recovery, are highly increased. In contrast, control dKo Fbs show high α values that result significantly decreased upon wounding. Significance denoted with [*] for $\alpha < 0.05$, [**] for $\alpha < 0.01$, and [***] for $\alpha < 0.001$.

same trend was observed for the wounded WT samples, with no statistical differences with respect to the corresponding control; in contrast, 24 h after wounding, C_m values of dKo fibroblasts were significantly increased when compared to PW values, which were re-gained upon 48 h of recovery. Accordingly, wounding caused a transitory increase in the capacitance of dKo cells. In general, this cell line also showed lower C_m values than WT cells, hence pointing at the involvement of mDia1 and mDia3 in the regulation of membrane roughness.

The height of the cleft between cells and substrate is inversely proportional to α which, upon applying the Lo-Ferrier model, can be retrieved from the time resolved impedance spectra acquired with the ECIS. In figure 6.6, a clear difference could be observed between the positive controls of WT and dKo cells: while the former presented narrow distributions, the high variability in dKo samples suggests the involvement of formins in the regulation of the cell-substrate distance. The medians of the distributions are detailed in table 6.1. As indicated, α decreased in time for WT control samples. Upon wounding, a significant drop was also observed; however, it was followed by a high increase in α by the 48 h time point, hence suggesting that cells lifted from the substrate during the first recovery stage to then approach it in a second wound-healing phase. Similarly, upon wounding dKo fibroblasts, α showed a significant decrease with respect to PW levels followed by a small increase. In this case, however, values remained significantly lower than PW levels, possibly indicating a delayed or impaired regulation of the cell-substrate distance in the absence of formins.

Table 6.1: **Comparison of α values in control and wounded samples of WT and dKo fibroblasts**. The table illustrates the median and mean absolute deviations of the α distributions (units of $\Omega^{1/2}$ cm) determined following the Lo-Ferrier model and presented in Fig. 6.6.

Category	α(PW)	α(24h)	α(48h)
WT ct.	0.114 ± 0.444	0.055 ± 0.523	0.030 ± 0.655
WT rec.	/	0.011 ± 0.003	1.62 ± 0.28
dKo ct.	1.89 ± 1.30	3.30 ± 1.33	0.121 ± 1.862
dKo rec.	/	0.030 ± 0.269	0.056 ± 0.996

Cellular micromotions in wound recovery

As a result of the metabolic activity, the ventral membranes of adherent cells undergo minuscule height fluctuations that mirror the activity of the living systems but that also enclose signatures of long-term correlations in motility. This biological noise, referred to

as micromotions, is readily monitored by the ECIS and can be analysed based on three parameters: α_{DFA}, *variance* and S_{PSD}. The evolution of the three factors is presented, for control and wounded samples of WT and dKo fibroblasts, in figure 6.7.

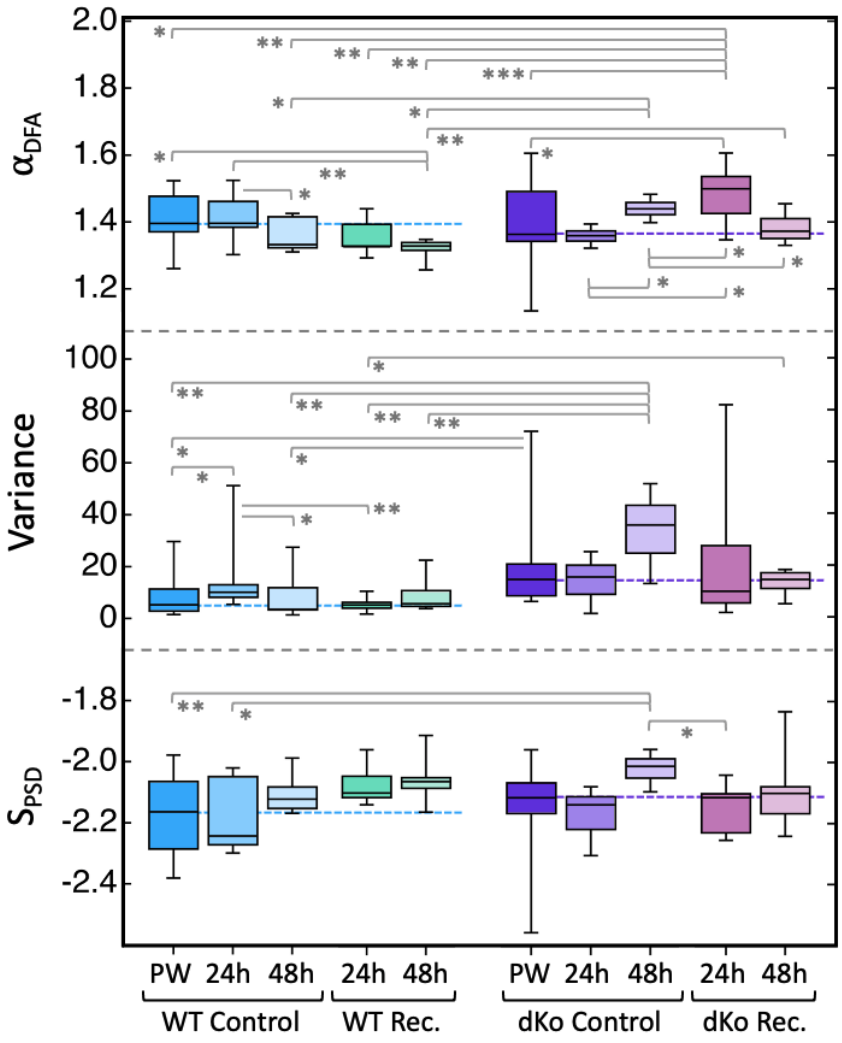

Figure 6.7: **Cellular micromotions of WT and dKo fibroblasts upon growth and recovery.** Values are presented for WT (■; n = 5, m = 5) and dKo (■; n = 3, m = 3) cells during wound closure and for their respective positive controls (■; n = 22, m = 6 and ■; n = 7, m = 5). Control WT and dKo samples show similar α_{DFA} and S_{PSD} values; *var* is higher for dKo, indicating increased number of fluctuations in the absence of formins. Upon wounding of WT Fbs, small variations are observed with a significant decrease in α_{DFA} by the 48 h time point accompanied by a decrease in $|S_{PSD}|$, hence suggesting lower metabolic activity in the reconstituted and densely populated cell layer. In contrast, wounded dKo cells show a significant peak in α_{DFA} in the 24 h stage, reflecting the active wound closure process. Significance denoted with [*] for $\alpha < 0.05$, [**] for $\alpha < 0.01$, and [***] for $\alpha < 0.001$.

The parameter a_{DFA} relates to the appearance of long-term memory effects within the micromotions which, in the context of time series, involve the presence of strong dependences between present and past values that are far removed in time, hence highlighting their correlation. Shape fluctuations in cytoskeletal reorganisations and adhesions are important factors in determining a_{DFA}. *Variance* (*var*) mirrors the magnitude of the basal membrane fluctuations, hence reflecting cellular dynamics [29]. Finally, S_{PSD} is characteristic of the type and source of the cues contributing to the micromotion signal; biological noise is characterised by a non-zero linear slope of $1/f$ with the frequency f, whereas Brownian motion follows a $1/f^2$ power law and white noise is independent of frequency [136].

In figure 6.7, WT and dKo control samples showed comparable a_{DFA} and S_{PSD}, but higher *var* for the latter, indicating that the lack of formins could lead to increased number of fluctuations in the cell-substrate cleft. For WT control cells, a decrease in a_{DFA} and in the absolute S_{PSD} values were observed by the third day of culture, possibly reflecting a decrease in cell activity driven by cell-cell contact inhibition in the densely populated monolayer. In contrast, for the same time interval, a_{DFA} and *var* of control dKo fibroblasts showed higher values with respect to the initial monolayer, hence indicating an increase in the number and magnitude of fluctuations that could also be affected by the increment in the height of the cell-substrate cleft. Upon wounding of WT fibroblasts, *var* remained comparable to the PW values while a_{DFA} and $|S_{PSD}|$ decreased, possibly indicating a fast reconstitution of cell layer integrity and reduced motility in the increasingly dense population. In contrast, for dKo cells, *var* and S_{PSD} remained similar to dKo control values and a_{DFA} increased significantly during the first 24 h of recovery to return to the PW level in the next 24 h interval, thus reflecting a decrease in micromotions upon gap closure. Overall, the sensitivity of the parameters describing micromotions increased, in order, from S_{PSD} to *var* and a_{DFA}.

6.1.4 Influence of formin inhibitor SMIFH2 on the properties of fibroblast cultures

In order to gain deeper understanding of the influence of formins in wound-healing dynamics, the general inhibitor SMIFH2 was employed. This drug targets formin homology 2 (FH2) domains, hence preventing formin-mediated actin nucleation and filament elongation. Accordingly, WT fibroblasts were exposed to 30-min pulses of SMIFH2 at different concentrations ranging from 1 to 66 µM. Thereafter, the drug was washed off and the cellular behaviour monitored for the following 48 h. Figure 6.8 shows R_b, C_m and α for WT control samples (already presented in figure 6.6), and for 24 and 48 h after

exposure to SMIFH2. For simplicity, pre-exposure (PE) values, hence corresponding to the intact cell layer 24 h after seeding, are only shown for control samples since they represent equivalent experimental conditions without statistical deviations.

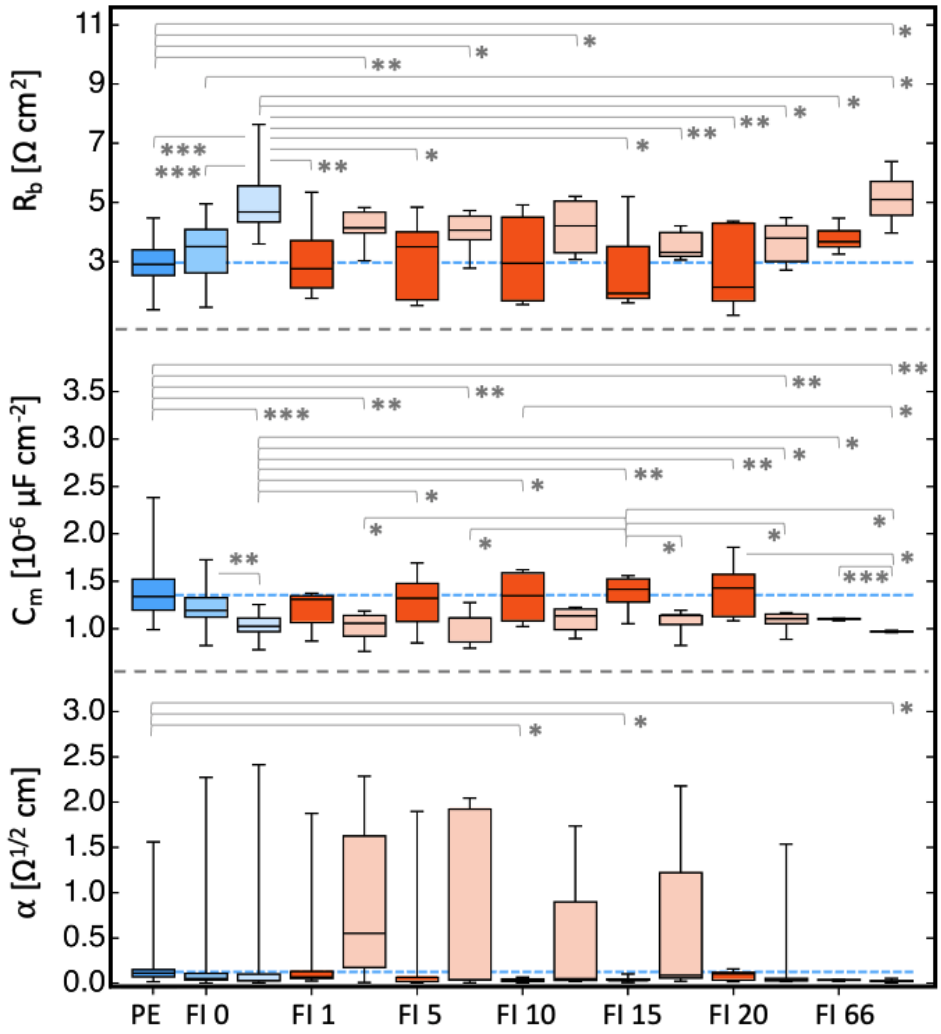

Figure 6.8: **Parameters derived from the Lo-Ferrier model upon exposure of WT cells to SMIFH2.** Values are presented for control samples (■; n = 20, m = 14) and cells exposed to different concentrations of the formin inhibitor (FI) SMIFH2 (indicated in µM; n ⩾ 3, m ⩾ 3). Pre-exposure (PE) values determine the properties of the initial monolayer (baseline indicated with dotted line) and provide a reference for control (FI 0) cells and samples exposed to SMIFH2. 24 h after exposure to the drug (■), R_b and C_m show, respectively, lower and higher values compared to control samples; after 48 h (■), exposed samples recover the behavior of control Fbs except for high SMIFH2 concentrations (⩾ 15 µM). Even at low drug concentrations, α presents higher sensitivity, which leads to an increase in variability and magnitude, hence reflecting a reduction in the cell-substrate distance, 48 h upon exposure. Significance denoted with [*] for $\alpha < 0.05$, [**] for $\alpha < 0.01$, and [***] for $\alpha < 0.001$.

As described, control samples presented an increase in R_b with time due to cell layer maturation and cell-cell contact formation. Within the first 24 h upon exposure to SMIFH2, a non-significant decrease in R_b was found for all drug concentrations. After 48 h, the samples that had been exposed to 1 to 10 µM SMIFH2 showed recovery of R_b to levels comparable to those of control samples; upon exposure to 15 and 20 µM concentrations, recovery was still observed at the 48 h interval, but R_b values remained significantly lower. Fibroblasts exposed to 66 µM SMIFH2 showed no significant differences in R_b with respect to control cells, possibly pointing at a saturation effect.

The general trend established by the adaptations observed in R_b was inversely reflected by C_m. Accordingly, C_m decreased with time for control samples, and the same pattern was reflected upon exposure to SMIFH2, albeit with non-significantly higher C_m values especially 24 h upon exposure. Only upon addition of SMIFH2 at 20 µM, a significantly higher C_m was observed with respect to control values at the 48 h interval, hence indicating that the general inhibitor has a larger impact in the regulation of the cell-cell contacts than in membrane ruffling. Upon exposure to 66 µM SMIFH2, a saturation effect was also observed.

Regarding α, control samples showed a decreasing trend with time that reflected an increase in the cell-substrate cleft with the degree of cell layer maturation. Upon exposure to SMIFH2, a clear change was observed between the 24 and 48 h intervals, hence indicating a high sensitivity to the drug in the mechanism regulating the cleft's height. Table 6.2 presents the median values of the α distributions in figure 6.8.

Table 6.2: **Adaptation of α in WT fibroblasts upon exposure to SMIFH2**. The table illustrates the median and mean absolute deviations of the α distributions (units of $\Omega^{1/2}$ cm) determined following the Lo-Ferrier model and presented in Fig. 6.8. Prior to exposure (t = 0 h), the intact monolayer presented a median α value of 0.114 ± 0.444 $\Omega^{1/2}$ cm.

Concentration	α(24h)	α(48h)
0 µM (control)	0.055 ± 0.523	0.030 ± 0.655
1 µM	0.071 ± 0.501	0.553 ± 0.748
5 µM	0.022 ± 0.598	0.043 ± 0.943
10 µM	0.035 ± 0.023	0.054 ± 0.635
15 µM	0.031 ± 0.028	0.090 ± 0.792
20 µM	0.108 ± 0.053	0.035 ± 0.481
66 µM	0.042 ± 0.009	0.022 ± 0.019

Within the first 24 h after exposure to SMIFH2, α decreased, for all drug concentrations, with respect to PE control values. 48 h upon exposure to a concentration range

from 1 to 15 µM, α increased with respect to the previous 24 h and presented a large variability, albeit with no statistically significant deviations, also with respect to control samples. At higher concentrations, thus 20 and 66 µM, the adaptation of α followed that of control samples, possibly reflecting saturation at lower drug concentrations due to the increased sensitivity of this parameter to the role of formins.

Cellular micromotions upon exposure to SMIFH2

Analysis of the corresponding cellular micromotions showed, in figure 6.9, different trends in the evolution of the parameters of interest in relation to SMIFH2 exposure. After addition of low drug concentrations (1 - 5 µM), α_{DFA}, *var* and $|S_{PSD}|$ presented slightly lower values with respect to control samples both at the 24 and 48 h interval. However, differences resulted non-significant, thus indicating a low influence in micromotions at this concentration range. Upon addition of 15 to 20 µM SMIFH2, an inhibitory effect was detected in the progressive decrease of $|S_{PSD}|$ with increasing concentration: after exposure to 20 µM, $|S_{PSD}|$ was higher 48 h after recovery than 24 h upon exposure, thus indicating an increase in biological activity at the later stage; exposure to 66 µM led, in contrast, to lower $|S_{PSD}|$ values at the 48 h interval. Accordingly, the lack of recovery at the highest concentration could result from the incapacity of Fbs to overcome the effects linked to such SMIFH2 dose. Correspondingly, *var* and α_{DFA} remained low after exposure to 66 µM of SMIFH2, but 24 h upon addition of 20 µM, both parameters showed a peak in metabolic activity with important long-term correlations, which could reflect the cellular effort in counteracting the influence of the drug.

With intermediate concentrations (10 - 15 µM), $|S_{PSD}|$ showed an increase with concentration in which values at the 48 h interval remained comparable to those observed 24 h after exposure, whereas for control samples, a progressive decrease was observed with time. For the same SMIFH2 concentrations, *var* remained comparable to control samples except for a high distribution 48 h upon exposure to 10 µM, whereas in the case of α_{DFA} , higher variability was observed: while for a 10 µM SMIFH2 concentration α_{DFA} increased at the 48 h interval with respect to the previous 24 h, for a 15 µM concentration, α_{DFA} remained constant and lower than PE values at both time points.

Overall, high SMIFH2 concentrations over 20 µM showed an inhibitory or even toxic effect in Fbs cultures, whereas almost no influence in the micromotions was detected below 5 µM concentrations. Accordingly, intermediate values caused SMIFH2 concentration-dependent effects in the cellular fluctuations, as reflected in the increased variability in the three parameters.

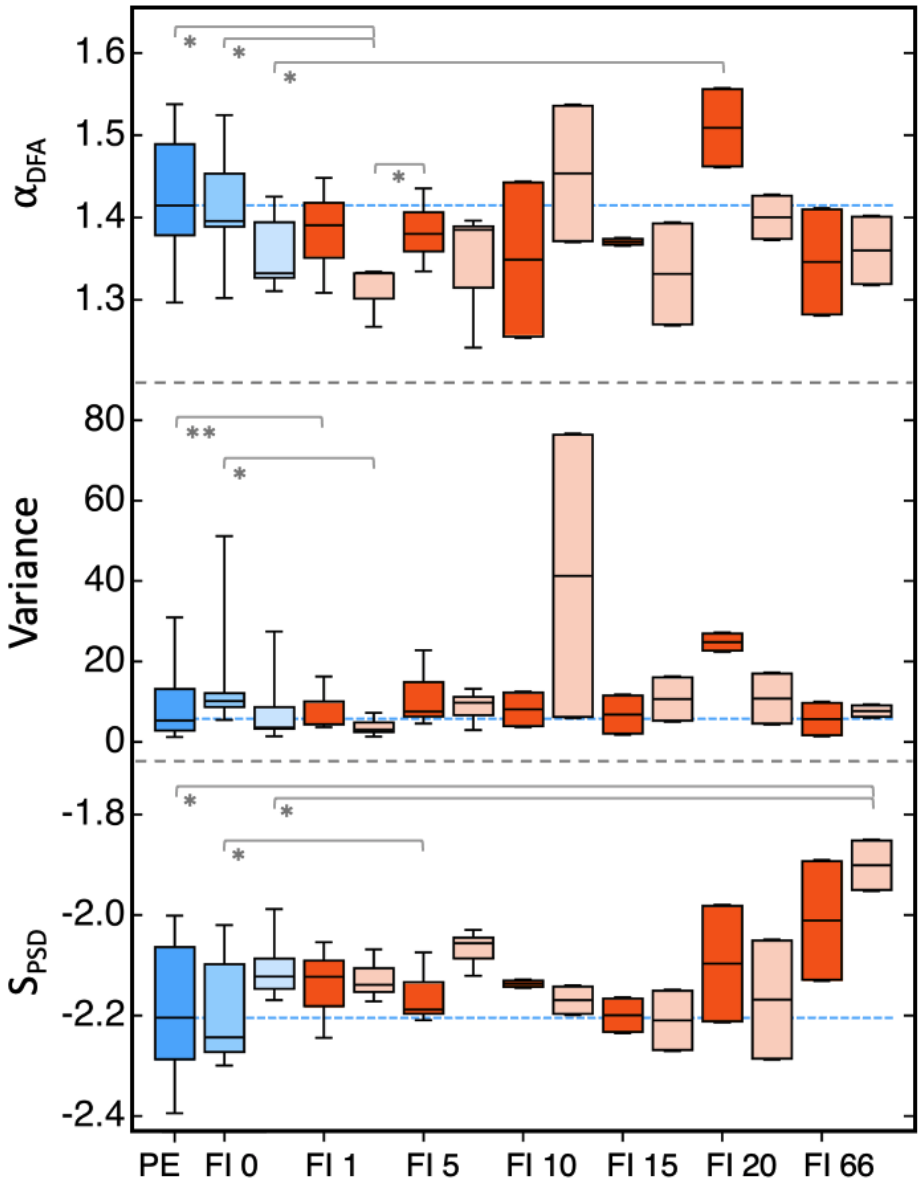

Figure 6.9: **Cellular micromotions of WT fibroblasts exposed to SMIFH2.** Values are presented for control WT cells (■; n = 22, m = 6) and cells exposed to different concentrations of the formin inhibitor (FI) SMIFH2 (indicated in µM; n = 3, m = 3 for FI 1-5 µM; n = 2, m = 2 for FI 10-66 µM). Pre-exposure (PE) values determine the properties of the initial monolayer (baseline indicated with dotted line) and provide a reference for control (FI 0) cells and samples exposed to SMIFH2. Drug concentration-dependent effects are observed, through an increase in the variability of the three parameters 24 (■) and 48 (■) h upon exposure, in the interval of 10 to 20 µM. Significance denoted with [*] for $\alpha < 0.05$ and [**] for $\alpha < 0.01$.

Determination of IC_{50} for the influence of SMIFH2 in WT cultures

In the fields of pharmacological and toxicological research, the use of the half maximal inhibitory concentration (IC_{50}) is widespread, as it provides a measure of the potency of a substance by defining the concentration required to alter a particular biological process by 50 %. Accordingly, classical IC_{50} curves show sigmoidal trends between the intervals defined by the concentrations that provide maximal and minimal biological action, also based on individual cellular activity.

Even though SMIFH2 concentration-dependent effects have been shown in the parameters describing cell layer integrity (R_b, C_m and α) and in those describing micromotions (a_{DFA}, var and S_{PSD}) through figures 6.8 and 6.9, no characteristic IC_{50} patterns were observed. Figure 6.10 shows the standardised maximum real part of the impedance values of WT fibroblasts 48 h after exposure to different SMIFH2 concentrations. For each concentration, the plot indicates the mean and standard deviations obtained from averaging the measurements of three independent impedance courses. Upon exposure to the lowest concentration tested, 1 µM, Z_{real} values showed a small decrease that led, within the 5-20 µM SMIFH2 interval, to comparable Z_{real} values and a stable Plateau with a slight deviation at 15 µM. By applying a sigmoidal fit to the distribution, a very narrow curve indicated concentration-dependent effects centered at the 1 µM; beyond the 5 µM, only a saturated effect could be observed. Accordingly, figure 6.10 led to IC_{50}(SMIFH2) = 1 µM, with which Z_{real} would present higher sensitivity than the parameters derived from the Lo-Ferrier model and those describing cellular fluctuations.

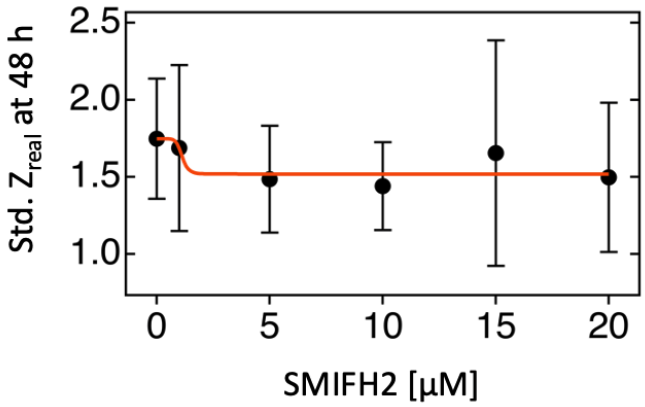

Figure 6.10: **SMIFH2 IC_{50} of non-wounded WT fibroblasts.** The standardised maximum values of the real part of the impedance of WT fibroblasts, 48 h after exposure to different SMIFH2 concentrations, are shown. Data points indicate mean and standard deviation (n = 3; m = 3). A sigmoidal fit (orange line) shows concentration-dependent SMIFH2 effects around the 1 µM concentration (IC_{50}), whereas beyond 5 µM, a saturation is observed in the impact on Z_{real} values.

6.1.5 Influence of formin inhibitor SMIFH2 in the wound healing of fibroblasts

Based on the IC_{50} curve obtained upon exposing integral cell layers to SMIFH2, the same process was followed for wounded samples. Accordingly, 24 h after cell seeding, a high amplitude and frequency electric pulse was applied in order to create a wound, after which the cellular debris was washed off to then perform a 30 min incubation with SMIFH2. After the pulsed exposure, the media was refreshed and the recovery of the samples monitored for the following 48 h.

Figure 6.11 shows the IC_{50} curve obtained based on the recovery half times of the resulting impedance spectra, centered at a drug concentration of ~0.6 µM. Beyond 1-5 µM, a Plateau was observed. Over a concentration of 15 µM, a secondary effect was detected, possibly linked to cytotoxic or saturation effects.

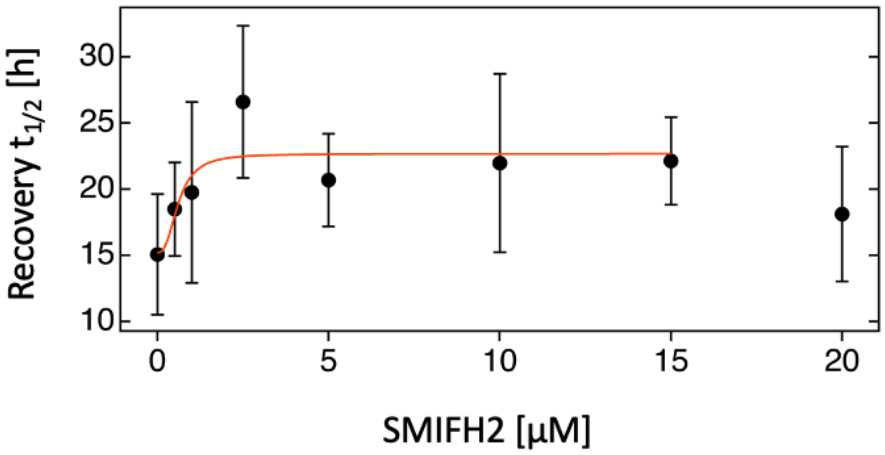

Figure 6.11: ***IC₅₀* of wounded WT fibroblasts exposed to SMIFH2.** The recovery half time ($t_{1/2}$) of WT fibroblast cultures wounded and consecutively exposed to different SMIFH2 concentrations for periods of 30 min are shown; exposure causes a delay in recovery with an IC_{50} value of 0.611 ± 0.389 µM. The decrease in $t_{1/2}$ upon addition of 20 µM SMIFH2 points at a secondary effect in combination to the wounding process. Data points indicate mean and standard deviations (n ⩾ 3; m ⩾ 3).

Micromotion analysis was performed on wounded samples upon exposure to two SMIFH2 concentrations: 10 and 20 µM. The resulting a_{DFA}, *var* and S_{PSD} values are compared in figure 6.12 to those of control and wounded samples (introduced in Fig. 6.7 and described in detail in page 121). Addition of 10 µM SMIFH2 upon wounding caused no significant differences in a_{DFA} and *var* with respect to wounded samples, albeit the former was slightly higher at the 24 h time point. In contrast, absolute S_{PSD} values

showed a significant increase compared to wounded samples but not compared to control samples. Addition of 20 µM, on the other hand, caused a small decrease in $|S_{PSD}|$ but significant decreases, with respect to control samples, in α_{DFA} and *var*. Accordingly, results suggest recovery progression upon exposure to 10 µM SMIFH2, but not after exposure to 20 µM.

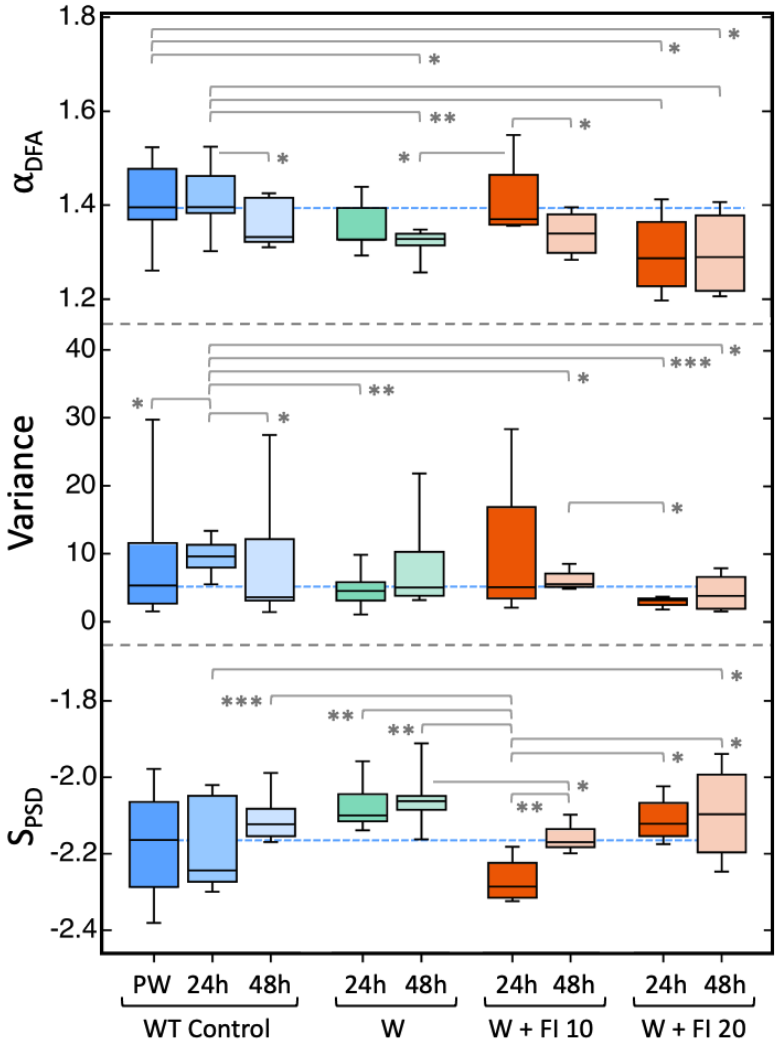

Figure 6.12: **Micromotions of WT fibroblasts upon exposure to SMIFH2.** Values are presented for control WT cells (■; n = 22, m = 6), wounded samples (■; n = 3, m = 3) and samples wounded and sequentially exposed to SMIFH2 (■; ; n = 3, m = 3). Upon wounding and SMIFH2 addition, recovery is observed only for the 10 µM drug concentration. Significance denoted with [*] for $\alpha < 0.05$, [**] for $\alpha < 0.01$, and [***] for $\alpha < 0.001$.

6.2 Discussion

In a cell wounding scenario, a number of mechanical [52] and chemical [56, 57] cues are relevant in the initiation of the healing response and in the promotion of cell migration towards the injured area in order to close it and reinstate, to the extent possible, its original properties. In the case of fibroblasts, these cues also elicit the fibroblast-to-myofibroblast transition [55], in which a cytoskeletal re-organisation takes place upon the expression of α-SMA [6] and increased number of cell-cell contacts [8]. All together, the healing response bestows a demanding toll in the maintenance and re-organisation of the cellular architecture. For this reason, proteins involved in the synthesis and turnover of the cytoskeletal elements become relevant. This is the case of formins, which participate in the nucleation and elongation of actin filaments.

Within this context, the role of mDia-family formins in the wound healing dynamics of NIH 3T3 fibroblasts has been investigated in this chapter by comparing the behavior of wild type cells against that of fibroblasts lacking the isoforms mDia1 and mDia3, and against that of wild type cells exposed to the generic formin inhibitor SMIFH2, therefore also capable of influencing the third family member mDia2.

6.2.1 Recovery kinetics of WT and dKo fibroblasts

Fibroblasts simultaneously carrying mDia1 and mDia3 knock-out forms present a delayed recovery upon wounding with respect to wild type cells. This was shown in the impedance time courses of figure 6.2, where an interval of approximately 13 h separated the two cell lines in reaching pre-wounding Z_{real} values. Therefore, while necessary for optimal recovery kinetics, formins are not essential in initiating wound closure.

A comparison between the influence of the double formin modulation and a partial silencing is presented in figure 6.13, where the impedance time courses and derived recovery half times of WT and dKo cells are contrasted against results obtained on single mDia1 and mDia3 fibroblasts, provided by V. Scheller [149]. As shown, all forms of formin deletion led to significant delays in $t_{1/2}$ with respect to WT cells. This was mostly accentuated in mDia1 followed by dKo cells; based on comparison of the medians, the absence of mDia3 led to a delay of only 1 h. Accordingly, the role of mDia1 is especially relevant to recovery kinetics, whereas mDia3 becomes specifically significant, in this context, in the absence of mDia1, hence suggesting that it presents a compensatory function in agreement with previous reports [16]. Even though a more detailed discussion on the roles of formins will be provided in chapter 8, it was already shown, in chapter 5, that

the cortices of weakly and strongly adherent cells lacking mDia1 presented important structural defects, further accentuated in dKo fibroblasts and, at a lesser extent, in mDia3 cells. This parallelism between closure kinetics and cortical dynamics underline their interconnection and point at a strong link between optimal migration and the role of formins, especially mDia1.

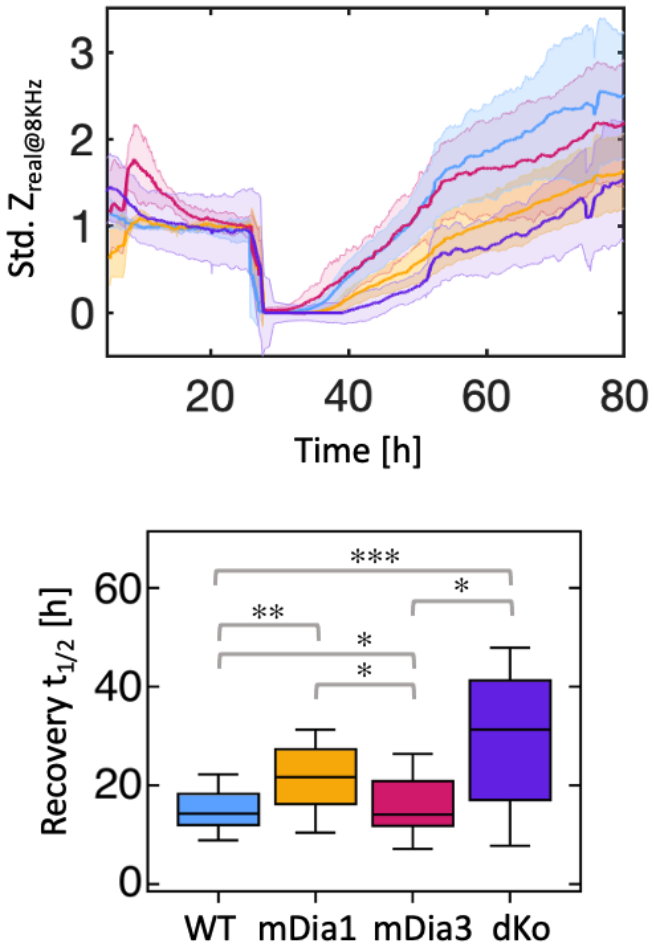

Figure 6.13: **Wound recovery time courses and derived $t_{1/2}$ of fibroblasts with different formin modulations. Top:** averaged real part of standardised impedance time courses for WT (■), mDia1 (■), mDia3 (■) and dKo (■) fibroblasts (n ⩾ 6; m ⩾ 3). **Bottom:** recovery half time determined upon applying a sigmoid fit to the recovery time courses. From left to right, $t_{1/2}$ (median ± mean absolute deviations) are 14.3 ± 3.8; 21.2 ± 6.4; 15.1 ± 5.8; 31.3 ± 13.3. Here, time = 0 is defined by the wounding time. Significance denoted with [*] for $\alpha < 0.05$, [**] for $\alpha < 0.01$, and [***] for $\alpha < 0.001$. As both panels indicate, all formin modulations cause a significant delay in recovery; this is magnified in mDia1 cells and specially in dKo cells.

With the objective of correlating recovery impedance time courses to the progression of electrode re-colonisation, fluorescence microscopy was employed. In the resulting micrographs, morphological dissimilarities could be already observed between WT and dKo cell lines upon monolayer formation (Fig. 6.4). Even though both showed similar actomyosin distributions with F-actin prominent at the cellular periphery and basal levels of myosin expression, dKo fibroblasts spread over larger areas, thus leading to less densely packed monolayers. In addition, they presented gaps between adjacent cells around which actin aggregates, rather than filamentous structures, could be observed. Actin filaments use cell-cell contacts such as cadherin-mediated adherent junctions as anchoring points [109]. It is conceivable that higher concentrations of cell-cell interactions were established in the areas where the membranes of neighbouring dKo fibroblasts became into contact, thus forming clusters of high actin concentration; the formation of cadherin-mediated contacts is moreover formin-dependent and directly involves the participation of mDia1 in epithelial cells [188, 189]. Accordingly, in the absence of mDia1 and mDia3, stability of cadherin-mediated junctions could result impaired, further contributing to the discontinuity in cell-cell interactions.

Micrographs also reflected the differences in recovery rates between WT and dKo: for equivalent time points, dKo cells showed reduced extent of electrode re-population. This delay was especially noticeable at the 10 h time point when while WT had covered almost the entire electrode area, only around 50 % of its surface had been re-colonised by dKo cells (Fig. 6.4). In the wound closure process, WT and dKo fibroblasts shared the same migratory mechanism as, based on figures 6.3 and 6.4, both initiated electrode re-colonisation via active cell crawling. Accordingly, cells became polarised and migrated towards the gap through lamellipodia formation [18], process in which F-actin nucleation is essential [190]. In the lamellipodia, a large number of adhesions with a high turnover rate are formed as a double approach to sense the environment and anchor the cellular displacement [23]. This was reflected in the appearance of small, dot-like actin aggregations towards the leading edges of the cells that revealed the formation of nascent adhesions. In the transition from 6 to 10 h intervals for WT fibroblasts, these actin aggregations grew in size, indicating maturation into focal and fibrillar adhesions [103, 104], and became less associated to the leading edge of cells. Incidentally, several cells became more widespread and lost the highly directional organisation of actin bundles characteristic of cell migration [18], thus indicating a shift from directional motility to static adhesion in the advanced re-colonisation stages.

In order to provide traction forces during migration, the expression of myosin was increased after wounding. As shown in figures 6.3 and 6.4, myosin motors were then arranged in filament-like structures associated to F-actin, hence promoting bundling and

contractility of stress fibers [191]. Upon monolayer reconstitution, myosin expression was down-regulated close to pre-wounding basal levels (17 h interval in Fig. 6.3). In dKo cells, the association of myosin in filamentous bundles after wounding was increased with respect to WT; at the same time, even in the migratory state, dKo cells remained more spread. Accordingly, an unbalance between the internal forces and cortical tension of cells lacking mDia1 and mDia3 formins could lead to the formation of the transmembrane macroapertures observed in figures 6.4 and 6.5. In addition, the widespread morphology of dKo cells, both when static and during migration, suggest an impaired ability to become polarised, which could lead to the formation of multiple cell fronts in detriment of the migratory speed. Both topics will be further elaborated on in chapter 8.

6.2.2 Recovery of cell layer integrity upon wounding

In order to assess the passive electrical properties of the cell layer throughout the wound-healing process, the Lo-Ferrier model was applied to retrieve the physiologically relevant parameters R_b, C_m and α which, respectively, relate to cell-cell connectivity, membrane rigidity or composition, and cell-substrate distance [25].

As shown in figure 6.6, WT control samples presented a progressive increase in R_b with time, indicative of cell-cell contact formation and layer maturation. The chemistry of the cell membrane is tightly linked to the cell cycle [192], which enters into arrest upon contact inhibition of proliferation in a confluent state. Accordingly, cell layer maturation could lead to adaptations in the lipid composition of the cell membrane that could cause, together with a reduction in the membrane roughness, the gradual decrease observed in C_m. Control dKo samples followed the same general trend. However, they presented lower C_m values that decreased at a lower rate over time, thus indicating formin involvement in the regulation of membrane roughness and smoother cellular surface in their absence. Strikingly, they also presented R_b values that were globally higher than for WT. As shown in the micrographs of figure 6.4, dKo fibroblasts formed cell layers with gaps between neighbouring cells, hence showcasing an intercellular space less obstructed by cell-cell contacts that, accordingly, should have resulted less restrictive to the flow of the electric current. Furthermore, the formation of cadherin-mediated adherent junctions is formin-dependent [188, 189], which would be expected to contribute to a reduction of R_b in dKo cells. However, due to the impaired cell-cell communication, contact inhibition of proliferation could be down-regulated, leading to increased cellular density and even multilayer, factors that would increase R_b. Although these could explain the increase of R_b with time in dKo cells, micrographs 24 h after cell seeding do not indicate cell crowding but rather a less dense cellular layer. Overall, results rise an interesting

experimental question for which additional work will be necessary in order to provide an answer.

Upon wounding, no significant differences could be detected in the recovery of WT fibroblasts with respect to control samples. In contrast, 24 h after wounding dKo cells, these presented significantly lower R_b and higher C_m values. C_m was fully recovered after 48 h, whereas for the same interval, R_b presented a significant delay since values corresponded to the 24 h time point in dKo controls. As shown in figure 6.1, the impedance-based wounding process elicited the FMT response, which led to an increase in the intercellular expression of Cx43 gap junctions. Expression of Cx43 and cadherin-based cell-cell contacts are sequentially related to FMT progression [26, 147, 193] which, due to the involvement of formins in the establishment of the latter [188, 189], contributed to the delay in R_b observed for dKo cells. Accordingly, in the absence of mDia1 and mDia3, the recovery of the cell layer integrity was impaired especially for R_b, whereas upon wounding WT fibroblasts, these reinstated normal cell layer properties without delay.

The height (h) of the cell-substrate cleft is inversely proportional to α according to the following expression, where W is the cell width and ρ the resistivity of the culture medium in the confined space:

$$h = \frac{\rho}{\left(\frac{2\alpha}{W}\right)^2} \tag{6.1}$$

Based on this equation, table 6.3 shows the cell-substrate distance corresponding to the α distributions of figure 6.6. Control samples showed little variation in the cleft over time: WT fibroblasts presented a distance of approximately 4 µm with respect to the electrode surface, whereas dKo cells remained closer at 0.1-0.2 µm. Specifically for WT fibroblasts, the cell-substrate distance was relatively large in comparison to values reported in the bibliography, usually in the range of 30-100 nm [25, 150]. These deviations could arise from the choices in parameterisation when describing the cellular geometry, as it has a direct impact in the definition of the electric path under the cell and can lead to over- or under- estimations of the parameters [150]. However, they could also appear due to changes in the resistivity of the electrolyte in the cleft caused by the cellular metabolic activity.

Applying eq. 6.1 to the 24 h recovery intervals led to h distances beyond the sensitivity of the ECIS method, which could result from important changes in the electrolyte resistivity due to the intense metabolic activity during the first stages of recovery and

Table 6.3: **Cell-electrode distance of WT and dKo fibroblasts**. The table illustrates the height (average ± standard deviation; µm units) of the cell-substrate cleft calculated upon the average values of the α distributions in Fig. 6.6 following eq. 6.1. Cleft height is indicated for control WT and dKo samples, and for cells 48 h upon wounding. After recovery, WT fibroblasts approach the surface, whereas dKo remain lifted.

Parameter	PW (t=0)	24 h	48 h
WT ct.	4.45 ± 6.55	4.86 ± 10.2	3.06 ± 5.90
WT rec.	/	/	0.250 ± 0.062
dKo ct.	0.293 ± 0.276	0.114 ± 0.078	0.230 ± 0.282
dKo rec.	/	/	1.35 ± 2.37

migration. Furthermore, intercellular gaps and poor cell-cell connectivity in the still recovering and semi-confluent monolayer could hamper the application of the Lo-Ferrier model, hence leading to the high h values. Accordingly, these are not included in table 6.3. Qualitatively following table 6.1, α values indicated that 24 h after wounding, WT and dKo fibroblasts lifted from the substrate. This observation is in agreement with literature reports describing the lifting of the cell sheet upon injury [26] or for processes resembling the FMT such as the epithelial-to-mesenchymal transition after exposure to TGF-β [29]. By the 48 h time point, cells approached the substrate again. Interestingly, the cleft under the WT cell sheet resulted smaller than for dKo cells, indicating the involvement of formins in the regulation of the distance and, possibly, reflecting a delayed recovery with respect to WT cells.

6.2.3 WT and dKo cellular micromotions during wound recovery

Fluctuations in the height of the ventral membrane can be analysed by transforming the impedance time course for a selection of frequencies into a power spectral density. Detrended fluctuation analysis allows the calculation of α_{DFA}, which is a measure of long-term correlations in the impedance time course, whereas computation of variance (var) and the slope of the power spectral density (S_{PSD}) relate to the number and magnitude of the fluctuations, and to the source of the signal [29, 136]. In order to carry the measurement of cellular micromotions with the ECIS, it is important to look at results in relation to the brown/white noise obtained on cell-free electrodes as it provides a baseline for the system. For the setup employed, α_{DFA}, var and S_{PSD} values corresponded to 0.776 ± 0.136, 0.051 ± 0.034 and -1.17 ± 0.34, which were significantly different from the values presented in figure 6.7, and thus confirmed their portrayal of biological noise. Incidentally, while the α_{DFA} and S_{PSD} baselines were very similar for WT and dKo cells,

the latter presented significantly higher variance throughout the different experimental conditions. Therefore, the amplitude of the impedance fluctuations hinted at a higher biological activity in the absence of formins, which could also reflect transmembrane tunnel dynamics.

For WT control cells, α_{DFA} and $|S_{PSD}|$ decreased with time, which could result from a decrease in cell activity due to cell-cell contact inhibition in the densely populated monolayer. Surprisingly, the same trend was observed upon wounding, whereas an increase in fluctuations would have been expected during migratory and wound-closure events. This is especially relevant for α_{DFA} which, as a measure of long-term correlations, was expected to increase due to the cytoskeletal adaptations and turnover of cellular adhesions involved in the FMT and migratory processes [29, 135]. As indicated by the fluorescence imaging and the parameters derived from the Lo-Ferrier model, WT fibroblasts were able to re-populate 250 µm circular wounds and reinstate pre-wounding cellular properties in a short period close to 24 h. It is therefore possible that the peak in micromotion activity was given before the 24 h recovery time point. In contrast, dKo fibroblasts presented a significant delay both in wound closure and in the recovery of the properties of the initial monolayer. This difference could have allowed the observation of the increase in α_{DFA} 24 h after wounding, which would reflect the long memory effects due to cytoskeletal re-organisation and migration, and the sequential decrease to pre-wounding levels by the 48 h time point. Interestingly, dKo control fibroblasts presented an increase of the three parameters at the later stage. Due to the impaired cell-cell and cell-substrate connectivity caused by the absence of mDia1 and mDia3, it is possible that dKo cultures presented an increased rate of cell death combined with an absence of contact inhibition which, in this case, would have triggered higher activity in the neighbouring cells, hence leading to the increase in α_{DFA} and *var*.

6.2.4 Effect of SMIFH2 exposure on the cell layer properties and micromotions of WT cultures

In this chapter, the influence of the generic formin inhibitor SMIFH2 on WT cultures was tested in a concentration range of 1 to 66 µM. Such range encompasses typical IC_{50} values for different species (5-15 µM), including mice [24].

Based on figure 6.8, SMIFH2 affected cell-cell formation only upon a concentration over 15 µM since, beyond this range, a significant decrease in R_b was observed 24 after addition of the drug. Between this and the 48 h time points, R_b then increased at a similar rate with respect to control samples, hence showing recovery. However, due to the decrease in the junctional resistance 24 h after SMIFH2 exposure, R_b values

remained lower than for control samples when comparing the 48 h intervals. Similar observations were made regarding adaptations in C_m, but this parameter resulted less sensitive: differences between control and exposed samples 48 h after drug addition were significant only for concentrations beyond 20 µM.

In contrast to R_b and C_m, α showed sensitivity to SMIFH2 already at low concentrations. The drug caused, similar to wounding, the lifting of the cell sheet and its sequential approximation to the substrate. Table 6.4 shows the height of the cell-substrate clefts for the range of SMIFH2 concentrations tested. 24 h after addition of the drug at concentrations over 10 µM, h values were out of the sensitivity scope of the ECIS. The same was true for the 48 h interval upon addition of SMIFH2 66 µM. Accordingly, these values were not included in the table. As discussed above, the deviations could indicate the need of optimising ρ which, based on the experimental conditions in which the results were unrealistic, could be highly affected by the metabolic response to the presence of SMIFH2. Furthermore, cellular rounding caused by the drug could generate unconstricted electric flows that could therefore interfere in the application of the Lo-Ferrier model [28].

Table 6.4: **Cell-electrode distance of WT cells upon exposure to SMIFH2**. The table illustrates the height (average ± standard deviation; µm units) of the cell-substrate cleft calculated upon the α distributions in Fig. 6.8 following eq. 6.1. Cleft height is indicated for control samples and WT cells 24 and 48 h after exposure to SMIFH2. Drug addition causes cell sheet lifting; sequential approximation to the substrate is impaired at high SMIFH2 doses.

Concentration	24 h	48 h
1 µM	4.70 ± 9.30	0.867 ± 0.927
5 µM	4.03 ± 8.36	0.992 ± 1.315
10 µM	/	3.00 ± 5.46
15 µM	/	1.27 ± 1.72
20 µM	/	5.81 ± 11.64

According to table 6.4, the increase in SMIFH2 concentration resulted in a diminished approximation of the cell sheet to the substrate 48 h after drug addition. Overall, the parameters derived from the Lo-Ferrier model indicated increasing formin participation in the regulation of membrane roughness, cell-cell connectivity, and cell-substrate space. Therefore, the high sensitivity of α should relate to a high sensitivity in cellular micromotions.

For the same range of SMIFH2 concentrations, micromotion analysis showed a broad spectrum of responses, thus confirming their higher sensitivity to the effects of the drug. Cellular responses deviated from the fluctuations of control samples upon exposure to low concentrations over 5 µM. Beyond this point, an increment in a_{DFA} and $|S_{PSD}|$ indicated an increase in the biological activity and in the long-term correlations. As discussed above, FMT progression could lead to higher a_{DFA} due to the cytoskeletal reorganisation that it involves. In these experiments, however, SMIFH2 was added to the intact monolayer 24 h after cell seeding. Accordingly, in the absence of wounding, the FMT should have not been triggered. Nevertheless, formins are involved in the regulation of a large number of cytoskeletal components such as the cellular cortex [16], cell-cell interactions [188] and cell-substrate adhesion via lamellipodia and filopodia formation [194]. Furthermore, formins can associate to microtubules to increase their stability [195, 196]. This relation has also been specifically identified for mDia2 [197], which is lethal in the knock-out form but can be transiently silenced via SMIFH2. Through this formin-microtubule interaction, it has been observed that SMIFH2 can lead to microtubule depolymerisation [198]. Altogether, the broad scope of the SMIFH2 affects the cellular architecture, which therefore causes an increase in the long-term correlations, and hence in a_{DFA}. Moreover, recently it has also been observed that SMIFH2 presents the off-target inhibition of members of the myosin family [186], which could have caused the reduction in *var* observed upon SMIFH2 addition but not for dKo fibroblasts. However, the alteration of non-muscle myosin 2A relates to an IC_{50} of $\sim$ 50 µM. Accordingly it is more likely that in dKo cells, compensatory activity of other formin forms led to increased *var* values whereas, due to the general inhibition caused by SMIFH2, the compensatory effects did not take place.

Above 20 µM concentrations and, specially for 66 µM, cytotoxic effects were reflected in the combined decrease in $|S_{PSD}|$, a_{DFA} and *var*. These observations are in agreement with the results of Rizvi *et al.*, who reported SMIFH2-elicited cytotoxicity in NIH 3T3 fibroblasts with an IC_{50} of 28 µM [24].

The IC_{50} value of 1 µM determined in figure 6.10 illustrates even higher sensitivity to the influence of SMIFH2 in the increase of the real part of the impedance than in micromotions. The trend differs from that observed in the R_b values at the 48 h time point in figure 6.8, hence indicating the presence of other factors, besides R_b, contributing to Z_{real}. Testing a wider range of SMIFH2 concentrations close to the IC_{50} value found and with increased number of replicates could lead to the identification of IC_{50} curves to describe the changes in the passive electrical properties of the monolayer and the cellular micromotions.

6.2.5 Influence of SMIFH2 addition upon wounding of WT fibroblasts

Addition of SMIFH2 immediately after wounding WT cultures led, based on the resulting recovery half times (Fig. 6.11), to similar but slightly higher sensitivity to the drug: IC_{50}(SMIFH2) = 0.611 ± 0.389 µM. Formins actively participate in the regulation of the cytoskeletal architecture specially during migration, when cellular polarisation, filopodia and lamellipodia formation, and adhesion turnover become specially relevant. Accordingly, formin inhibition in a recovery scenario is expected to cause a bigger impact in the cellular behavior, thus in agreement with the results.

Interestingly, even in the Plateau phase of the IC_{50} curve, SMIFH2 addition caused a smaller impact in the recovery half time compared to the absence of mDia1 and mDia3 in dKo cells ($t_{1/2}$ = 31.3 ± 13.3 h), hence reflecting the fast recovery of the cellular normal behavior once the drug was removed, compared to the effect of the sustained inhibition of the two isoforms. Furthermore, upon the exposure to SMIFH2 concentrations below 20 µM, recovery impedance time courses resulted similar to those presented in figure 6.13, where the stabilisation of Z_{real} was given for values larger than those of the initial monolayer. This was not the case for the wounded samples exposed to 20 µM SMIFH2, for which recovery was initiated with a significant delay, and stabilisation of Z_{real} (determining the interval to be fitted by a sigmoidal curve to calculate $t_{1/2}$) showed values lower than those of the initial monolayer. Accordingly, while recovery progression was observed, it was not completed during the experimental duration and the corresponding $t_{1/2}$ in the IC_{50} curve reflects only partial recovery.

The influence of SMIFH2 in the cellular micromotions within the Plateau and the secondary effect detected in the IC_{50} curve are analysed in figure 6.12. As described above, the wounding of WT cultures led, compared to control samples, to similar trends due to their fast recovery. Specially 48 h after wounding, fluctuations decreased due to cellular crowding and derived contact inhibition effects. Upon combining wounding and SMIFH2 addition, fluctuations changed. For the 10 µM concentration, $|S_{PSD}|$ reflected a peak in biological activity 24 h after wounding and drug addition, hence suggesting a delay in recovery with respect to wounded samples due to the influence of SMIFH2. With this delay, correspondingly higher α_{DFA} and *var* could have been expected. However, due to the formin inhibition provided by SMIFH2, cytoskeletal adaptations following the FMT and the polarisation of migrating cells, together with the magnitude of the ventral fluctuations, would have resulted impaired, thus leading to the low α_{DFA} and *var*. Still, 24 h after wounding and drug addition, α_{DFA} was significantly higher than

for the second recovery interval, indicating higher long-term correlations due to the cytoskeletal re-organisations.

The addition of 20 µM SMIFH2 to wounded samples caused a significant decrease in a_{DFA}, var and $|S_{PSD}|$ that remained comparable between the two recovery time points. Accordingly, the combination of treatments caused a large impact in the cellular vitality, which was not recovered for the duration of the experiments. Despite this, wound closure was still observed albeit with a great delay, as described above regarding $t_{1/2}$ in the IC_{50} curve.

Conclusions

In the absence of formins, wound closure results increasingly delayed for mDia3, mDia1 and dKo fibroblasts. WT and dKo cells present important morphological differences, such as extended cell-substrate contact area and discontinuous distribution of cell-cell contacts between adjacent cells, that generate specific passive electrical properties in the intact monolayers. Upon wounding, R_b and C_m are recovered by WT cells in the first 24 h, whereas for dKo fibroblasts, recovery is significantly delayed, hence indicating the participation of mDia1 and mDia3 in the regulation of cell-cell adhesions and membrane roughness. Upon wounding, the cell sheet lifts to later approach the substrate. This process is also delayed in dKo fibroblasts, which additionally present ventral fluctuations of higher magnitude. Addition of SMIFH2 to WT cultures causes impaired regulation of R_b and C_m upon drug concentrations above 15 and 20 µM. Inversely reflecting the height of the cell-substrate cleft, α shows higher sensitivity. The same is true for cellular micromotions, which indicate a decrease in the fluctuations and, hence, in metabolic activity, upon exposure to SMIFH2 concentrations over 20 µM due to cytotoxic effects. In a range between 5 and 15 µM, concentration-dependent effects are observed. Addition of SMIFH2 upon wounding generates higher sensitivity to the drug. Still, recovery takes place -with increasing delay- except after exposure to SMIFH2 20 µM, case in which it is significantly impaired.

Overall, wound closure by fibroblasts is given even upon formin inhibition. Accordingly, despite necessary for optimal recovery, it is not essential to initiate the process. Addition of SMIFH2 causes a significant reduction of cellular micromotions, whereas for dKo cells, the effects of the inhibition are specially relevant in the recovery of the cell layer integrity.

Chapter 7

Influence of gap size on wound closure dynamics

In order to investigate the recovery kinetics of NIH 3T3 fibroblasts and the role that formins play in the process, initial ECIS-based wound healing assays compared cell lines with different formin modulations on 250 µm wide circular wounds. In this chapter, the study is continued with a shift of focus towards the influence of wound size, an important factor in determining the closure mechanism undertaken by cells during the healing process [18, 30]. Studies on 2D epithelial cultures have led to the identification of two distinct strategies: active crawling of individual, highly polarised cells, and purse-string contraction via the formation of a supracellular actin cable at the leading edge of a cellular collective. The latter has been traditionally ascribed to epithelial wounds, but recent studies challenge this view due to the identification of actomyosin cables in fibroblast populations closing voids [19] or advancing on 3D clefts [21].

Accordingly, and aiming to contribute to this open topic, this chapter focuses on analysing the effect of wound size on the recovery of NIH 3T3 fibroblasts via the use of ECIS-based wound healing assays in combination to fluorescence microscopy.

7.1 Results

7.1.1 Influence of wound size on the recovery rate of fibroblasts with different formin modulations

In order to study the influence of wound size on recovery dynamics, ECIS chip arrays combining electrodes of 31, 63, 127 and 255 µm in diameter were employed in the follow-

ing experimental methodology: 24 h after cell seeding and upon monolayer formation, a wound circumscribed to the electrode area was formed by exposing the cell layer to a high intensity and frequency electric pulse, after which the recovery process was monitored for the following 48 h. It is noteworthy that the smallest electrode diameter, 31 µm, falls in range with the size of a single cell. Due to the fact that the Lo-Ferrier model was developed for cell layers, it cannot be applied to the resulting impedance time courses, hence not included in the following results and discussion. On the other hand, measurements performed on the largest electrode of the array, 255 µm wide, were pooled together with those obtained on the 250 µm wide electrodes used for the experiments described in the previous chapter due to the comparability of the results.

Accordingly, figure 7.1 presents the recovery rates observed for WT, mDia1, mDia3 and dKo fibroblasts closing gaps of 250, 127 and 63 µm in diameter upon fitting the impedance time courses to a sigmoidal curve.

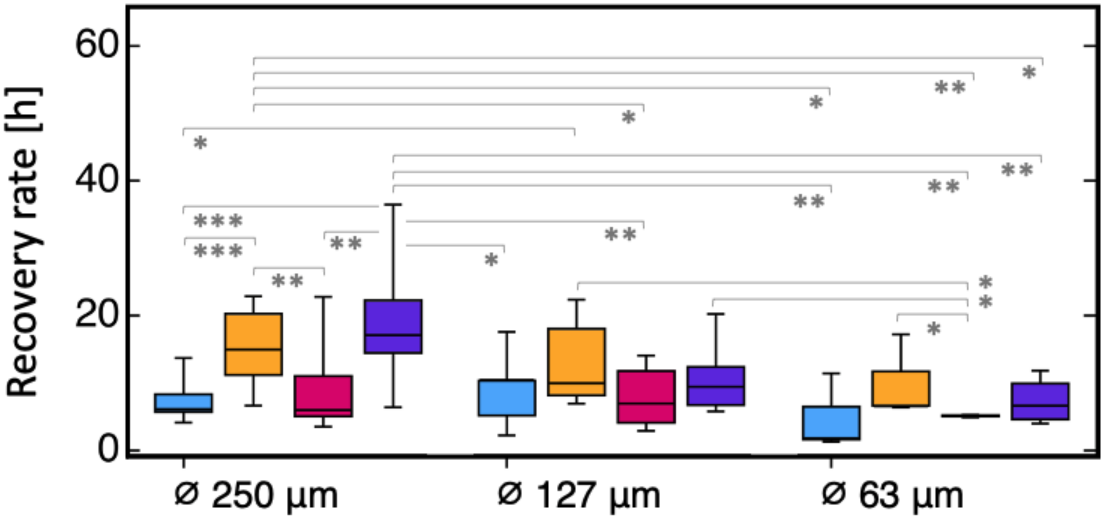

Figure 7.1: **Dependence of the recovery rate of fibroblasts on the wound size and formin modulation.** Values are presented for WT (■), mDia1 (■), mDia3 (■) and dKo (■) fibroblasts upon recovery from wounds spanning over a diameter range of 250, 127 and 63 µm ($n \geqslant 13$, $\geqslant 5$, $\geqslant 3$; $m \geqslant 4$). Regardless of the wound size, WT fibroblasts present the fastest recovery rate, followed by mDia3 cells and, with a larger delay, by mDia1. With respect to WT cells, mDia1 and dKo are significantly slower only in the closure of the largest wound size. Significance denoted with [*] for $\alpha < 0.05$, [**] for $\alpha < 0.01$, and [***] for $\alpha < 0.001$.

Within this range of wound sizes, a similar pattern was repeated for all wounds by which WT fibroblasts resulted the fastest in closing the open gaps, followed by cells

lacking the mDia3 formin isoform and, with a larger delay, by cells lacking mDia1. Such differences were more noticeable on the 250 µm diameter gaps, where WT and mDia3 cells presented a significantly faster recovery than mDia1 and dKo cells. In contrast, no statistically significant differences were observed within the 127 µm wounds and, within the 63 µm wounds, only when comparing the two single formin knock-outs. When comparing the behavior of the different cell lines across the range of wound sizes, only dKo fibroblasts presented a significantly faster recovery rate in the closure of 63 µm gaps than in the closure of 250 µm wounds. However, a decrease in the recovery rate with wound size was also observed for mDia1 cells.

Focusing on WT fibroblasts, figure 7.2 expands on the previous results by including recovery rate values obtained together with V. Scheller on 100 and 50 µm wide electrodes. As shown, a distinction appeared in the recovery rate when comparing the results obtained on 250 and 127 µm electrodes against those obtained on smaller electrodes by which larger wounds were closed slowlier. Accordingly, a wound size-depending discrimination in the recovery rate was found, with a threshold around the 100 µm wide gap.

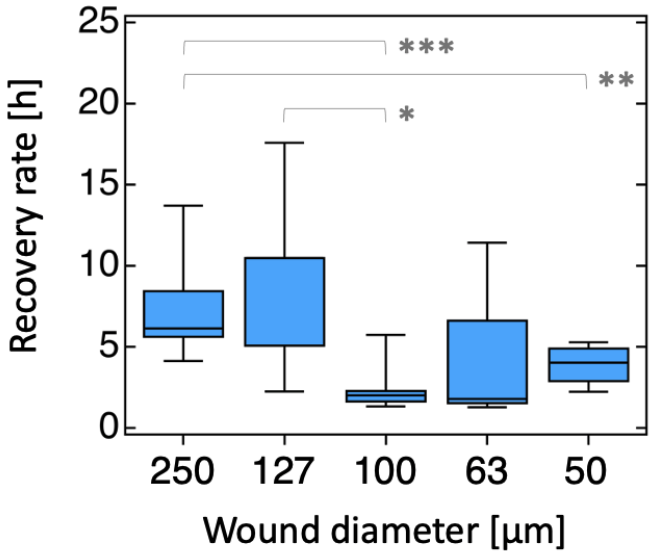

Figure 7.2: **Recovery rate of WT fibroblasts on wounds of different size.** Values are presented for WT fibroblasts upon recovery from wounds spanning over a diameter range of 250 (n = 20), 127 (n = 5), 100 (n = 7), 63 (n = 4) and 50 (n = 4; m $\geqslant$ 3 for all categories) µm. Larger wounds are closed slowlier, than smaller wounds, being the discriminating threshold around 100 µm wide gaps. Significance denoted with [*] for $\alpha < 0.05$, [**] for $\alpha < 0.01$, and [***] for $\alpha < 0.001$.

7.1.2 Identification of closure mechanism based on fluorescence microscopy

In order to identify the closure mechanism undertaken by WT fibroblasts during the healing of wounds of different sizes, fluorescence micrographs were obtained at different time points of the first 24 h of the recovery process. Figure 7.3 shows the re-colonisation of 250, 127 and 67 µm wounds, and the actomyosin distribution within the cells during the process.

As discussed in the previous chapter, 250 µm wide gaps were closed via the active crawling mechanism, characterised by the lamellipodia-based migration following leader cells. In the case of 127 µm wide gaps, almost no recovery could be observed 3 h after applying the wounding. However, at the 10 h time point, migrating cells with clear body polarisation and localised, discrete actin aggregations where focal adhesion were being formed could be observed. Despite the difference in wound size, and based on a qualitative assessment, at the 10 h time point both the 250 and 127 µm wide wounds presented a similar degree of area re-colonisation.

Focusing on the 67 µm wound, a divergent actomyosin distribution could be observed at the 3 h time point. In this case, myosin expression was highly localised following the periphery of the wound, and co-localised to actin filaments following the same disposition. The asterisk in the micrograph indicates a region where the co-localisation is better observed. Additionally, deformation of the cellular nuclei towards the center of the wound, hence centripetal, was observed on the fibroblasts at the wound perimeter. After 17 h of recovery, the entire surface of the wound was repopulated and showed multilayer formation, already detected at the 3 h time point where a small number of cells overlaid close to the wounded area as indicated by the triangles.

7.2 Discussion

7.2.1 Wound closure mechanisms of fibroblasts

In the *in vitro* study of 2D epithelial wound healing cellular dynamics, two closure mechanisms have been identified: cell crawling and purse-string contraction. In the first one, leader cells initiate migration towards the wounded area through multiple fronts in order to re-colonise it [18], whereas in the second one, cells at the edge of the wound establish supracellular actomyosin cables that allow gap closure via their collective contraction [20]. Both strategies were first identified in epithelial cultures, which constitute tissues

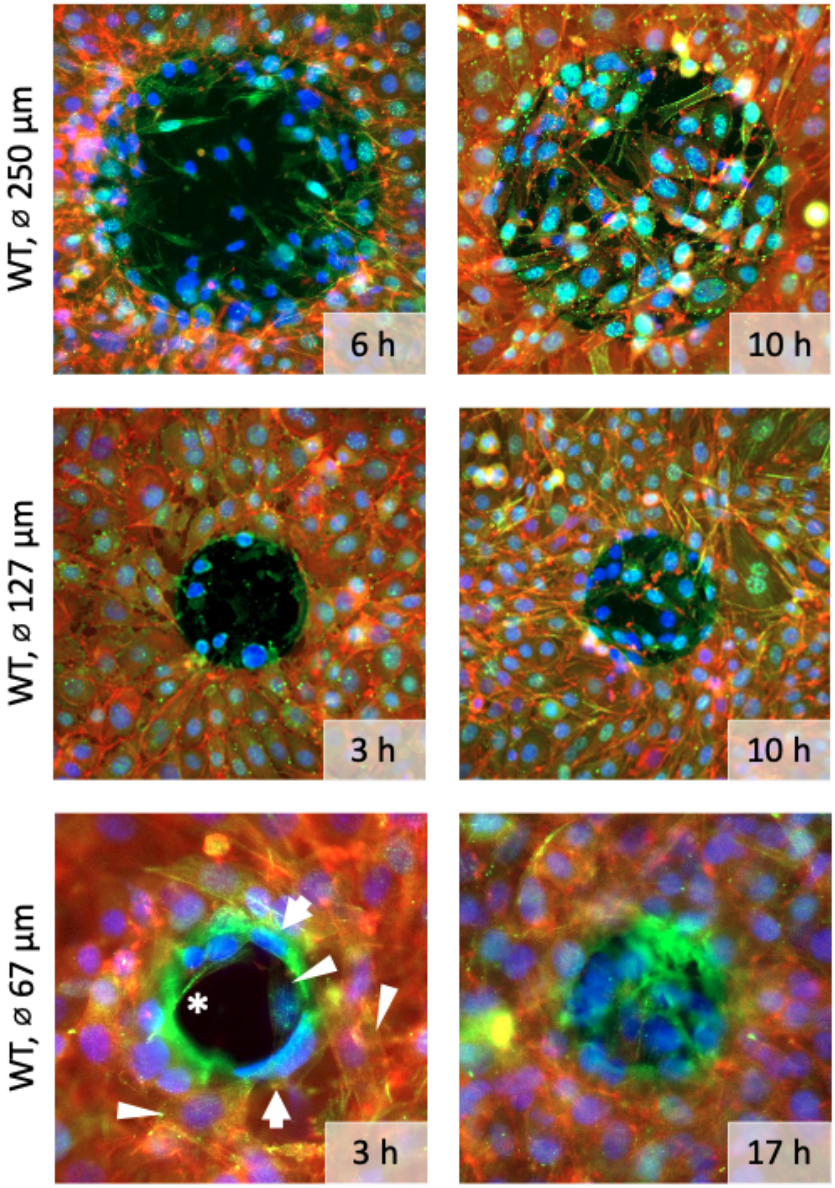

Figure 7.3: **Actomyosin distribution in WT fibroblasts closing gaps of different sizes.** Staining: actin filaments (red), myosin (green) and nuclei (blue). Micrographs present wounds of 250, 127 (both obtained at 40x magnification) and 67 (100x magnification) µm in diameter; inlets indicate post-wounding time stamps. Cellular polarisation and actin localisation at focal points suggest that larger wounds are closed via cell crawling. The centripetal nuclear deformation (arrows) observed on the 67 µm wound micrograph (3 h time point), together with the co-localisation of myosin and actin structures (*), potentially indicate the progression of a purse-string-like closure. Triangles point at multilayer formation.

prone to injury due to their barrier function, and have therefore become a widespread subject in the *in vitro* study of wound healing dynamics. In contrast, fibroblasts have been considered to target wound closure only via cell crawling [17], contributing to the idea that purse-string mechanism is exclusive to epithelial cells. However, recent findings challenge this view, as the architectural organisation characteristic of the purse-string strategy has been observed in fibroblasts on distinct scenarios: supracellular actomyosin cables have been identified in fibroblasts forming free-standing bridges in order to overcome up to 300 µm wide voids [19] and, in 3D systems, they have been detected in the advancing front of fibroblasts closing 3D clefts [21].

In an effort to better understand the wound closure capabilities of fibroblasts in 2D systems, ECIS-based wound healing assays have been used in this chapter in order to assess the influence of wound size on the cellular response. Wound size is known to be a decisive parameter -together with wound curvature and the physicochemical cues in the surrounding microenvironment- in determining the closure strategy that cells will follow upon injury: while epithelial cell crawling is commonly observed in the healing of large gaps expanding over several cell sizes, smaller wounds in the range of tens of microns to single-cell defects are closed through purse-string contraction [18, 30]. Accordingly, by employing ECIS chip arrays combining electrodes of different sizes, thus leading to circular wounds of different diameters, the ability of fibroblasts in producing supracellular actomyosin cables to close a gap via the purse-string mechanism was investigated.

In figure 7.1, the recovery rates of WT, mDia1, mDia3 and dKo fibroblasts on wounds 250, 127 and 63 µm wide were presented. In contrast to the recovery half time, which is dependent on the wound size as is delimited by the time interval defined between the wounding and recovery time points, the recovery rate is constant throughout the recovery process, which renders the parameter more suitable for the comparison of the recovery dynamics on wounds of different sizes. A lower recovery rate relates to a faster gap closure, thus leading to the same trend between this parameter (Fig. 7.1) and the recovery half time (Fig. 6.13). Accordingly, both figures show that on 250 µm wide gaps, the faster recovery was given for WT cells, closely followed by mDia3 and, significantly slower, by mDia1 and dKo cells. As discussed in the previous chapter, such results indicate that the mDia1 isoform is specially relevant to cellular migration. At the same time, the extensive delay in dKo recovery suggests that the single knock-outs may present compensatory effects.

The same pattern between cell lines was observed on the smaller wound sizes, but the differences became non-significant. In fact, on the smallest gap, almost no differences were observed between WT, mDia3 and dKo cells. It is thus conceivable that if the

smallest wound size promoted gap closure via purse-string contraction, dKo cells, which present defective migration, could result less impaired with respect to WT fibroblasts since motility would be less relevant to the healing process.

Interestingly, figure 7.2 indicates that the fastest recovery rate is given for the threshold wound diameter of 100 µm, thus rising the question whether the two mechanisms, cell crawling and purse-string contraction, could be simultaneously executed to provide a faster wound closure.

Although based on these results wound size is identified as a relevant parameter in promoting the purse-string mechanism in fibroblasts, it could have been supported by another geometrical cue: ECIS chips present an insulating layer that is 500 nm high, thus generating a step between the electrode (wounding area) and the surrounding cell layer. Even though for large wounds this increment results negligible, it is possible that the smaller the electrode, the more influential the step results by being detected by the cells as a 3D-like structure or an element of substrate micropatterning which, in turn, could elicit the activation of the purse-string mechanism.

7.2.2 Influence of the wound closure mechanism on the integrity of the resulting cellular layer

Assuming correlation between the closure mechanism and the differences in recovery rate, it is also conceivable that variations would arise in the properties of the semi-recovered cell layer. To test this hypothesis, the Lo-Ferrier model [25] was applied in order to compare the R_b, C_m and α parameters of WT, mDia1, mDia3 and dKo cells on wounds corresponding to the two distinct regimes shown by figure 7.2, specifically, 250 and 100 µm wide. These results are presented in figure 7.4, where the values acquired 48 h post-wounding are normalised to the pre-wounding levels.

In this figure, a clear difference in the recovery of the pre-wounding levels as well as in the effect of the suppression of formin isoforms was observed in dependence to wound size. On smaller wounds, recovery of the pre-wounding R_b and α values was found for all cell lines, whereas C_m values were only recovered by WT cells. This suggests that the cell lines containing formin deletions could present alterations in the surface of the cell membrane or in its lipid composition. Interestingly, after 48 h of recovery, mDia1 cells showed higher values than at the pre-wounding stage, whereas the inverse behavior was shown by mDia3 and dKo cells, thus suggesting involvement of the formin isoforms in different cellular functions.

On larger wounds, only R_b values were recovered by all cell lines except for mDia3

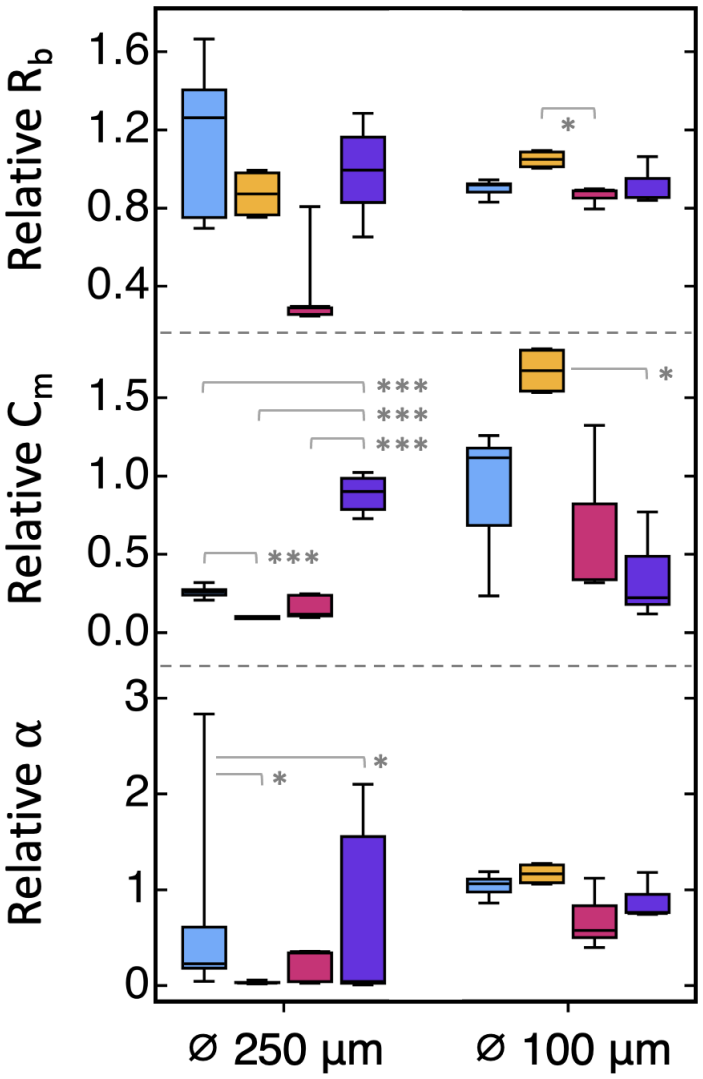

Figure 7.4: **Cell layer properties upon recovery on wounds of different sizes.** The parameters R_b, C_m and α, derived from applying the Lo-Ferrier model and obtained after 48 h of recovery on 250 (n $\geqslant$ 4; m $\geqslant$ 3) and 100 (n = 3; m = 3) µm wide wounds, are relativised with respect to the pre-wounding levels for WT (■), mDia1 (■), mDia3 (■) and dKo (■) fibroblasts. The evolution of the parameters indicates different behaviours in dependence to wound size and formin modulation. On smaller wounds, pre-wounded values are recovered by WT cells and exceeded by mDia1 cells, whereas on large wounds, WT cells present recovery of only R_b values, whereas dKo cells show pre-wounding values for all parameters. Significance denoted with [*] for $\alpha < 0.05$ and [***] for $\alpha < 0.001$.

cells. In fact, WT fibroblasts presented $R_b \geqslant 1$, which could indicate fibrosis progression. This phenomena is not observed on the smallest wound size, hinting at the possibility that fibrosis could be linked to the active crawling closure mechanism. Alternatively, it is also possible that in small wounds, the cell-cell connectivity is not significantly disrupted. In addition, and as discussed in the previous chapter, the lower C_m and α values could be consequence of the increase in cell density upon recovery, which could lead to a smaller degree of cell spreading and fluctuations in the cell-substrate distance. In this case, the morphological differences of the dKo cells, which spread over larger areas, could justify the differences with respect to WT behavior. All together, the different patterns in the evolution of R_b, C_m and α upon the healing of wounds of different sizes support the idea that cell layer integrity reflects the co-existence of different mechanisms in gap closure.

Aiming to provide visual support to the observations pointing at the ability of fibroblasts to close wounds via the purse-string mechanism, immunostaining of the actomyosin structures of WT fibroblasts was performed at different time points while closing wounds of 250, 127 and 63 µm in diameter. As established, WT fibroblasts closed 250 µm wide wounds via cell crawling. Fluorescence micrographs showing re-colonisation progression on 127 µm wide gaps indicated that the same mechanism was followed, since actin aggregations at the focal adhesions forming at the advancing front of polarised cells were identified, hence in agreement with the characteristics of the mechanism. In contrast, micrographs on 67 µm wide wounds did not show polarised cells migrating towards the center of the wound. Instead, fibroblasts at the perimeter of the wound had smooth edges -hence no protruding migrating cells- and, in addition, some of them presented centripetal nuclear deformation, which could be a consequence of lateral tensions following the wound perimeter. Such forces could be provided by the contraction of actomyosin cables, the presence of which is supported by the increased expression and, more importantly, the co-localisation of myosin and actin markers at the wound edge.

In order to provide conclusive proof that fibroblasts are able to heal wounds following the purse-string closure mechanism, a quantitative evaluation of the fluorescence micrographs with increased number of experimental replicates should be performed. However, together with the behavioral differences observed on wounds of different sizes provided by the analysis of the recovery rate and of the properties of the cell cultures upon recovery, the qualitative analysis of the fluorescence micrographs here presented is enough to suggest that the purse-string mechanism may not be exclusive to epithelial cells, and that fibroblasts may be able to follow it for the closure of small quasi-2D wounds. In this regard, when studying the healing mechanisms of wounded fibroblast cultures, Sakar *et al.* were able to observe purse-string contraction-mediated wound closure only on sus-

pended cultures. In contrast, and as demonstrated via blebbistatin assays that inhibited the action of myosin II motors and therefore prevented the contraction of actomyosin cables, 2D cultures followed a different mechanism [22], presumably cell crawling. Possibly, the reason behind it is that in their 2D assays, the scratch-based wounds that they performed had dimensions of 100 x 200 μm^2, thus exceeding the size of the geometrical cue triggering the purse-string mechanism. However, it is also possible that the relevance of the height step generated by the insulating layer of the ECIS chips, hence missing in the setup of Sakar *et al.*, provides a sensitive triggering effect.

Conclusions

In summary, even though the purse-string mechanism has been traditionally ascribed to epithelial cultures, recent literature and the observations herein presented support the idea that fibroblasts may be able to exert it as well. In this chapter two distinct recovery dynamics have been shown in dependence to wound size: with a boundary diameter around 100 µm, fibroblasts closing small wounds present a faster recovery rate than on large wounds. Based on fluorescence imaging, which allowed the identification of actomyosin structures characteristic of cell crawling and purse-string contraction, both mechanism would take place, respectively, in the closure of large and small wounds. This idea is further supported by the differences in integrity of cell layer upon recovery from wounds of different size. In this regard, the comparison of cell lines with different formin modulation suggest that each formin isoform may play specific roles depending on the closure mechanism, further discussed in the next chapter.

Chapter 8

Transectional discussion

Throughout the four results chapters composing this thesis, the findings on the cortical properties and the wound healing dynamics of WT, mDia1, mDia3 and dKo fibroblasts have been individually presented and analysed. Biophysically, however, both aspects are tightly related: the wound healing process involves cell migration [52], proliferation and even cell differentiation [7], the three of which require extensive cell morphology adaptations and, therefore, a stringent control and regulation of the actomyosin cortex [10, 11]. Accordingly, the aim of this transectional discussion chapter lays on examining the correlations between the two biological aspects -the cortical rheology and the wound closure dynamics of fibroblasts- and, in addition, determine the relevance of formins in the subject.

8.1 Impact of cortical rheology in wound healing dynamics

In the first two results chapters of this thesis, the rheological properties of the actomyosin cortex of fibroblasts were described in dependence to formin modulation and degree of cell adhesion. Simultaneously comparing both aspects, figure 5.5 indicated that for weakly adherent cells, the lack of formin isoforms led to lower pre-stress while, for strongly adherent fibroblasts, the contrary was observed. These differences increased, in this order, for mDia3, mDia1 and dKo cells. Accordingly, from the two isoforms, mDia1 resulted more essential for the maintenance and regulation of the actomyosin cortex. Moving to the results chapters focusing on the collective dynamics of fibroblasts during wound recovery, figures 6.13 and 7.1 indicated that for a range of wound sizes, the lack of mDia1 led to longer delays in recovery than the lack of mDia3. The fact that the pattern in cortical rheology arising from the different formin modulations was conserved

in the dynamics of wound closure, specially when involving mDia1, hints at a strong correlation between the two cellular aspects.

A bidirectional regulatory interplay exists between the cortical stress and the membrane tension [177, 178]. In translocation events such as migration, however, this relation is poorly understood. Generally, a higher displacement speed and directionality has been observed in cells upon increasing their membrane tension. Mechanistically, this phenomena has been ascribed to the ability of the tensed membrane to confine cellular protrusions, such as lamellipodia, towards a specific front. Figure 8.1 illustrates this regulatory activity, synergistically inhibiting protrusion formation far from the leading edge, and confining neighbouring protrusions to further promote cell polarisation [177].

Excessive membrane tension, however, can result detrimental to cell migration. Actin polymerisation is stalled against the membrane [177, 178], but if adhesion to the substrate is also weakened, high membrane tension can also cause retrograde cellular flow: slippage between the cytoskeleton and its substrate adhesion complexes leads to cellular displacement away from the leading edge [177]. Accordingly, and exclusively considering the membrane contribution in the process, an intermediate tension could optimally promote migration speed as illustrated in figure 8.2.

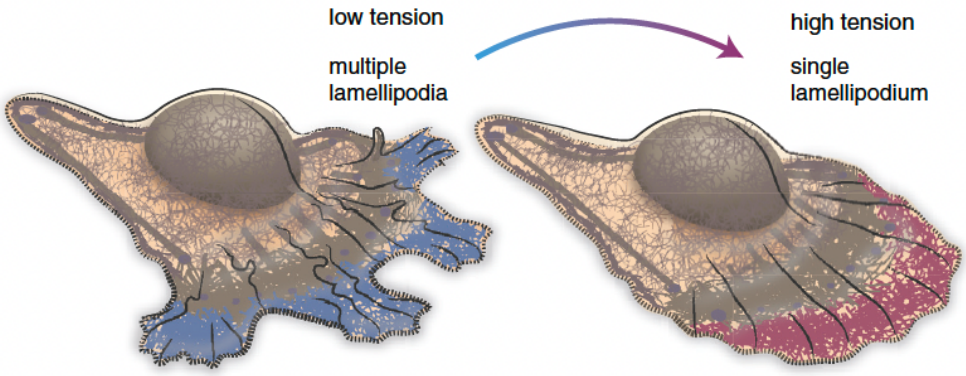

Figure 8.1: **Contribution of the cell membrane tension to cell polarity.** The degree of membrane tension can allow the co-existence of several lamellipodia fronts (low tension) or promote their coalescence and directionality (high tension). Reprinted with permission from [177].

Fully spread dKo fibroblasts present a characteristic tent-like morphology that is acquired upon expressing several lamellipodial fronts pointing at different directions, thus displaying lost polarity. As shown in the results of this thesis, the latter, characteristic as well of single mDia1 and mDia3 knock-outs, could be the result of a very low membrane tension (Fig. 8.2). This could interfere with cellular migration and lead to

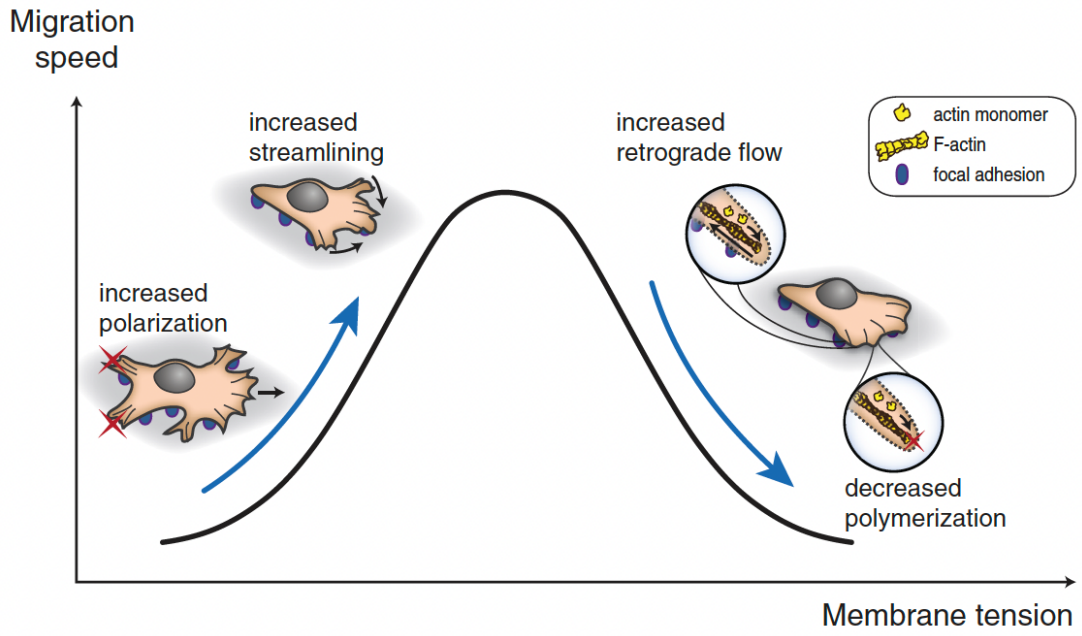

Figure 8.2: **Influence of membrane tension in migrating speed.** Very low membrane tension leads to defects in polarisation that act in detriment of migration, whereas very high membrane tension can interfere with actomyosin polymerisation or cause retrograde flows, thus pointing at an intermediate membrane tension leading to optimal migration speed. Reprinted with permission from [177].

the slow recovery rates observed in ECIS-based wound healing assays when compared to WT fibroblasts (Fig. 6.13). Due to their tent-like spreading, dKo fibroblasts also present a cell-substrate area that is significantly larger than that of spindle-like WT fibroblasts. To support such expansion of the geometrical area, it can be assumed that upon adhesion, dKo cells retain little to no internal membrane reservoirs, and membrane tension is maximised. Membrane tension T_t arises from its in-plane stress due to membrane inextensibility, and from the tension resulting from its attachment sites to the actomyosin cortex [177]. Accordingly, even if the membrane is expanded to its limit, membrane tension could be relatively low if its attachment to the actomyosin cortex is impaired due to loss of formins, thus allowing the co-existence of multi-directional protrusions in a widespread tent-like dKo cell.

As already advanced in the introduction of this section, the lack of Diaphanous-related formin isoforms led to a pattern in the rheology of the actomyosin cortex (Fig. 5.5) that was linked to the recovery rate of large wounds (Fig. 6.13). Normal behaviour (WT) was specially impaired by the lack of mDia1, which presented a negative synergistic effect with mDia3 in dKo cells.

In the following sections, the specific roles of mDia1 and mDia3 will be briefly presented, to later discuss their specific contribution to the regulation of cortical rheology and wound closure kinetics.

8.1.1 The roles of mDia1 and mDia3

In the last years, mDia1 has been described, together with the Arp2/3 complex, as the larger contributor to **cortical actin** [180, 183]. Even though mDia1-nucleation produces only 10 % of the cortical filaments in HeLa cells, these account for 20-25 % of the total actin network since they are 10 times longer than the filaments produced by Arp2/3 [180]. Such different distributions suggest that the actions of the two actin-nucleators produce actin architectures with specific functions within the actomyosin cortex. Scanning electron microscopy analysis has further indicated that mDia1 inhibition leads to inhomogeneous cortices with areas of high filament density and 100-200 nm gaps devoid of actin filaments. In contrast, depletion of Arp2/3 leads to cortices with longer filaments [183]. Fritzsche *et al.* have suggested that the long mDia1-nucleated filaments provide mechanical integrity by distributing stress loads over length scales comparable to that of the cell size [180]. In fact, in combination with the Rho-associated kinase ROCK, which has a bundling function, mDia1 carries **stress fiber formation** [199, 200]. Computational modeling analysis has indicated that decreasing the density of crosslinks in stress fibers could result in the dissipation of myosin contractility by causing slippage of actin filaments, hence impairing the transmission of forces from and to the ECM [201]. It is possible that the lowering of F-actin density in stress fibers caused in the absence of mDia1 led to similar results. It is worth noticing that Arp2/3 can also nucleate stress fibers. However, while those nucleated by mDia1 connect the dorsal cortex to the substrate, Arp2/3 leads to transverse arcs connected at the lamella [200]. These observations are in line with a a role of mDia1 crucial in the overall regulation of the actomyosin cortex.

In order to sense their external environment, cells form **filopodia**. These highly dynamic protrusions are cooperatively formed between formins and the Arp2/3 complex: Arp2/3 creates a base of branched actin, from which long filaments can then be nucleated by mDia2 or mDia3 [202]. However, it has been also suggested that while these isoforms could initiate nucleation, mDia1 could be responsible for filament elongation [194]. Similarly, cooperation between the actin nucleators has also been found in the formation of **lamellipodia** though, in this case, mDia1 localises in nascent and mature membrane ruffles to provide the base for sequential Arp2/3 branching. Formation of

membrane ruffles is believed to be mDia2- and mDia3-independent [190].

Both mDia1 and mDia3 have been linked to the regulation of microtubule anchoring in a non-redundant manner [203]. Microtubules participate in cellular migration by contributing in establishing directionality of **cell polarity** [204], and in the regulation of **adhesion turnover** [203], both essential for effective migration. Via the interaction with microtubules and the nucleation of actin filaments, mDia1 is able to direct recruitment of the molecular machinery necessary to promote cellular polarisation and disassembly of focal adhesions [205].

In B16-F1 mouse melanoma cells, expression of active mDia1 and mDia3 has been localised at the rear cortex of polarised cells [16]. During normal cell migration, cortical tension is higher in this region, powering **cell body retraction** [10]. It can therefore be argued that if the cortical mesh is compromised, it will have a negative impact in the effective retraction of the cell body during migration, thus potentially reducing the speed of cell displacement.

8.1.2 Influence of mDia1 and mDia3 in the regulation of the cortex and wound closure kinetics

Even though a disparity exists between the level of description and extent of knowledge on mDia1 and mDia3 functionality, literature reflects their tight involvement in the regulation of the cellular cytoskeleton both in static and dynamic scenarios.

Considering the contribution of mDia1 to the bulk of the cortical actin, the resulting impoverished cortex in its absence would be expected to present less resistance to external deformation. This is exactly what the rheological properties obtained from compression-relaxation force curves on weakly adherent fibroblasts reflected in figure 5.5. At a minor extent, the same was observed for mDia3, hence indicating its (smaller) contribution to the nucleation of cortical actin. In contrast, for strongly adherent cells, an increase in the prestress was observed. As previously discussed, however, this stands in agreement with the effects of a defective cortex since it could make accessible the contribution of cellular organelles in the force measurements. In addition, in the absence of long actin fibers, the activity of myosin motors could cause the excessive contraction of the cortex due to defective force distribution within the cell.

Both mDia1 and mDia3 participate in cellular polarisation and in the retraction of the rear end of the cell body. The hampering of either process would result in impaired migration and undefined polarised front. Additionally, mDia1 regulates lamellipodia and

adhesion turnover. Accordingly, its absence further obstructs the process by limiting the formation of new adhesions at the cell front, and by retaining the focal adhesions at the cell rear. These differences in the involvement of mDia1 and mDia3 could explain the increased delay observed in the recovery of mDia1, compared to the recovery of mDia3.

Moreover, the two isoforms participate as well in the formation of filopodia. In the absence of formins, these structures can be formed by the over-activation of secondary components [202]. MDia1 and mDia3 also present compensatory over-expression upon deletion of one of the forms [16, 93], which probably extends to other formins. Accordingly, both aspects could contribute to the increased magnitude in the micromotions of dKo cells (Fig. 6.7) which, upon exposure to the general formin inhibitor SMIFH2, is no longer detected.

Finally, in the absence of mDia1, stress fibers promoted by the Arp2/3 complex could result more prominent. In U2OS osteosarcoma cells, Arp2/3 leads to transversal arcs that are thicker compared to mDia1-nucleated stress fibers. This difference could justify the prominent actomyosin structures observed in migrating dKo cells (Fig. 6.4).

In conclusion, and based on the observations made in this section and on the results presented throughout this thesis, the following interconnection between cortex and wound closure is proposed: in the absence of mDia1 and mDia3, the actin mesh conforming the cortex is impoverished which, in strongly adherent fibroblasts leads to an excessive cortical contraction facilitated by the absence of long actin fibers capable of force distribution. Simultaneously, and triggered by the chemical cues inducing a wound closure response, migrating cells present defective polarisation with multiple fronts, and defective rear end contraction. In cell lines lacking mDia1, this migration is further impaired by a reduction of the focal adhesion turnover at the rear of the cell, which retains the cell anchored in position, and lamellipodia formation at the advancing front. Collectively, these defects cause delayed wound closure for mDia3 and, at a major extent, mDia1 cells. In the absence of both isoforms, hence preventing compensating over-expression of the remaining form, dKo cells show even more impaired recovery.

8.2 Role of formins in the wound closure mechanisms

The involvement of formins in cellular migration, relevant during wound closure via cell crawling, has been thoroughly discussed. Their participation in the purse-string mechanism, however, is less clear. Purse strings are involved in several biological processes,

including cell division, morphogenesis, and single- and multiple-cell wound healing [206]. Consensus is that formins, as Rho effectors, are involved in the process, but which specific forms and the underlying generalised mechanism are still open topics.

In eukaryotic cytokinesis, mDia2 depletion leads to 40 % failure of cell division due to interference with nucleation and elongation of actin cables, whereas in the absence of mDia1 and mDia3, the process is not significantly affected [207]. Interestingly, the indirect participation of the Arp2/3 complex has been shown to be necessary for optimal cell division in *Caenorhabditis elegans*: in the absence of the complex, formins nucleate excessive cortical F-actin, detrimental to the necessary geometrical adaptations [208]. Accordingly, not only the role of the formins directly participating in the formation of the cables could be relevant for optimal purse-string contraction also in mammals.

Regarding the mechanism itself, purse-string contraction could involve different strategies. For example, wounding of *C. elegans*' dermis has shown closure via actin rings that are independent of myosin II activity. In this case, microtubule recruitment at the wound periphery is necessary for the formation of Arp2/3-mediated actin rings that close the gaps in the skin of the worms via branched actin polymerisation [209]. Both in single- and multiple-cell wounds, microtubules have also been shown to be essential for actomyosin recruitment and wound closure in *Xenopus laevis* frog oocytes and tadpoles. In both cases, microtubule disposition is perpendicular to actomyosin direction, hence resembling their distribution during cytokinesis [210].

Furthermore, purse string contraction can take place both in the presence and absence of substrate adhesion. For this reason, it is also unclear to which degree purse string and lamellipodial formation can cooperate during wound healing. Both mechanisms have been observed taking place during gap closure in MDCK II epithelial sheets. In apoptotic extrusion, early formation of lamellipodia allows the orientation of actomyosin purse strings, which are discontinuously distributed. Le *et al.* ascribe the ratio of the two structural arrangements to an equilibrium between radial forces pointing outwards, provided by lamellipodia, and tangential or radially inwards, originating from the purse-string cables. Towards the end of the closure, the balance favors lamellipodial protrusions [211]. A similar progression has been observed during wound closure, with a balance between lamellipodial protrusions and purse-string cables. In this case, Ajeti *et al.* observed that in the transition from one architecture to the other, the average force is maintained and that the actin filaments in the lamellipodia are integrated as cable filaments when the lamella overcomes the lamellipodial edge [212].

Such a mechanistic variability with respect to the canonical myosin II-dependent contractile actin cable, summarised in table 8.1, indicates the possible existence of sec-

ondary approaches for wound closure that could result activated in the down-regulation of formins. One of the essential characteristics of actomyosin cables is that these are supracellular structures that connect the cells at the rim of the wound. Accordingly, the strain is transmitted through the cells, which requires of cell-cell connections that allow the anchoring and propagation of the cables and constricting forces: adherent junctions. In fact, interference with E-cadherin-based adherent connections leads to disrupted actomyosin cables in epithelial wounds [213], which can render closure fully dependent on lamellipodia extension [211].

Results presented in this thesis have shown that in the absence of mDia1 and mDia3, no significant delays can be observed in the closure of small wounds, believed to be carried via purse-string contraction. Together with the literature available, these suggest that it is unlikely that either of the isoforms actively participates in the formation of actomyosin cables. However, they could participate in the organization of the microtubules supporting the formation and orientation of the purse-string, which could lead to the small delays in recovery observed in knock-out cells (Fig. 7.1). Furthermore, absence of mDia1 could negatively impact wound closure if lamellipodia did indeed contribute to the process. This cooperation could be more pronounced in the closure of wounds of intermediate size, hence at the threshold differentiating closure dictated via cell crawling or purse-string contraction. Accordingly, for these wounds (100-127 µm), delay in mDia1 cells should be more pronounced due to the participation of the isoform in lamellipodia formation [190] which, in fact, is reflected in figure 7.1. Finally, as previously discussed, dKo cells present impaired cell-cell connectivity due to the involvement of mDia1 in the formation of cadherin-mediated contacts [188], and due to the favorable effect that adherent and gap junctions present in their formation [193]. Therefore, mDia1 knock-outs could present delayed recovery due to the direct interference with the formation of the supracellular actomyosin cable in the presence of defective adherent junctions.

8.3 Transcellular macroapertures

NIH 3T3 fibroblasts presenting the double mDia1 and mDia3 knock-outs are characterised by their spreading tent-like morphology, but also by the spontaneous formation of transient transcellular macroapertures (TMs). As shown in figure 8.3 (also previously in 6.5), these appear as tunnels of varying sizes connecting the apical and basal cellular membranes until, eventually, are closed.

Table 8.1: **Mechanisms in gap closure**. Gap closure is driven, depending on the organism, tissue and gap properties, by a number of mechanisms involving purse string (PS), lamellipodia (L), and microtubule (MT) participation.

Cell or tissue	Type of gap	Closure mechanism	Formula	Reference
C. elegans	Dermal closure	Arp2/3-actin L waves with MT support	-	[209]
X. laevis	Single- & multiple-cell defects	F-actin and myosin-II PS with MT support	-	[210]
MDCK II	Apoptotic extrusion	L orients discontinuous PS, with balance of radial and tangential forces	$\sigma_{r=R(t)} = P_c + \sigma_P + \sigma_\mu + \frac{\tau}{R(t)}$	[211]
MDCK II	Adherent wound closure	L and PS, with constant effective power & total F-actin	$W = \Sigma\omega$	[212]
NIH 3T3 Fb	3D microgap	Cellular recruitment, active ECM synthesis and PS closure	-	[19]
Primary NHDF	3D cleft	FMT at advancing front with actin cable at the edge	-	[21]
NIH 3T3 Fb	Wounded suspended microtissues	Tangential cellular recruitment with active ECM synthesis	-	[22]

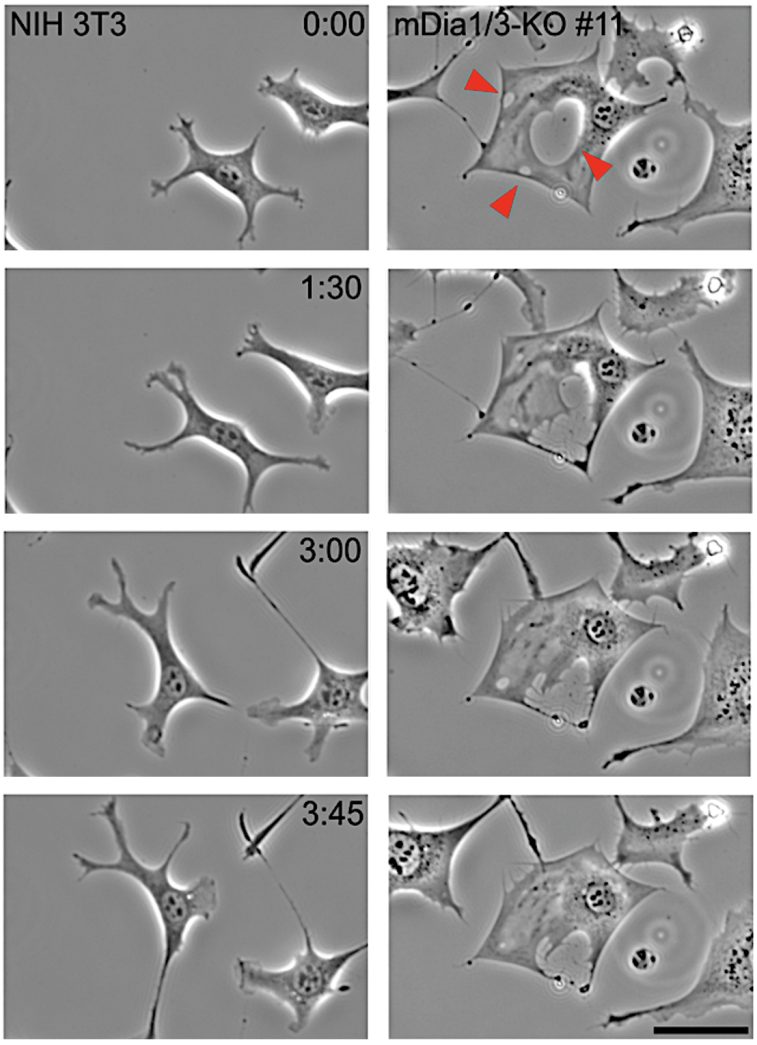

Figure 8.3: **Transcellular macroapertures.** Phase contrast live imaging of WT and dKo NIH 3T3 fibroblasts. DKo cells present a tent-like morphology and can show several TMs simultaneously (red arrows) that are independently closed. Scale bar: 50 µm; time indicated in h:mm.

The formation of transcellular tunnels in homeostatic conditions is common and contributes to the balance of body fluid and particle exchange in the endothelium, the inner cellular lining separating blood vessels from the neighbouring tissues. These transendothelial cell macroapertures (TEMs) can be also triggered by pathogens as a mechanism to rupture the endothelial barrier. This is the case for the bacteria *Staphylococcus aureus* [214] and *Bacillus anthracis*, responsible for anthrax disease [215]. Despite producing toxins with different molecular targets, both pathogens inhibit the function

of the small GTPase RhoA, which regulates actomyosin contractility and formation of stress fibers [216]. As shown in figure 8.4, due to the disruption of the cortex, the intoxicated cells acquire a spread tent-like morphology -like dKo fibroblasts- that leads to an increase in membrane tension. Boyer *et al.* have suggested that TEMs could therefore arise from pores formed by the contact between the apical and basal cell membranes, the fusion of which would be promoted by the flattening and spreading of the cells and the depletion of actin stress fibers [214, 216].

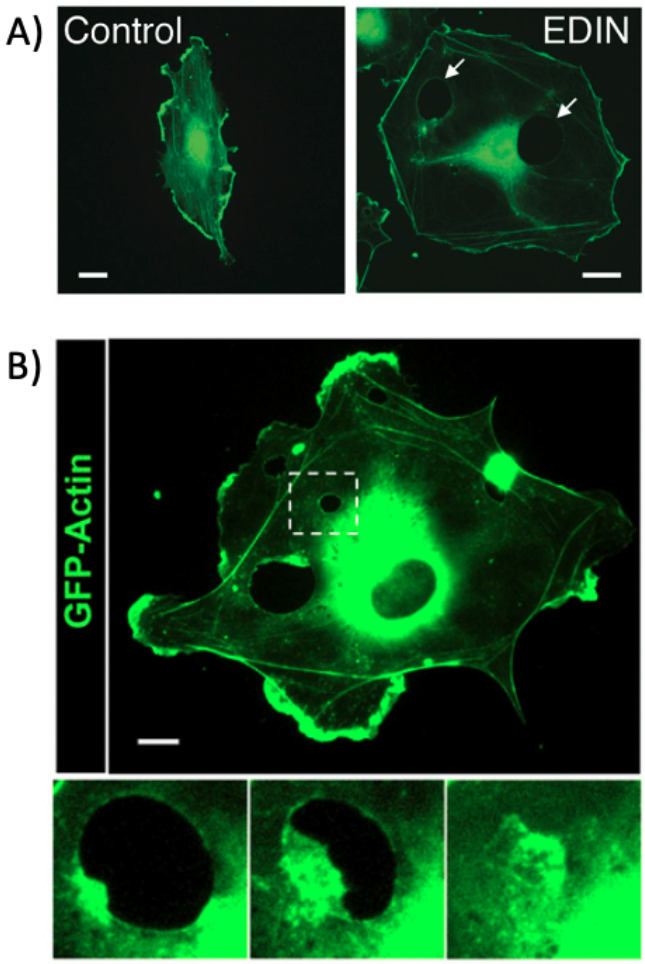

Figure 8.4: **Transendothelial macroapertures.** TEM closure in human umbilical vein endothelial cells (HUVECs) presenting fluorescently-labeled actin. **A)** Effect of intoxication with epidermal cell differentiation inhibitor (EDIN), produced by *Staphylococcus aureus*. Upon intoxication, cells lose their normal elongated morphology to acquire a tent-like architecture. A single cell can present several TEMs simultaneously (arrows). Reprinted with permission from [214]. **B)** Effect of intoxication with the edema toxin produced by *Bacillus anthracis*. Inlets at the bottom panel show the TEM closure via the formation of actin-rich waves. Reprinted with permission from [215]. Scale bars: 10 µm.

Once the formation of a TEM has been initiated, its widening resembles viscous liquid dewetting. Accordingly, it is accompanied by the formation of an actin-rich rim around the gap that, due to its stiffness, stabilises TEM expansion. Simultaneously, its curvature promotes the recruitment, in a time frame of 0.2 s, of the I-BAR domain of the protein Missing in Metastasis (MIM), which triggers the recruitment of Arp2/3 and sequential polymerisation of branched, lamellipodia-like actin membrane waves that will close the TEMs [215, 217] (Fig. 8.4).

Given the morphological similarities between the dKo fibroblasts and the intoxicated endothelial cells, it is conceivable that both transcellular tunnels could share a common mechanism. However, while TEMs are actively induced by toxins or internally regulated cellular processes, the aperture of TMs is passive. Furthermore, some phenomenological differences exist. TEMs show a maximum size upon which their enlargement stops ($\sim$10 µm) regardless of the pathogen inducing their formation [214, 215]; additionally, the total duration of TEM opening and closure is below 10 min [215, 216]. In contrast, as shown in figures 6.5 and 8.3, TM occurrence overcomes both limits: besides expanding over lengths beyond 10 µm, TMs can remain open over 1-3 h. This differences suggest that fibroblasts undertake a different closure strategy in order to seal TMs. In this regard, MIM knock-out cells have shown a delay in TEM closure of 30-80 min [215]. The resulting proximity to life-times characteristic of TMs suggest that their closure could be passively achieved.

The size constraint in TEMs is facilitated by the rigidity of the actin ring formed at the edge of the tunnels. In dKo cells, the formation of the ring could be disrupted, which would facilitate the expansion of TMs beyond 10 µm. Furthermore, in advanced stages, TMs lose the circular smoothness characteristic of TEMs, which supports the idea that the formation of the actin ring could be impaired in dKo cells. Inhomogeneities in the density of the cortex caused by the lack of mDia1 [183] could further promote the initiation of TM formation by facilitating the contact between the apical and basal cell membranes of dKo cells.

Summary

In this thesis, the relevance of mDia1 and mDia3 formins in wound healing dynamics of NIH 3T3 fibroblasts and in the cortical adaptations involved in the adhesive process have been investigated. To guide the research, four questions were stated at the beginning of this work. In this summary, they will be answered while highlighting the main results of the thesis.

I. How do the rheological properties of the actomyosin cortex adapt during cell adhesion?

While in suspension, fibroblasts adopt a globular shape through cortex contraction that leads to high prestress, but simultaneously preserve high fluidity to readily interact with the surroundings and initiate adhesion. When this happens, cellular prestress decreases, thus allowing the formation of a first cell-substrate contact area. At the same time, this relies on a low membrane tension that supports the formation of blebs and protrusions. To spread, the cell fluidises and ensures membrane integrity. Depletion of membrane reservoirs promotes the re-organisation of the cortex and the formation of hierarchical actomyosin structures. Consequently, prestress increases with the stabilisation of the cytoskeleton.

To carry this characterisation work, the experimental and analytical methodologies, based on the application of the Evans model, were optimised. In the process, the influences on cortical dynamics of blebbistatin and calyculin A, which alter the activity of non-muscle myosin II motors, and of GDA, which causes cross-linking and stiffening of the membrane, were analysed, further supporting that the cellular response to deformation is dominated by myosin II motor activity and contractility.

II. What is the role that mDia1 and mDia3 play in the regulation of the cortical adaptations upon (de)adhesion?

In the absence of formins, and especially in the lack of mDia1 which, together with the Arp2/3 complex, nucleates the bulk of actin filaments, the cortex results impoverished. In a weakly adherent state, this translates into an increasing degree of vulnerability to external deformation for mDia3, mDia1 and dKo cells. In an adherent state, cortical deficiencies additionally lead to slower relaxation times of the cortical shell due to the absence of long, linear and formin-nucleated actin filaments.

III. How is the activity of formins impacting the motile capabilities of fibroblasts during cell migration?

The migrating process can be simplified, based on its inherent adhesion-deadhesion cycle, into the transition from strongly to weakly adherent cells and vice versa. While both mDia1 and mDia3 are necessary for the formation of filopodia at the advancing edge of migrating cells, and they co-localise at the rear end to promote adhesion turnover, mDia1 is additionally involved in cellular polarisation and rear end retraction. Furthermore, due to the cortical defects in the spreading state, knock-out fibroblasts present an unbalanced adhesion strength that further hampers motility. As a consequence, migration results increasingly impaired in the absence of mDia3 and of mDia1. Additionally, both isoforms show compensatory effects, which causes a higher defective motility in dKo fibroblasts.

IV. Are fibroblasts able to close wounds via the purse-string mechanism, and is gap size a relevant geometrical trigger?

In this thesis, the ECIS has been employed, for the first time, in combination to electrodes of varying diameters, immunostaining and formin knock-out cell lines, to assess the possible connection between geometrical cues and the wound closure mechanisms of fibroblasts. As a result, two closure rates have been identified in relation to the wound size. While larger gaps are closed via cell crawling at a slower pace, structural elements of the purse-string mechanism, traditionally ascribed to epithelial cultures, have been identified in the closure of small wounds, thus supporting recent literature reports. Furthermore, both mechanisms could co-exist in the threshold wound diameter (100 µm), hence contributing to a faster closure.

Due to the essential role that formins play in cellular motility, their impact in the closure of small wounds, directed via purse-string contraction, is significantly reduced.

In conclusion, this work has demonstrated the close interplay between cortical mechanics and recovery kinetics of fibroblasts, and the relevance of formins in the regulation of both processes. The answers to the four research questions stated above contribute to the basic knowledge that, one day, may lead to the development of effective biomedical strategies to enhance the natural healing response, and thus reduce the risk of derived complications such as hypertrophy or fibrosis. With this, the present thesis ultimately aims to contribute to the eradication of CVDs, limiting their prevalence and impact in the worldwide population.

As a personal and final comment, a day may come when this goal is achieved. However, it is not this day. Accordingly, the author would like to remind the reader that today's lifestyle, where a poor diet, stress and long working hours tend to combine with a lack of physical exercise, is a major factor leading to the suffering of CVDs. Hypertension, high cholesterol and smoking are still regarded as the main risk factors, accompanied by sedentary behavior, consumption of alcohol and refined sugars, overweight, obesity, and diabetes. Accordingly, it seems to be a good ending note to remind you, the reader, to lead a healthy life and thus make you a participant in the eradication of CVDs.

Bibliography

[1] World Health Organization (WHO). (2021). Cardiovascular diseases (CVDs). Retrieved from www.who.int/news-room/fact-sheets/detail/cardiovascular-diseases-(cvds). (Accessed: 14.09.2021)

[2] Ripplinger, C. M., Lou, Q., Li, W., Hadley, J., & Efimov, I. R. (2009). Panoramic imaging reveals basic mechanisms of induction and termination of ventricular tachycardia in rabbit heart with chronic infarction: Implications for low-voltage cardioversion. *Heart Rhythm*, *6*(1), 87–97. doi:10.1016/j.hrthm.2008.09.019

[3] Liang, C., Wang, K., Li, Q., Bai, J., & Zhang, H. (2019). Influence of the distribution of fibrosis within an area of myocardial infarction on wave propagation in ventricular tissue. *Sci. Rep. 9*(14151). doi:10.1038/s41598-019-50478-5

[4] Burlew, B. S., & Weber, K. T. (2000). Connective Tissue and the Heart: Functional Significance and Regulatory Mechanisms. *Cardiol. Clin. 18*(3), 435–442. doi:10.1016/S0733-8651(05)70154-5

[5] Parichatikanond, W., Luangmonkong, T., Mangmool, S., & Kurose, H. (2020). Therapeutic Targets for the Treatment of Cardiac Fibrosis and Cancer: Focusing on TGF-β Signaling. *Front. Cardiovasc. Med. 7*(34). doi:10.3389/fcvm.2020.00034

[6] Baum, J., & Duffy, H. S. (2011). Fibroblasts and Myofibroblasts: What are we talking about? *J. Cardiovasc. Pharmacol. 57*(4), 376–379. doi:10.1097/FJC.0b013e3182116e39

[7] Frantz, C., Stewart, K. M., & Weaver, V. M. (2010). The extracellular matrix at a glance. *J. Cell Sci. 123*(24), 4195–4200. doi:10.1242/jcs.023820

[8] Hinz, B. (2016). The role of myofibroblasts in wound healing. *Curr. Res. Transl. Med. 64*(4), 171–177. doi:10.1016/j.retram.2016.09.003

[9] Cordes, A., Witt, H., Gallemí-Pérez, A., Brückner, B., Grimm, F., Vache, M., ... Janshoff, A. (2020). Prestress and Area Compressibility of Actin Cortices Determine the Viscoelastic Response of Living Cells. *Phys. Rev. Lett. 125*(6), 068101. doi:10.1103/PhysRevLett.125.068101

[10] Chugh, P., & Paluch, E. (2018). The actin cortex at a glance. *J. Sci. 131*(14), jcs186254. doi:10.1242/jcs.186254

[11] Salbreux, G., Charras, G., & Paluch, E. (2012). Actin cortex mechanics and cellular morphogenesis. *Trends Cell Biol. 22*(10), 536–545. doi:10.1016/j.tcb.2012.07.001

[12] Pollard, T. D. (2007). Regulation of actin filament assembly by Arp2/3 complex and formins. *Annu. Rev. Biophys. Biomol. Struct. 36*, 451–477. doi:10.1146/annurev.biophys.35.040405.101936

[13] Breitsprecher, D., & Goode, B. L. (2013). Formins at a glance. *J. Cell Sci. 126*(1), 1–7. doi:10.1242/jcs.107250

[14] Lammers, M., Rose, R., Scrima, A., & Wittinghofer, A. (2005). The regulation of mDia1 by autoinhibition and its release by Rho·GTP. *EMBO J. 24*(23), 4176–4187. doi:10.1038/sj.emboj.7600879

[15] Etienne-Manneville, S., & Hall, A. (2002). Rho GTPases in cell biology. *Nature*, *420*, 629–635. doi:10.1038/nature01148

[16] Litschko, C., Brühmann, S., Csiszár, A., Stephan, T., Dimchev, V., Damiano-Guercio, J., ... Faix, J. (2019). Functional integrity of the contractile actin cortex is safeguarded by multiple Diaphanous-related formins. *PNAS*, *116*(9), 3594–3603. doi:10.1073/pnas.1821638116

[17] Schreier, T., Degen, E., & Baschong, W. (1993). Fibroblast migration and proliferation during in vitro wound healing. *J. Exp. Med. 193*(1), 195–205. doi:10.1007/BF02576227

[18] Rausch, S., Das, T., Soiné, J. R. D., Hofmann, T. W., Boehm, C. H. J., Schwarz, U. S., ... Spatz, J. P. (2013). Polarizing cytoskeletal tension to induce leader cell formation during collective cell migration. *Biointerphases*, *8*(32). doi:10.1186/1559-4106-8-32

[19] Dos Santos Da Costa, A., Subbiah, R., Oh, S. J., Jeong, H., Na, J.-I., Park, K., ... Shin, J. H. (2022). Fibroblasts close a void in free space by a purse-string mechanism. *ACS Appl. Mater. Interfaces*, *14*, 40522–40534. doi:10.1021/acsami.2c07952

[20] Martin, P., & Lewis, J. (1992). Actin cables and epidermal movement in embryonic wound healing. *Nature*, *360*, 179–183. doi:10.1038/360179a0

[21] Kollmannsberger, P., Bidan, C. M., Dunlop, J. W. C., Fratzl, P., & Vogel, V. (2018). Tensile forces drive a reversible fibroblast-to-myofibroblast transition during tissue growth in engineered clefts. *Science Advances*, *4*(1), eaao4881. doi:10.1126/sciadv.aao4881

[22] Sakar, M. S., Eyckmans, J., Poeters, R., Eberli, D., Nelson, B. J., & Chen, C. S. (2016). Cellular forces and matrix assembly coordinate fibrous tissue repair. *Nature Communications*, *7*. doi:10.1038/ncomms11036

[23] Parsons, J. T., Horwitz, A. R., & Schwartz, M. A. (2010). Cell adhesion: integrating cytoskeletal dynamics and cellular tension. *Nat. Rev. Mol. Cell Biol. 11*, 633–643. doi:10.1038/nrm2957

[24] Rizvi, S. A., Neidt, E. M., Cui, J., Feiger, Z., Skau, C. T., Gardel, M. L., ... Kovar, D. R. (2009). Identification and Characterization of a Small Molecule Inhibitor of Formin-Mediated Actin Assembly. *Chem. Biol. 16*(11), 1158–1168. doi:10.1016/j.chembiol.2009.10.006

[25] Lo, C.-M., & Ferrier, J. (1998). Impedance analysis of fibroblastic cell layers measured by electric cell-substrate impedance sensing. *Phys. Rev. E*, *57*(6), 6982–87. doi:10.1103/PhysRevE.57.6982

[26] Cavallini, F., & Tarantola, M. (2019). ECIS based wounding and reorganization of cardiomyocytes and fibroblasts in co-cultures. *Prog. Biophys. Mol. Biol. 144*, 116–127. doi:10.1016/j.pbiomolbio.2018.06.010

[27] Hung, Y.-H., Chiu, W.-C., Fuh, S.-R., Lai, Y.-T., Tung, T.-H., Huang, C.-C., & Lo, C.-M. (2022). ECIS Based Electric Fence Method for Measurement of Human Keratinocyte Migration on Different Substrates. *Biosensors*, *12*, 293. doi:10.3390/bios12050293

[28] Tarantola, M., Sunnick, E., Schneider, D., Marel, A.-K., Kunze, A., & Janshoff, A. (2011). Dynamic Changes of Acoustic Load and Complex Impedance as Reporters for the Cytotoxicity of Small Molecule Inhibitors. *Chem. Res. Toxicol. 24*, 1494–1506. doi:10.1021/tx200115q

[29] Schneider, D., Tarantola, M., & Janshoff, A. (2011). Dynamics of TGF-β induced epithelial-to-mesenchymal transition monitored by Electric Cell-Substrate Impedance Sensing. *BBA - Mol. Cell Res. 1813*(12), 2099–2107. doi:10.1016/j.bbamcr.2011.07.016

[30] Begnaud, S., Chen, T., Delacour, D., Mège, R.-M., & Ladoux, B. (2016). Mechanics of epithelial tissues during gap closure. *Curr. Opin. Cell Biol. 42*, 52–62. doi:10.1016/j.ceb.2016.04.006

[31] World Health Organization (WHO). (2020). The top 10 causes of death. Retrieved from www.who.int/news-room/fact-sheets/detail/the-top-10-causes-of-death. (Accessed: 14.03.2022)

[32] Kirchberger, I., Heier, M., Kuch, B., Wende, R., & Meisinger, C. (2011). Sex Differences in Patient-Reported Symptoms Associated With Myocardial Infarction (from the Population-Based MONICA/KORA Myocardial Infarction Registry). *Am. J. Cardiol. 107*(11), 1585–1589. doi:10.1016/j.amjcard.2011.01.040

[33] Wu, J., Gale, C. P., Hall, M., Dondo, T. B., Metcalfe, E., Oliver, G., ... West, R. M. (2018). Impact of initial hospital diagnosis on mortality for acute myocardial infarction: A national cohort study. *EHJ-ACVC*, *7*(2), 139–148. doi:10.1177/2048872616661693

[34] European Heart Network (EHN). (2017). European Cardiovascular Disease Statistics 2017. Retrieved from www.ehnheart.org/cvd-statistics.html. (Accessed: 14.03.2022)

[35] Momin, J. A. (2023). Heart Disease Risk Factors In Young Adults. Retrieved from www.sprintmedical.in/blog/heart-disease-risk-factors-in-young-adults. (Accessed: 24.01.2023)

[36] Maghin, E., Garbati, P., Quarto, R., Piccoli, M., & Bollini, S. (2020). Young at Heart: Combining Strategies to Rejuvenate Endogenous Mechanisms of Cardiac Repair. *Front. Bioeng. Biotechnol. 8*, 447. doi:10.3389/fbioe.2020.00447

[37] Gilbert, T. W., Sellaro, T. L., & Badylak, S. F. (2006). Decellularization of tissues and organs. *Biomat. 27*(19), 3675–3683. doi:10.1016/j.biomaterials.2006.02.014

[38] Tomov, M. L., Gil, C. J., Cetnar, A., Theus, A. S., Lima, B. J., Nish, J. E., ... Serpooshan, V. (2019). Engineering Functional Cardiac Tissues for Regenerative Medicine Applications. *Curr. Cardiol. Rep. 21*, 105. doi:10.1007/s11886-019-1178-9

[39] Hashimoto, H., Olson, E. N., & Bassel-Duby, R. (2018). Therapeutic approaches for cardiac regeneration and repair. *Nat. Rev. Cardiol. 15*, 585–600. doi:10.1038/s41569-018-0036-6

[40] Ramasubramanian, L., Du, S., Gidda, S., Bahatyrevich, N., Hao, D., Kumar, P., & Wang, A. (2022). Bioengineering Extracellular Vesicles for the Treatment of Cardiovascular Diseases. *Adv. Biol. 6*(10), 2200087. doi:10.1002/adbi.202200087

[41] Mancuso, A., Barone, A., Cristiano, M. C., Cianflone, E., Fresta, M., & Paolino, D. (2020). Cardiac Stem Cell-Loaded Delivery Systems: A New Challenge for Myocardial Tissue Regeneration. *Int. J. Mol. Sci. 21*(20), 7701. doi:10.3390/ijms21207701

[42] Luisi, P. L., Ferri, F., & Stano, P. (2006). Approaches to semi-synthetic minimal cells: a review. *Naturwissenschaften*, *93*, 1–13. doi:10.1007/s00114-005-0056-z

[43] Göpfrich, K., Platzman, I., & Spatz, J. P. (2018). Mastering Complexity: Towards Bottom-up Construction of Multifunctional Eukaryotic Synthetic Cells. *Trends Biotechnol. 36*(9), 938–951. doi:10.1016/j.tibtech.2018.03.008

[44] Li, J., Jamieson, W. D., Dimitriou, P., Xu, W., Rohde, P., Martinac, B., ... Barrow, D. A. (2022). Building programmable multicompartment artificial cells incorporating remotely activated protein channels using microfluidics and acoustic levitation. *Nat. Commun. 13*, 4125. doi:10.1038/s41467-022-31898-w

[45] Weiss, M., Frohnmayer, J. P., Benk, L. T., Haller, B., Janiesch, J.-W., Heitkamp, T., ... Spatz, J. P. (2018). Sequential bottom-up assembly of mechanically stabilized synthetic cells by microfluidics. *Nature Mater. 17*, 89–96. doi:10.1038/nmat5005

[46] Goers, R., Thoma, J., Ritzmann, N., Di Silvestro, A., Alter, C., Gunkel-Grabole, G., ... Meier, W. (2018). Optimized reconstitution of membrane proteins into synthetic membranes. *Commun. Chem. 1*, 35. doi:10.1038/s42004-018-0037-8

[47] Hu, S., Ogle, B. M., & Cheng, K. (2018). Body builder: from synthetic cells to engineered tissues. *Curr. Opin. Cell Biol. 54*, 37–42. doi:10.1016/j.ceb.2018.04.010

[48] Doll, S., Dreßen, M., Geyer, P. E., Itzhak, D. N., Braun, C., Doppler, S. A., ... Mann, M. (2017). Region and cell-type resolved quantitative proteomic map of the human heart. *Nat. Commun. 8*, 1469. doi:10.1038/s41467-017-01747-2

[49] Litviňuková, M., Talavera-López, C., Maatz, H., Reichart, D., Worth, C. L., Lindberg, E. L., ... Teichmann, S. A. (2020). Cells of the adult human heart. *Nature*, *588*, 466–472. doi:10.1038/s41586-020-2797-4

[50] Xin, M., Olson, E. N., & Bassel-Duby, R. (2013). Mending broken hearts: cardiac development as a basis for adult heart regeneration and repair. *Nat. Rev. Mol. Cell Biol. 14*, 529–541. doi:10.1038/nrm3619

[51] Tracy, L. E., Minasian, R. A., & Caterson, E. J. (2016). Extracellular Matrix and Dermal Fibroblast Function in the Healing Wound. *Adv. Wound Care (New Rochelle)*, *5*(3), 119–136. doi:10.1089/wound.2014.0561

[52] Dick, M. K., Miao, J. H., & Limaiem, F. (2022). Histology, Fibroblast. Retrieved from www.ncbi.nlm.nih.gov/books/NBK541065/. (Accessed: 24.10.2022)

[53] Polo, J. M., & Hochedlinger, K. (2010). When Fibroblasts MET iPSCs. *Cell Stem Cell*, *7*(1), 5–6. doi:10.1016/j.stem.2010.05.018

[54] Thiery, J. P., Acloque, H., Huang, R. Y. J., & Nieto, M. A. (2009). Epithelial-Mesenchymal Transitions in Development and Disease. *Cell*, *139*(5), 871–890. doi:10.1016/j.cell.2009.11.007

[55] Tomasek, J. J., Gabbiani, G., Hinz, B., Christine, C., & Brown, R. A. (2002). Myofibroblasts and mechano-regulation of connective tissue remodelling. *Nat. Rev. Mol. Cell Biol. 3*, 349–363. doi:10.1038/nrm809

[56] Matsuzaki, S., Hiratsuka, T., Taniguchi, M., Shingaki, K., Kubo, T., Kiya, K., ... Katayama, T. (2015). Physiological ER Stress Mediates the Differentiation of Fibroblasts. *PLoS ONE*, *10*(4), e0123578. doi:10.1371/journal.pone.0123578

[57] Klingberg, F., Chau, G., Walraven, M., Boo, S., Koehler, A., Chow, M. L., ... Hinz, B. (2018). The fibronectin ED-A domain enhances recruitment of latent TGF-β-binding protein-1 to the fibroblast matrix. *J. Cell Sci. 131*(5), jcs201293. doi:10.1242/jcs.201293

[58] Zent, J., & Guo, L.-W. (2018). Signaling mechanisms of myofibroblastic activation: outside-in and inside-out. *Cell Physiol Biochem. 49*(3), 848–868. doi:10.1159/000493217

[59] Wipff, P.-J., & Hinz, B. (2008). Integrins and the activation of latent transforming growth factor β1 – An intimate relationship. *Eur. J. Cell Biol. 87*(8-9), 601–615. doi:10.1016/j.ejcb.2008.01.012

[60] Cordeiro, M. F., Bhattacharya, S. S., Schultz, G. S., & Khaw, P.T. (2000). TGF-β1, -β2, and -β3 In Vitro: Biphasic Effects on Tenon's Fibroblast Contraction, Proliferation, and Migration. *Invest. Ophthalmol. Vis. Sci. 41*(3), 756–763.

[61] Peacock, H. M., Tabibian, A., Criem, N., Caolo, V., Hamard, L., Deryckere, A., ... Jones, E. A. V. (2020). Impaired SMAD1/5 Mechanotransduction and Cx37 (Connexin37) Expression Enable Pathological Vessel Enlargement and Shunting. *ATVB*, *40*(4), e87–e104. doi:10.1161/ATVBAHA.119.313122

[62] Piersma, B., Bank, R. A., & Boersema, M. (2015). Signaling in fibrosis: TGF-β, WNT, and YAP/TAZ converge. *Front. Med. 2*, 59. doi:10.3389/fmed.2015.00059

[63] Walker, E. J., Heydet, D., Veldre, T., & Ghildyal, R. (2019). Transcriptomic changes during TGF-β-mediated differentiation of airway fibroblasts to myofibroblasts. *Sci. Rep. 9*, 20377. doi:10.1038/s41598-019-56955-1

[64] Hammer, J. A., & Sellers, J. R. (2012). Walking to work: roles for class V myosins as cargo transporters. *Nat. Rev. Mol. Cell Biol. 13*, 13–26. doi:10.1038/nrm3248

[65] McIntosch, B. B., & Ostap, E. M. (2016). Myosin-I molecular motors at a glance. *J. Cell Sci. 129*(14), 2689–2695. doi:10.1242/jcs.186403

[66] Brito, C., & Sousa, S. (2020). Non-Muscle Myosin 2A (NM2A): Structure, Regulation and Function. *Cells*, *9*(7), 1590. doi:10.3390/cells9071590

[67] Noorman, M., Van der Heyden, M. A. G., van Veen, T. A. B., Cox, M. G. P. J., Hauer, R. N. W., de Bakker, J. M. T., & van Rijen, H. V. M. (2009). Cardiac cell–cell junctions in health and disease: Electrical versus mechanical coupling. *J. Mol. Cell. Cardiol. 47*(1), 23–31. doi:10.1016/j.yjmcc.2009.03.016

[68] Kohl, P., & Gourdie, R. G. (2014). Fibroblast–myocyte electrotonic coupling: Does it occur in native cardiac tissue? *J. Mol. Cell Cardiol. 70*(100), 37–46. doi:10.1016/j.yjmcc.2013.12.024

[69] Rog-Zielinska, E. A., Norris, R. A., Kohl, P., & Markwald, R. (2016). The Living Scar – Cardiac Fibroblasts and the Injured Heart. *Trends Mol. Med. 22*(2), 99–114. doi:10.1016/j.molmed.2015.12.006

[70] Kostecki, G. M., Shi, Y., Chen, C. S., Reich, D. H., Entcheva, E., & Tung, L. (2021). Optogenetic current in myofibroblasts acutely alters electrophysiology and conduction of co-cultured cardiomyocytes. *Sci. Rep. 11*, 4430. doi:10.1038/s41598-021-83398-4

[71] Gourdie, R. G., Dimmeler, S., & Kohl, P. (2016). Novel therapeutic strategies targeting fibroblasts and fibrosis in heart disease. *Nat. Rev. Drug Discov. 15*, 620–638. doi:10.1038/nrd.2016.89

[72] Nagaraju, C. K., Dries, E., Gilbert, G., Abdesselem, M., Wang, N., Amoni, M., ... Sipido, K. R. (2019). Myofibroblast modulation of cardiac myocyte structure and function. *Sci. Rep. 9*, 8872. doi:10.1038/s41598-019-45078-2

[73] Hinz, B., Pittet, P., Smith-Clerc, J., Chaponnier, C., & Meister, J.-J. (2004). Myofibroblast Development Is Characterized by Specific Cell-Cell Adherens Junctions. *Mol. Biol. Cell*, *15*(9), 4310–4320. doi:10.1091/mbc.E04-05-0386

[74] Hutcheson, J. D., Chen, J., Sewell-Loftin, M. K., Ryzhova, L. M., Fisher, C. I., Ru Su, Y., & Merryman, W. D. (2013). Cadherin-11 Regulates Cell–Cell Tension Necessary for Calcific Nodule Formation by Valvular Myofibroblasts. *Arterioscler. Thromb. Vasc. Biol. 33*, 114–120. doi:10.1161/ATVBAHA.112.300278

[75] Thompson, S. A., Copeland, C. R., Reich, D. H., & Tung, L. (2011). Mechanical Coupling Between Myofibroblasts and Cardiomyocytes Slows Electric Conduction in Fibrotic Cell Monolayers. *Circulation*, *123*, 2083–2093. doi:10.1161/CIRCULATIONAHA.110.015057

[76] Woodcock, E. A., & Matkovich, S. J. (2005). Cardiomyocytes structure, function and associated pathologies. *Int. J. Biochem. Cell Biol. 37*(9), 1746–1751. doi:10.1016/j.biocel.2005.04.011

[77] Leri, A., Rota, M., Pasqualini, F. S., Goichberg, P., & Anversa, P. (2015). Origin of Cardiomyocytes in the Adult Heart. *Circ. Res. 116*(1), 150–166. doi:10.1161/CIRCRESAHA.116.303595

[78] Garbern, J. C., Mummery, C. L., & Lee, R. T. (2013). Model Systems for Cardiovascular Regenerative Biology. *Cold Spring Harb. Perspect. Med. 3*(4), a014019. doi:10.1101/cshperspect.a014019

[79] Shenoy, S. K., & Rockman, H. A. (2011). Heart fails without pump partner. *Nature*, *477*, 546–547. doi:10.1038/477546a

[80] Czubryt, M. P. (2012). Common threads in cardiac fibrosis, infarct scar formation, and wound healing. *Fibrogenesis Tissue Repair*, *5*(19). doi:10.1186/1755-1536-5-19

[81] Omelchenko, T., Vasiliev, J. M., Gelfand, I. M., Feder, H. H., & Bonder, E. M. (2003). Rho-dependent formation of epithelial "leader" cells during wound healing. *PNAS*, *100*(19), 10788–10793. doi:10.1073/pnas.1834401100

[82] Ravasio, A., Cheddadi, I., Chen, T., Pereira, T., Ting Ong, Hui, Bertocchi, C., ... Ladoux, B. (2015). Gap geometry dictates epithelial closure efficiency. *Nat. Commun. 6*, 7683. doi:10.1038/ncomms8683

[83] Adams, J. U. (2014). Cytoskeletal Networks Provide Spatial Organization and Mechanical Support to Eukaryotic Cells. In C. O'Connor (Ed.): *Essentials of Cell Biology. Cambridge, MA: NPG Education.* Retrieved from www.nature.com/scitable/ebooks/essentials-of-cell-biology-14749010/

[84] Dominguez, R. (2016). The WH2 Domain and Actin Nucleation – Necessary but Insufficient. *Trends Biochem. Sci. 41*(6), 478–490. doi:10.1016/j.tibs.2016.03.004

[85] Chesarone, M. A., & Goode, B. L. (2009). Actin nucleation and elongation factors: mechanisms and interplay. *Curr. Opin. Cell Biol. 21*(1), 28–37. doi:10.1016/j.ceb.2008.12.001

[86] Goley, E. D., & Welch, M. D. (2006). The ARP2/3 complex: an actin nucleator comes of age. *Nat. Rev. Mol. Cell Biol. 7*, 713–726. doi:10.1038/nrm2026

[87] MB INFO. (n.d.). How does Arp2/3-mediate the nucleation of branched filaments? Retrieved from www.mechanobio.info/cytoskeleton-dynamics/what-is-the-cytoskeleton/what-are-actin-filaments/how-does-arp23-mediate-the-nucleation-of-branched-filaments/. (Accessed: 28.02.2023)

[88] Shemesh, T., Otomo, T., Rosen, M. K., Bershadsky, A. D., & Kozlov, M. M. (2005). A novel mechanism of actin filament processive capping by formin : solution of the rotation paradox. *J. Cell Biol. 170*(6), 889–893. doi:10.1083/jcb.200504156

[89] MB INFO. (n.d.). What is the role of formin in actin polymerization? Retrieved from www.mechanobio.info/cytoskeleton-dynamics/what-is-the-cytoskeleton/what-are-actin-filaments/what-is-the-role-of-formin/#ITEM-1825-4. (Accessed: 02.11.2022)

[90] Jaffe, A. B., & Hall, A. (2005). Rho GTPases: Biochemistry and Biology. *Annu. Rev. Cell Dev. Biol. 21*, 247–269. doi:10.1146/annurev.cellbio.21.020604.150721

[91] Thumkeo, D., Watanabe, S., & Narumiy, S. (2013). Physiological roles of Rho and Rho effectors in mammals. *Eur. J. Cell Biol. 92*, 303–315. doi:10.1016/j.ejcb.2013.09.002

[92] Rivero, F., Muramoto, T., Meyer, A.-K., Urushihara, H., Uyeda, T. Q. P., & Kitayama, C. (2005). A comparative sequence analysis reveals a common GBD/FH3-FH1-FH2-DAD architecture in formins from *Dictyostelium*, fungi and metazoa. *BMC Genom. 6*, 28. doi:10.1186/1471-2164-6-28

[93] Ecke, M., Prassler, J., Tanribil, P., Müller-Taubenberger, A., Körber, S., Faix, J., & Gerisch, G. (2020). Formins specify membrane patterns generated by propagating actin waves. *J. Mol. Cell Biol. 31*(5), 373–385. doi:10.1091/mbc.E19-08-0460

[94] Cartagena-Rivera, A. X., Logue, J. S., Waterman, C. M., & Chadwick, R. S. (2016). Actomyosin Cortical Mechanical Properties in Nonadherent Cells Determined by Atomic Force Microscopy. *Biophys. J. 110*(11), 2528–2539. doi:10.1016/j.bpj.2016.04.034

[95] Rotsch, C., & Radmacher, M. (2000). Drug-Induced Changes of Cytoskeletal Structure and Mechanics in Fibroblasts: An Atomic Force Microscopy Study. *Biophys. J. 78*(1), 520–535. doi:10.1016/S0006-3495(00)76614-8

[96] Bufi, N., Durand-Smet, P., & Asnacios, A. (2015). Single-cell mechanics: The parallel plates technique. *Methods Cell Biol. 125*, 187–209. doi:10.1016/bs.mcb.2014.11.002

[97] Smeets, B., Cuvelier, M., Pešek, J., & Ramon, H. (2019). The Effect of Cortical Elasticity and Active Tension on Cell Adhesion Mechanics. *Biophys. J. 116*(5), 930–937. doi:10.1016/j.bpj.2019.01.015

[98] Ding, Y., Xu, G.-K., & Wang, G.-F. (2017). On the determination of elastic moduli of cells by AFM based indentation. *Sci. Rep. 7*, 45575. doi:10.1038/srep45575

[99] Fabry, B., Maksym, G. N., Butler, J. P., Glogauer, M., Navajas, D., & Fredberg, J. J. (2001). Scaling the Microrheology of Living Cells. *Phys. Rev. Lett. 87*, 148102. doi:10.1103/PhysRevLett.87.148102

[100] Rother, J., Nöding, H., Mey, I., & Janshoff, A. (2014). Atomic force microscopy-based microrheology reveals significant differences in the viscoelastic response between malign and benign cell lines. *Open Biol. 4*(5), 140046. doi:10.1098/rsob.140046

[101] Hubrich, H., Mey, I. P., Brückner, B. R., Mühlenbrock, P., Nehls, S., Grabenhorst, L., ... Janshoff, A. (2020). Viscoelasticity of Native and Artificial Actin Cortices Assessed by Nanoindentation Experiments. *Nano Lett. 20*, 6329–6335. doi:10.1021/acs.nanolett.0c01769

[102] Broedersz, C., Depken, M., Yao, N., Pollak, M., Weitz, D., & MacKintosh, F. (2010). Cross-Link-Governed Dynamics of Biopolymer Networks. *Phys. Rev. Lett. 105*, 238101. doi:10.1103/PhysRevLett.105.238101

[103] Stumpf, B. S., Ambriović-Ristov, A., Radenovic, A., & Smith, A.-S. (2020). Recent Advances and Prospects in the Research of Nascent Adhesions. *Front. Physiol. 11*, 574371. doi:10.3389/fphys.2020.574371

[104] Vicente-Manzanares, M., & Horwitz, A. R. (2011). Adhesion dynamics at a glance. *J. Cell Sci. 124*(23), 3923–3927. doi:10.1242/jcs.095653

[105] Van der Flier, Arjan. (2001). Function and interactions of integrins. *Cell Tissue Res. 305*, 285–98. doi:10.1007/s004410100417

[106] Harjunpää, H., Asens, M. L., Guenther, C., & Fagerholm, S. C. (2019). Cell Adhesion Molecules and Their Roles and Regulation in the Immune and Tumor Microenvironment. *Front. Immunol. 10*, 1078. doi:10.3389/fimmu.2019.01078

[107] Sun, Z., Guo, S. S., & Fässler, R. (2016). Integrin-mediated mechanotransduction. *J. Cell Biol. 215*(4), 445–456. doi:10.1083/jcb.201609037

[108] Cox, E. A., Sastry, S. K., & Huttenlocher, A. (2017). Integrin-mediated Adhesion Regulates Cell Polarity and Membrane Protrusion through the Rho Family of GTPases. *MBoC*, *12*(2), 251–510. doi:10.1091/mbc.12.2.265

[109] Gauthier-Rouvière, C., Causeret, M., Comunale, F., & Charrasse, S. (2013). Cadherin-mediated cell-cell adhesion and the microtubule network. In: *Madame Curie Bioscience Database. Landes Bioscience*. Retrieved from www.ncbi.nlm.nih.gov/books/NBK6079/

[110] Ballestrem, C., Hinz, B., Imhof, B. A., & Wehrle-Haller, B. (2001). Marching at the front and dragging behind: differential alphaVbeta3-integrin turnover regulates focal adhesion behavior. *J. Cell Biol. 155*(7), 1319–1332. doi:10.1083/jcb.200107107

[111] Palecek, S. P., Huttenlocher, A., Horwitz, A. F., & Lauffenburger, D. A. (1998). Physical and biochemical regulation of integrin release during rear detachment of migrating cells. *J. Cell Sci. 111*(7), 929–940. doi:10.1242/jcs.111.7.929

[112] Binnig, G., Quate, C. F., & Gerber, C. (1986). Atomic Force Microscope. *Phys. Rev. Lett. 56*(9), 930–933. doi:10.1103/PhysRevLett.56.930

[113] Bustamante, C., Rivetti, C., & Keller, D. J. (1997). Scanning force microscopy under aqueous solutions. *Curr. Opin. Struct. Biol. 7*(5), 709–716. doi:10.1016/S0959-440X(97)80082-6

[114] Alessandrini, A., & Facci, P. (2005). AFM: a versatile tool in biophysics. *Meas. Sci. Technol. 16*, R65–R92. doi:10.1088/0957-0233/16/6/R01

[115] Sirghi, L. (2010). Atomic Force Microscopy indentation of living cells. In A. Méndez-Vilas and J. Díaz (Ed.): *Microscopy : science, technology, applications and education. Microscopy Series. No. 4, Vol. 1. Formatex*, 433–440.

[116] Hinterdorfer, P., Kienberger, F., Raab, A., Gruber, H. J., Baumgartner, W., Kada, G., ... Schindler, H. (2000). Poly(Ethylene Glycol): An Ideal Spacer for Molecular Recognition Force Microscopy/Spectroscopy. *Single Mol. 1*(2), 99–103.

[117] JPK Instruments. (2012). NanoWizard® AFM Handbook. Retrieved from www.nanophys.kth.se/nanolab/afm/jpk/manuf-manuals/handbook-2.2a.pdf. (Accessed: 26.10.2022)

[118] Hutter, J. L., & Bechhoefer, J. (1993). Calibration of atomic-force microscope tips. *Rev. Sci. Instrum. 64*(7), 1868–1879. doi:10.1063/1.1143970

[119] Butt, H.-J., & Jaschke, M. (1995). Calculation of thermal noise in atomic force microscopy. *Nanotechnol. 6*(1), 1–7. doi:10.1088/0957-4484/6/1/001

[120] Sneddon, I. N. (1965). The relation between load and penetration in the axisymmetric boussinesq problem for a punch of arbitrary profile. *Int. J. Eng. Sci. 3*(1), 47–57. doi:10.1016/0020-7225(65)90019-4

[121] Lin, D. C., Dimitriadis, E. K., & Horkay, F. (2007). Robust Strategies for Automated AFM Force Curve analysis-I. Non-adhesive Indentation of Soft Inhomogeneous Materials. *J. Biomech. Eng. 129*(3), 430–440. doi:10.1115/1.2720924

[122] Garcia, R. (2020). Nanomechanical mapping of soft materials with the atomic force microscope: methods, theory and applications. *Chem. Soc. Rev. 49*, 5850–5884. doi:10.1039/d0cs00318b

[123] Harris, A. R., & Charras, G. T. (2011). Experimental validation of atomic force microscopy-based cell elasticity measurements. *Nanotech. 22*(34), 345102. doi:10.1088/0957-4484/22/34/345102

[124] Stamm, A., Reimers, K., Strauß, S., Vogt, P., Scheper, T., & Pepelanova, I. (2016). *In vitro* wound healing assays – state of the art. *BioNanoMaterials*, *17*(1-2), 79–87. Retrieved from www.degruyter.com/view/journals/biomat/17/1-2/article-p79.xml

[125] Challa, S., & Chan, F. K.-M. (2010). Going up in Flames: Necrotic Cell Injury and Inflammatory Diseases. *Cell. Mol. Life Sci. 67*(19), 3241–3253. doi:10.1007/s00018-010-0413-8

[126] Poujade, M., Grasland-Mongrain, E., Hertzog, A., Jouanneau, J., Chavrier, P., Ladoux, B., ... Silberzan, P. (2007). Collective migration of an epithelial monolayer in response to a model wound. *PNAS*, *104*(41), 15988–15993. doi:10.1073/pnas.0705062104

[127] Renken, C., Keese, C., & Giaver, I. (2010). Automated assays for quantifying cell migration. *BioTechniques*, *49*, 844. doi:10.2144/000113554

[128] Giaever, I., & Keese, C. R. (1991). Micromotion of mammalian cells measured electrically. *Proc. Natl. Acad. Sci. USA*, *88*(17), 7896–7900. doi:10.1073/pnas.88.17.7896

[129] Keese, C. R., Wegner, J., Walker, S. R., & Giaever, I. (2004). Electrical wound-healing assay for cells *in vitro*. *PNAS*, *101*(6), 1554–1559. doi:10.1073/pnas.0307588100

[130] Keese, C. R., & Giaever, I. (1984). Monitoring fibroblast behavior in tissue culture with an applied electric field. *Proc. Natl. Acad. Sci. USA*, *81*, 3761–3764. doi:10.1073/pnas.81.12.3761

[131] Krinke, D., Jahnke, H.-G., Pänke, O., & Robitzki, A. A. (2009). A microelectrode-based sensor for label-free in vitro detection of ischemic effects on cardiomyocytes. *Biosens. Bioelectron. 29*(9), 2798–2803. doi:10.1016/j.bios.2009.02.006

[132] Rümenapp, C., Remm, M., Wolf, B., & Gleich, B. (2009). Improved method for impedance measurements of mammalian cells. *Biosens. Bioelectron. 24*(9), 2914–2919. doi:10.1016/j.bios.2009.02.030

[133] Cho, S., & Thielecke, H. (2008). Electrical characterization of human mesenchymal stem cell growth on microelectrode. *Microelectron. Eng. 85*(5-6), 1272–1274. doi:10.1016/j.mee.2008.01.004

[134] Tarantola, M., Marel, A.-K., Sunnick, E., Adam, H., Wegener, J., & Janshoff, A. (2010). Dynamics of human cancer cell lines monitored by electrical and acoustic fluctuation analysis. *Integr. Biol. 2*(2-3), 139–150. doi:10.1039/b920815a

[135] Lovelady, D. C., Richmond, T. C., Maggi, A. N., Lo, C.-M., & Rabson, D. A. (2007). Distinguishing cancerous from noncancerous cells through analysis of electrical noise. *Phys. Rev. E*, *76*, 041908. doi:10.1103/PhysRevE.76.041908

[136] Sapper, A., Wegener, J., & Janshoff, A. (2006). Cell Motility Probed by Noise Analysis of Thickness Shear Mode Resonators. *Anal. Chem. 75*, 5184–5191. doi:10.1021/ac060094g

[137] Peng, C. K., Buldyrev, S. V., Havlin, S., Simons, M., Stanley, H. E., & Goldberger, A. L. (1994). Mosaic organization of DNA nucleotides. *Phys. Rev. E*, *49*, 1685–1689. doi:10.1103/physreve.49.1685

[138] Peng, C. K., Havlin, S., Stanley, H. E., & Goldberger, A. L. (1995). Quantification of scaling exponents and crossover phenomena in nonstationary heartbeat time series. *Chaos*, *5*(1), 82–87. doi:10.1063/1.166141

[139] Todaro, G. J., & Green, H. (1963). Quantitative studies of the growth of mouse embryo cells in culture and their development into established lines. *J. Cell Biol. 17*(2), 299–313. doi:10.1083/jcb.17.2.299

[140] American Type Culture Collection (ATCC). (n.d.). 3T3-Swiss albino. Retrieved from www.atcc.org/products/ccl-92. (Accessed: 05.07.2022)

[141] Eagle, H., & Levine, E. M. (1967). *Nature*, *213*, 1102–1106. doi:10.1038/2131102a0

[142] Kage, F., Winterhoff, M., Dimchev, V., Mueller, J., Thalheim, T., Freise, A., ... Rottner, K. (2017). FMNL formins boost lamellipodial force generation. *Nat. Commun. 8*, 14832. doi:10.1038/ncomms14832

[143] Watanabe, T., Hosoya, H., & S., Y. (2007). Regulation of Myosin II Dynamics by Phosphorylation and Dephosphorylation of Its Light Chain in Epithelial Cells. *Mol. Biol. Cell*, *18*(2), 605–616. doi:10.1091/mbc.e06-07-0590

[144] Kovács, M., Tóth, J., Hetényi, C., Málnási-Csizmadia, A., & Sellers, J. R. (2004). Mechanism of Blebbistatin Inhibition of Myosin II. *J. Biol. Chem. 279*(34), 35557–35563. doi:10.1074/jbc.M405319200

[145] Fabian, L., Troscianczuk, J., & Forer, A. (2007). Calyculin A, an enhancer of myosin, speeds up anaphase chromosome movement. *6*, 1. doi:10.1186/1475-9268-6-1

[146] Schneider, C. A., Rasband, W. S., & Eliceiri, K. W. (2012). NIH Image to ImageJ: 25 years of image analysis. *Nat. Methods*, *9*, 671–675. doi:10.1038/nmeth.2089

[147] Rother, J., Richter, C., Turco, L., Knoch, F., Mey, I., Luther, S., ... Tarantola, M. (2015). Crosstalk of cardiomyocytes and fibroblasts in co-cultures. *Open Biol. 5*(6), 150038. doi:10.1098/rsob.150038

[148] Mamoyan, L. (2022). *Impedance analysis of cardiac cultures under formin modulation for wound healing* (Georg-August-Universität Göttingen).

[149] Scheller, V. (2020). *Switchable polymeric microcarriers for remodeling of wound healing* (Georg-August-Universität Göttingen).

[150] Balasubramanian, L., Yip, K.-P., Hsu, T.-H., & Lo, C.-M. (2008). Impedance analysis of renal vascular smooth muscle cells. *Am. J. Physiol. Cell Physiol. 295*, c954–c965. doi:10.1152/ajpcell.00009.2008

[151] Tarantola, M., Pietuch, A., Schneider, D., Rother, J., Sunnick, E., Rosman, C., ... Janshoff, A. (2011). Toxicity of gold-nanoparticles: Synergistic effects of shape and surface functionalization on micromotility of epithelial cells. *Nanotoxicol. 5*(2), 254–268. doi:10.3109/17435390.2010.528847

[152] Biophysics, A. (n.d.). Tutorial on Phase-Contrast & Fluorescence Microscopy of Adherent Cells grown on ECIS Electrodes. Retrieved from www.ibidi.com/img/cms/products/instruments/I_700XX_ECIS/ECIS_Microscopy.pdf. (Accessed: 11.2022)

[153] Nichols, D. (n.d.). Coloring for Colorblindness. Retrieved from www.davidmathlogic.com/colorblind. (Accessed: 14.04.2022)

[154] Evans, E., & Kukan, B. (1984). Passive material behavior of granulocytes based on large deformation and recovery after deformation tests. *Blood*, *64*(5), 1028–1035. doi:10.1182/blood.V64.5.1028.1028

[155] Yeung, A., & Evans, E. (1989). Cortical shell-liquid core model for passive flow of liquid-like spherical cells into micropipets. *Biophys. J. 56*(1), 139–149. doi:10.1016/S0006-3495(89)82659-1

[156] Needham, D., & Hochmuth, R. M. (1990). Rapid Flow of Passive Neutrophils Into a 4 µm Pipet and Measurement of Cytoplasmic Viscosity. *J. Biomech. Eng. 112*(3), 269–278. doi:10.1115/1.2891184

[157] Méndez-Méndez, J. V., Alonso-Rasgado, M. T., Correia Faria, E., Flores-Johnson, E. A., & Snook, R. (2014). Numerical study of the hydrodynamic drag force in atomic force microscopy measurements undertaken in fluids. *Micron*, *66*, 37–46. doi:10.1016/j.micron.2014.05.004

[158] Berthold, T., Benstetter, G., Frammelsberger, W., Rodríguez, R., & Nafría, M. (2017). Numerical Study of Hydrodynamic Forces for AFM Operations in Liquid. *Scanning*, *2017*, 6286595. doi:10.1155/2017/6286595

[159] Spedden, E., & Staii, C. (2013). Neuron Biomechanics Probed by Atomic Force Microscopy. *Int. J. Mol. Sci. 14*, 16124–16140. doi:10.3390/ijms140816124

[160] Chugh, P., C., A. G., Smith, M. B., Cassani, D. A. D., Dierkes, K., Ragab, A., ... Paluch, E. K. (2017). Actin cortex architecture regulates cell surface tension. *Nat. Cell Biol. 19*, 689–697. doi:10.1038/ncb3525

[161] Clark, A. G., & Paluch, E. K. (2011). Mechanics and Regulation of Cell Shape During the Cell Cycle. In J. Z. Kubiak (Ed.): *Cell Cycle in Development. Springer*, 31–74. doi:10.1007/978-3-642-19065-0

[162] Vanden Berghe, T., Vanlangenakker, N., Parthoens, E., Deckers, W., Devos, M., Festjens, N., ... Vandenabeele, P. (2010). Necroptosis, necrosis and secondary necrosis converge on

similar cellular disintegration features. *Cell Death Differ. 17*, 922–930. doi:10.1038/cdd.2009.184

[163] Freddo, A. M., Shoffner, S. K., Shao, Y., Taniguchi, K., Grosse, A. S., Guysinger, M. N., … Gumucio, D. L. (2016). Coordination of signaling and tissue mechanics during morphogenesis of murine intestinal villi: a role for mitotic cell rounding. *Integr. Biol. 8*(9), 918–928. doi:10.1039/c6ib00046k

[164] Murphy-Ullrich, J. E. (201). The de-adhesive activity of matricellular proteins: Is intermediate cell adhesion an adaptive state? *J. Clin. Investig. 107*(7), 785–790. doi:10.1172/JCI12609

[165] Tschumperlin, Daniel J. (2013). Fibroblasts and the ground they walk on. *Physiology*, *28*(6), 380–390. doi:10.1152/physiol.00024.2013

[166] Manso, A. M., Kang, S.-M., & Ross, R. S. (2009). Integrins, Focal Adhesions and Cardiac Fibroblasts. *J. Investig. Med. 57*(8), 856–860. doi:10.231/JIM.0b013e3181c5e61f

[167] Ruoslahti, E. (1996). RGD and other recognition sequences for integrins. *Annu. Rev. Cell Dev. Biol. 12*, 697–715. doi:10.1146/annurev.cellbio.12.1.697

[168] Pierschbacher, M. D., & Ruoslahti, E. (1984). Cell attachment activity of fibronectin can be duplicated by small synthetic fragments of the molecule. *Nature*, *309*, 30–33. doi:10.1038/309030a0

[169] SenGupta, S., Parent, C. A., & Bear, J. E. (2022). The principles of directed cell migration. *Nat. Rev. Mol. Cell Biol. 22*(8), 529–547. doi:10.1038/s41580-021-00366-6

[170] Doane, K. J., Yang, G., & Birk, D. E. (1992). Corneal Cell-Matrix Interactions: Type VI Collagen Promotes Adhesion and Spreading of Corneal Fibroblasts. *Exp. Cell Res. 200*, 490–499. doi:10.1016/0014-4827(92)90200-R

[171] Maheshwari, G., Brown, G., Lauffenburger, D. A., Wells, A., & Griffith, L. G. (2000). Cell adhesion and motility depend on nano-scale RGD clustering. *J. Cell Sci. 113*, 1677–1686. doi:10.1242/jcs.113.10.1677

[172] Gauthier, N., Rossier, O., Mathur, A., Hone, J., & Sheetz, M. (2009). Plasma membrane area increases with spread area by exocytosis of a GPI-anchored protein compartment. *Mol. Biol. Cell*, *20*, 3261–3272. doi:10.1091/mbc.e09-01-0071

[173] Morris, C. E., & Homann, U. (2001). Cell Surface Area Regulation and Membrane Tension. *J. Membrane Biol. 179*, 79–102. doi:10.1007/s002320010040

[174] Lembo, S., Strauss, L., Cheng, D., Vermeil, J., Siggel, M., Toro-Nahuelpan, M., … Diz-Muñoz, A. (2023). The distance between the plasma membrane and the actomyosin cortex acts as a nanogate to control cell surface mechanics. *bioRxiv*, 1–20. doi:10.1101/2023.01.31.526409

[175] Kolega, J. (1986). Effects of mechanical tension on protrusive activity and microfilament and intermediate filament organization in an epidermal epithelium moving in culture. *J. Cell Biol. 102*, 1400–1411. doi:10.1083/jcb.102.4.1400

[176] Raucher, D., & Sheetz, M. P. (2000). Cell spreading and lamellipodial extension rate is regulated by membrane tension. *J. Cell Biol. 148*, 127–136. doi:10.1083/jcb.148.1.127

[177] Sens, P., & J., P. (2015). Membrane tension and cytoskeleton organization in cell motility. *J. Phys.: Condens. Matter. 27*, 273103. doi:10.1088/0953-8984/27/27/273103

[178] Pietuch, A., & Janshoff, A. (2013). Mechanics of spreading cells probed by atomic force microscopy. *Open Biol. 3*, 130084. doi:10.1098/rsob.130084

[179] Nietmann, P., Bodenschatz, J. E. F., Cordes, A. M., Gottwald, J., Rother-Nöding, H., Oswald, T., & Janshoff, A. (2022). Epithelial cells fluidize upon adhesion but display mechanical homeostasis in the adherent state. *Biophys. J. 121*(3), 361–373. doi:10.1016/j.bpj.2021.12.042

[180] Fritzsche, M., Erlenkämper, C., Moeendarbary, E., Charras, G., & Kruse, K. (2016). Actin kinetics shapes cortical network structure and mechanics. *Sci. Adv. 2*(4), e1501337. doi:10.1126/sciadv.1501337

[181] Svitkina, T. M. (2020). Actin Cell Cortex: Structure and Molecular Organization. *Trends Cell. Biol. 30*(7), 556–565. doi:10.1016/j.tcb.2020.03.005

[182] Homma, K., Yoshimura, M., Saito, J., Ikebe, R., & Ikebe, M. (2001). The core of the motor domain determines the direction of myosin movement. *Nature*, *23*(412), 831–834. doi:10.1038/35090597

[183] Bovellan, M., Romeo, Y., Biro, M., Boden, A., Chugh, P., Yonis, A., ... Charras, G. (2014). Cellular control of cortical actin nucleation. *Curr. Biol. 24*(14), 1628–1635. doi:10.1016/j.cub.2014.05.069

[184] Liman, J., Bueno, C., Eliaz, Y., Schafer, N. P., Waxham, M. N., Wolynes, P. G., ... Cheung, M. S. (2020). The role of the Arp2/3 complex in shaping the dynamics and structures of branched actomyosin networks. *PNAS*, *117*(20), 10825–10831. doi:10.1073/pnas.1922494117

[185] Zidovska, A. (2020). The rich inner life of the cell nucleus: dynamic organization, active flows, and emergent rheology. *Biophys. Rev. 12*, 1093–1106. doi:10.1007/s12551-020-00761-x

[186] Nishimura, Y., Shi, S., Zhang, F., Liu, R., Takagi, Y., Bershadsky, A. D., ... Sellers, J. R. (2021). The formin inhibitor SMIFH2 inhibits members of the myosin superfamily. *J. Cell Sci. 134*(8), jcs253708. doi:10.1242/jcs.253708

[187] Chan, C. J., Ekpenyong, A. E., Golfier, S., Li, W., Chalut, K. J., Otto, O., ... Lautenschläger, F. (2015). Myosin II Activity Softens Cells in Suspension. *Biophys J. 108*(8), 1856–1869. doi:10.1016/j.bpj.2015.03.009

[188] Carramusa, L., Ballestrem, C., Zilberman, Y., & Bershadsky, A. D. (2007). Mammalian diaphanous-related formin Dia1 controls the organization of E-cadherin-mediated cell-cell junctions. *J. Cell Biol. 120*, 3870–3882. doi:10.1242/jcs.014365

[189] Rao, M. V., & Zaidel-Bar, R. (2016). Formin-mediated actin polymerization at cell–cell junctions stabilizes E-cadherin and maintains monolayer integrity during wound repair. *Mol. Biol. Cell*, *27*(18), 2844–2856. doi:10.1091/mbc.E16-06-0429

[190] Isogai, T., Van der Kammen, R., Leyton-Puig, D., Kedziora, K. M., Jalink, K., & Innocenti, M. (2015). Initiation of lamellipodia and ruffles involves cooperation between mDia1 and the Arp2/3 complex. *J. Cell Sci. 128*(20), 3796–3810. doi:10.1242/jcs.176768

[191] Sandbo, N., & Dulin, N. (2011). The actin cytoskeleton in myofibroblast differentiation: Ultrastructure defining form and driving function. *Trans. Res. 158*(4), 181–196. doi:10.1016/j.trsl.2011.05.004

[192] Sanchez-Alvarez, M., Zhang, Q., Finger, F., Wakelam, M. J. O., & Bakal, C. (2015). Cell cycle progression is an essential regulatory component of phospholipid metabolism and membrane homeostasis. *Open Biol. 5*(9), 150093. doi:10.1098/rsob.150093

[193] Derangeon, M., Spray, D. C., Bourmeyster, N., Sarrouilhe, D., & Hervé, J.-C. (2009). Reciprocal influence of connexins and apical junction proteins on their expressions and functions. *BBA - Biomemb. 1788*(7), 768–778. doi:10.1016/j.bbamem.2008.10.023

[194] Goh, W. I., & Ahmed, S. (2012). mDia1-3 in mammalian filopodia. *Commun. Integr. Biol. 5*(4), 340–344. doi:10.4161/cib.20214

[195] Young, K. G., Thurston, S. F., Copeland, S., Smallwood, C., & Copeland, J. W. (2008). *Mol. Biol. Cell*, *19*(12), 5168–5180. doi:10.1091/mbc.e08-05-0469

[196] Gaillard, J., Ramabhadran, V., Neumanne, E., Gurel, P., Blanchoin, L., Vantard, M., & Higgs, H. N. (2011). *Mol Biol. Cell. 22*(23), 4575–4587. doi:10.1091/mbc.E11-07-0616

[197] Bartolini, F., Moseley, J. B., Schmoranzer, J., Cassimeris, L., Goode, B. L., & Gundersen, G. G. (2008). The formin mDia2 stabilizes microtubules independently of its actin nucleation activity. *J. Cell Biol. 181*(3), 523–536. doi:10.1083/jcb.200709029

[198] Isogai, T., Van der Kammen, R., & Innocenti, M. (2015). SMIFH2 has effects on Formins and p53 that perturb the cell cytoskeleton. *Sci. Rep. 5*, 9802. doi:10.1038/srep09802

[199] Watanabe, N., Kato, T., Fujita, A., Ishizaki, T., & Narumiya, S. (1999). Cooperation between mDia1 and ROCK in Rho-induced actin reorganization. *Nature Cell Biol. 1*, 136–143. doi:10.1038/11056

[200] Hotulainen, P., & Lappalainen, P. (2006). Stress fibers are generated by two distinct actin assembly mechanisms in motile cells. *J. Cell Biol. 173*(3), 383–394. doi:10.1083/jcb.200511093

[201] Katsuta, H., Okuda, S., Nagayama, K., Machiyama, H., Kidoaki, S., Kato, M., ... Hirata, H. (2023). Actin crosslinking by α-actinin averts viscous dissipation of myosin force transmission in stress fibers. *iScience*, *26*(3), 106090. doi:10.1016/j.isci.2023.106090

[202] Mellor, H. (2010). The role of formins in filopodia formation. *BBA - Mol. Cell Res. 1803*(2), 191–200. doi:10.1016/j.bbamcr.2008.12.018

[203] Daou, P., Hasan, S., Breitsprecher, D., Baudelet, E., Camoin, L., Audebert, S., ... Badach, A. (2005). Essential and nonredundant roles for Diaphanous formins in cortical microtubule capture and directed cell migration. *MBoC*, *25*(5), 549–727. doi:10.1091/mbc.e13-08-0482

[204] Watanabe, T., Noritake, J., & Kaibuchi, K. (2005). Regulation of microtubules in cell migration. *Trends Cell Biol. 15*(2), 76–83. doi:10.1016/j.tcb.2004.12.006

[205] Yamana, N., Arakawa, Y., Nishino, T., Kurokawa, K., Tanji, M., Itoh, R. E., ... Narumiya, S. (2006). The Rho-mDia1 Pathway Regulates Cell Polarity and Focal Adhesion Turnover in Migrating Cells through Mobilizing Apc and c-Src. *Mol. Cell Biol. 26*(18), 6844–6858. doi:10.1128/MCB.00283-06

[206] Kiehart, D. P. (1999). Wound healing: The power of the purse string. *9*(16), 602–605. doi:10.1016/S0960-9822(99)80384-4

[207] Pollard, T. D. (2010). Mechanics of cytokinesis in eukaryotes. *COCEBI*, *22*(1), 50–56. doi:10.1016/j.ceb.2009.11.010

[208] Chan, F.-Y., Silva, A. M., Saramago, J., Pereira-Sousa, J., Brighton, H. E., Pereira, M., ... Carvalho, A. X. (2019). The ARP2/3 complex prevents excessive formin activity during cytokinesis. *MBoc*, *30*(1), 96–1007. doi:10.1091/mbc.E18-07-0471

[209] Taffoni, C., Omi, S., Huber, C., Mailfert, S., Fallet, M., Rupprecht, J.-F., ... Pujol, N. (2020). Microtubule plus-end dynamics link wound repair to the innate immune response. *eLife*, *9*, e45047. doi:10.7554/eLife.45047

[210] Bement, W. M., Mandato, C. A., & Kirsch, M. (1999). Wound-induced assembly and closure of an actomyosin purse string in *Xenopus* oocytes. *Curr. Biol. 9*(11), 579–587. doi:10.1016/s0960-9822(99)80261-9

[211] Le, A. P., Rupprecht, J. F., Mége, R.-M., Toyama, Y., Lim, C. T., & Ladoux, B. (2021). Adhesion-mediated heterogeneous actin organization governs apoptotic cell extrusion. *Nat. Commun. 12*, 397. doi:10.1038/s41467-020-20563-9

[212] Ajeti, V., Tabatabai, A. P., Fleszar, A. J., Staddon, M. F., Seara, D. S., Suarez, C., ... Murrell, M. P. (2019). Wound healing coordinates actin architectures to regulate mechanical work. *Nat. Phys. 15*, 696–705. doi:10.1038/s41567-019-0485-9

[213] Danjo, Y., & Gipson, I. K. (1998). Actin 'purse string' filaments are anchored by E-cadherin-mediated adherens junctions at the leading edge of the epithelial wound, providing coordinated cell movement. *J. Cell Sci. 111*(22), 3323–3332. doi:10.1242/jcs.111.22.3323

[214] Gonzalez-Rodriguez, D., Maddugoda, M. P., Stefani, C., Janel, S., Lafont, F., Cuvelier, D., ... Brochard-Wyart, F. (2012). Cellular Dewetting: Opening of Macroapertures in Endothelial Cells. *Phys. Rev. Lett. 108*, 218105. doi:10.1103/PhysRevLett.108.218105

[215] Maddugoda, M. P., Stefani, C., Gonzalez-Rodriguez, D., Saarikangas, J., Torrino, S., Janel, S., ... Lemichez, E. (2011). cAMP Signaling by Anthrax Edema Toxin Induces Transendothelial Cell Tunnels, which Are Resealed by MIM via Arp2/3-Driven Actin Polymerization. *Cell Host Microbe. 10*, 464–474. doi:10.1016/j.chom.2011.09.014

[216] Boyer, L., Doye, A., Rolando, M., Flatau, G., Munro, P., Gounon, P., ... Lemichez, E. (2006). Induction of transient macroapertures in endothelial cells through RhoA inhibition by *Staphylococcus aureus* factors. *J. Cell Biol. 173*(5), 809–819. doi:10.1083/jcb.200509009

[217] Stefani, C., Gonzalez-Rodriguez, D., Senju, Y., Doye, A., Efimova, N., Janel, S., ... Lemichez, E. (2017). Ezrin enhances line tension along transcellular tunnel edges via NMIIa driven actomyosin cable formation. *Nature Comms. 8*, 15839. doi:10.1038/ncomms15839

List of Figures

List of Tables

Acknowledgements

I would like to start this very important section thanking my PhD supervisor, Dr. Marco Tarantola, for his kind -and sometimes very necessary- guidance in the process of becoming a „Doctor rerum naturalium“ myself. Since the beginning, you were always available to address any doubts or challenges I may have faced, showing a patience and passion for our shared research that I really appreciate. Thank you for your steering and corrections, and yet, for giving me the space to grow in independence and as researcher.

I would also like to thank Prof. Dr. Claudia Steinem and Prof. Dr. Sarah Köster, members of my thesis committee, for their insightful suggestions and helpful advice. Having such achieved women so closely associated to my thesis was intimidating at times out of the respect that you inspire me. Thank you for your support during the advisory sessions and for keeping your doors open in case I needed your advise. The appreciation is also extended to Prof. Dr. Stefan Klumpp, Dr. David Zwicker and Prof. Dr. Burkhard Geil, who kindly joined the evaluation committee for my defence.

I would also like to thank Prof. Dr. Andreas Janshoff for the tight collaboration and for being so helpful and patient during several Zoom sessions destined to solve my doubts. Of course, I would have not been able to perform any experiment had it not been for the efforts of the wonderful technicians at the cell labs, both at the MPIDS, and at the University; Maren, Sarah, Angela and Tabea: thank you. Katharina, I have to specially mention you, as you have helped me so much, also in defining protocols. I really appreciated it.

I need to mention as well Antje Erdman and Frauke Bergmann, from the International Max Planck Research School Physics of Biological and Complex Systems, for answering my mails like lightning regarding the more bureaucratic aspects of the doctorate. Following this line, thank you as well to the secretaries of the LFPB group and specially to Caroline Siebert.

Leaning now towards my dear sources of moral support: thanks to all my MPIDS colleagues for sharing hardships in between coffees, teas and cakes. It was wonderful to share this time with all of you. I'll miss the breaks at the terrace. Also thanks to everybody who, even in the lack of snacks, has supported me by simply being kind and making life fun. Thanks as well to those of you that albeit in the distance -except for those wonderful occasions in which we crossed countries to hug and laugh together-, have shown me the wonders of friendship once more. Nanos, això va especialment per vosaltres, ja ho sabeu! Aviat totes i tots doctores; festa a mundo?

A la meva meravellosa família: moltes gràcies pel vostre suport, els ànims i les visites. Us he trobat a faltar però ha valgut la pena, ja sabeu que us estimo molt!

Torben, thank you feels quite short here. I love that you've been by my side almost since the beginning of this adventure; I hope you're ready for some more!

Finally, thank you to my PhD. Weirdly enough, you've allowed me to get to know myself better. This work starts with a quote from Terry Pratchett that I find very fitting to the process of becoming an independent researcher. It comes to this: mistakes will be made, but even from these we can learn. I find it a good life philosophy, and decided to apply it to the cover of the thesis, which is the beautiful result of an unsuccessful staining. Hence, to the future mistakes, *Prost*! I can say the following now:

„I am ready to face any challenge that might be foolish enough to face me.“
-Dwight Schrute

Supplementary information

Statistical comparison of WT and dKo fibroblasts regarding cell layer integrity

Supplementary figures 1 and 2 show the complete analysis of statistical significance corresponding to the simplified figure 6.6 (page 120). For more information refer to the text.

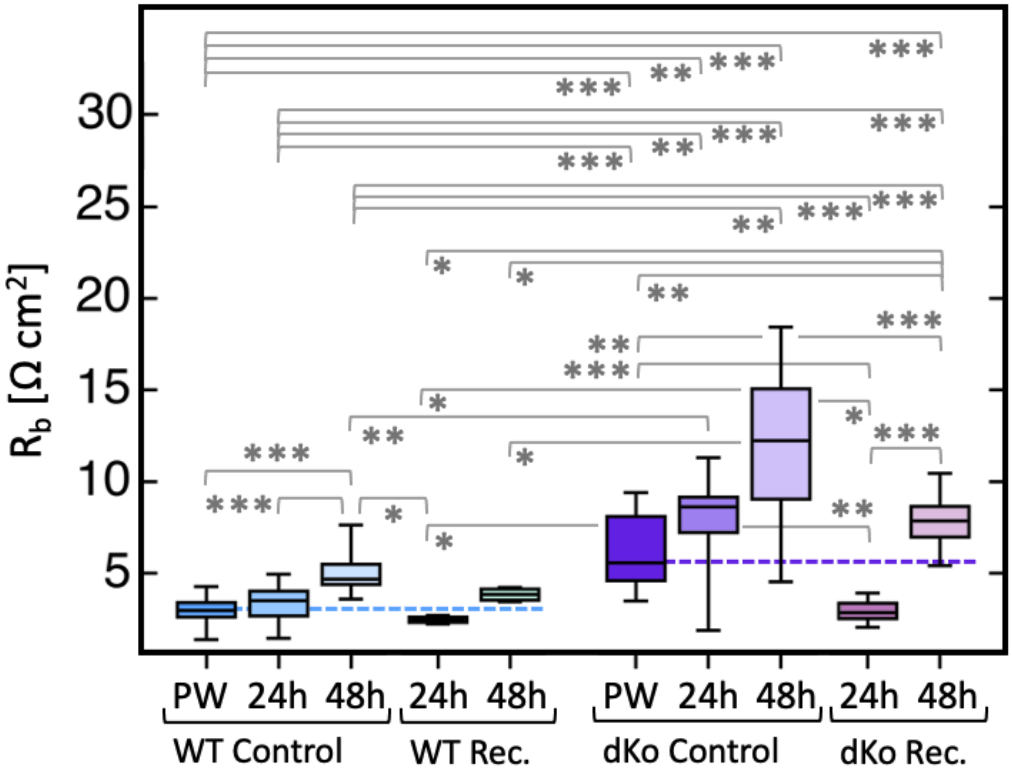

SI figure 1: **Evolution of junctional resistance of WT and dKo cells upon growth and recovery.** R_b values obtained upon fitting discrete intervals of impedance time courses to the Lo-Ferrier model are presented for WT (■; n = 2, m = 2) and dKo (■; n = 33, m = 7) cells that have been wounded and for their respective positive controls (■; n = 20, m = 14 and ■; n = 7, m = 7). With respect to the characteristic R_b of the initial monolayer (PW; t = 0 h), indicated with the dotted line, the junctional resistance of undisturbed WT fibroblasts increases until the end of the experiment as a result of monolayer maturation and formation of cell-cell contacts. In contrast, wounded cells show a decreased resistance after 24 h of recovery that surpasses, though non-significantly, the PW R_b values after 48 h. DKo fibroblasts present the same pattern. However, their characteristic R_b values are overall significantly higher than their corresponding equivalents on WT cells. Significance denoted with [*] for $\alpha < 0.05$, [**] for $\alpha < 0.01$, and [***] for $\alpha < 0.001$.

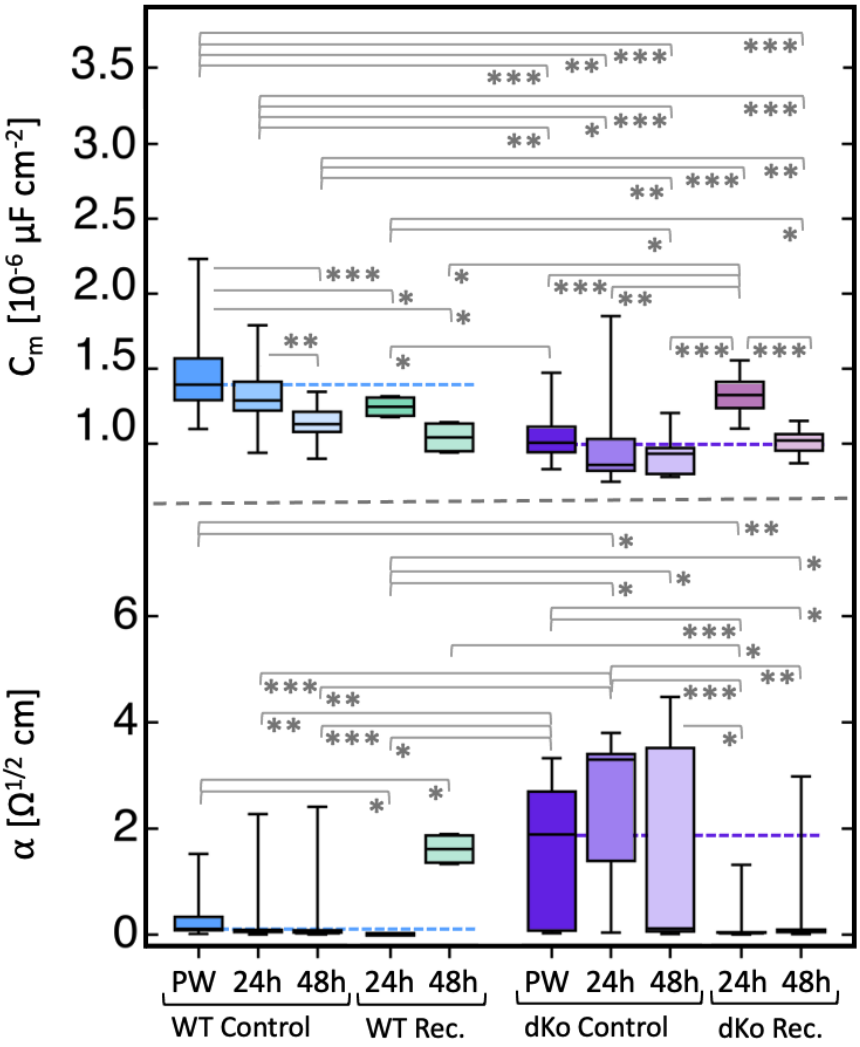

SI figure 2: **Evolution of the Lo-Ferrier parameters C_m and α of WT and dKo cells upon growth and recovery.** Values are presented for WT (■; n = 2, m = 2) and dKo (■; n = 33, m = 7) cells that have been wounded and for their respective positive controls (■; n = 20, m = 14 and ■; n = 7, m = 7). In control samples, C_m values decrease in time, both for WT and dKo cells. Upon wounding, the same pattern is observed for WT fibroblasts. In contrast, dKo cells present an increase in capacitance that is later lowered to pre-wounding (PW; t = 0 h) values (dotted lines). Inversely reflecting the basal-substrate distance, α values present high variability. For WT cells, α values decrease with time on control samples, whereas upon 48 h of recovery, are highly increased. In contrast, control dKo samples show high α values that result significantly decreased upon wounding. Significance denoted with [*] for $\alpha < 0.05$, [**] for $\alpha < 0.01$, and [***] for $\alpha < 0.001$.